Reactive transport models of low permeability structured porous and fractured media

Jesús Fernández Águila

Doctoral Thesis UDC 2017 (reduced version)

Advisor: Francisco Javier Samper Calvete

Civil Engineering Ph.D. Program

Civil Engineering School

UNIVERSIDADE DA CORUÑA

Modelos de transporte reactivo en medios porosos y fracturados estructurados de baja permeabilidad

Jesús Fernández Águila

Tesis Doctoral UDC 2017 (versión reducida)

Director: Francisco Javier Samper Calvete

Programa de Doctorado en Ingeniería Civil

E.T.S. Ingenieros de Caminos, Canales y Puertos

UNIVERSIDADE DA CORUÑA

Dr. Francisco Javier Samper Calvete, Ph.D. from University of Arizona (USA) and the Polytechnical University of Madrid (Spain), Full Professor, certifies that this doctoral thesis, entitled **Reactive transport models of low permeability structured porous and fractured media**, has been performed by Jesús Fernández Águila under his supervision in order to obtain the Doctor of Philosophy degree with the International Mention by the University of A Coruña.

Dr. Francisco Javier Samper Calvete, Doctor por la Universidad de Arizona (EEUU) y por la Universidad Politécnica de Madrid (España), Catedrático de Universidad, certifica que la tesis doctoral con título, ***Reactive transport models of low permeability structured porous and fractured media****, ha sido desarrollada por Jesús Fernández Águila bajo su supervisión para obtener el grado de Doctor y con Mención Internacional por la Universidad de A Coruña.*

A Coruña, November 2017

A Coruña, Noviembre 2017

Jesús Fernández Águila	Dr. F. Javier Samper Calvete
PhD. Student	Advisor
Doctorando	*Director*

After the public defense of the Doctoral Thesis of Jesús Fernández Águila, this Dissertation Committee have decided to award this Doctoral Thesis with a mark of:

_____

Habiendo deliberado tras el acto de defensa pública de la Tesis Doctoral realizada por Jesús Fernández Águila, este Tribunal ha decidido otorgar a dicha tesis la calificación de:

_____

For the records and for the appropriate action, this is signed in A Coruña on 9th February 2018.

Y para que conste, a los efectos oportunos, se firma la presente en A Coruña, a 9 de Febrero de 2018.

Chairman / *Presidente* **Paloma Gómez González**	
Commitee Member / *Vocal* **Wilfried Pfingsten**	
Committee Secretary/ *Secretario* **Luis Montenegro Pérez**	

ACKNOWLEDGEMENTS

Almost 4 years ago I started this path and now that the end is near I want to thank everyone who with their help have been made possible to carry out this dissertation. Firstly, this dissertation would not have been possible without its advisor, Javier Samper, who has given me the opportunity to work with him and be part of his research group. I thank him for everything he has taught me, as well as for the confidence he has shown me during this time.

I thank the Ministry of Economy and Competitiveness (Government of Spain) for the grant I was awarded within the National Programme for the Promotion of Talent and its Employability. This grant has funded my entire predoctoral stage and has allowed me to carry out two stays in the research centres at PSI (Villigen, Switzerland) and CIEMAT (Madrid, Spain) of 3 months each. This dissertation has been developed within the framework of research projects funded by ENRESA, the European Commission (CEBAMA project) and the CICYT (CGL2012-36560 project, which had the research grant associated with).

I would specially like to highlight the work carried out during the course of this dissertation for the numerical modelling on the site of the Centralised Temporary Storage (CTS) of Villar de Cañas (Cuenca, Spain). I have been involved in this project since the first day I started this dissertation and, despite its complexity, I have learned many things working in this project. I thank Juan Carlos Mayor and Jesus Mª Suso for their trust and support in this project.

I would like to thank also all the members of the LES group of the PSI for the kindness I was treated with. I especially thank Wilfried Pfingsten and Georg Kosakowski for their kindness and for making possible this stay. The time that I spent in Switzerland was a very enriching experience. Thanks also to Jenna Poonoosamy with whom I have exchanged many emails during these years.

I would like to thank the members of CIEMAT who treated me as if I were a member of their team from the first day I arrived in Madrid. They made very pleasant my stay at their centre. I thank especially Javier Peña and Paloma Gómez for their attention and help during the stay.

I would like to thank also all my colleagues of the research group *Agua y Suelo* with whom I have shared these years and I wish them all the best. Many thanks to Bruno Pisani, Alba Mon, Luis Montenegro and Acacia Naves.

Finally, I dedicate this dissertation to my parents Suso and Luisa. Thank you for a never-ending support and for trusting me more than myself

AGRADECIMIENTOS

Hace casi 4 años que empezó este camino y ahora que el final está próximo quiero dar las gracias a todas las personas que con su ayuda han hecho factible realizar esta tesis doctoral. En primer lugar, esta tesis no hubiese sido posible sin su director, Javier Samper, quien me ha dado la oportunidad de trabajar con él y formar parte de su equipo de investigación. Le agradezco todo lo que me ha enseñado y también la confianza que me ha demostrado durante todo este tiempo.

Agradezco al Ministerio de Economía y Competitividad por la concesión de una beca del Programa Estatal de Promoción del Talento y su Empleabilidad en I+D+i. Esta beca FPI ha financiado toda mi etapa predoctoral y me ha permitido realizar dos estancias en los centros de investigación PSI (Villigen, Suiza) y CIEMAT (Madrid, España) de 3 meses de duración cada una de ellas. Esta tesis se enmarca dentro de proyectos de investigación financiados por ENRESA, por la Comisión Europea (proyecto CEBAMA) y por la CICYT (proyecto CGL2012-36560 al que se le asignó la beca FPI).

Quiero destacar especialmente los trabajos realizados durante el desarrollo de esta tesis doctoral para la modelización numérica en el emplazamiento del Almacén Temporal Centralizado (ATC) de Villar de Cañas (Cuenca, España). He trabajado en este proyecto desde el primer día que comencé esta tesis y a pesar de su complejidad he aprendido muchas cosas trabajando en este proyecto. Le doy las gracias a Juan Carlos Mayor y a Jesús Mª Suso por su confianza y ayuda en este proyecto.

Me gustaría agradecer también a todos los miembros del grupo LES del PSI por lo bien que me han tratado durante mi estancia en este centro. Agradezco especialmente a Wilfried Pfingsten y a Georg Kosakowski por su amabilidad y por hacer posible mi estancia en el PSI. La estancia en Suiza fue una experiencia muy enriquecedora. Gracias también a Jenna Poonoosamy con la que he intercambiado tantos correos durante estos años.

Quiero dar las gracias a los integrantes del CIEMAT que me trataron como uno más desde el primer día que llegué a Madrid y contribuyeron a que la estancia que realicé en este centro fuese muy agradable. Debo agradecer muy especialmente a Javier Peña y a Paloma Gómez por lo mucho que estuvieron pendientes de mí y por todo lo que me ayudaron.

También quiero agradecer a todos los compañeros del grupo de *Agua y Suelo* con los que he compartido el día a día durante estos años y a los que les deseo todo lo mejor. Muchas gracias a Bruno Pisani, Alba Mon, Luis Montenegro y Acacia Naces.

Por último, dedico esta tesis doctoral a mis padres Suso y Luisa. Gracias por vuestro apoyo incondicional y por confiar en mí más que yo mismo.

Reactive transport models of low permeability structured porous and fractured media

Abstract

Groundwater flow and reactive transport models are essential tools for the analysis of coupled physical, chemical and biological processes in Earth systems. This dissertation aims at improving flow and reactive transport models of low-permeability structured porous and fractured media and applying them to radioactive waste disposal. These improvements were implemented in the codes of the CORE series. CORE^{2D}V5 was improved to deal with the feedback effect of porosity changes due to mineral dissolution/precipitation. Model and code improvements have been tested with laboratory data and with code benchmarking. In addition, reactive transport models have been performed to hydrogeological field conditions such as the Centralised Temporary Storage (CTS) facility in Villar de Cañas (Cuenca), Spain which will host the spent fuel and high-level radioactive waste (HLW) from the Spanish nuclear power plants. Groundwater flow and reactive transport models of the CTS site have been most useful to: 1) Confirm the hydrogeological conceptual model; 2) Quantify hydraulic heads, groundwater flows and groundwater balance; 3) Evaluate the impact of the construction of the facility on hydraulic heads; 4) Evaluate the impact of the water supply pumping well; and 5) Study the hydrogeochemical patterns of the site and the time evolution of gypsum affected by dissolution.

Modelos de transporte reactivo en medios porosos y fracturados estructurados de baja permeabilidad

Resumen

Los modelos de flujo subterráneo y transporte reactivo son herramientas esenciales para analizar procesos acoplados físicos, químicos y biológicos. El principal objetivo de esta Tesis Doctoral es la mejora de modelos de flujo y transporte reactivo en medios porosos y fracturados de baja permeabilidad para su aplicación en almacenamientos de residuos radioactivos. Se han implementado mejoras en los códigos de la serie CORE. CORE^{2D}V5 ha sido actualizado para la retroalimentación de la porosidad debido a la disolución/precipitación de minerales. Las mejoras en modelos y códigos han sido comprobadas con datos medidos y con otros códigos. Además, modelos de transporte reactivo se han aplicado a sistemas hidrogeológicos reales como en el emplazamiento del Almacén Temporal Centralizado (ATC) de Villar de Cañas (Cuenca, España) que almacenará combustible gastado y residuos radioactivos de alta actividad (RAA) de centrales nucleares españolas. Los modelos realizados han servido para: 1) Confirmar el modelo conceptual hidrogeológico; 2) Cuantificar los niveles piezométricos, velocidades de flujo y balance de las aguas subterráneas; 3) Evaluar el impacto de la construcción del ATC sobre los niveles piezométricos; 4) Evaluar los efectos del pozo de bombeo; y 5) Estudiar la hidrogeoquímica de la zona y la evolución temporal de la disolución de yeso.

Modelos de transporte reactivo en medios porosos e fracturados estruturados de baixa permeabilidade

Resumo

Os modelos de fluxo subterráneo e transporte reactivo son ferramentas esenciais para analizar procesos acoplados físicos, químicos e biolóxicos en sistemas terrestres. O principal obxectivo desta Tese Doutoral é a mellora dos modelos de fluxo e transporte reactivo en medios porosos e fracturados de baixa permeabilidade para a súa aplicación en almacenamentos de residuos radioactivos. Implementáronse melloras nos códigos de transporte reactivo da serie CORE. CORE^{2D}V5 foi actualizado para a retroalimentación da porosidade debido a disolución/precipitación de minerais. As melloras nos modelos e códigos comparáronse cos datos medidos e con outros códigos. Ademais, modelos en medios porosos e fracturados aplicáronse a sistemas hidroxeológicos reais como no emprazamento do Almacén Temporal Centralizado (ATC) de Villar de Cañas (Cuenca, España) que almacenará o combustible gastado e os residuos radioactivos de alta actividade (RAA) das centrais nucleares españolas. Os modelos numéricos realizados foron moi útiles para: 1) Confirmar o modelo conceptual hidroxeolóxico; 2) Cuantificar os niveis piezométricos, as velocidades de fluxo e o balance das augas subterráneas; 3) Avaliar o impacto da construción do ATC sobre os niveis piezométricos; 4) Avaliar os efectos do pozo de bombeo; e 5) Estudar os patróns da hidroxeoquímica da zona e a evolución temporal da disolución de xeso.

Preface

The discipline of reactive transport modelling draws on numerous fields in the Earth sciences, including hydrology, geochemistry, biogeochemistry, soil physics and fluid dynamics. Numerical formulations of reactive transport in porous media inherit all of the difficulties associated with these individual disciplines and then introduce additional complexities related to the coupling of processes. Since its inception a few decades ago, the field of reactive transport models in the geosciences has evolved to allow for more realistic numerical representations of nature. Applications of reactive transport models include geothermal systems, nuclear waste repositories, geological carbon dioxide storage and environmental remediation.

The main objective of this dissertation is the improving and the updating of the flow and reactive transport models of low permeability structured porous and fractured media for their application in radioactive waste storage and disposal. Improvements have been implemented in the conceptual models and reactive transport codes of the CORE series developed at the University of A Coruña since 1991. Most of the improvements have been performed in the code CORE^{2D}V5, although updates have been performed also in other codes such as INVERSE-CORE^{2D}, BIOCORE^{2D} and CORE^{3D} (TRANMEF-3D). Particularly noteworthy is the extension of CORE^{2D}V5 to take into account porosity changes due to mineral precipitation/dissolution and dynamically update the flow, transport and chemical parameters. In addition, flow and reactive transport models have been performed during the course of this dissertation to simulate laboratory and field-scale test. Models and code improvements have been checked against measured data and other codes (*benchmarking*).

The safety assessment of disposal facilities for radioactive waste requires the use of reactive transport models. The long-term management of radioactive waste envisages the disposal of high-level radioactive waste (HLW) from nuclear power plants in low permeability media. High-level radioactive waste usually are stored first in a Centralised Temporary Storage (CTS) facility and later in a deep geological repository (DGR). A large research effort has been devoted in the field of the radioactive waste repositories which in Spain has been promoted by ENRESA (Empresa Nacional de Residuos Radiactivos S.A.). The most important research carried out by ENRESA have been those related to the DGR. However, the Government of Spain has prioritized the construction of a CTS instead of DGR in recent years.

DGR is based on a multibarrier concept which combines natural barriers such as the geological formation and artificial barriers including the chemical forms of the waste, the metallic container, and the clay and concrete buffer and sealing materials. Reactive transport models are tools that help to understand and predict the time evolution of a DGR. In this dissertation, a long-term reactive transport

model of the interactions of concrete, compacted bentonite and clay in a HLW repository in clay have been performed by taking into account the porosity changes due to mineral dissolution/precipitation reactions. In addition, reactive transport models have been performed to simulate the non-linear sorption behaviour of caesium through Opalinus clay which is considered as a potential host rock for radioactive waste repositories.

On the other hand, CTS is a storage system designed to host the spent fuel and HLW for a limited time period. On 30 December 2011, the Government of Spain designated the municipality of Villar de Cañas in Cuenca (Spain) as the site to build a Centralised Temporary Storage (CTS) which will storage all spend fuel and HLW from Spanish nuclear power plants for 60 years. From the beginning of 2012, ENRESA has been working on the characterisation of the CTS site and the detailed design of the facility. As part of the characterization work, groundwater flow, heat transport, groundwater age, hydrogeochemical mixing and reactive transport models have been performed at the CTS site. These mathematical models are a very important part of this dissertation. The numerical models of the CTS site have been most useful to: 1) Confirm the hydrogeological conceptual model; 2) Quantify the hydraulic heads, groundwater flows and groundwater balance; 3) Evaluate the impacts of the construction of the facility on hydraulic heads; 4) Evaluate the impact of the water supply pumping well; and 5) Study the hydrogeochemical patterns of the site and the time evolution of gypsum affected by dissolution.

Finally, a parametric and numerical analysis of the estimation of groundwater recharge from water table fluctuations (WTF method) in unconfined aquifers with 1-D and 2-D deterministic and stochastic models have also been carried out in this dissertation. The objective of this analysis is to quantify the errors made when the groundwater recharge is estimated from water table rises recorded in wells near a river. The numerical models have been applied to the Guadalquivir River alluvial aquifer in Andújar (Jaén, Spain) near the uranium mill tailing plant which operated from 1957 until 1981.

Contents

List of Figures

List of Tables

List of term and abbreviations

Greek Terms

α	Leakage coefficient
α_D	Angle between the direction of the first component of the diffusion coefficient tensor and the *x*-coordinate
α_L, α_T	Longitudinal and transverse dispersivities
α^*, λ^*, Φ_1, ξ_l, β^*, γ^*, θ^*, μ^*, α_1, α_2	Arbitrary constants
Δt	Time increment
Δx	Grid size of the finite element mesh
ε_{max}	Maximum absolute value of relative change in pressure heads at all nodes of an unsaturated flow model
Γ	Boundary of the model
γ_i	Activity coefficient of the *i*-th dissolved primary species
δ	Constrictivity
ϕ	Porosity
ϕ_{ac}	Accessible porosity
ϕ_0	Initial or reference porosity
ϕ^t, ϕ^{t+1}	Porosities for the time steps *t* and *t+1*
$\boldsymbol{\lambda}$	Thermal conductivity tensor
η_{mk}	Order of kinetic reactions
ν_{ij}	Stoichiometric coefficient of the *i*-th primary species in the dissociation reaction of the *j*-th secondary species
ν_{mi}^p	Stoichiometric coefficient of the dissolution reaction of the *m*-th solid phase
θ	Volumetric water content
θ_{mk}	Experimental parameter of kinetic reactions
σ^2	Variance
ρ	Water density
ρ_m	Bulk density
ρ_s	Density of the solids
τ	Medium tortuosity
τ^*	Tortuosity factor
ψ	Pressure head
Ω_m	Ratio between the ion activity product and the equilibrium constant
ω	Specified convergence tolerance
$\nabla\cdot(\ )$	Divergence operator
$\nabla(\ )$	Gradient operator

Latin Terms

A	Area of models
A_m	Specific surface area of the *m*-th mineral
A_m^t, A_m^{t+1}	Specific surfaces of the *m*-th mineral for the time steps *t* and *t+1*
A_0	Constant representing the specific surface area
a, a_1, a_2	Arbitrary constants
a^{pmki}	Catalytic effect factor
B_p, B_q, B_r	Rate of consumption of the *p*-th substrates, *q*-th electron and *r*-th nutrient due to microbial processes
b_i^e, c_i^e	Coefficients of the *e*-th element which depend on the geometry of the element
C_a^{ie}	Concentration of the *ie*-th electron acceptor
C_b^i	Aqueous concentration of *i*-th microbe of the *b* biotic species
C_c^p	Competition and/or metabolic factor for microbial species
C_j	Total concentration of *j*-th aqueous primary species
C_j^*	Dissolved concentration of external fluid sources *w*
C_s^p ,C_a^q, C_n^r	Concentration of the *p*-th substrate, the *q*-th electron acceptor and *r*-th nutrient
C_{01}, C_{02}	Initial concentrations estimated by INVERSE-CORE^{2D}
C_{B1}, C_{B2}	Boundary concentrations estimated by INVERSE-CORE^{2D}
C_1, x_0	Integration constants
$c(t)$, $c(t-1)$	Concentrations at the time steps *t* and *t-1*
c_i	Concentration of *i*-th primary species
c_w, c_s, c_m	Specific heat of water, solids and bulk porous medium
$\boldsymbol{D}$	Dispersion tensor
D_a	Apparent diffusion coefficient
$\boldsymbol{D_e}$	Effective diffusion tensor
D_e	Effective diffusion coefficient
$\boldsymbol{D_h}$	Hydrodynamic dispersion tensor
D_x, D_y	First and second principal components of the diffusion coefficient tensor
D_0	Pore diffusion coefficient in pure water
E_a	Apparent activation energy of the reaction
e	Aquifer thickness
$f_a^{i,j,q}$	Coefficient of proportionality between consumed substrate and consumed electron acceptor
f_{ea}^i	Electron acceptor consumption coefficient of the *i*-th microbe endogenous process
f_m	Volume fraction of the *m*-th mineral
$f_n^{i,j,r}$	Coefficient of proportionality between consumed substrate and consumed nutrient
$G^{i,k}$	Microbial growth factor of *i*-th microbe in its *k*-th growth phase
$G_L^{i,k}$	Lag factor which accounts for the time elapsed since a microbe encounter a substrate to the time it is able to build the enzymatic system required to use it

$G_{pH}^{i,k}$	Environment limitation (pH) of *i*-th microbe in its *k*-th growth phase
$G_{T}^{i,k}$	Environment limitation (temperature) of *i*-th microbe in its *k*-th growth phase
H	Specified head
h	Hydraulic head
h_i^e	Hydraulic head in the *i*-th node of the *e*-th element
h_0	Initial head
$\boldsymbol{I}$	Identity tensor
IAP	Ion activity product
i_{emax}	Node number with convergence problems in unsaturated flow models
$\boldsymbol{K}$	Saturated hydraulic conductivity tensor
K	Solubility constant of minerals
K_a^{ie}	Half-saturation constant of the *ie*-th electron acceptor
$K_b^{i,k}$	Growth constant of *i*-th microbe of the *k*-th growth process of the *b* biotic species
K_d	Adsorption-desorption distribution coefficient
K_d^i	Decay rate of the *i*-th microbe
K_j	Equilibrium constant of *j*-th chemical reaction
K_r	Relative hydraulic conductivity
K_s^p, K_a^q, K_n^r	Half-saturation constant of the *p*-th substrate, the *q*-th electron acceptor and the *r*-th nutrient
K_{sel}	Selectivity coefficient for cation exchange
K_{xx}^e, K_{xy}^e, K_{yy}^e	Components of the hydraulic conductivity tensor in the *e*-th element
K_1, K_2	First and second principal components of the hydraulic conductivity tensor
k	Intrinsic permeability
k_{mk}	Kinetic rate constant of the *k*-th kinetic reaction of the *m*-th mineral
k_{rl}	Relative permeability
k_0	Initial or reference permeability
L	Length of aquifer
$M^{i,k}$	Overall limiting factor of *i*-th microbe of the *k*-th growth process
$M_s^{i,k}$, $M_a^{i,k}$,$M_n^{i,k}$	Limitation factor of substrates, electron acceptors and nutrients of *i*-th microbe of the *k*-th growth process
m	Cementation exponent
m	Number of elements of the finite element mesh in the output files in VTK format
m, n, α	Constants of the van Genuchten equation
N_b	Total number of microbial species
N_c	Number of primary species
N_k	Number of kinetic mineral dissolution/precipitation reaction
N_p	Total number of minerals involved in dissolution/precipitation reactions
N_R	Number of chemical reactions

N_x	Number of aqueous secondary species
n	Number of nodes of the finite element mesh in the output files in VTK format
$\boldsymbol{n}$	Unit vector normal to the boundary of the model pointing outwards
P	Concentration of the mineral phase
p	Number of components of the connectivity matrix in the VTK output files
p^{mki}	Dimensionless parameter for the *i*-th aqueous species of the *m*-th mineral in the *k*-th kinetic reaction
p_{k1}, p_{k2}	Catalytic exponent estimated by INVERSE-CORE^{2D}
Q	Specified water flux
Q_i^p	Chemical formulae of *i*-th primary
Q_j^s	Chemical formulae of *j*-th secondary species
$\boldsymbol{q}$	Darcy's velocity
q_x^e, q_y^e	Components of the Darcy's velocity vector in the *e*-th element
R	Gas constant
R	Groundwater recharge rate
R	Retardation coefficient factor of the advection-dispersion equation
R_j	Chemical sink/source term which includes all the chemical interactions of the *j*-th component with solid species
R_m	Reaction rate
r_i	Sink/source term of *i*-th primary aqueous species associated to mineral associated to mineral kinetically-controlled reactions
r_m	Mineral dissolution/precipitation rate of *m*-th mineral
S	Reactive surface area of the mineral
S_l	Liquid saturation degree
S_s	Specific storage coefficient
S_s^p	Inhibition/stimulation factor of the *p*-th substrate
S_y	Specific yield
S_w	Water saturation degree
s	Level rise/drawdown
s	Concentration of sorbed species
s_m	Factor for dissolution (1) and precipitation (-1) of *m*-th mineral
s_{plan}, $s_{Type\text{-}II}$, s_{FES}	Cation exchange sites
T	Temperature
T	Transmissivity
T_s	Mean temperature of the solid
t	Time
V_m	Mineral molar volume
$V_n(t)$, $V_n(t\text{-}1)$	Nodal water volumes at the time steps *t* and *t-1*
V_x, V_y, V_z	Components of the water flow velocity vector

w	Specific fluid sink/source
x_j	Concentration of j-th secondary species
$Y_s^{i,j,p}$	Yield coefficient of the p-th substrate being used by the i-th microbe in its j-th growth process
z	Topographic elevation

Abbreviations

AE	Algebraic equation
AGP	Almacenamiento geológico profundo
ANDRA	Agence National Pur la Gestion des Dechets Radioactifs (France)
Äspö HRL	Äspö Hard Rock Laboratory
ATC	Almacén Temporal Centralizado
CEC	Cation exchanged capacity
CERBERUS	Control experiment with radiation of the Belgian repository for underground storage
CFCs	Chlorofluorocarbons
CIEMAT	Centro de Investigaciones Energéticas, Medioambientales y Tecnológicas
CSN	Consejo de Seguridad Nuclear
CTS	Centralised temporary storage
DEM	Digital elevation model
DGR	Deep geological repository
DOC	Dissolved organic carbon
DR	Diffusion and retention experiments
DSA	Direct substitution approach
ENRESA	Empresa Nacional de Residuos Radiactivos S.A. (Spain)
EURATOM	European Atomic Energy Community
FUA	Fábrica de uranio de Andújar
GIS	Geographic information system
GRWP	General Radioactive Waste Plan
GUI	Graphical user interface
HLW	High-level radioactive waste
IRB	Iron-reducing bacteria
JNC	Japan Nuclear Cycle Development Institute
LBI	Lutitas inferiores de Balanzas
LBS	Lutitas superiores de Balanzas
MAGRAMA	Ministerio de Agricultura, Alimentación y Medio Ambiente
masl	Meters above sea level
MDT	Modelo digital del terreno

MINETUR	Ministerio de Industria, Energía y Turismo
PDE	Partial differential equations
POC	Particular organic matter
PSI	Paul Scherrer Institut
RAA	Residuos de alta actividad
REX	Redox experiment in detailed scale
SIA	Sequential iteration approach
SKB	Swedish nuclear waste management company
SRB	SO_4^- reducing bacteria
THBC	Thermo-hydro-biological-chemical
UDC	Universidade da Coruña
UI	Unidad Inferior
UPN	Unidad Paleógena-Neógena
URL	Underground research laboratory
VTK	Visualization Toolkit
WTF	Water table fluctuations
YB	Yesos de Balanzas

CHAPTER 1. INTRODUCTION

1.1 Motivation, objectives and methodology

Understanding natural groundwater systems, quantifying groundwater pollution and assessing the performance of waste disposal facilities require modelling tools capable to simulate simultaneously groundwater flow, heat transfer, solute transport and chemical reactions such as acid-base, redox, aqueous complexation, biodegradation, surface complexation, cation exchange, mineral precipitation/dissolution and gas dissolution/exsolution. Significant progress has been made in flow and reactive transport models and codes during the last decades which have increased their use to multiple disciplines, especially in connection with the storage of radioactive waste.

The main objective of this dissertation is the improving and the updating of the flow and reactive transport models of low permeability structured porous and fractured media for their application in radioactive waste storage. To achieve this objective, the following activities were carried out:

1) Updating and improving the conceptual and numerical models and the flow and reactive transport codes of the CORE series developed at the University of A Coruña. These activities included:
    a. Improvements in the code CORE^{2D}V5 dealing with porosity changes due to mineral precipitation/dissolution and the feedback effect on flow, transport and chemical parameters.
    b. Update of CORE^{2D}V5 to use available public-domain post-processing tools.
    c. Update of CORE^{2D}V5 to run models with purely conservative transport in an efficient manner.
    d. Update of CORE^{2D}V5 to compute and print out water velocities and boundary inflows and outflows for several types of boundary conditions.
    e. Improve the convergence criteria to solve flow in variably saturated porous media in CORE^{2D}V5.
    f. Update of INVERSE-CORE^{2D} to estimate large sets of variables.
    g. Development of a database with the microbiological input parameters of BIOCORE^{2D}.

2) Performing flow and reactive transport models for laboratory and field-scale tests. The model results obtained with the codes of the CORE series have been checked with measured data and with the model results obtained with other reactive transport codes (*benchmarking*). These activities included:
    h. Numerical flow and reactive transport models of laboratory experiments with strong porosity changes due to dissolution/precipitation reactions performed at the Paul Scherrer Institut (Switzerland).
    i. Single-species and multi-species transport models to simulate the non-linear sorption and transport of caesium through Opalinus clay.
    j. Long-term reactive transport model of the interactions of concrete, compacted bentonite and clay in a high-level radioactive waste (HLW) repository in clay taking into account the porosity changes due to mineral dissolution/precipitation reactions and the feedback on flow, transport and chemical parameters.
    k. Numerical groundwater flow and solute transport models for pumping test analysis carried out on the site of the Centralised Temporary Storage (CTS) located in Villar de Cañas (Cuenca, Spain).
3) Performing field-scale flow and reactive transport models in porous and fractured media related to radioactive waste storage. These activities included:
    l. 2-D flow models in vertical profiles at local and site scales and a fully 3-D flow model for the CTS site. These models were performed for the site characterization and predict the effect of the construction of the nuclear facilities on the hydraulic heads.
    m. 2-D heat transport, groundwater age, hydrogeochemical mixing and reactive transport models of the CTS site.
    n. A numerical analysis of the estimation of groundwater recharge from water table fluctuations in unconfined aquifers with 1-D and 2-D deterministic and stochastic models. These models were applied to the Guadalquivir River alluvial aquifer near the uranium mill tailings of Andújar (Jaén, Spain).

1.2 State-of-the-art

1.2.1 Reactive transport modelling

Reactive transport modelling is an essential tool for the analysis of coupled physical, chemical and biological processes in Earth systems. The discipline of reactive transport modelling draws on

numerous fields in the Earth sciences such as hydrology, geochemistry, biogeochemistry, soil physics and fluid dynamics. Numerical formulations of reactive transport in porous media inherit all of the difficulties associated with these individual disciplines and then introduce additional complexities related to the coupling of processes (Lichtner et al., 1996; Steefel et al., 1996).

Multicomponent reactive transport models that could treat any combination of transport and biogeochemical processes date back to the mid-1980s. Reactive transport models are based on two basic sets of equations. The transport of solutes is described by a set of partial differential equations (PDEs) while chemical processes are described by a set of nonlinear algebraic equations (AEs). In general, three major approaches have been used for solving reactive transport problems (Yeh and Tripathi, 1989) which include: 1) Coupling existing geochemical or microbiological codes to solute transport codes, 2) Direct substitution of the nonlinear chemical reactions into the transport equations leading to a set of nonlinear PDEs and 3) Sequential iteration approach (SIA) in which linear transport PDEs and nonlinear AEs are solved sequentially in an iteration manner (two-step method). The general philosophy of multicomponent reactive transport modelling is discussed in depth by Rubin and James (1973), Rubin (1983), Kirkner and Reeves (1988) and Reeves and Kirkner (1988) among others. These authors describe various solution methods and identify the optimal approaches suitable for specific chemical reactions. The numerical efficiency of these three approaches has been compared by Xu (1996), Lichtner et al. (1996) and Saaltink (1999).

In the direct substitutive approach, chemical equations are incorporated directly into the transport equations. This approach has been employed by, among others, Valocchi et al. (1981), Jennings et al. (1982), Miller and Benson (1983), Carnahan (1990), Steefel and Lasaga (1990), Xu (1996) and Saaltink et al. (1997).

The two-step method divides the solution into a transport step where the aqueous components are transported individually by advection and dispersion and a chemical step where aqueous and solid components react with each other. The two steps are coupled either sequentially or iteratively. Since the sets of equations that are solved simultaneously are much smaller than those of the direct approach, larger systems with larger sets of chemical components can be handled. The two-step method has been used by Kirkner et al. (1984), Walsh et al. (1984), White et al. (1984), Cederberg et al. (1985), Narasimhan et al. (1986), Liu and Narasimhan (1989), Yeh and Tripathi (1991) and Engesgaard et al. (1992). Lensing et al. (1994) developed a model based on the two-step method that handles both equilibrium and kinetic reactions, while Zysset et al. (1994a, b) achieved the same objective with two parallel codes.

According to Xu (1996) the sequential iteration approach (two-step method) has advantages with respect to the direct substitution approach for chemically complex large-size reactive transport problem. On the other hand, the direct substitution method can yield high accuracy for a limited number of chemical species and reactions and its disadvantage is the very high demand on computing resources, which limits the number of components, species, and reactions that can be handled (Yeh and Tripathi, 1989; Mangold and Tsang, 1991). Saaltink (1999) presented a comparison of the two methods. He concluded that the direct substitution approach (DSA) performs better numerical efficiency than the sequential iteration method for chemically complex small dimensional reactive transport problems while DSA is worse for chemically simple large dimensional problems. However, as pointed out by Cederberg et al. (1985), the sequential iteration approach takes advantage of the fact that only the physical transport equations are spatially connected, while the chemical equations depend strictly on local conditions at each point in the system.

Mangold and Tsang (1991) presented a comprehensive and systematic summary of subsurface hydrologic and hydrochemical models. A detailed comparison of the different approaches available is also presented in Volume 14, Issue 3 of the Computational Geosciences journal (2010).

The last decades have witnessed a considerable progress in reactive transport modelling. The University of A Coruña (UDC) has developed a series of general-purpose codes named as CORE dealing with non-isothermal flow and solute transport coupled with a set of comprehensive geochemical processes in porous and fractured media. One of the objectives of this dissertation is to improve and extend the capabilities of the existing CORE codes to solve for coupled thermal-hydro-bio-geochemical processes in porous and fractured media. There is a need to evaluate the capabilities and the correctness of the implemented features and the performance of reactive transport codes. This process is known as *benchmarking* and is normally done by comparing model results with analytical solutions, by reproducing results from laboratory or field experiments and by code inter-comparison. Several flow and reactive transport models have been performed with the codes of the CORE series during the course of this dissertation to simulate laboratory and field-scale tests. The model results obtained have been checked with measured data and the model results obtained with other reactive transport codes.

1.2.2 Modelling of porosity changes due to mineral dissolution/precipitation in reactive transport codes

The changes of the porosity in a porous medium due to mineral alteration processes, and the associated change of transport parameters are important processes which influence the evolution of natural geological environments or engineered underground (disposal) systems. Porosity changes in natural porous media occur normally very slowly, but in a long-term can be of pivotal importance for

the migration of fluids and solutes. If porosity increases substantially, preferential fluid migration pathways may developed, accelerating solute transport. On the other hand, a significant porosity decrease may inhibit fluid and solute transport. Clogging occurs when the porosity is close to cero and the aqueous phase may completely vanish. Porosity changes are being actively investigated in connection with the deep geological disposal of nuclear waste where chemically very different materials such as clay and concretes come into contact with one another (Gaucher and Blanc, 2006).

Porosity changes due to precipitation/dissolution reactions and their feedback on transport properties are accounted for in numerical models by considering empirical formulae such as the Kozeny-Carman for porosity/permeability (Carman, 1937) and Archie's law for porosity/diffusivity (Archie, 1942). Several computer codes handle the feedback of chemistry on flow and mass transport such as HYTEC (van der Lee and De Windt, 2001; van der Lee et al., 2003: van der Lee, 2005), TOUGHREACT (Xu et al., 2004, 2006, 2011), PHREEQC (Parkhurst and Appelo, 1999), MIN3P (Mayer et al., 2002, 2010), PHAST (Parkhurst et al., 2002) and CRUNCH (Steefel, 2001).

In this dissertation, the reactive transport code CORE^{2D}V5 (Samper et al., 2009, 2011) has been extended to take into account the porosity changes due to mineral dissolution/precipitation and dynamically update the flow, transport and chemical parameters every time step.

1.2.3 Application of reactive transport models to radioactive waste storage

The long-term management of radioactive waste envisages the disposal of high-level radioactive waste (HLW) in low permeability media. High-level radioactive waste usually are stored first in a Centralised Temporary Storage (CTS) facility and later in a deep geological repository (DGR).

DGR is based on a multibarrier concept which combines natural barriers such as the geological formation and artificial barriers including the chemical forms of the waste, the metallic container, and the clay and concrete buffer and sealing materials. Reactive transport models are tools that help to understand and predict the time evolution of a DGR (De Windt et al., 2004, 2007; Samper et al., 2008a,b; Zheng et al., 2010, 2011; Kosakowski and Berner, 2013; Berner et al. 2013; Samper et al., 2016; Mon et al.,2017). In this dissertation, a non-isothermal multicomponent reactive transport model of the long-term interactions of compacted bentonite with the corrosion products of a carbon-steel canister and the concrete liner of the engineered barrier of a HLW repositories in clay has been carried out which takes into account the porosity changes due to mineral dissolution/precipitation and the feedback on flow, transport and chemical parameters. In addition, reactive transport models have been performed in this dissertation to simulate the non-linear transport and sorption of caesium through Opalinus clay which is considered a potential host rock for radioactive waste disposal.

CTS is a storage system designed to host the spent fuel and high-level radioactive waste from nuclear power plants. The CTS facilities are the most ideal temporary solution from the security point of view since they allow the monitoring measures to be concentrated on a single facility and are the most convenient ones for leaving the way open for the eventual dismantling of the nuclear power plants themselves. These facilities have a concrete structure as a radiation shield and as security against unauthorised entries. Within the facility, the use of vaults or chambers enables the storage of a greater number of fuel assemblies at the lowest cost for both irradiated fuel and vitrified high-level radioactive waste. The results and experience accumulated by the international technical community are able to ensure the temporary storage of irradiated fuel for periods of 50 years or more. However, CTS facilities cannot be considered as a final permanent solution.

A large research effort has been devoted in the field of the radioactive waste repositories which in Spain has been promoted by ENRESA (Empresa Nacional de Residuos Radiactivos S.A.).

1.2.3.1. Centralised Temporary Storage (CTS) in Spain

On 30 December 2011, the Government of Spain designated the municipality of Villar de Cañas in Cuenca as the site of the Centralised Temporal Storage (CTS) and its Associated Technology Centre. (Figure 1.1). This facility will provide temporary storage for spent fuel and high-level radioactive waste from Spanish nuclear power plants. From the beginning of 2012, ENRESA has been working on the characterisation of the CTS site and the detailed design of the facility. In January 2014, applications for the prior (siting) authorisation and the construction permit were submitted to the Ministry of Industry, Energy and Tourism (MINETUR). These permits, granted by the MINETUR subsequent to approval by the Nuclear Safety Council (CSN), issued on 28 July 2015, and the Environmental Impact Statement from the Ministry of Agriculture, Food and the Environment (MAGRAMA), are required, along with the mandatory construction permit issued by Villar de Cañas Council, before the construction of the CTS site can begin. Once the construction of the CTS is complete, it will require an operating permit issued by the MINETUR, which must be accompanied by further authorisation from the autonomous communities and the EU (EURATOM).

The CTS has been designed for a 100-year life, although the current General Radioactive Waste Plan (GRWP) sets out an operational life of 60 years. After this time, the radioactive material will be removed for subsequent management and the facility will be dismantled, as with any other nuclear facility at the end of its operational life. The CTS will be a dry storage surface facility, ensuring the confinement of spent fuel from Spanish nuclear power plants and other high-level radioactive waste. According to the current GRWP, 12,000 m^3 of nuclear materials will be stored at the CTS site. Most of

them are spent fuel (about 20,000 fuel assemblies). There are only small quantities of vitrified waste (less than 70 canisters) and special waste.

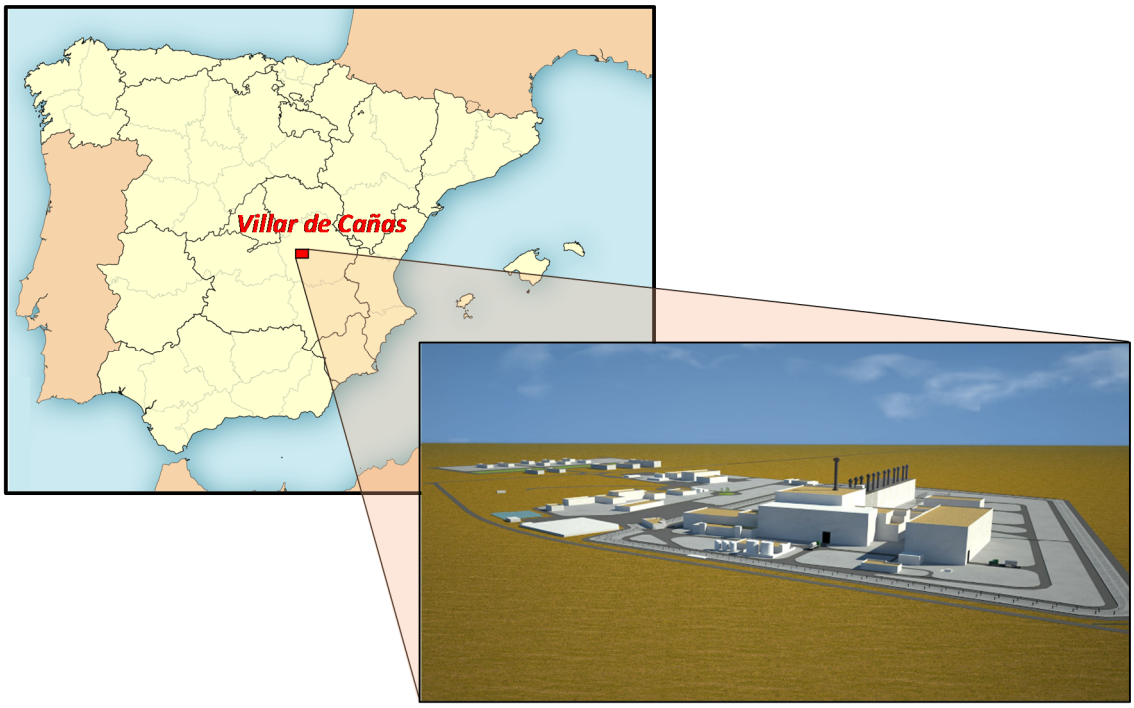

Figure 1.1. Location of the municipality of Villar de Cañas where the construction of the CTS is planned and 3-D view of the future nuclear facilities (www.enresa.es).

Several numerical flow and reactive transport models have been performed by the University of A Coruña as part of the CTS site characterization activities. These numerical flow models which have been carried out during the course of this dissertation have been performed in several stages. Two flow models in vertical profiles in East-West direction at local and site scales were carried out in the first stage of the project in June 2014 (Samper et al., 2014a). In the second stage of the project (in December 2014), the two models performed in the previous stage were updated with additional measured data and an additional numerical model in a vertical profile in North-South direction at site scale was carried out (Samper et al., 2014b). The predictions of the effects of the construction of the nuclear facilities on the hydraulic heads were also performed with the numerical model in the second stage of the project. In the third stage of the project (in September 2016), the model in a vertical profile in East-West direction at local scale was updated and the following numerical models were carried out (Samper et al., 2016): 1) A 2-D horizontal flow model to simulate a long-term pumping test carried out in the creek located east of the nuclear zone of the CTS, 2) A 2-D horizontal flow model performed to analyse the potential impact of the Chaparral pumping well on the hydrogeological conditions in the nuclear zone of the CTS and 3) A 3-D flow model at local scale. In addition, heat transport, groundwater age, hydrogeochemical mixing and reactive transport models at the CTS site have been performed. Figure 1.2 shows the domain of the all numerical models performed in this dissertation.

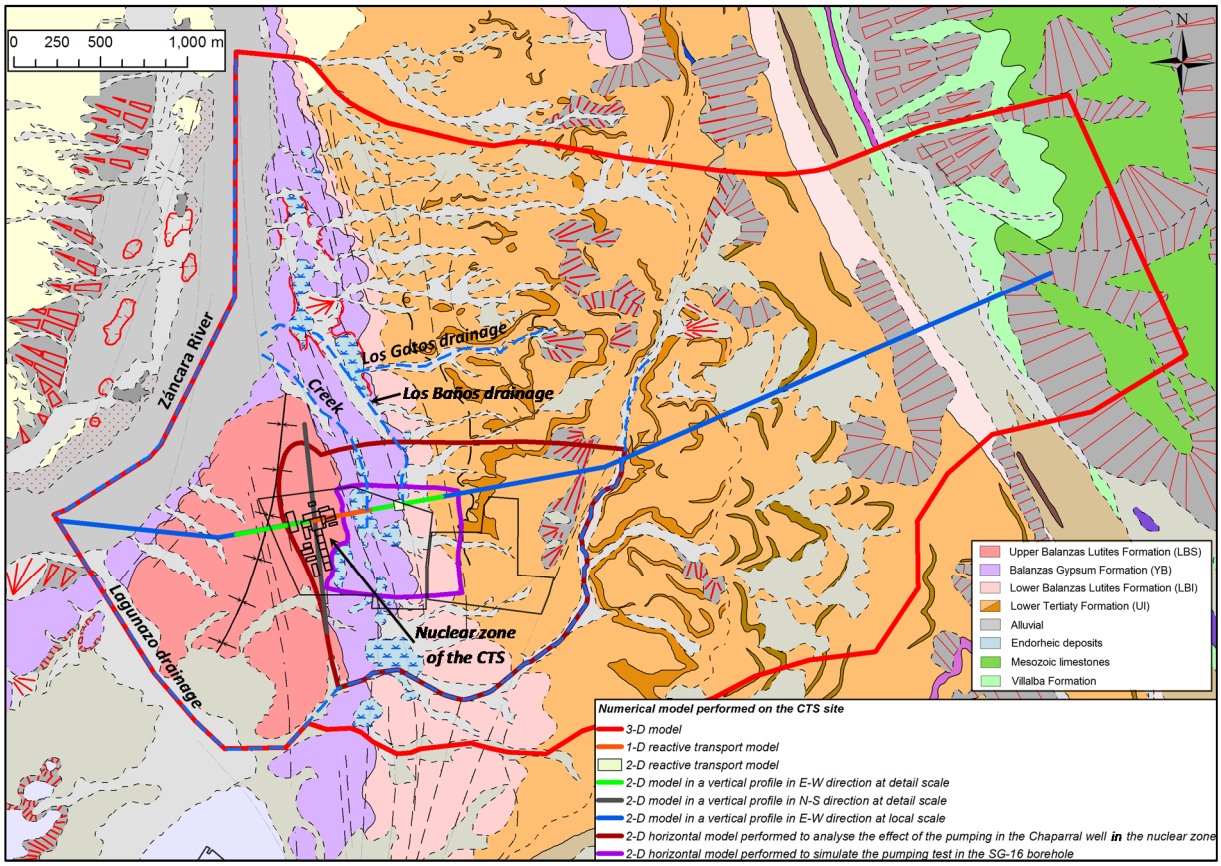

Figure 1.2. Geological map of the CTS showing the domains of the numerical models. The Záncara River, the groundwater drainages defined in the 3-D model and the nuclear zone of the CTS site are also shown.

1.3 Scope

This dissertation includes an Extended Summary with 12 chapters describing the main contents of the dissertation and 11 appendixes which present all the details of the work done in this dissertation. Appendix 11 contains the Spanish version of the Extended Summary.

Chapter 2 presents the mathematical formulation of the thermo-hydro-biological-chemical (THBC) models including the formulation implemented in CORE^{2D}V5 dealing with porosity changes due to mineral dissolution/precipitation and the feedback effect on flow, transport and chemical parameters.

Chapter 3 presents the improvements, updates, corrections and extensions of the codes of the CORE series. Particularly noteworthy are the improvements implemented in CORE^{2D}V5 dealing with porosity changes and its verification. This chapter includes also the long-term non-isothermal reactive transport model of the interactions of concrete, compacted bentonite and clay in a HLW repository in clay of Mon et al. (2017), which incorporates the porosity feedback.

Chapter 4 presents numerical flow and reactive transport models of laboratory experiments with strong porosity changes due to precipitation/dissolution reactions carried out in the Paul Scherrer Institut (PSI) (Poonoosamy et al., 2015). The results obtained with the updated version of CORE^{2D}V5 have been compared with experimental data and with the numerical results obtained with other codes.

Chapter 5 presents single- and multi-species transport models to simulate the non-linear transport and sorption of caesium through Opalinus clay, a potential host rock for a HLW repository.

Chapters 6, 7, 8 and 9 are devoted to the numerical flow and reactive transport models of the CTS site. Chapter 6 presents the horizontal models to simulate a pumping test carried out in creek located east of the nuclear zone and to quantify the potential impact of the Chaparral pumping well on the hydrogeological conditions of the nuclear zone of the CTS site. Three numerical models in vertical profiles at the CTS site are presented in Chapter 7. Chapter 8 describes the fully 3-D numerical flow model of the CTS site. Heat transport, groundwater age, hydrogeochemical mixing and reactive transport models of the CTS site are presented in Chapter 9.

Chapter 10 presents a parametric and numerical analysis of the estimation of groundwater recharge from water table fluctuations (WTF method) in unconfined aquifers using 1-D and 2-D deterministic and stochastic numerical models. These models have been applied to the Guadalquivir River alluvial aquifer in Andújar (Jaén, Spain) near an old uranium tailing pile.

Chapter 11 summarizes the main conclusions of the dissertation and a lot of recommendations for future works.

CHAPTER 2. MATHEMATICAL FORMULATION OF THBC MODELS

2.1 Introduction

Progress in coupled thermal, hydrodynamic, geochemical and microbial models in porous and fracture media is essential to improve the understanding of how physical, geochemical and biological processes are coupled in groundwater and their effect on groundwater chemistry evolution and the reactive transport of contaminants and microorganisms. The safety assessment of underground disposal facilities for radioactive waste requires the use of models which are able to consider simultaneously groundwater flow, heat transfer, solute transport, geochemical reactions and microbiological processes. In recent years, porosity changes due to mineral precipitation/dissolution are being actively investigated in connection with the deep geological disposal of nuclear waste where chemically very different materials such as clays and concretes come into contact with one another (Gaucher and Blanc, 2006). These investigations indicate that porosity changes due to precipitation/dissolution reactions and their feedback on flow, transport and chemical properties must be considered in numerical models.

This chapter presents the mathematical formulation of the coupled THBC (Thermo-Hydro-Biological-Chemical) models. This formulation has been borrowed from the CORE family (Samper et al., 2000). The formulation includes the description of the formulation implemented in the code CORE^{2D}V5 in this dissertation dealing with porosity changes due to mineral dissolution/precipitation and dynamically update the flow, transport and chemical parameters. The details of the new features implemented in CORE^{2D}V5 are presented in Appendix 2. A microbiological database with the input parameters used by BIOCORE^{2D} has been prepared (see Appendix 1). The parameters and the formulation of microbial processes are also presented in this chapter.

2.2 Hydrobiogeochemical processes

A hydrobiochemical system is an integration of motion and transformation of substances and energy in the subsurface environment involved in different processes including groundwater flow, heat and solute transport, and geochemical and biological processes. Reactive transport models are a collection of process representations (physical, chemical and biological) of varying accuracy and

sophistication that are used to describe a coupled dynamic system. Figure 2.1 illustrates the processes of THBC models and their interplays.

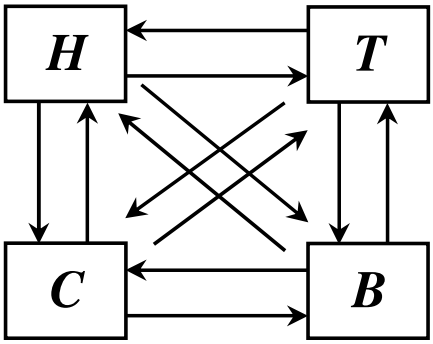

Figure 2.1. Scheme of the couplings between thermal (*T*), hydrodynamic (*H*), chemical (*C*) and biological (*B*) processes.

Dissolved species are subject to hydrodynamic, chemical and microbiological processes. Hydrodynamic processes include advection, diffusion and dispersion. Geochemical reactions can be divided into: 1) Homogeneous reactions which occur in the liquid phase, such as aqueous complexation, acid-base and redox reactions and 2) Heterogeneous reactions that involve exchange of the matter between the liquid and the solid/gas phases and include mineral precipitation/dissolution, surface complexation, cation exchange and gas dissolution/exsolution. Heat transport in porous media is governed by: 1) Conduction in the solid matrix; 2) Transport by fluid phases (advection); 3) Conduction in the fluid phase and 4) Heat exchange between solid and liquid depending on their temperature difference. Microbiological processes include the microbial growth, metabolic competition, decay, metabiosis, endogenous respiration and attachment/detachment to the solids.

Since the interactions among the four kinds of processes are relevant in most natural environmental systems, a more complete understanding of the behavior of these systems is achieved by studying simultaneously thermal, hydrodynamic, biological and chemical processes. Geochemical processes are involved in the substance and energy cycles, which are mainly mediated by water and especially by groundwater. Therefore, geochemical processes are related to hydrodynamic processes. On the other hand, geochemical processes can also affect hydrodynamic processes. Transport properties may also vary as a function of geochemical reactions: precipitation/dissolution of mineral phases alter local porosity and permeability of geologic media. This feedback mechanism is particularly important at engineering buffers such as concrete and clay to be used in radioactive waste repositories. Biologically-controlled processes are affected by abiotic processes and can, in turn, alter the chemical evolution of the system. Interactions between the four kinds of processes control the fate of thermal-

hydro-bio-geochemical systems. Geochemical and microbial processes such as the solubility of minerals, gas dissolution, and microbial growth depend also on the environmental temperature.

2.3 Mathematical formulation

2.3.1 Groundwater flow

Water flow through porous media is governed by Darcy's Law. By combining Darcy's Law with the mass balance equation, the governing equation for flow in variably saturated porous media can be written as (Bear, 1979):

$$\nabla \cdot [K_r \boldsymbol{K} \nabla(\psi + z)] + w = \left(\phi \frac{\partial S_w}{\partial \psi} + S_w S_s\right) \frac{\partial \psi}{\partial t} \tag{2.1}$$

where z is elevation, t is time, ψ is pressure head and w is a fluid source/sink per unit volume of medium. The hydraulic conductivity is written as the product of relative conductivity K_r (a function of pressure head; for fully saturated media, $K_r = 1$) and saturated conductivity $\boldsymbol{K}$. S_w is the water saturation which is defined as the ratio of volumetric water content θ to porosity ϕ (for fully saturated media $S_w = 1$), S_s is the specific storage coefficient, and $\nabla\cdot[\ ]$ and $\nabla(\ )$ are the divergence and gradient operators, respectively.

2.3.2 Multicomponent reactive transport

Dissolved species in saturated media are subject to solute transport and chemical reactions. Transport processes include advection, molecular diffusion and hydrodynamic dispersion. The equation governing solute transport through porous media is derived from the principle of mass conservation. Reactive transport equations can be written in terms of total dissolved component concentrations, C_j. If diffusion and dispersion coefficients are the same for all aqueous species, the transport equations are given by (Yeh, 2000):

$$\nabla \cdot \left(\theta \boldsymbol{D} \nabla C_j\right) - \boldsymbol{q} \nabla\left(C_j\right) + w\left(C_j^* - C_j\right) + \theta R_j = \frac{\partial(\theta C_j)}{\partial t} \qquad j = 1,2,\dots,N_c \tag{2.2}$$

where $\boldsymbol{D}$ is the dispersion tensor, $\boldsymbol{q}$ is Darcy velocity which is derived from the solution of the flow equation, θ is volumetric water content, w is external fluid source term, C_j^* is dissolved concentration of external fluid sources w, j refers to the chemical component from 1 to N_c, and R_j is the chemical sink/source term which includes all the chemical interactions of the j-th component with solid species, such as precipitated, exchanged and adsorbed surface species (Xu et al., 1999). Chemical sink/source

terms depend nonlinearly on the concentrations of dissolved species, which make (Equation 2.2) to become a set of coupled highly nonlinear partial differential equations (PDEs).

For practical purposes, the effects of molecular diffusion and hydrodynamic dispersion are usually lumped in a single dispersion tensor $\boldsymbol{D}$ which takes the form:

$$\theta \boldsymbol{D} = I\boldsymbol{D_e} + \theta \boldsymbol{D_h} \tag{2.3}$$

where $\boldsymbol{I}$ is the identity tensor and $\boldsymbol{D_e}$ and $\boldsymbol{D_h}$ are the effective diffusion and hydrodynamic dispersion tensors, respectively.

2.3.3 Geochemical reactions

A subset of N_C chemical species is selected as components or primary species to describe a chemical system. The rest of the species are called secondary species and can be represented as linear combinations of the set of primary species:

$$Q_j^s = \sum_{i=1}^{Nc} v_{ij} Q_i^p \qquad j = 1, \dots, N_R \tag{2.4}$$

where Q_j^s and Q_i^p are the chemical formulae of the j-th secondary species and i-th primary species, respectively, N_R is the number of reactions (or secondary species) and v_{ij} is stoichiometric coefficient of the i-th primary species in the dissociation reaction of the j-th secondary species.

The total dissolved concentration of a given component, C_k, can be written in an explicit form as a function of the concentration of the N_C primary species as:

$$C_k = c_k + \sum_{j=1}^{Nx} v_{jk} x_j = c_k + \sum_{j=1}^{Nx} v_{jk} \left(K_j^{-1} \gamma_j^{-1} \prod_{i=1}^{Nc} c_i^{v_{ji}} \gamma_i^{v_{ji}} \right) \tag{2.5}$$

where K_j is the equilibrium constant which depends on the pressure and temperature of the system; x_j and c_i are molal concentrations of secondary and primary species, respectively, and γ_i and γ_j are thermodynamic activity coefficients and N_x is the number of secondary species. It should be noticed that the difference between the concentration of primary species c_k and the total dissolved concentration C_k. Mathematical expressions of other types of chemical reactions are given by Xu et al. (1999) and Samper et al. (2000).

2.3.4 Mathematical formulation of porosity changes due to mineral dissolution/precipitation

In this dissertation, the reactive transport code CORE^{2D}V5 has been improved and extended to take into account porosity changes and update flow, transport and chemical parameters (see Appendix 2). The porosity is updated each time step from the computed changes in the mineral volume fractions. The porosity of the medium, ϕ, is computed from:

$$\phi = 1 - \sum_{m=1}^{N_p} f_m \tag{2.6}$$

where N_p is the number of minerals and f_m is the volume fraction of mineral the m-th mineral. The porosity is not allowed to be less than a prescribed threshold.

The changes in the permeability are calculated from the Kozeny-Carman equation in the updated version of CORE^{2D} (Carman, 1937). This is one of the most widely accepted and simplest permeability-porosity relationships which provides a link between media properties and flow resistance in pore channels. The Kozeny-Carman equation relates the permeability k to porosity ϕ through:

$$k = k_0 \frac{(1-\phi_0)^2}{(1-\phi)^2}\left(\frac{\phi}{\phi_0}\right)^3 \tag{2.7}$$

where k_0 is the reference permeability and ϕ_0 is the initial or reference porosity.

The pore diffusion coefficients in the revised version of the code are updated based on Archie's law (Archie, 1942) which describes the ratio between the effective diffusivity of solute in a porous medium and the diffusion coefficient of such species in pure water. This ratio is a function of the tortuosity of the material and its constrictivity which in turn depend on porosity. Tortuosity and the constrictivity are difficult to measure experimentally. Their ratio is often described as the geometrical factor. The relationship can be written as follows:

$$\frac{D_e}{D_0} = \frac{\delta}{\tau} = \phi^m \tag{2.8}$$

where D_0 is the pore diffusion coefficient in pure water, D_e is the effective diffusion coefficient, τ is the tortuosity, δ is the constrictivity, ϕ is the porosity and m is the cementation exponent.

CORE^{2D}V5 provides several options to define the dispersion coefficient, D, and the tortuosity, τ, by setting different parameters in the input files. The details of the different options can be found in the Appendix 2.

The sink/source term r_i (mol/m^3/s) for the i-th primary aqueous species associated to kinetically-controlled mineral reactions is given by:

$$r_i = \sum_{m=1}^{N_p} v_{mi}^{p} r_m A_m \tag{2.9}$$

where r_m is the mineral dissolution/precipitation rate (mol/m^2/s) of the m-th mineral, v^p_{mi} is the stoichiometric coefficient of i-th species in the m-th mineral, N_p is the number of minerals and A_m is the specific surface of the m-th mineral (expressed as the surface of mineral per unit volume of water).

In the extended version of CORE^{2D}V5, the mineral specific surface is updated each time steps according to:

$$A_m^{t+1} = A_m^t \frac{\phi^t}{\phi^{t+1}} \tag{2.10}$$

where A_m^{t+1} and A_m^t are the specific surfaces of the m-th mineral and ϕ^{t+1} and ϕ^t are the porosities for the time step $t+1$ and t, respectively.

2.3.5 Heat transport

According to the principle of heat conservation, the equation governing heat transport is given by (Samper et al., 2000):

$$\nabla(\boldsymbol{\lambda}\nabla \mathrm{T} - \rho c_w \boldsymbol{q} T) = \theta \rho c_w \frac{\partial T}{\partial t} + (1-\theta)\rho_s c_s \frac{\partial T_s}{\partial t} = \rho_m c_m \frac{\partial T}{\partial t} \tag{2.11}$$

where $\boldsymbol{\lambda}$ is thermal conductivity tensor, T is temperature, $\boldsymbol{q}$ is water content, ρ is water density, c_w is the specific heat of water, ρ_s and c_s are the density and the specific heat of solid phase at a temperature $T_s = T$, and ρ_m and c_m are the density and the specific heat of the bulk porous medium (water plus solid), so that $\rho_m c_m = \phi\, \rho\, c_w + (1 - \theta)\, \rho_s c_s$.

2.3.6 Microbiological processes

Microbial growth depends strongly on substance and energy supply from the environment. Microbes gain energy and substances from carbon compounds by oxidizing carbon and other compounds. The products of microbial metabolism are inorganic carbons such as bicarbonate, methane and carbon dioxide. During energy generation, dissolved oxygen, nitrate, Mn (IV), Fe (III), sulphate or carbon dioxide are employed as electron acceptors in redox reactions and in turn they are reduced. These processes can be the dominant redox processes of the system. Microbial processes depend also on environment factors such as temperature, pressure, pH and Eh (Rheinheimer et al., 1992).

Chemical species used by microorganisms for energy generation or (and) material supply for enzyme synthesis are known as *substrates*. Chemical species which gain electrons in redox reactions for the microbial energy generation are called *electron acceptors*. Chemoautotrophic microorganisms can use substrates only to gain energy while they need some source of inorganic carbon for the synthesis. In this case, the inorganic carbon is called *nutrient*. Endogenous respiration is a process by which cell reserves are used as substrates when other organic substrates are not available.

Microbial metabolism is the process by which microbes use organic matter (heterotrophic bacteria) or other chemical compounds (such as CO_2, CH_4 for autotrophic bacteria) to build enzyme and in turn to grow. The chemical composition of the system is altered during metabolic processes. Main biological processes taking place in subsurface microbial ecosystems include: 1) Biomass growth, 2) Oxidation and consumption of substrates, 3) Reduction of electron acceptors and 4) Transformation of nutrients. Biomass growth is the domain mass transformation process and it comes mostly from consumed substrates. Microbial growth depends on four main factors: 1) Its inherent generative power usually measured by the specific generation time or specific growth rate, 2) Its concentration defined as microbial population per unit volume of water, 3) Concentrations of substrates, electron acceptors and nutrient species and 4) Environments factors such as temperature, pH and Eh.

A brief description of the microbiological process is presented in this section. This description has been taken from Zhang (2001).

The overall microbial rate is equal to the sum of the rates of microbial growth, metabolic decay and endogenous respiration (Samper et al., 2006):

$$\frac{\partial C_b^i}{\partial \mathrm{t}} = \frac{\partial C_b^i}{\partial \mathrm{t}}\Big|_{growth} + \frac{\partial C_b^i}{\partial \mathrm{t}}\Big|_{decay} + \frac{\partial C_b^i}{\partial \mathrm{t}}\Big|_{endogenous} \tag{2.12}$$

where C_b^i is the aqueous concentration of the *i*-th microbe in the system and the subscript *b* refers to biotic species. Microbial growth rate can be written as:

$$\frac{\partial C_b^i}{\partial \mathrm{t}} \Big|_{growth} = \sum_{k=1}^{N_b^i} G^{i,k} M^{i,k} C_b^i \tag{2.13}$$

where $G^{i,k}$ is the microbial growth factor of *i*-th microbe in its *k*-th growth phase, which is equal to the product of: (1) The growth constant $K_b^{i,k}$ (T^{-1}), (2) The lag factor $G_L^{i,k}$ which accounts for the time elapsed since a microbe encounter a substrate to the time it is able to build the enzymatic system required to use it and, (3) The environment limitations $G_T^{i,k}$ (temperature) and $G_{pH}^{i,k}$ (pH). $M^{i,k}$ is the overall limiting factor of the *k*th growth process and is equal to the product of the limitation factors of substrates (subindex *s*), electron acceptors (subindex *a*) and nutrients (subindex *n*):

$$M^{i,k} = M_s^{i,k}\, M_a^{i,k} M_n^{i,k} \tag{2.14}$$

where $M_s^{i,k}$ is the dimensionless limitation factor of the substrate involved in the *k*-th growth process for the *i*-th microbe and it is given by:

$$M_s^{i,k} = \frac{C_s^p}{K_s^p S_s^p + C_s^p + C_c^p} \tag{2.15}$$

where C_s^p is the concentration of the *p*-th substrate, K_s^p is the half-saturation constant and S_s^p is a substrate inhibition/stimulation factor which is greater than 1 for inhibition and less than 1 for stimulation. C_c^p is a competition and/or metabiosis factor for the *i*-th microbe which accounts for interactions among two or more microbial species when they cooperate or depend on each other to use the same substrate (metabiosis) or compete for the same "food" and space (competition).

$M_a^{i,k}$ is the dimensionless limitation factor for the *q*-th electron acceptor which is given by:

$$M_a^{i,k} = \frac{C_a^q}{K_a^q + C_a^q} \tag{2.16}$$

where C_a^q and K_a^q are the concentration and the half-saturation constant of the *q*-th electron acceptor, respectively. Finally, $M_n^{i,k}$ is the dimensionless limitation factor for *r*-th nutrient which is given by:

$$M_n^{i,k} = \frac{C_n^r}{K_n^r + C_n^r} \tag{2.17}$$

where C_n^r and K_n^r are the concentration and the half-saturation constant of the *r*-th nutrients respectively.

Metabolic decay is the biological death, the rate of which is described by first order kinetics according to:

$$\frac{\partial C_b^i}{\partial \mathrm{t}} \Big|_{decay} = -K_d^i C_b^i \tag{2.18}$$

where K_d^i is the decay rate of the *i*-th microbe.

Endogenous respiration is the process by which microbes consume cell reserves in the absence of sufficient substrates and continue to use the *ie*-th electron acceptor. It rate is given by:

$$\frac{\partial C_b^i}{\partial \mathrm{t}} \Big|_{endogenous} = -k_e^i C_b^i \frac{C_a^{ie}}{K_a^{ie} + C_a^{ie}} \tag{2.19}$$

where C_a^{ie} is the concentration of the *ie*-th electron acceptor that can be used by microbe *i*. Endogenous respiration occurs only when the substrate is short in the system, but the system contains enough electron acceptors.

Microbial metabolism depends strongly on variables such as temperature, pressure, turbidity, pH, Eh, and concentrations of organic and inorganic compounds. The dependence on concentrations of organic and inorganic matters is taken into account by growth limitation factors. The overall rate of change of the concentration of the *i*-th microbe is given by:

$$\frac{\partial C_b^i}{\partial \mathrm{t}} = \sum_{k=1}^{N_b^i} G^{i,k} M^{i,k} C_b^i - K_d^i C_b^i - k_e^i C_b^i \frac{C_a^{ie}}{K_a^{ie} + C_a^{ie}} \tag{2.20}$$

Since microbial processes involve the consumption of substrates, reduction of electron acceptors and transformation of nutrients, microbial processes are coupled with geochemical or abiotic processes through yield coefficient. The yield coefficient is defined as the ratio of the microbial growth rate to that of the substrate consumption. It ranges from 10^{-4} to 0.9 depending on the type of microorganism, substrate and other environments factors. Changes in the concentrations of substrates can be related to

microbial growth rates by means of yield coefficients. The rate of consumption of the *p*-th substrate due to microbial processes, B_p, is given by:

$$B_p = \frac{\partial C_s^p}{\partial \mathrm{t}} = -\sum_{i=1}^{N_b}\sum_{j=1}^{N_b^i} \frac{1}{Y_s^{i,j,p}} \frac{\partial C_b^i}{\partial \mathrm{t}} \Big|_{growth} \tag{2.21}$$

where $Y_s^{i,j,p}$ is the yield coefficient of the *p*-th substrate being used by the *i*-th microbe in its *j*-th growth process.

The amount of electron acceptors required by metabolic processes depends not only on microbial growth rate but also on the coefficient of proportionality between substrates and electron acceptors which is given by the stoichiometric coefficient of the redox reaction. The rate of consumption of the *q*-th electron acceptor due to microbial processes, B_q, is given by:

$$B_q = \frac{\partial C_a^q}{\partial \mathrm{t}} = -\sum_{i=1}^{N_b}\sum_{j=1}^{N_b^i} \frac{f_a^{i,j,q}}{Y_s^{i,j,p}} \frac{\partial C_b^i}{\partial \mathrm{t}} \Big|_{growth} + \sum_{j=1}^{N_b} f_{ea}^i \frac{\partial C_b^i}{\partial \mathrm{t}} \Big|_{endogenous} \tag{2.22}$$

where $f_a^{i,j,q}$ is the coefficient of proportionality defined as the ratio of the rate of consumption of electron acceptor to that of the substrate, and f_{ea}^i is the electron acceptor consumption coefficient for the endogenous respiration of the *i*-th microbial species.

Changes in the concentrations of nutrients are caused also by microbial growth. The rate of consumption of the *r*-th nutrient, B_r, is given by:

$$B_r = \frac{\partial C_n^r}{\partial \mathrm{t}} = -\sum_{i=1}^{N_b}\sum_{j=1}^{N_b^i} \frac{f_n^{i,j,r}}{Y_s^{i,j,p}} \frac{\partial C_b^i}{\partial \mathrm{t}} \Big|_{growth} \tag{2.23}$$

where $f_n^{i,j,r}$ is the coefficient of proportionality between consumed substrate and consumed nutrient.

CHAPTER 3. IMPROVEMENTS, UPDATES, CORRECTIONS AND EXTENSIONS OF THE CODES OF THE CORE SERIES

3.1 Introduction

CORE is a series of reactive transport codes developed at the University of A Coruña. CORE stands for *"a COde for modeling water flow (saturated and unsaturated), heat transport and multi-component REactive solute transport under both local chemical equilibrium and kinetic conditions"*. The reactive transport codes developed since 1991 include: TRANQUI (ENRESA, 1995; Xu, 1996); CORE-LE-2D (Samper et al., 1998); FADES-CORE-LE (Juncosa et al., 1999); CORE^{2D}V2 (Samper et al., 2000); CORE^{2D}V4 (Samper et al., 2003); TRANMEF-3D (Juanes, 1997; Juanes and Samper, 2001); VISUAL-CORE-LE (Samper et al., 1999); CORE Graphics (Samper et al., 1999); INVERSE-CORE^{2D} (Dai and Samper, 1999; Dai, 2000); BIOCORE^{2D} (Zhang, 2001; Zhang and Samper, 2001); CORE^{3D} (Yang et al., 2003); INVERSE-FADES-CORE (Zheng and Samper, 2005) and INVERSE-FADES-COREV2 (Mon, 2017).

This chapter presents the improvements, updates, corrections and extensions of the codes of the CORE series. Most of these improvements have been performed during the course of this dissertation in CORE^{2D}V5, although updates have been performed also in other codes such as INVERSE-CORE^{2D}, BIOCORE^{2D} and CORE^{3D} (TRANMEF-3D). Particularly noteworthy are the improvements implemented in CORE^{2D}V5 dealing with porosity changes and its verification. CORE^{2D}V5 has been extended to take into account porosity changes due to mineral precipitation/dissolution and dynamically update the flow, transport and chemical parameters. The feedback effect of porosity changes on transport parameters has been applied to the long-term non-isothermal reactive transport model of the interactions of concrete, compacted bentonite and clay in a high-level radioactive waste repository in clay reported by Mon et al. (2017). Model results calculated with and without the porosity feedback are presented in this chapter.

The details of the improvements and extensions implemented in the codes of the CORE series are provided in Appendix 1. The improvements implemented in CORE^{2D}V5 to deal with porosity changes due to mineral dissolution/precipitation and verifications of the new features are presented in Appendix 2.

3.2 Main features of CORE^{2D}V5

Most of the flow and reactive transport models presented in this dissertation have been performed with CORE^{2D}V5, a code for transient saturated and unsaturated water flow, heat transport and multicomponent reactive solute transport under both local chemical equilibrium and kinetic conditions in heterogeneous and anisotropic media (Samper et al., 2009, 2011). The flow and transport equations are solved with Galerkin finite elements and an Euler scheme for time discretization. The chemical formulation is based on the ion association theory and uses an extended version of Debye-Hückel equation (B-dot) for the activity coefficients of aqueous species. CORE^{2D}V5 relies on the com thermodynamic database of EQ3/6 (Wolery, 1992). CORE^{2D}V5 is based on the sequential iteration approach to solve for chemical reactive solute transport. Iterations are repeated until prescribed convergence criteria are attained (Xu et al., 1999). CORE^{2D} has been extensively verified against analytical solutions and other reactive transport codes. In addition, CORE^{2D} has been widely used to model laboratory and in situ experiments (Samper et al., 2008b; Zheng and Samper, 2008; Zheng et al., 2010; 2011), model the interactions of corrosion products and bentonite (Samper et al., 2008a) and evaluate the long-term geochemical evolution of repositories in granite and clay (Samper et al., 2016; Mon et al., 2017).

3.3 Improvements and updates

A brief summary of the improvements, updates, corrections and extensions of the codes of the CORE series is presented next. Improvements and extensions implemented in the codes of the CORE series are described in detail in Appendixes 1 and 2.

3.3.1 Update of CORE^{2D}V5 to use ParaView post-processing tools

CORE^{2D}V5 has been updated to allow the use of ParaView for post-processing model results. ParaView is one of the best known and used post-processing tools (Ahrens et al., 2005; Ayachit, 2015). The front end graphical user interface (GUI) has an open, flexible and intuitive user interface that gives fine-grained and open-ended control of the data manipulation and display processing needed to explore and present complex data. CORE^{2D}V5 has been modified to print out the model results in the VTK format supported by ParaView. The modifications performed have taken into account the different options allowed by the reactive transport code (1-D vertical and horizontal models, 2-D models, 2-D axisymmetric models and 3-D axisymmetric models). The user can choose the format of the output files in the updated version of the code: 1) Original format, 2) VTK format or 3) Output files printed out in both formats. The updated version of CORE^{2D}V5 has been verified for all possible models carried out

with the code. The output files with the results of these models were printed out in two formats (the original format and the VTK format) and both files were compared.

3.3.2 Update of CORE^{2D}V5 for conservative solute transport

In the absence of chemical reactions with other solutes or interactions with the solid phase, it is only necessary to solve the solute transport equation to carry out conservative solute transport. However, it is not possible to discern between conservative transport and reactive transport in the current version of CORE^{2D}V5. In this way, the code uses the same subroutines for solving a conservative and a reactive transport problem. CORE^{2D}V5 has been modified to run models with conservative solute transport in a more efficient and effective way. In the updated version of CORE^{2D}V5, the code does not solve the chemical equations for conservative solute transport. The sink/source chemical term is always equal to 0. This update avoids convergence problems and reduces calculation times.

3.3.3 Update of CORE^{2D}V5 to compute and print out relevant variables

CORE^{2D}V5 has been updated to compute and print out relevant variables for water flow and reactive transport problems such as: 1) Water inflows and outflows for several types of boundary conditions (Dirichlet and Cauchy conditions) and 2) Flow velocity vectors. These variables are printed out in new output files in the updated version of the code. In addition, flow velocity vectors are also printed out in VTK format which can be post-processed with ParaView. The update of CORE^{2D}V5 facilitates the calculation of groundwater balances in the model domain. These improvements of CORE^{2D}V5 have been tested and verified with several test cases.

3.3.4 Improvement of convergence criteria in CORE^{2D}V5 to solve unsaturated flow

The flow equation for variably saturated media is highly nonlinear. CORE^{2D} solves flow in variably saturated media by a Newton-Raphson iterative method based on the linearization of the problem by using a Taylor series expansion. CORE^{2D}V5 has been updated to improve the convergence of the iterative method for solving unsaturated flow model. The details of this code improvement can be found in Appendix 1.

3.3.5 Update of INVERSE-CORE^{2D} to deal with large numbers of parameters

INVERSE-CORE^{2D} is a reactive transport code of the CORE series to solve inverse problems by minimizing a generalized least squares criterion by means of Gauss-Newton-Levenberg-Marquadt (Dai and Samper, 1999; Dai, 2000). It calibrates automatically the parameters of reactive transport

models (Dai and Samper, 2004). In the current version of INVERSE-CORE^{2D}, it was possible to perform reactive transport models with up to 10 material zones. INVERSE-CORE^{2D} has been extended to deal with problems with up to 50 material zones. INVERSE-CORE^{2D} uses an identification number for each parameter estimated by the code. These identification numbers have been modified in the updated version of the code. The updated version of INVERSE-CORE^{2D} has been verified with three synthetic 2-D numerical models.

3.3.6 Development of a microbiological database for BIOCORE^{2D}

BIOCORE^{2D} (Zhang, 2001; Zhang and Samper, 2001) is a coupled biogeochemical reactive transport code for biogeochemical reactive transport accounting for biofilms and the interactions among microbes. A microbiological database is attached to the code BIOCORE^{2D} for calculations of microbiological processes. Basic data for kinetic dissolution-precipitation and microbiological metabolism and biotransformation is read from a database. A microbiological database with the input parameters of BIOCORE^{2D} has been performed in this dissertation (see Appendix 1).

3.3.7 Other improvements and corrections of bugs in source codes of CORE series

Other minor improvements have been implemented in the codes of the CORE series. Some bugs in the source codes have been corrected also. The details of these improvements and corrections can be found in Appendix 1.

3.3.8 Improvements to deal with porosity changes and feedback of transport parameters

Mineral dissolution and precipitation generally modify the pore space geometry of rocks, which in turn changes flow and influences transport parameters. Porosity changes induced by mineral dissolution/precipitation are important for the description of various hydrogeological processes and influence the evolution of natural geological environments and underground systems. CORE^{2D}V5 has been extended to take into account porosity changes due to mineral dissolution/precipitation and dynamically update the flow, transport and chemical parameters every time step. The details of the improvements and the verification of CORE^{2D}V5 of the porosity feedback can be found in Appendix 2.

The porosity is updated at each time step according to the changes of the volume fractions of the minerals in the updated version of CORE^{2D}V5. The code checks that the sum of the porosity and the volume fractions of the minerals is equal to 1 for all nodes of the grid. The porosity is not allowed to be less than a prescribed threshold (clogging) specified by the user in the input files of CORE^{2D}V5 (a value

between 10^{-4} and 10^{-10} is suggested). Minerals are not allowed to precipitate anymore when the porosity is smaller than this threshold.

When the porosity changes, the flow, transport and chemical parameters are updated in the following time step. The feedback on flow and transport parameters is commonly accounted for in numerical models by considering empirical formulae. The Kozeny-Carman equation is used to describe the changes in permeability as a function of porosity in the updated version of CORE^{2D}V5 (Carman, 1937). Pore diffusion coefficients and tortuosities are updated according to Archie's law (Archie, 1942).

In addition, other parameters such as water contents, water velocities, nodal concentrations and specific surfaces of minerals (expressed as the surface of mineral per unit volume of water) are also updated each time step. The changes in time in the hydraulic conductivity, pore diffusion coefficient and mineral specific surfaces can be printed out in the updated version of the code.

CORE^{2D}V5 incorporates a restart option which allows to restart the simulation at the time a run that has stopped by modifying some parameters such as the maximum number of iterations and the number of time steps in a time period. The restart option has been modified in the revised version of CORE^{2D} to take into account the porosity changes. The porosities in the current time step and the porosities in the previous time step are printed and saved in an appropriate manner. The restart option clearly improves the overall efficiency of numerical modelling for complex problems.

3.3.8.1. Verification of the improvements implemented in CORE^{2D}V5 dealing with porosity changes

The modifications implemented in CORE^{2D}V5 to take into account porosity changes and the update of the flow, transport and chemical parameters have been extensive and have required a significant effort. For this reason, an extensive verification of the updated version of the code has been performed. The improvements of CORE^{2D}V5 dealing with porosity changes have been verified with analytical solutions for diffusion problems coupled with precipitation-dissolution reactions and feedback of porosity change in one-dimension (Hayek et al., 2011) and two-dimensions (Hayek et al., 2012). Figure 3.1 shows the comparison of the computed porosity profiles with the analytical solutions for two cases proposed by Hayek et al. (2011) and Hayek et al. (2012).

In addition, a benchmark test case has been used to verify the updated version of CORE^{2D}V5 with other reactive transport codes (CrunchFlow, HP1, MIN3P, Pflotran and TOUGHREACT) (Xie et al., 2015). This benchmark considers advective-dispersive transport in saturated media with aqueous complexation and kinetically-controlled mineral precipitation and dissolution leading to porosity

changes. Figure 3.2 shows the comparison of the porosity profiles computed with MIN3P and the updated version of CORE^{2D}V5 at several times for two benchmark cases proposed by Xie et al. (2015).

The model results computed with the updated version of CORE^{2D} reproduce the analytical solutions and the numerical solutions computed with other reactive transport codes.

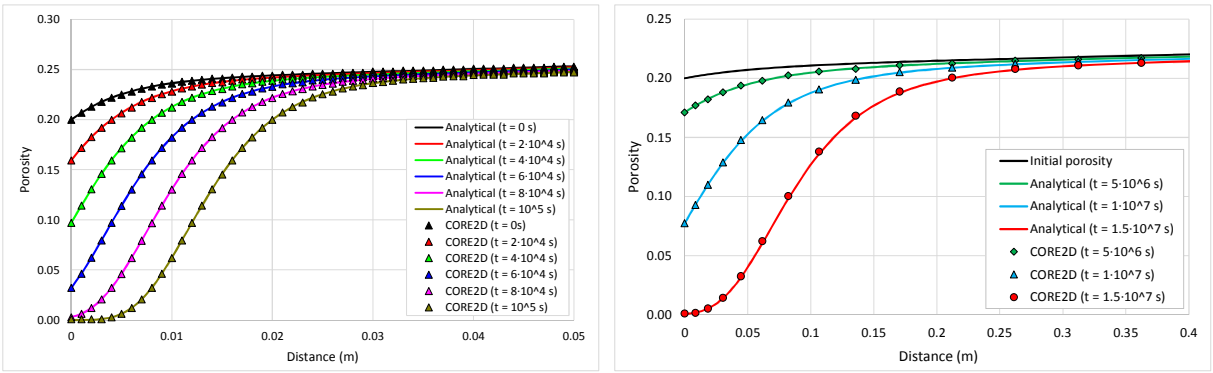

Figure 3.1. Comparison of the computed porosity profiles with the analytical solutions at selected times for a case proposed by Hayek et al. (2011) in 1-D (left) and another case proposed by Hayek et al. (2012) in 2-D (right).

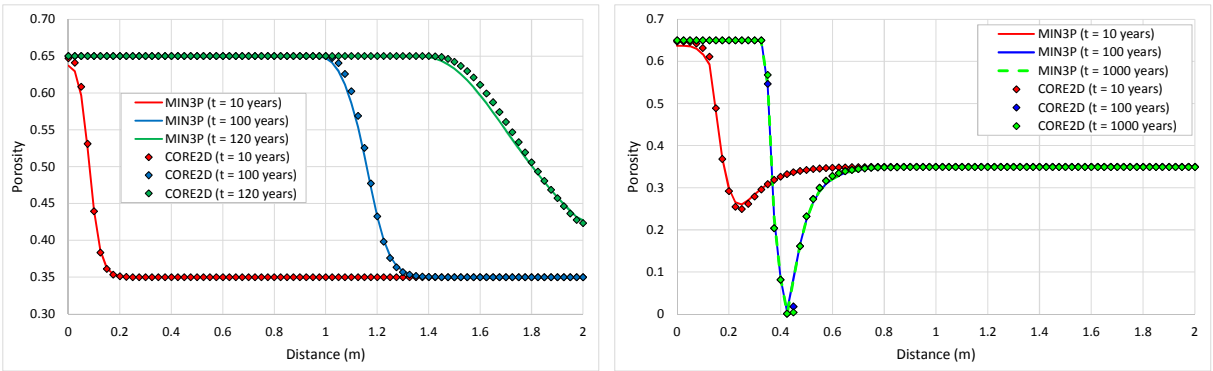

Figure 3.2. Comparison of the porosity profiles computed with MIN3P and the updated version of CORE^{2D}V5 for two benchmark cases proposed by Xie et al. (2015).

3.3.8.2. Porosity feedback for the long-term reactive transport model of the interactions of concrete, compacted bentonite and clay in a HLW repository in clay

Carbon steel, compacted bentonite and concrete have been proposed as candidate materials for the engineered multi-barrier system of deep geological repositories (DGR) for high-level radioactive waste (HLW) in clay formations. A non-isothermal multicomponent reactive transport model of the long-term interactions of compacted bentonite with the corrosion products of a carbon-steel canister and the concrete liner of the engineered barrier of a high-level radioactive waste repositories in clay was performed by Mon et al. (2017). This model was calculated with the reactive transport code CORE^{2D}V4

(Samper et al., 2009, 2011) which assumes that the porosity remains constant in the transport and chemical equations. The changes in porosity that could be caused by mineral dissolution/precipitation reactions were calculated from model results. In this dissertation, the model of Mon et al. (2017) has been calculated with the updated version of CORE^{2D}V5 which takes into account the porosity changes due to mineral dissolution/precipitation reactions and the feedback on flow, transport and chemical parameters. The results calculated with and without the feedback effect up to 40000 years have been compared. The material presented here has been partly published in Samper et al. (2017).

The model corresponds to a radioactive waste repository in clay according to the Spanish Reference Concept (ENRESA, 2004). Cylindrical carbon steel canisters with 0.9 m diameter are emplaced in horizontal galleries and embedded into a 0.75 m thick bentonite buffer. A 0.3 m thick concrete support is located between the bentonite buffer and the clay formation (Figure 3.3). Heat and solute transport processes were assumed to have axial symmetry with respect to the axis of the galleries. Therefore, the model is discretized with a 1-D axisymmetric grid which accounts for the canister (8 elements), the bentonite (31 elements), the concrete (31 elements) and the clay formation (78 elements) (Figure 3.3). The simulations starts when the bentonite buffer fully saturated and, therefore, there is no water flow through the system. The numerical model accounts for the thermal transient stage and the cooling of radioactive waste (ENRESA, 2004). Flow and transport parameters as well as the initial porewater chemical composition of the bentonite, the concrete and the clay were taken from Yang et al. (2008). The model accounts for canister corrosion, aqueous complexation, acid/base, redox reactions, mineral dissolution/precipitation, surface complexation of Fe^{2+} and H^+ on three types of sorption sites and cation exchange reactions of Ca^{2+}, Mg^{2+},Na^+, K^+ and Fe^{2+}. The chemical system is defined in terms of the following 13 primary species: H_2O, H^+, Ca^{2+}, Mg^{2+}, Na^+, K^+, Cl^-, SO_4^{2-}, HCO_3^-, $SiO_2(aq)$, $O_2(aq)$, Fe^{2+} and $AlOH_4^-$. The model considers 16 minerals (brucite, calcite, gyrolite, tobermorite, quartz, dolomite, portlandite, sepiolite, gypsum, ettringite, Fe(s), magnetite, siderite, goethite, smectite, analcime) and 58 aqueous complexes. All the reactions except for canister corrosion and smectite dissolution are assumed at chemical equilibrium. The corrosion rate is constant and equal to 2 μm/year (Samper et al., 2016).

The canister is made entirely of Fe(s). The bentonite contains initially 0.36% (vol) of calcite, 1.19% of quartz, 0.083% of gypsum and 57.667% of smectite. The porosity of the bentonite is equal to 0.407. The concrete liner contains initially 0.1% of calcite, 1% of brucite, 16.5% of portlandite, 36.6% of tobermorite and 37.3% of nonreactive quartz. The porosity of the concrete is equal to 0.085. The clay has a porosity of 0.37. It is composed of calcite (11.3%), gypsum (1.2%), quartz (2.4%), dolomite (2.4%) and nonreactive clay mineral phases (45.7%). More details about the long-term non-isothermal reactive transport model in a HLW repository in clay can be found in Mon et al. (2017).

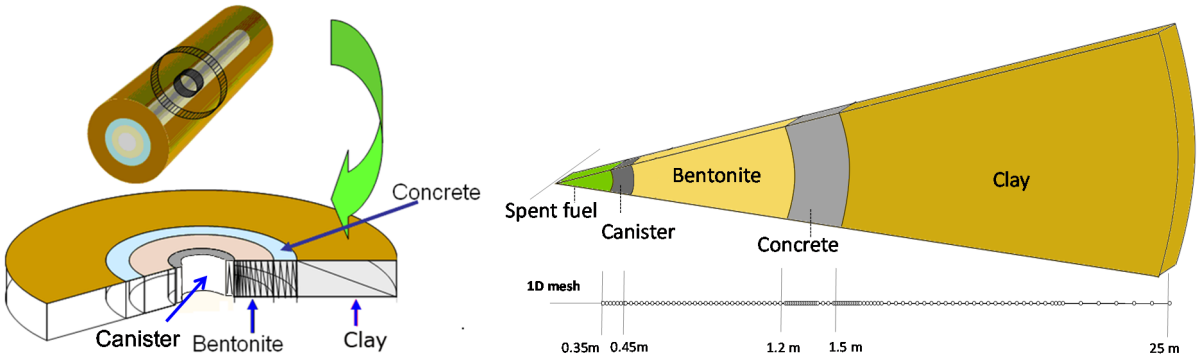

Figure 3.3. Scheme of the multibarrier system of a HLW repository in clay according to the Spanish Reference Concept (Yang et al., 2008) (left) and 1-D finite element grid which accounts for the canister, the bentonite barrier, the concrete liner and the clay formation (Mon et al., 2017) (right).

The porosity is updated each time step according to the computed changes in the mineral volume fractions in the numerical model calculated with the updated version of CORE^{2D}V5. However, the porosity is not allowed to be less than 10^{-4}. The pore diffusion coefficients and the solute tortuosities are updated based on Archie's law with an exponent equal to 4/3 (Archie, 1992). Other flow and transport parameters such as nodal volumes, water velocities, mineral specific surface areas and nodal dissolved concentrations are also updated every time step to account for the changes in the porosities. The permeability has not been updated because there is no water flow.

Figure 3.4 shows the radial distribution of the porosity and the effective diffusion coefficient with and without the porosity feedback at 40000 years. The major differences in the porosities computed with and without the feedback effect occur in the concrete and the concrete-clay and canister-bentonite interfaces. Pore clogging thickness in the concrete and at the concrete-clay interface considering the porosity feedback is smaller than that computed without the porosity feedback. Pore clogging in the concrete at 40000 years is predicted from r = 1.33 m to r = 1.34 m with the porosity feedback, and from r = 1.24 m to r = 1.28 m without the porosity feedback. The pore clogging computed in the concrete near the clay interface is 2.5 cm without the porosity feedback and clogging does not occur in the model with the porosity feedback. The clogging thickness in the clay near the concrete interface is 0.83 cm and 1.67 cm with and without the porosity feedback, respectively. The radial distribution of the effective diffusion coefficients computed with the model with porosity feedback after 40000 years is greatly influenced by the changes in the computed porosities.

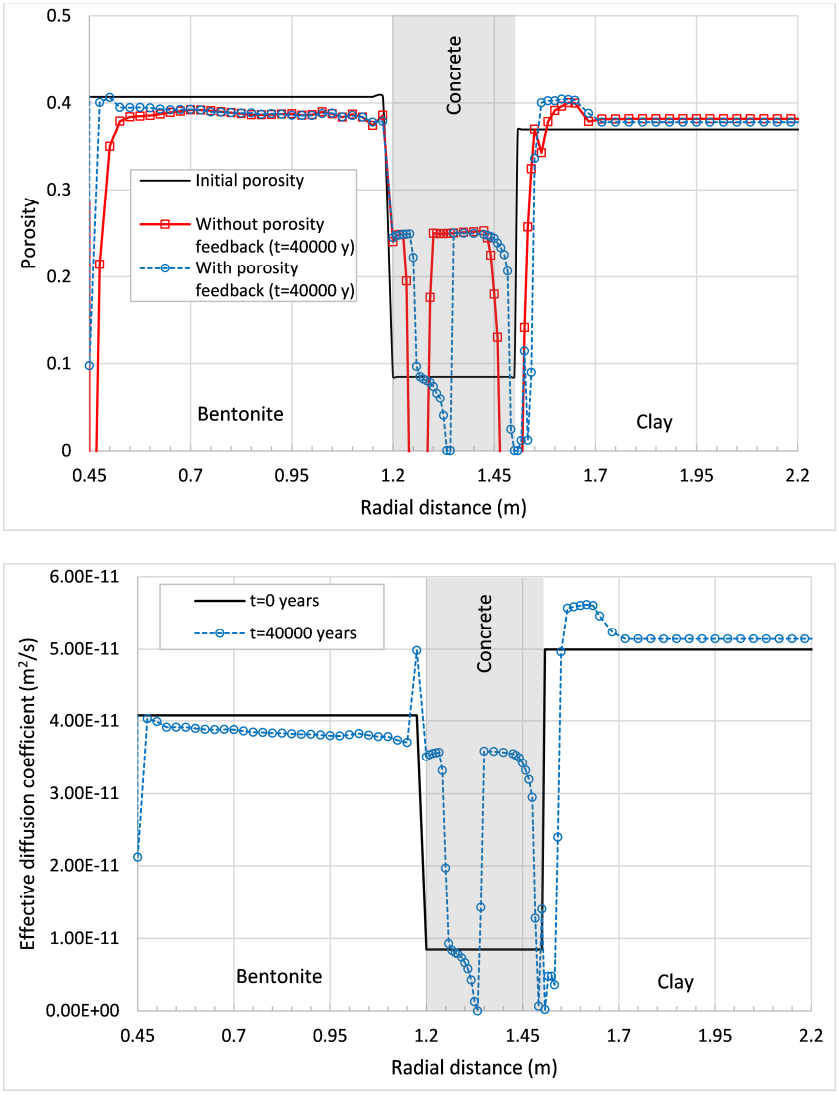

Figure 3.4. Radial distribution of the porosity (top) and the effective diffusion coefficient (bottom) at t = 0 and 40000 years computed with and without the porosity feedback.

Figure 3.5 shows the time evolution of the concentration of the cumulative mineral precipitation/dissolution in the bentonite near the concrete interface (r = 1.125 m), the concrete midpoint (r = 1.35 m) and the clay near the concrete interface (r = 1.525 m) computed with and without porosity feedback. The results with the porosity feedback indicate less brucite precipitation in the clay near the concrete interface (r = 1.125 m). In the concrete midpoint (r = 1.35 m), portlandite dissolution in the model without the porosity feedback is slightly faster than that computed with the porosity feedback. In fact, portlandite is exhausted at t = 20000 years in the model without the porosity feedback and at t = 25000 years in the model with the porosity feedback. There are significant differences between the time evolution of the cumulative gypsum, brucite, sepiolite and calcite precipitation computed with and without porosity feedback in the clay near the concrete interface (r = 1.525 m).

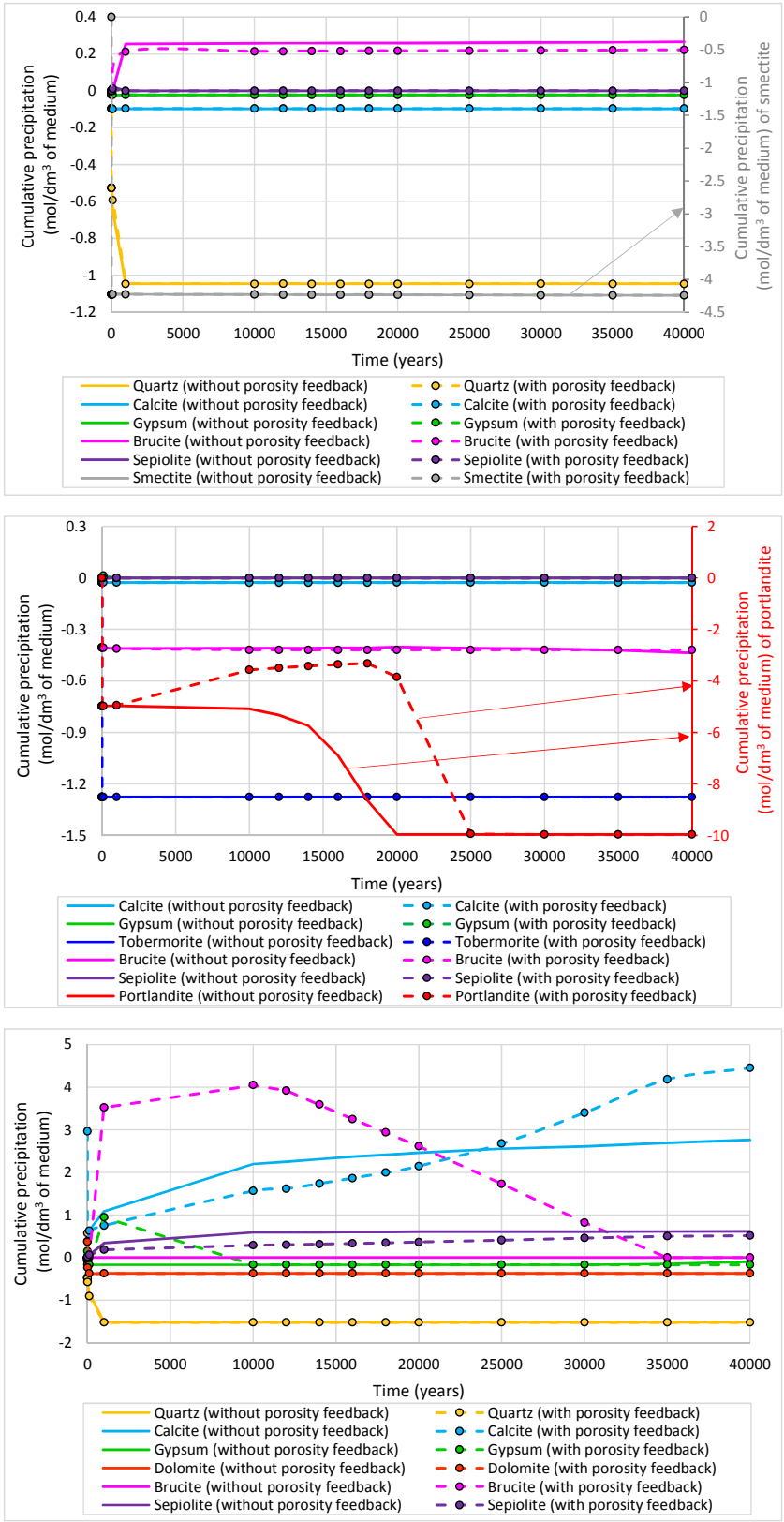

Figure 3.5. Time evolution of the cumulative mineral dissolution/precipitation in the bentonite buffer near the concrete interface (r = 1.125 m) (top), at the midpoint of the concrete liner (r = 1.35 m) (intermediate) and in the clay formation near the concrete interface (r = 1.525 m) (bottom) computed with and without the porosity feedback (positive for precipitation and negative for dissolution).

Figure 3.6 shows the mineral volume fractions at t = 40000 years computed with and without porosity feedback. The model with porosity feedback calculates less magnetite precipitation than the model without porosity feedback in the bentonite-canister interface. For this reason, the computed reduction of the porosity with the porosity feedback is smaller than that computed without the porosity feedback in the bentonite-canister interface (Figure 3.4). In the concrete, portlandite dissolution is significantly different with and without porosity feedback. After 40000 years, there is still portlandite from r = 1.23 m to r = 1.3 m in the model without porosity feedback whereas portlandite remains from r = 1.24 m to r = 1.35 m in the model with porosity feedback. The results in the concrete and the clay near the concrete interface after 40000 years with feedback porosity indicate less precipitation of gypsum, brucite, sepiolite and analcime and more precipitation of calcite than those calculated without porosity feedback.

The largest differences in the computed pH after 40000 years with and without the porosity feedback occur at both sides of the concrete-clay interface (Figure 3.7).

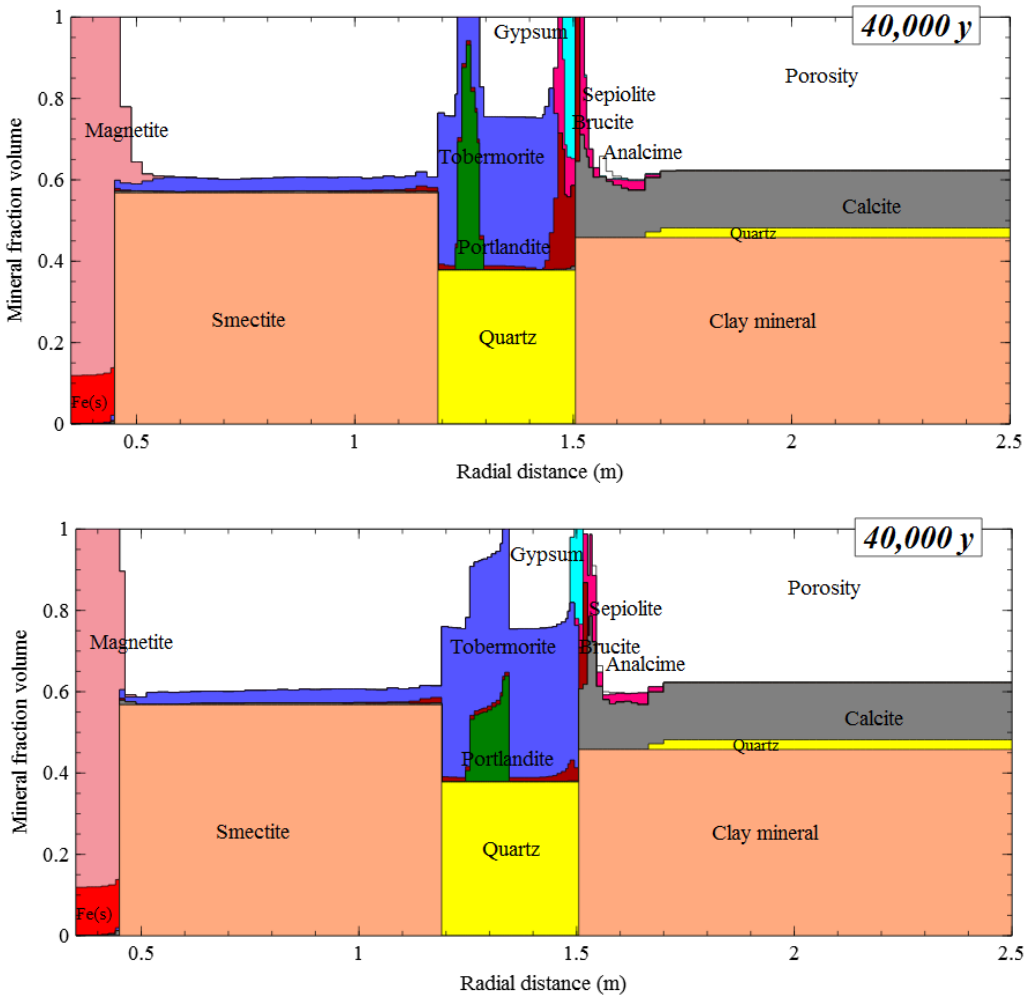

Figure 3.6. Mineral volume fractions at t = 40000 years computed without the porosity feedback (top) and with the porosity feedback (bottom).

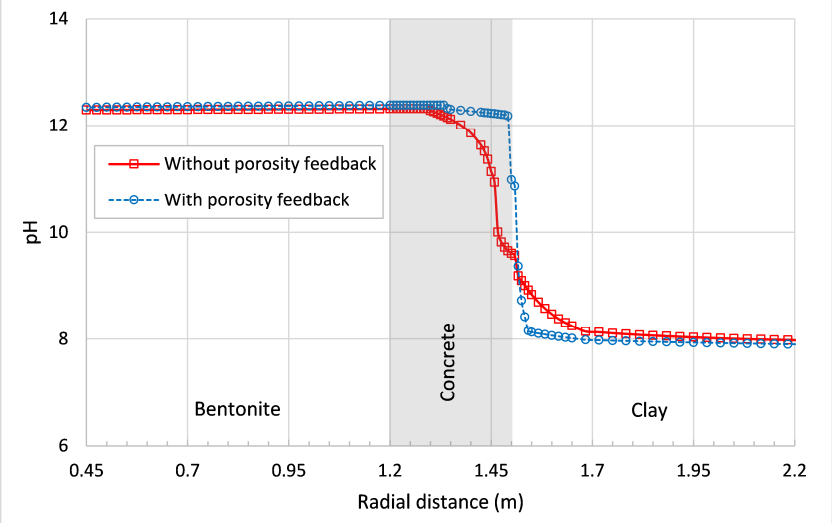

Figure 3.7. Radial distribution of the pH computed at t = 40000 years with and without the porosity feedback.

3.4 Conclusions

Improvements, updates, corrections and extensions of the codes of the CORE series have been performed in this dissertation. These improvements facilitate the development of flow and reactive transport models and the analysis of model results. Most of the improvements have been carried out in CORE^{2D}V5, although updates have been performed also in other codes such as INVERSE-CORE^{2D}, BIOCORE^{2D} and CORE^{3D} (TRANMEF-3D).

Particularly noteworthy are the improvements implemented in CORE^{2D}V5 dealing with porosity changes and its verification. CORE^{2D}V5 has been extended to take into account porosity changes due to mineral precipitation/dissolution and dynamically update the flow, transport and chemical parameters. The updated version of the code has been extensively verified against analytical solutions (Hayek et al., 2011, 2012) and by comparison with other reactive transport codes (Xie et al., 2015).

A non-isothermal reactive transport model of the interactions of compacted bentonite with the corrosion products of a carbon-steel canister and the concrete liner of the engineered barrier of a HLW in clay reported by Mon et al. (2017) has been performed with the updated version of CORE^{2D}V5. The model results after 40000 years calculated with and without porosity feedback have been compared. The major differences of the porosity computed with and without the porosity feedback are located in the concrete and at the concrete-clay and canister-bentonite interfaces. The thickness of pore clogging in the concrete and in the concrete-clay interface computed with the model with the porosity feedback is smaller than that computed without the porosity feedback.

CHAPTER 4. NUMERICAL FLOW AND REACTIVE TRANSPORT MODELS OF LABORATORY EXPERIMENTS WITH STRONG POROSITY CHANGES

4.1 Introduction

Mineral dissolution/precipitation in interfaces between porous media with different properties can produce changes in porosity, which in turn causes changes in flow and transport parameters. The changes in the porosity due to mineral dissolution/precipitation and the associated changes in transport and chemical parameters are of great interest for natural geological environments and for engineered underground systems. In recent years, numerous investigations are being carried out on porosity changes due to mineral dissolution/precipitation in connection with deep geological disposal of nuclear waste where chemically very different materials come into contact one with another.

Reactive transport codes are commonly used to predict the evolution of systems that are not experimentally accessible in space and time. There is a need to evaluate the capabilities and the correctness of the implemented features and the performance of the reactive transport codes. A possible way to verify the codes consists on comparing the results obtained with several reactive transport codes (*benchmarking*) and comparing the results of laboratory and field experiments with numerical models. Benchmarking cases with porosity enhancement, reduction or clogging are of great interest because the coupling between transport and chemistry is commonly encountered in real geosystems.

This chapter presents flow and reactive transport numerical models of laboratory experiments with strong porosity changes due to dissolution/precipitation reactions. These laboratory experiments were carried out at the Paul Scherrer Institut (Switzerland). The models were performed with CORE^{2D}V5. The results obtained with CORE^{2D}V5 have been compared with the experimental data of Poonoosamy et al. (2015) and the computed results obtained with other reactive transport codes (TOUGHREACT, OpenGeoSys-GEM, Pflotran and MIN3P). In addition, CORE^{2D}V5 has been used also to perform reactive transport simulations under unsaturated conditions. The details of the numerical flow and reactive transport models of laboratory experiments with strong porosity changes due to mineral dissolution/precipitation reactions can be found in Appendix 3.

4.2 Laboratory experiments

The laboratory experiments were carried out at the Paul Scherrer Institut (PSI). The experiments were conducted in a transparent tank containing a reactive layer of strontium sulphate ($SrSO_4$(s), celestite), sandwiched between two layers of essentially non-reacting quartz sand (SiO_2(s)) (Figure 4.1). The tank is square and its dimensions are 10 x 10 cm. The tank has a thickness of 1 cm. The inlet and the outlet of the tank are located near the lower left corner and the upper right corner of the tank, respectively. The tank has three zones: 1) The first zone (*Z1*) is composed of quartz, has a width of 4.5 cm and the porosity is equal to 0.34 ± 0.02; 2) The second zone (*Z2*) is composed of celestite, has a width of 1 cm and the porosity is equal to 0.33 ± 0.02 and 3) The third zone (*Z3*) is composed of quartz, has a width of 4.5 cm and the porosity is equal to 0.40 ± 0.02.

Several types of tests were performed with this experimental setup (Poonoosamy et al., 2015). The following test were simulated with CORE^{2D}V5: 1) A test without chemical reactions and 2) A test focused on the porosity changes caused by precipitation of barium sulphate. In the first test, a pulse (0.5 mL at rate of 20 µL/min) of dye tracer with a concentration of 3 g/L was injected at the inlet followed by a continuous inflow of a saturated solution of strontium sulphate at a flow rate of 20 µL/min. The tracer evolution in the tank was monitored for about 20 hours. In the second test, a barium chloride solution ($BaCl_2$) with a concentration of 0.3 mol/L was injected at the inlet of the tank at a flow rate of 20 µL/min. The injection of $BaCl_2$ into the tank enhanced the dissolution of strontium sulphate and the precipitation of barium sulphate. The porosity changed during the experiment due to the differences in molar volumes of strontium sulphate and barium sulphate. The test lasted 300 hours. Both experiments were performed under saturated conditions at a temperature of 25 ± 1°C.

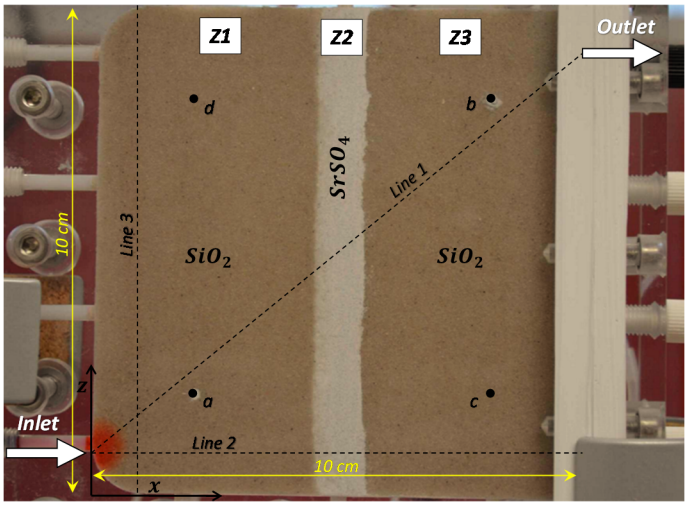

Figure 4.1. Experimental setup of the reactive transport tests performed by Poonoosamy et al. (2015). The zones *Z1* and *Z3* are made up of non-reacting quartz sand (SiO_2) while the zone Z2 is a reactive layer of strontium sulphate. Data were collected at ports a, b, c and d. Lines 1, 2 and 3 were used for comparing model results.

4.3 Numerical models

Two numerical models were performed with the updated version of CORE^{2D}V5 which takes into account the feedback effect of the porosity changes due to mineral dissolution/precipitation on flow, transport and chemical parameters (see Appendix 2). Numerical models were performed for the following tests: 1) Conservative transport (Case 1) and 2) Reactive transport focused on porosity changes (Case 2). The model domain was discretized with a 2-D grid of triangular finite elements. Several runs were performed to evaluate the sensitivity of model results to the refinement of the grid.

The conservative transport model (Case 1) was performed for a total period of 24 hours. The tracer was injected only during the first 25 minutes of simulation. The reactive transport model (Case 2) was performed for a total period of 300 hours. Similar to Case 1, the water inflow is equal to 20 µL/min. However, a highly concentrated solution (0.3 mol/L) of $BaCl_2$ was injected into the tank in Case 2. The reactive zone *Z2* is composed of two grain size populations of $SrSO_4$(s) (small-grain celestite and large-grain celestite). Barite precipitation is assumed to occur at chemical equilibrium. The dissolution of strontium sulphate, however, is simulated with a kinetic law. Different kinetic rates of dissolution were used for two grain population of celestite. Small-grain celestite and large-grain celestite have surface areas equal to 20000 and 100 m^2 of mineral/m^3 of mineral, respectively.

4.4 Model results

4.4.1 Conservative transport model results (Case 1)

The results of the conservative transport model performed with CORE^{2D}V5 were compared with the measured data and the predictions performed with similar codes such as TOUGHREACT, OpenGeoSys-GEM, Pflotran and MIN3P. The tracer profiles computed with CORE^{2D}V5 were compared to experimental tracer profiles (Poonoosamy et al., 2015) at several times. Model results reproduce the patterns of the experimental data (Figure 4.2). The tracer contour plots describe concentric circles at the beginning of the simulation. The circles get slightly distorted as the tracer moves towards the less permeable zone (zone *Z2*). The maximum computed tracer concentrations decreases with time due to tracer dispersion. The maximum tracer concentrations is below 0.20 g/L after 15 hours.

The tracer breakthrough curves at ports *c* and *d* (Figure 4.1) computed with CORE^{2D}V5 were compared with those computed with other reactive transport codes. The arrival time of the tracer to port *c* is greater than the time of arrival of the tracer to port *d* because the port *c* is located downstream the low-permeability zone *Z2*. The tracer has to travel through the zone of low permeability (zone *Z2*) to reach port *c* (see Figure 4.1). There are some differences between the tracer breakthrough curves

computed with different reactive transport codes at ports *c* and *d* (see Figure 4.3). These differences are due to differences in the numerical methods and the dispersive parameters of the codes. In spite of these small differences, all the codes provide similar results for the tracer breakthrough curves and the general evolution of the tracer.

Water velocities along lines 1, 2 and 3 (see Figure 4.1) were computed with CORE^{2D}V5, TOUGHREACT, OpenGeoSys-GEM and Pflotran. The velocities computed with the codes agree for the most part. However, there are local differences near the inlet and the outlet (Figure 4.3). These differences are attributed to differences in the implementations of the boundary conditions in the reactive transport codes.

Numerical discretization errors of the simulations performed with CORE^{2D}V5 were quantified by performing simulations with several grids. Numerical dispersion is greatly reduced when the grid is sufficiently refined. The results confirm that the differences between the results computed with the five codes for Case 1 are due to numerical dispersion and the number of nodes used to simulate the inlet and the outlet of the tank.

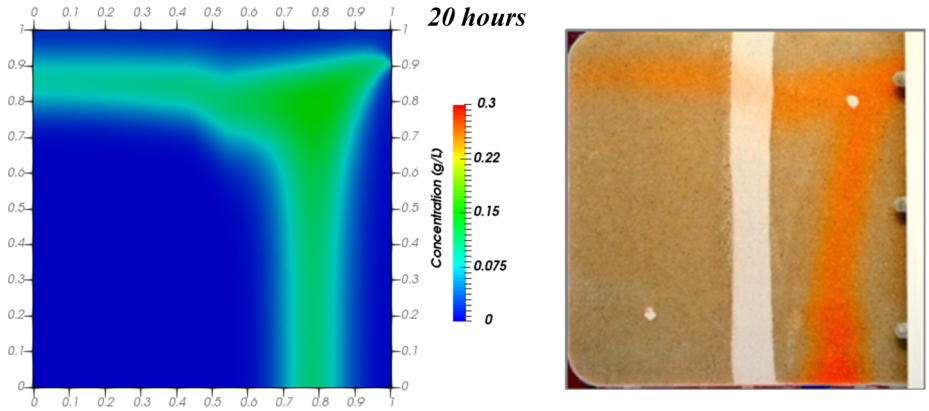

Figure 4.2. Tracer concentration contour plots at 20 hours computed with CORE^{2D}V5 (left) and tracer image recorded in the lab by Poonoosamy et al. (2015) (right).

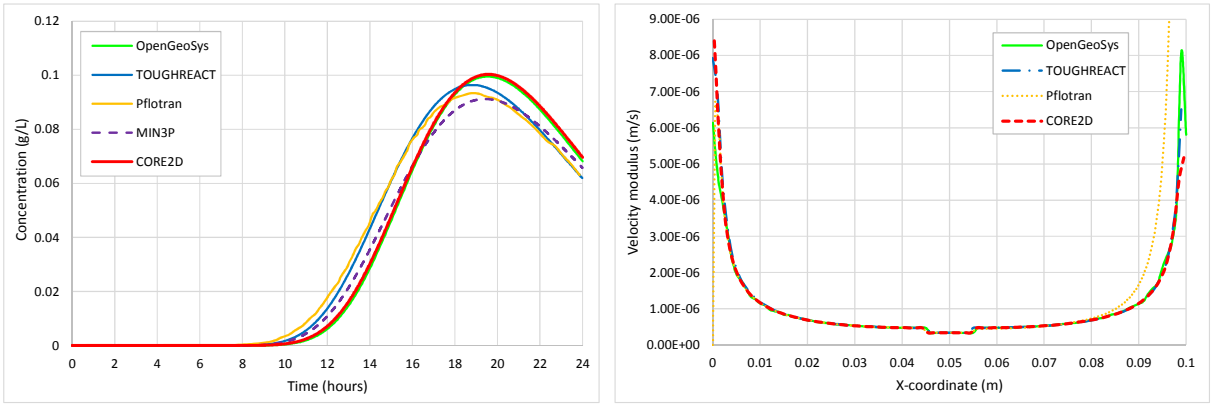

Figure 4.3. Tracer breakthrough curves at port *d* (left) and modulus of the velocity vector along the main diagonal (line 1) (right) computed with CORE^{2D}V5 and other reactive transport codes.

4.4.2 Reactive transport model results (Case 2)

When a concentrated $BaCl_2$ solution reaches the reactive zone (zone *Z2*), the dissolution of celestite is triggered and barite precipitates. Figure 4.4 shows the time evolution of the total amounts of $BaSO_4$(s) and $SrSO_4$(s) in the tank computed with CORE^{2D}V5, TOUGHREACT, OpenGeoSys-GEM, Pflotran and MIN3P. All the reactive transport codes give similar results. During the first 150 hours, $SrSO_4$(s) dissolves at a constant rate of 0.2 mmol/h. After 150 hours, the dissolution rate slows down. Similarly, the total amount of precipitated barite increases during the first 150 hours and slowly builds up to 0.043 mol at 300 hours.

The initial volume fraction of the small-grain celestite is equal to 0.223 in zone *Z2*. The small-grain celestite dissolves steadily in zone *Z2*. After 10 hours, the small-grain celestite begins to dissolve in the left part of zone *Z2*. The dissolution of the small-grain celestite after 50 hours of simulation occurs throughout the entire reactive zone. The volume fraction of the small-grain celestite is approximately equal to 0.09 in zone *Z2* after 150 hours and approximately equal to 0.03 after 300 hours. The changes in the volume fraction of the large-grain celestite during the 300 hours of simulation are extremely small because its reactive surface area is very small. The time evolution of barite dissolution is similar to the time evolution of the small-grain celestite precipitation.

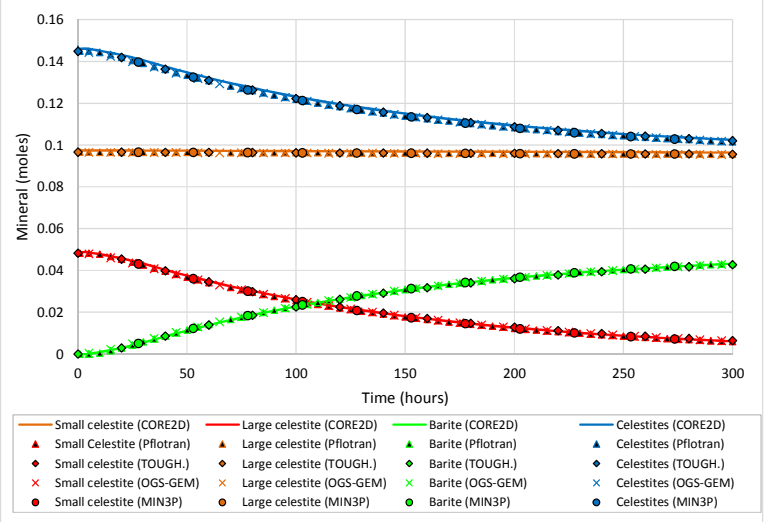

Figure 4.4. Time evolution of the bulk mineral composition in the tank computed with CORE^{2D}V5, TOUGHREACT, OpenGeoSys-GEM, Pflotran and MIN3P.

The concentrations of Cl^-, Sr^{2+} and Ba^{2+} computed with CORE^{2D}V5 along line 2 have been compared with those calculated with TOUGHREACT and OpenGeoSys-GEM. For the most part, the concentrations computed with CORE^{2D}V5 coincide with those computed with the other two codes. The computed concentration of Cl^- along line 2 after 150 h and 300 h of simulation is equal to the Cl^- concentration of the boundary water (0.6 mol/L) because Cl^- is a conservative species. On the other

hand, barite precipitation in the reactive zone causes a decrease of the concentration of dissolved Ba^{2+} in zones *Z2* and *Z3*. The dissolution of celestite causes an increase of the concentration of dissolved Sr^{2+} in zones *Z2* and *Z3*.

The simultaneous dissolution of celestite and the precipitation of barite involves an increase in mineral volume fraction of about 0.12. The porosity and the permeability decrease. Figure 4.5 shows the porosity and permeability profiles along line 2 at 300 hours computed with CORE^{2D}V5, TOUGHREACT and OpenGeoSys-GEM. The porosity and permeability changes calculated with CORE^{2D}V5 follow a trend similar to that of other codes. However, there are some differences at the interfaces related to differences in the spatial discretization and interpolation methods used by the three reactive transport codes. A sensitivity analysis to the grid discretization was performed with CORE^{2D}V5 for Case 2. The results confirmed that the differences at the interfaces are due to the spatial discretization.

Case 2 has been simulated with CORE^{2D}V5 with and without the feedback effect of the changes in porosity. Nodal results coincide during the first 50 hours of the simulation. Later, however, the amounts of barite and celestite in the tank computed with and without the feedback effect show important differences. The update of the flow, transport and chemical parameters due to the decrease of the porosity in the reactive zone of the tank (zone *Z2*) leads to less celestite dissolution and barite precipitation. The differences in the model results increase with time. The results of this comparison stresses the importance of updating the mineral reactive surface area for modelling mineral dissolution/precipitation reactions in porous media.

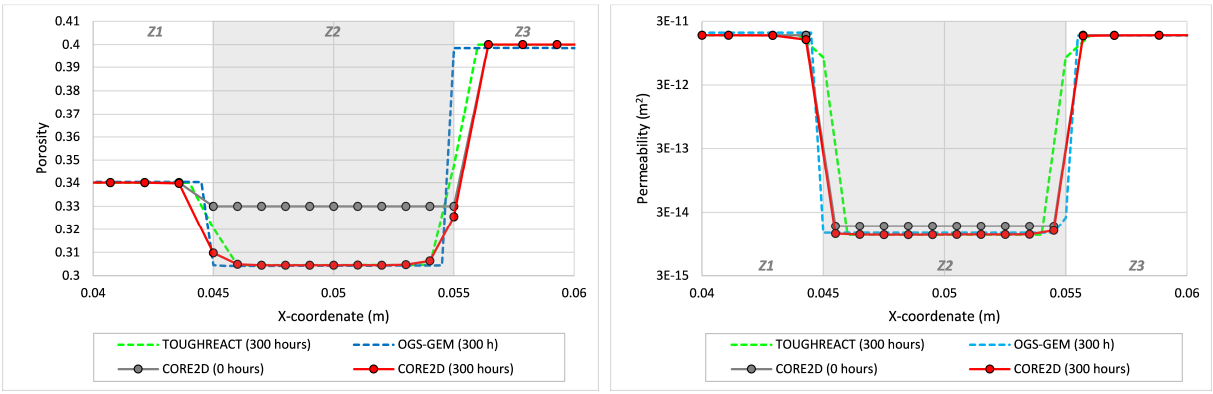

Figure 4.5. Porosity (left) and permeability (right) profiles along line 2 at 300 hours computed with CORE^{2D}V5, TOUGHREACT and OpenGeoSys-GEM. The grey area indicates the reactive zone (*Z2*).

4.4.3 Model results in unsaturated conditions

Before performing the laboratory tests, the tank was flushed with carbon dioxide (CO_2) to remove the air from the pores. The high solubility of CO_2 enabled the whole porous medium to be completely saturated with a saturated solution of strontium sulphate. CORE^{2D}V5 has been used to

simulate the laboratory test starting from unsaturated conditions. An initial saturation degree of 40% was assumed. The tank is saturated after about 17 hours. Tracer concentrations at ports *a* and *c* computed with the unsaturated model are greater than those computed with the saturated model for Case 1. However, the opposite occurs at ports *b* and *d*. The evolution of $BaCl_2$ in the tank changes considerably if the numerical model is saturated or unsaturated for Case 2. For this reason, the amount of precipitated barite and the area where this mineral precipitates computed with the unsaturated model are different than those calculated with the saturated nodal. Barite precipitates more strongly in the lower part of the reactive zone of the tank in the unsaturated model than in saturated model.

4.5 Conclusions

Numerical flow and reactive transport models were performed with the updated version of CORE^{2D}V5 to simulate laboratory experiments with strong porosity changes due to dissolution/precipitation reactions carried out at the Paul Scherrer Institut (Switzerland). The following test were simulated with CORE^{2D}V5: 1) A test without chemical reactions and 2) A test focused on the porosity changes caused by precipitation of barium sulphate.

A conservative transport model in an advective regime was performed with CORE^{2D}V5 in Case 1. The tracer breakthrough curves at several ports of the tank, the contour plots of tracer concentrations and velocity profiles along various lines of the tank were computed with CORE^{2D}V5 and compared with the measured data and the model predictions of other reactive transport codes such as TOUGHREACT, OpenGeoSys-GEM, Pflotran and MIN3P. The results obtained with CORE^{2D}V5 agree with the measured data and with the results computed with other reactive transport codes, although there are small differences due to differences in the numerical methods and dispersive parameters of the reactive transport codes.

A reactive transport model focused on porosity changes due to mineral dissolution/precipitation reactions was performed for Case 2. The injection into the tank of $BaCl_2$ enhanced the dissolution of strontium sulphate and the precipitation of barium sulphate. The porosity changed during the experiment due to the difference between strontium sulphate and barium sulphate molar volumes. The total amounts of $BaSO_4$(s) and $SrSO_4$(s) in the tank and the concentrations of Cl^-, Sr^{2+} and Ba^{2+} computed with CORE^{2D}V5 agree with those computed with other reactive transport codes. In addition, the porosity and permeability changes calculated with CORE^{2D}V5 and other codes are in good agreement, although there are slightly differences at the interfaces. A sensitivity analysis to the grid discretization performed with CORE^{2D}V5 for Case 2 confirmed that the differences at the interfaces are due to the differences in the spatial discretization used by the reactive transport codes

CHAPTER 5. CAESIUM MIGRATION THROUGH OPALINUS CLAY CALCULATED BY SINGLE-SPECIES AND MULTI-SPECIES TRANSPORT MODELS

5.1 Introduction

Clay formations are being considered as potential host rocks for deep geological disposal of radioactive waste repositories because these rocks have very low hydraulic conductivity and large sorption capacity for many radionuclides. Diffusion is the main transport mechanism through clay formations. Various experimental programs are being carried out at the Mont Terri Underground Research Laboratory (URL) in Switzerland to study the feasibility of the Opalinus clay formation to host a radioactive waste repository.

Caesium (Cs) diffusion through Opalinus clay is relevant for performance assessment purposes for nuclear waste repositories. Cs is a key radionuclide showing a non-linear sorption behaviour in clay (Van Loon et al., 2009). This chapter presents single-species and multi-species reactive transport models performed with CORE^{2D}V5 to simulate the non-linear sorption of caesium (Cs) in Opalinus clay. The numerical models are related to former work carried out by Jakob et al. (2009) and to laboratory diffusion experiments performed at the Paul Scherrer Institut (PSI), Switzerland. Cs breakthrough curves computed with CORE^{2D}V5 at several locations in the Opalinus clay have been compared with those computed with other reactive transport codes (*benchmarking*) such as COMSOL Multiphysics and MCOTAC.

The details of the single-species and the multi-species transport models performed to simulate the non-linear Cs sorption in Opalinus clay can be found in Appendix 4.

5.2 Laboratory experiments

The numerical models performed to simulate the non-linear sorption of caesium in Opalinus clay are related to former work carried out by Jakob et al. (2009) and to laboratory diffusion experiments performed at the Paul Scherrer Institut (PSI), Switzerland. Opalinus clay samples from the Mont Terri Underground Research Laboratory were used in the diffusion experiments. The experimental set-up includes a diffusion cell, an 8-channel peristaltic pump, two containers of $5.0 \cdot 10^{-4}$ m^3 and $1.0 \cdot 10^{-4}$ m^3

and two circuits. The first circuit connects the cell to a large container (high-concentration loop) and the second circuit connects the opposite boundary of the cell to the small container (low-concentration loop). Cs concentration in the large container was much greater than that in the small container. The tracer diffused through the cell from the boundary with high concentration to the boundary with low concentration. All the experiments were performed at 23 ± 2 ºC.

Batch sorption experiments were performed by Van Loon et al. (2009) on crushed and intact Opalinus clay samples. The results demonstrated that sorption of Cs on crushed and intact Opalinus clay is essentially identical. The distribution coefficient of Cs in Opalinus clay as a function of dissolved Cs concentration measured in batch experiments has been used in the single-species transport model to simulate the non-linear Cs sorption in Opalinus clay.

5.3 Numerical models

Two numerical models have been performed with CORE^{2D}V5 to simulate the non-linear sorption of caesium in Opalinus clay: 1) A single-species transport model and 2) A multi-species transport model. The model geometry corresponds to that of the clay samples from the Mont Terri Rock Laboratory used in the small-scale laboratory diffusion experiments (Jakob et al., 2009). The samples are cylindrical with a diameter of 25.7 mm, a cross-sectional area of 518.7 mm^2 and a length L of 1 cm. The porosity is equal to 0.15 and the bulk density of the clay is 2400 kg/m^3 (Pfingsten and Jakob, 2014). The effective diffusion coefficient, D_e, is equal to $1.5 \cdot 10^{-11}$ m^2/s. Transport calculations were performed for a time of 10 years.

The domain of the numerical model performed with CORE^{2D}V5 was discretized with a uniform 2-D mesh of triangular finite elements with a size, Δx, equal to 0.02 cm. The single-species transport model assumes clay porewater (Mont Terri PI-Water) with "high" Cs concentration ranging from 10^{-7} to 10^{-3} M at $x = 0$ and a clay porewater with 10^{-10} M Cs concentration at $x = 1$ cm. The solution in both containers of the laboratory experiments are assumed to behave as concentration boundary conditions. The initial Cs concentration is uniform and equal to 10^{-10} M.

The non-linear sorption of Cs in Opalinus clay in the single-species transport model was simulated with a tabulated list of distribution coefficients measured in the laboratory (Van Loon et al., 2009). CORE^{2D}V5 has been modified and updated to allow the use of a tabulated K_d. The sorption isotherm has been implemented in the code in the form of a look-up table with given K_d values for pairs of Cs data. In this case, two other codes were used to perform the single-species transport model: COMSOL Multiphysics (http://www.comsol.com) and MCOTAC (Pfingsten 1994, 2002, 2005).

Ten primary species and 22 aqueous complexes were considered in the multicomponent reactive transport model. The sorption model of Bradbury and Baeyens (2000) was used to simulate the non-linear sorption of Cs on Opalinus clay. This model assumes three different cation exchange sites. The multi-species transport model was performed also with the code MCOTAC.

5.4 Model results

5.4.1 Single-species model

Dissolved Cs concentrations were calculated with CORE^{2D}V5, MCOTAC and COMSOL at x = 1, 5, 7 and 9 mm. Figure 5.1 shows the Cs breakthrough curves calculated with the three transport codes with the single-species transport model at x = 1, 5, 7 and 9 mm for Cs concentrations at the "high" concentration container equal to 10^{-3}, 10^{-5} and 10^{-7} mol/L. The arrival of the Cs concentration front for a boundary Cs concentration equal to 10^{-3} mol/L is faster than the arrival for Cs concentrations equal to 10^{-5} and 10^{-7} mol/L. The Cs retardation is stronger in the models with lower Cs boundary concentrations due to the non-linear Cs sorption in Opalinus clay (the K_d of Cs decreases with increasing dissolved Cs concentration). The computed Cs concentrations with the three codes for the three Cs boundary concentrations (10^{-3}, 10^{-5} and 10^{-7} mol/L) agree for the most part. However, there are small differences at x = 1 mm. The steady Cs concentration plateaus computed with the three codes at late times are similar.

Possible reasons for the small differences between the Cs concentrations computed with the three codes include: 1) Differences in the spatial discretization used in the codes (a coarse mesh with 50 nodes was used in MCOTAC calculations, an intermediate grid with 102 nodes was used in CORE^{2D}V5 calculations and a fine logarithmically-expanding mesh with more than 500 nodes was used in COMSOL calculations); 2) Differences in the implementation of the sorption isotherm in the transport codes; and 3) Differences in the interpolation procedures.

A sensitivity analysis was performed with CORE^{2D}V5 to analyse the numerical discretization errors. Sensitivity runs were carried out by using a very fine grid with 2002 nodes (Δx = 0.001 cm) for the three Cs boundary concentrations. These sensitivity runs were used also to quantify the errors caused by the fact that K_d values are defined elementwise in CORE^{2D}V5, whereas the concentrations are computed at the nodes of the mesh. The numerical errors of the numerical solutions obtained with the very fine grid decrease largely. Cs breakthrough curves computed with the very fine grid show a dispersion smaller than that computed with the coarse mesh. The results of the sensitivity runs confirm that the use of a coarse mesh in MCOTAC may have produced numerical dispersion.

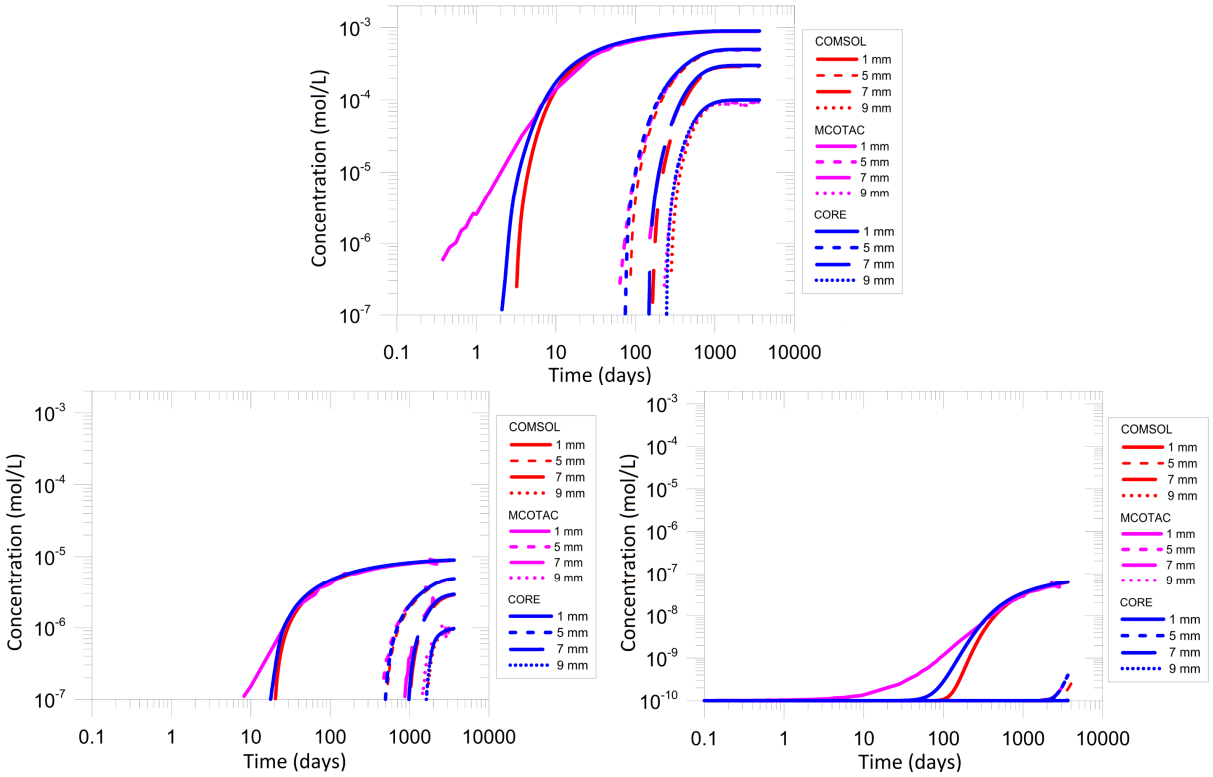

Figure 5.1. Cs breakthrough curves calculated with the single-species transport models at x = 1, 5, 7 and 9 mm with CORE^{2D}V5, MCOTAC and COMSOL. The Cs concentrations in the "high" concentration container are equal to 10^{-3} mol/L (top), 10^{-5} mol/L (bottom left) and 10^{-7} mol/L (bottom right).

5.4.2 Multi-species model

Figure 5.2 shows the Cs breakthrough curves calculated with CORE^{2D}V5 and MCOTAC at x = 1, 5, 7 and 9 mm for Cs boundary concentrations at the "high" concentration container equal to 10^{-3}, 10^{-5} and 10^{-7} mol/L. The results computed with both codes with the multi-species transport models performed for several Cs boundary concentrations generally agree. However, there are slight differences in the Cs breakthrough curves calculated with the two codes near the "high" Cs concentration boundary (x = 1 mm) for the three Cs boundary concentrations. These differences are due to the differences in the spatial discretization. The results computed with MCOTAC show slightly more dispersion than those computed with CORE^{2D}V5.

Several sensitivity runs were performed with CORE^{2D}V5 to analyse the sensitivity of the model results to changes in the convergence tolerance for solving the nonlinear set of chemical reactions in the model results. The computed dissolved Cs concentrations are very sensitive to the convergence tolerance, especially for a Cs boundary concentration equal to 10^{-7} mol/L. It was necessary to use a

convergence tolerance equal to 10^{-7} to achieve very small numerical errors in the computed Cs concentrations.

A detailed analysis of the exchanged concentrations computed with the multi-species transport model performed with CORE^{2D}V5 was performed. Cs^+ exchanges with other cations present in the cation exchange sites (K^+, Na^+, Mg^{2+} and Ca^{2+} in the first type of cation exchange sites and K^+ and Na^+ in the second and third types of sites). The concentrations of exchanged K^+, Na^+, Mg^{2+} and Ca^{2+} decrease slightly when the concentration of exchanged Cs^+ increases. On the other hand, the time evolution of the concentrations of dissolved K^+ and Cs^+ correlate well. The concentration of dissolved K^+ increases with time throughout the Opalinus clay sample. The concentration of dissolved K^+ begins to decrease when the concentration of dissolved Cs^+ begins to increase. Later, the computed concentration of dissolved K^+ decreases to its initial value.

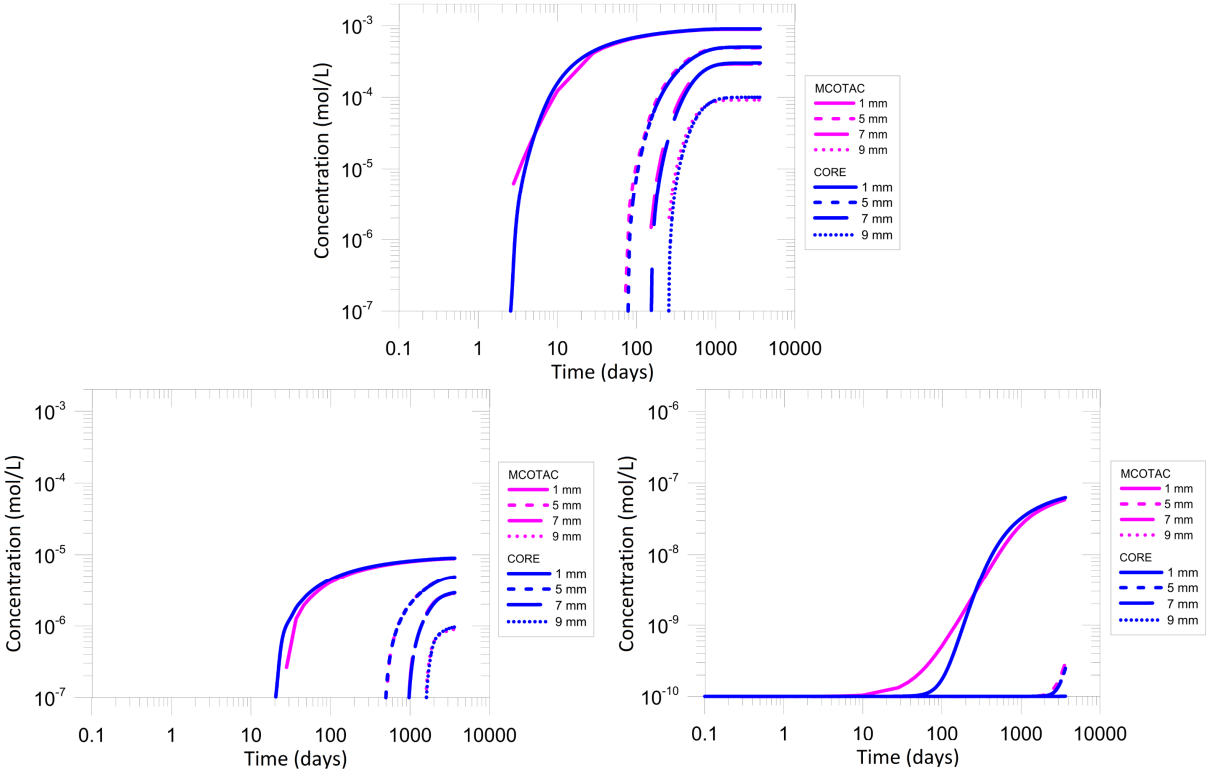

Figure 5.2. Cs breakthrough curves calculated with the multi-species transport models at x = 1, 5, 7 and 9 mm with CORE^{2D}V5 and MCOTAC. The Cs concentrations at the "high" concentration container were equal to 10^{-3} mol/L (top), 10^{-5} mol/L (bottom left) and 10^{-7} mol/L (bottom right).

5.4.3 Comparison of single-species and multi-species models

A detailed study of the Cs breakthrough curves at x = 1, 5, 7 and 9 mm computed with CORE^{2D}V5 with the single-species and the multi-species transport models for Cs boundary

concentrations equal to 10^{-3}, 10^{-5} and 10^{-7} mol/L was performed. The results were computed with the finite element mesh with 102 nodes. The results computed with the two numerical models are similar for the three Cs concentrations despite the differences in the formulations of the non-linear Cs sorption in Opalinus clay.

5.5 Conclusions

Single-species and multi-species transport models were performed with CORE^{2D}V5 to simulate the non-linear sorption of caesium (Cs) in Opalinus clay. The numerical models are related to former work carried out by Jakob et al. (2009) and to laboratory diffusion experiments performed at the Paul Scherrer Institut (PSI), Switzerland.

The single-species transport model uses a tabulated non-linear sorption isotherm measured in the laboratory to simulate the non-linear Cs sorption in Opalinus clay (Van Loon et al., 2009). CORE^{2D}V5 was modified to implement the tabulated sorption isotherm in a look-up table form with given values of K_d for pairs of Cs data: Cs in solution versus K_d. The results of the single-species transport model performed with CORE^{2D}V5 were compared with the results of COMSOL Multiphysics and MCOTAC. Cs breakthrough curves were computed at several locations for three Cs boundary concentrations with the three transport codes. The three codes give similar results. However, there are small differences between the results computed with the three codes due to: 1) Differences in the spatial discretization used in the codes, 2) Differences in the implementation of the sorption isotherm and 3) Differences in the interpolation procedures. A sensitivity analysis was performed with CORE^{2D}V5 to evaluate the numerical discretization errors. The computed results confirm that coarse grids lead to numerical dispersion.

The non-linear Cs sorption in Opalinus clay has been simulated also with a multi-species reactive transport model with cation exchange in three sites (Bradbury and Baeyens, 2000). Cs breakthrough curves computed with CORE^{2D}V5 at several locations in the Opalinus clay for three Cs boundary concentrations were compared with those computed with the reactive transport code MCOTAC. The results of both codes generally agree. However, there are slight differences between the results computed with CORE^{2D}V5 and MCOTAC due to the differences in the spatial discretization. In the models carried out with CORE^{2D}V5, the convergence tolerance to solve the chemical reactions had to be reduced to 10^{-7} to minimize the numerical errors.

The Cs breakthrough curves at several locations in the Opalinus clay computed with CORE^{2D}V5 with the single-species and the multi-species transport models using the same finite element mesh generally agree despite the differences in the formulation of the non-linear Cs sorption in Opalinus clay.

CHAPTER 6. NUMERICAL FLOW MODELS OF GROUNDWATER PUMPING AT THE CENTRALISED TEMPORARY STORAGE (CTS) OF RADIOACTIVE WASTE AT THE VILLAR DE CAÑAS SITE (CUENCA), SPAIN

6.1 Introduction

Pumping tests are commonly used to estimate aquifer properties. A pumping test consists on pumping water from a well at a known flow rate while the drawdown in the pumping well and in observation wells located some distance from the pumping well are recorded. Pumping tests are often interpreted with analytical methods which depend on the type of aquifer and well characteristics. Analytical solutions are based on simplifying assumptions which limit their application to real field conditions in heterogeneous aquifers. Numerical models overcome the limitations of analytical solutions for pumping test analysis in complex aquifers.

A Centralised Temporary Storage (CTS) to provide temporary storage spent fuel and high level radioactive waste from Spanish nuclear power plants is planned to be built in the municipality of Villar de Cañas in Cuenca (Spain). Several pumping test were carried out in the creek located east of the nuclear zone of the CTS site. The interpretation of the measured drawdowns with analytical solutions is prone to large identification and interpretation errors due to the large heterogeneities of the subsurface. The interpretation of these pumping tests with the help of numerical flow models overcomes these errors. This chapter presents 2-D horizontal groundwater flow models for the simulation of groundwater pumping at the CTS site. These models were performed to:

1) Interpret a long-term pumping test carried out in June 2016 in the creek located east of the nuclear zone of the CTS site, estimate the hydrogeological parameters of the subsurface and characterize the horizontal and vertical extent of the gypsum affected by dissolution within the Balanzas Gypsum Formation. The model of the pumping test takes into account the delayed drainage from the unsaturated zone and the water table evapotranspiration. The numerical model was successful in reproducing the measured drawdowns in the observation wells during the pumping test, estimating the hydrodynamic parameters of the Balanzas Gypsum Formation and characterizing the horizontal and vertical extent of the gypsum affected by dissolution within the Balanzas Gypsum Formation.

2) Simulate the potential impact of the Chaparral water supply pumping well on the hydrogeological conditions of the nuclear zone of the CTS site. These simulations were performed for several hypothesis and pumping schemes. Model results show that the drawdown of the water table produced by the Chaparral pumping well in the nuclear zone of the CTS site will be on the order of 0.4 m and will be much smaller than the changes in hydraulic heads caused by other planned actions such as the excavations of the basements of the nuclear buildings and the waterproofing of the built-up area.

The full version of Chapter 6 is not included in this reduced version of the dissertation. The numerical models performed during the course of this dissertation at the site of the Centralised Temporary Storage (CTS) located in Villar the Cañas (Cuenca, Spain) are subjected to data protection due to a confidentiality commitment from ENRESA. The full content of the Chapter 6 can be found in the full version of the dissertation. A brief summary of the numerical flow models of groundwater pumping at the CTS site is shown in Appendix 5 of this reduced version of the dissertation.

CHAPTER 7. 2-D FLOW MODELS IN VERTICAL PROFILES AT LOCAL AND DETAIL SCALES FOR THE CENTRALISED TEMPORARY STORAGE (CTS) FACILITY OF RADIOACTIVE WASTE AT THE VILLAR DE CAÑAS SITE (CUENCA), SPAIN

7.1 Introduction

Groundwater flow models are commonly used as interpretative tools for investigating groundwater system dynamics and understanding the flow patterns. However, flow models can be also used for predicting future conditions or impacts of human activities or as simulation tools for analysing responses of the groundwater system to stresses (Zhou and Li, 2011). The construction of a Centralised Temporary Storage (CTS) in Villar de Cañas (Cuenca, Spain) which will store the spent fuel from Spanish nuclear power plants and high-level radioactive waste for 60-100 years requires a detailed characterization of the site where this facility will be built and the analysis of the effect of the construction of the nuclear facilities on the hydraulic heads.

This chapter presents three numerical flow models performed with the code CORE^{2D}V5 in vertical profiles used to characterize the CTS site from a hydrogeological point of view and to predict future conditions at the CTS site. The first numerical model was performed in a vertical profile in East-West direction at a local scale. The main objectives of this model are to confirm the hydrogeological conceptual model proposed by Suso (2016) and to quantify the hydraulic heads and the groundwater flow field in the domain of the numerical model. The second numerical model was performed in a vertical profile in East-West direction at site scale. Predictions of the effects of the construction of the nuclear facilities on the hydraulic heads were carried out with this numerical model. The third numerical flow model was carried out in a vertical profile in North-South direction at site scale. The model was useful to ascertain the role of a drain to the north of the nuclear zone of the CTS site.

7.2 Numerical model in a vertical profile in East-West direction at a local scale

The numerical model has a length of 6045 m and extends from the Záncara River to the west to the Mesozoic limestones to the east. The upper boundary of the model coincides with the estimated water table under natural conditions. The bottom boundary of the model is located at an elevation of 450 masl. The numerical model was calibrated first in steady-state condition. The computed heads match the measured head data with calibration errors being smaller than 1 m. The numerical model was later extended to transient conditions. The computed hydrographs reproduce the measured fluctuations of the piezometric data, although there is time-lag in the maximum hydraulic heads. The numerical model confirms the hydrogeological conceptual model of the site and ratifies that the flows and volumes of water drained from (to) the Mesozoic formations to (from) the Tertiary materials are very small. The groundwater flow system includes a regional component from the Lower Tertiary Formation (UI+LBI) to the creek located in the vicinity of borehole SVC-8, the creek located to the east of the CTS site and the alluvial of the Záncara River. In addition, there are local flows which are controlled by the topography. The nuclear zone of the CTS site is located in a recharge area where groundwater percolates first vertically down. Later, some groundwater flows towards the west to the Záncara River and its alluvial and some groundwater recharge flows to the creek located to the east of the CTS site. The Balanzas Gypsum Formation (YB) behaves as a semi-confined layer which separates the groundwater local flow from the deep regional groundwater flow.

The 2-D local-scale flow model in a vertical profile in East-West direction of the CTS site has been useful to confirm the hydrogeological conceptual model and quantify hydraulic heads, groundwater flows and groundwater balance.

7.3 Site-scale numerical models in vertical profiles in East-West and North-South directions

Two numerical flow models in vertical profiles at site scale were performed at the Centralised Temporary Storage (CTS) site located in the municipality of Villar de Cañas in Cuenca (Spain). These groundwater flow models were used as predictive tools for simulating the future conditions at the CTS site. The first numerical model was performed in a vertical profile in East-West direction at site scale. The flow model was calibrated in steady-state conditions. The computed hydraulic heads reproduce the measured head data. Once calibrated, the model was used to perform transient predictions of the effects of the construction of the nuclear facilities on the hydraulic heads. The model takes into account the decrease in groundwater recharge in the nuclear zone of the CTS site due to water proofing and the

changes in the hydrodynamic parameters caused by rock decompression. Numerical simulations were performed for a total period of 50 years for the following scenarios: 1) No drains in the excavations of the nuclear facilities and 2) Draining systems in the excavations of the nuclear facilities. The model provides reasonable estimates of the changes in water pressures, the drawdown of the water table and the groundwater flows collected at the drains.

The numerical flow model in North-South direction was also calibrated in steady-state conditions. The computed hydraulic heads also fit the measured data. Numerical simulations were performed for 50 years with and without taking into account the drainage system by assuming a complete reduction of groundwater recharge. Model results indicate that: 1) The flow collected by the drain will be very small and 2) The drainage system will not condition the long-term position of the water table.

The full version of Chapter 7 is not included in this reduced version of the dissertation. The numerical models performed during the course of this dissertation at the site of the Centralised Temporary Storage (CTS) located in Villar the Cañas (Cuenca, Spain) are subjected to data protection due to a confidentiality commitment from ENRESA. The full content of the Chapter 7 can be found in the full version of the dissertation. A brief summary of the numerical flow model in a vertical profile in East-West direction at local scale at the CTS site is shown in Appendix 6 of this reduced version of the dissertation. Appendix 7 shows a brief summary of the numerical models in vertical profiles in E-W and N-S directions at detail scale at the CTS site.

CHAPTER 8. 3-D LOCAL-SCALE FLOW MODEL FOR THE CENTRALISED TEMPORARY STORAGE (CTS) FACILITY OF RADIOACTIVE WASTE AT THE VILLAR DE CAÑAS SITE (CUENCA), SPAIN

8.1 Introduction

Conceptualisation of aquifer systems has traditionally relied upon 2-D geological maps and cross-sections in order to develop an understanding of groundwater flow in three dimensions. 2-D horizontal flow models and numerical models in vertical profiles typically involve significant simplification of the geological structure and a potential reduction in the understanding of hydrogeological systems (Wycisk et al., 2009). The development of 3-D models provides opportunities for improving the conceptualisation of groundwater systems and have proved especially helpful in interpreting areas with complex geology. An exponential growth of application of 3-D numerical models for groundwater flow study has been witnessed in the last 20 years.

The groundwater flow at the site of the Centralised Temporal Storage (CTS) in the municipality of Villar de Cañas in Cuenca (Spain) exhibits three-dimensional features. This chapter presents a fully 3-D local-scale flow model of the CTS site which carried out as part of the characterization work of the CTS site. The 3-D flow model was performed with the 3-D finite element code CORE^{3D}-TRANMEF (Juanes, 1997; Juanes et al., 2002; Yang et al., 2003).

8.2 3-D flow model

The 3-D flow model was performed to test the hydrogeological conceptual model (Suso, 2016) and extend the capabilities of the previous 2-D flow models in vertical profiles. The 3-D model covers an area of 16.7 km^2 and extends from the Záncara River (west) to the Mesozoic limestones (east). The north and south boundaries of the model are far enough away from the nuclear zone so that the conditions imposed on these boundaries do not affect the computed heads in the nuclear area of the CTS site. The upper boundary of the model coincides with the water table surface under natural conditions which was estimated with geostatistical methods by combining Kriging and regression of hydraulic heads and ground surface elevation. The bottom boundary of the model is located at an elevation of 450 masl. The

model domain was discretized with a 3-D finite element mesh of parallelepiped elements. The mesh reproduces reasonably well the complex geology of the CTS site. The 3-D geology of the site was built from several geological profiles constructed parallel to the geological profile used for the 2-D local-scale model in the vertical profile in East-West direction.

8.3 3-D flow model results

The numerical model was calibrated in steady-state conditions. The computed hydraulic heads generally agree with the measured heads. The 3-D local-scale flow model confirms the hydrogeological conceptual model. Groundwater flows from the outcrops of the Lower Tertiary Formation (UI+LBI) to the creek located east of the CTS site and to the Záncara River and its alluvial. The groundwater flow system includes local flows in the nuclear zone of the CTS site where some groundwater flows towards the west (Záncara River and its alluvial) and some groundwater flows to the creek east of the CTS site. The results obtained with the 3-D flow model are consistent with those obtained with the 2-D horizontal models and the numerical models performed in vertical profiles. In addition, the results of the 3-D model confirm the main hypothesis assumed in the vertical profile models, i.e. that groundwater flow occurs mostly within vertical planes in East-West direction.

The full version of Chapter 8 is not included in this reduced version of the dissertation. The numerical models performed during the course of this dissertation at the site of the Centralised Temporary Storage (CTS) located in Villar the Cañas (Cuenca, Spain) are subjected to data protection due to a confidentiality commitment from ENRESA. The full content of the Chapter 8 can be found in the full version of the dissertation. A brief summary of the fully 3-D numerical flow model at local scale at the CTS site is shown in Appendix 8 of this reduced version of the dissertation.

CHAPTER 9. WATER FLOW, HEAT TRANSFER, GROUNDWATER AGE, HYDROCHEMICAL MIXING AND MULTICOMPONENT REACTIVE TRANSPORT MODELS AT THE CENTRALISED TEMPORARY STORAGE (CTS) OF RADIOACTIVE WASTE AT THE VILLAR DE CAÑAS SITE (CUENCA), SPAIN

9.1 Introduction

Understanding groundwater systems requires the combination and integration of geological, geophysical, hydrogeological, hydrogeochemical and isotopic data. The analysis of these data allows to develop conceptual models for hydrogeological systems. Nevertheless, it is generally difficult to account for all processes in a single mathematical model although the assumptions in the conceptual model may be logical. Therefore, separate models are usually performed to analyse hydrodynamic and hydrochemical information in complex hydrogeological systems. However, if several models are proposed in the same hydrogeological system, their results must be consistent with each other.

There is a good scientific understanding of the Centralised Temporary Storage (CTS) site in Villar de Cañas (Cuenca) which is based on an extensive characterization of the geology, hydrogeology, topography, meteorology, geotechnics and geochemistry of the site. This information has been used to carry out flow, heat transport and reactive transport models with CORE^{2D}V5 (Samper et al., 2009; 2011). The following numerical models were carried: 1) A heat transport model in the vertical profile in East-West direction at local scale; 2) Solute transport models to simulate groundwater age (Goode, 1996) in the vertical profile in East-West direction at local scale; 3) A hydrochemical mixing model to quantify mixing fractions; 4) A 1-D multicomponent reactive transport model to test and confirm the prevailing hydrochemical conceptual model of the CTS site proposed by CIEMAT (Gómez et al., 2013; 2014; 2016); and 5) A 2-D multicomponent reactive transport model to study and quantify the mechanisms of gypsum dissolution at the contact between the YB and UI+LBI formations away of the nuclear zone of the CTS.

The computed temperatures generally agree with the measured temperatures at several depths in boreholes drilled at the CTS site. Groundwater ages were calculated with the following two methods:

1) By adding a pulse of a conservative tracer to groundwater recharge and analysing the tracer breakthrough curves at selected locations of the model domain and 2) By simulating the age as a hypothetical tracer which has a unit source term in the solute transport equation, and a zero concentration in the inflow boundaries model. The groundwater ages calculated with the numerical model with both methods are similar and agree with the measured water ages with CFCs (chlorofluorocarbons) and ^{14}C.

The full version of Chapter 9 is not included in this reduced version of the dissertation. The numerical models performed during the course of this dissertation at the site of the Centralised Temporary Storage (CTS) located in Villar the Cañas (Cuenca, Spain) are subjected to data protection due to a confidentiality commitment from ENRESA. The full content of the Chapter 9 can be found in the full version of the dissertation. A brief summary of the heat transport, groundwater age hydrochemical mixing and multicomponent reactive transport models at the CTS site are shown in Appendix 9 of this reduced version of the dissertation.

CHAPTER 10. PARAMETRIC/NUMERICAL ANALYSIS OF THE ESTIMATION OF GROUNDWATER RECHARGE FROM WATER TABLE FLUCTUATIONS IN UNCONFINED AQUIFERS WITH 1-D AND 2-D DETERMINISTIC AND STOCHASTIC MODELS

10.1 Introduction

Groundwater recharge is a fundamental component in the water balance of any watershed and in the groundwater flow and transport models. Recharge is usually difficult to estimate, especially when it involves unsaturated flow, because of the extreme variability of recharge rates and the fact that many relevant processes cannot be directly observed. The most common methods to estimate the groundwater recharge include: 1) Water Table Fluctuations (WTF) method, 2) Water budget methods, 3) Methods based on Darcy's law, 4) Methods based on empirical relationships relating groundwater recharge to rainfall based on seasonal groundwater balance studies, 5) Groundwater modelling and 6) Tracer and isotopic techniques.

The groundwater recharge produced by discrete precipitation events in unconfined aquifers is often estimated from data of the water table rises recorded in shallow wells (WTF method) when aquifer recharge is instantaneous and concentrated and the response of the hydraulic heads to the rain is fast. However, this method involves large uncertainties. This chapter addresses these uncertainties by means of a numerical/parametric analysis of the water table fluctuations caused by the groundwater recharge and by the variation of the level of a river in an unconfined aquifer. This analysis has been performed with 1-D and 2-D numerical flow models in homogeneous and heterogeneous aquifers with a stochastic hydraulic conductivity field generated by geostatistical simulations.

The details of the parametric and numerical analysis of the estimation of groundwater recharge from water table fluctuations in unconfined aquifers using 1-D and 2-D deterministic and stochastic numerical models can be found in Appendix 10.

10.2 Water Table Fluctuations (WTF) method

Techniques based on the rise of groundwater levels are among the most widely-applied methods for estimating recharge rates. The Water Table Fluctuations (WTF) method is only applicable to unconfined aquifers and it is based on the premise that rises in groundwater levels are due to an instantaneous pulse of recharge water arriving at the water table. The main advantage of the WTF method is its simplicity and ease of use. The WTF method assumes that water arriving at the water table goes immediately into storage. The WTF method is most appropriate over short periods of time (hours or a few days) and for shallow water tables that display sharp water-level rises. If water is transported away from the water table at a rate that is not significantly slower than the rate at which recharge water arrives at the water table, then the method is of little value. In addition, the application of the WTF method requires determining a proper value for specific yield.

10.3 Description of the numerical models

A numerical/parametric analysis of the water table fluctuations caused by groundwater recharge and by the change of the level of a river in an unconfined aquifer was performed. To quantify the uncertainties of the WTF method, 1-D and 2-D numerical flow models in homogeneous and heterogeneous aquifers with a spatial structure of the hydraulic conductivity generated by geostatistical simulations were performed. The flow models were solved with CORE^{2D}V5 (Samper et al. 2009; 2011). The conceptual model was inspired by the hydrogeological conditions of the Guadalquivir River alluvial aquifer in Andújar (Jaén, Spain) (Samper and Pisani, 2009).

The length, L, of the aquifer in the 1-D numerical models, is assumed equal to 1000 m. The model domain was discretized with a uniform grid with a size, Δx, of 50 m. The simulated unconfined aquifer has a thickness equal to 2 m and the base elevation is 190.27 m. The hydraulic conductivity, K, and the specific yield, S_y, are equal to 50 m/d and 0.1, respectively. Groundwater recharge, R, is equal to 100 mm/year. A river was simulated at the right boundary of the model (H = 192.27 m). Moreover, a 1-D flow model was performed with the actual hydrogeological parameters of the Guadalquivir River alluvial aquifer in Andújar (Jaén, Spain). In this model, actual daily recharge and water level data were used in the numerical model.

The flow domain in the 2-D numerical models is rectangular with a surface of 2 x 3 km. The domain was discretized with a uniform 2-D mesh of rectangular triangles finite elements with Δx = 50 m. The hydraulic parameters for the homogeneous 2-D models are the same as those used in the 1-D models. The spatial aquifer heterogeneity of K was generated by geostatistical simulations. The values of S_y and R are similar to those considered in the homogeneous model. The spatial structure of K

was generated by geostatistical simulations by assuming that the *Ln K* is a Gaussian random field with a spherical semivariogram. The generation of *K* fields was performed with GCOSIM3D (Gómez-Hernández and Journel, 1993). At the right boundary of the model (the longest side), a river was simulated (H = 192.27 m). 1-D and 2-D models were solved for a total period of one year with daily time increments.

10.4 Model results

10.4.1 1-D model results

The errors made in estimation the groundwater recharge with the WTF method were quantified by analysing the hydrographs. The parametric and numeric analysis was focused on: 1) The hydraulic parameters of the aquifer such as the hydraulic conductivity (K), the specific yield (S_y) and the aquifer thickness (e), 2) The length of the aquifer (L) perpendicular to the river, 3) The time distribution of the recharge and 4) The variations of the river stage.

The increase in the hydraulic conductivity and the aquifer thickness do not affect the maximum rises of the hydraulic heads caused by an instantaneous recharge. However, the recovery of hydraulic heads after the recharge period in more permeable or thicker aquifers is faster. This effect is more pronounced in wells located away from the river. For the same recharge, a reduction in the specific yield leads to an increase in the maximum rises of the hydraulic heads. In addition, the recovery of the levels is faster when the specific yield is reduced. The estimation of the groundwater recharge with the WFT method requires knowing the proper values of the specific yield of the aquifer.

The maximum rises of the hydraulic heads caused by an instantaneous recharge do not depend on the aquifer length. However, the aquifer length affects the way in which the hydraulic heads decrease after the recharge period. The recovery of the hydraulic heads is faster when the aquifer length is shorter.

Several runs were performed with the following temporal distribution of groundwater recharge: instantaneous recharge and distributed recharge during the first month of simulation (uniformly and variable). The maximum rises of the hydraulic heads computed in the runs with variably-distributed recharge are significantly smaller than those computed with the instantaneous recharge (Figure 10.1). The groundwater recharge is underestimated with the WTF method when the recharge is not instantaneous. Model results show that the recharge estimated from a hydrograph of a well located 100 m from the river would be less than 50% of the actual recharge. At 200 m from the river, the estimation error of the WTF method would be about 25%. At 400 m from the river, the error is about 5%. At 800 m from the river the error is negligible. On the other hand, the maximum hydraulic heads

computed with uniformly-distributed and variably-distributed recharge during the first month are very similar.

A step rise of the river stage of 2 m which least for a first week of the simulation was considered. Groundwater recharge is overestimated when there is a rise of the river stage simultaneously during the recharge period of the aquifer. The hydraulic heads in the points located near the river (100 and 200 m) are more influenced by the variations of the level of the river (Figure 10.1). Therefore, the recharge estimated from the hydrograph of a well located 100 m from the river would be greater than 50% of the actual recharge. At 200 m from the river, the error would be about 20%. The error in the estimation of the recharge at 400 m from the river is about 5% while at 800 m from the river the error is negligible.

1-D flow models performed by using actual hydrogeological parameters of the Guadalquivir River alluvial aquifer in Andújar (Jaén, Spain) confirm that the hydraulic heads are very sensitive to the temporal distribution of the recharge and the variations of the river stage. The estimation of the recharge from data of the water table rises recorded in wells near rivers may contain large errors. In addition, these models also confirm that the computed hydraulic heads are sensitive to the leakage coefficient used in the Cauchy condition to simulate the variations of the Guadalquivir River.

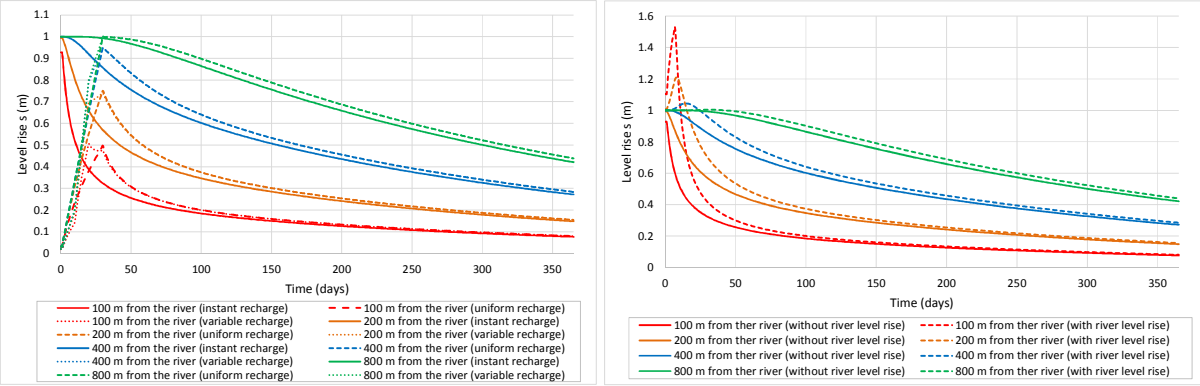

Figure 10.1. Sensitivity of the time evolution of the level rises at 100, 200, 400 and 800 m from the river to the time distribution of the recharge (left) and to changes in the river stage (right).

10.4.2 2-D model results

2-D flow models were performed by considering a homogeneous unconfined aquifer to verify the results obtained with 1-D models. The hydrographs calculated with the 2-D models are always identical to those computed with the 1-D models. Therefore, the conclusions of the parametric and numerical analysis performed with 1-D models apply also to the 2-D homogeneous aquifer.

The recharge estimated from water table rises recorded in wells located 100 m from the river would be underestimated by more than 80% when the groundwater recharge is not instantaneous in a

heterogeneous and isotropic aquifers in some areas. The estimated recharge at 400 m from the river, could be less than 60% of the actual recharge. However, the errors made in the estimation of recharge are less than 5% 800 m from the river. The errors made in the estimation of the recharge in areas near the river when there are changes in the river stage are similar to those committed when the recharge is not instantaneous. Nevertheless, the errors decrease with the distance to the river because the hydraulic heads are not affected by the changes in the river stage. There is a correlation between the errors made in the estimation of the recharge and the hydraulic conductivities. The errors are largest in the most permeable areas and smallest in the least permeable zones.

The maximum rises of the hydraulic heads decrease when the variance of *Ln K* increases. The maximum rises of the hydraulic heads increase with the variance of *Ln K* (σ^2) when rises of the river stage occur simultaneously during the recharge period. The errors in the estimation of groundwater recharge in wells near the river increase with increasing σ^2. The effect of the spatial heterogeneity of *Ln K* on the hydraulic heads decreases far from the river.

In heterogeneous and anisotropic aquifers, the hydraulic heads and, consequently, the errors made in estimating recharge with the WTF method depend on the main direction of anisotropy and the spatial connectivity of the most permeable zones near the river. The errors propagate in the main direction of anisotropy following the most permeable zones connected to the river (Figure 10.2). In isotropic aquifers, the errors 800 m from the river are very small (less than 5%). However, in anisotropic aquifers, the errors may be greater than 25% even 800 m from the river. In presence of anisotropy, the estimation errors may be important even at 1800 m from the river.

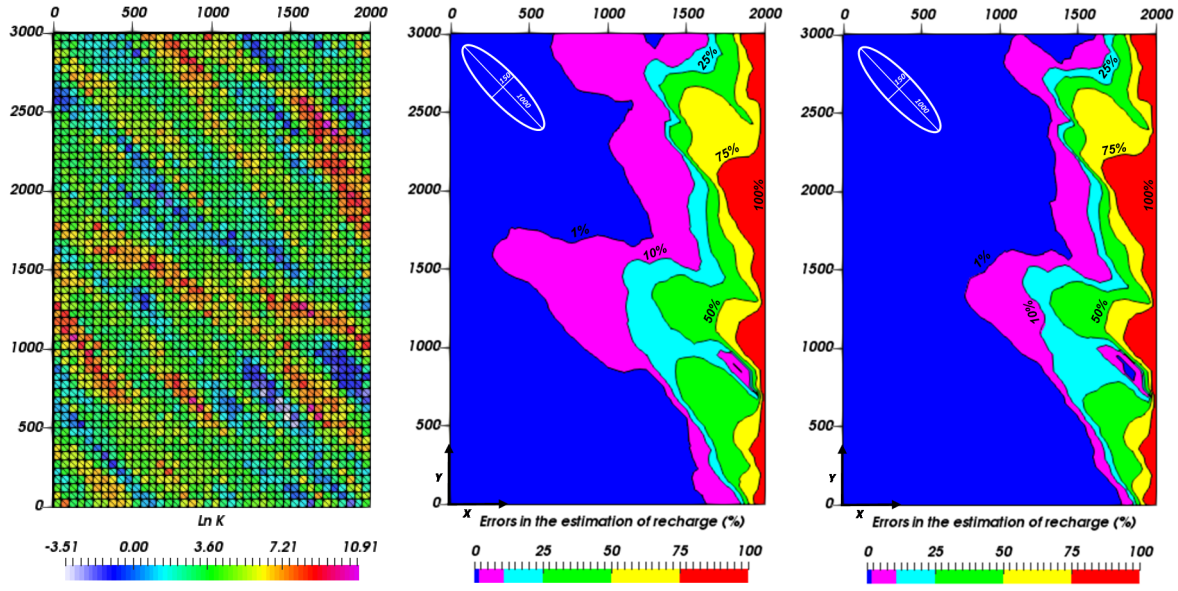

Figure 10.2. Spatial distribution of *Ln K* considering anisotropy in which the anisotropy axes form an angle of -45º with respect to the *X* axis (left) and spatial distribution of errors made in the estimation of recharge with the WTF method when the recharge is not instantaneous (intermediate) and when there is a rise of the river stage simultaneously during the recharge period of the aquifer (right).

The errors made in the estimation of the recharge in the numerical models where the main direction of anisotropy is perpendicular to the river are much greater than the errors made in the models in which the main direction of anisotropy is parallel to the river. In addition, in the models simulating a rise of the river stage simultaneously to the recharge period, the distance from the river in which errors are large is smaller than in the case where the heads are only affected by a non-instantaneous recharge.

10.5 Conclusions

A parametric and numerical analysis has been performed by means of 1-D and 2-D deterministic and stochastic models and it has allowed to quantify the errors made when the recharge is estimated from the piezometric oscillations recorded in wells in unconfined aquifers. The errors made in the estimation of the recharge depend on the parameters of the aquifer. The parametric and numerical analysis carried out indicates that the estimation of recharge from water table fluctuations (WTF method) may contain large errors, especially near a river with level rises simultaneously during the recharge period of the aquifer or when the recharge is not instantaneous. The results of the 1-D homogeneous models show that the errors made in estimating the groundwater recharge from a hydrograph of a well located 100 m from a river may be larger than 50% when the recharge is not instantaneous or there are variations of the level of the river.

In heterogeneous and anisotropic aquifers, the hydraulic heads and, consequently, the errors made in estimating groundwater recharge with the WTF method depend on the main direction of anisotropy and the spatial connectivity of the most permeable zones near the river. The errors propagate in the main direction of anisotropy following the most permeable zones connected to the river. In the presence of anisotropy, the estimation errors may be important even at 1800 m from the river.

The errors made in the estimation of the recharge in the numerical models where the main direction of anisotropy is perpendicular to the river are much greater than the errors made in the models in which the main direction of anisotropy is parallel to the river. In addition, in the models simulating a rise of the river stage simultaneously to the recharge period, the distance from the river in which errors are large is smaller than in the case where the heads are only affected by a non-instantaneous recharge.

CHAPTER 11. CONCLUSIONS AND FUTURE WORKS

11.1 Improvements and extensions of the codes of the CORE series

Improvements, updates, corrections and extensions of the codes of the CORE series have been performed in this dissertation. These improvements facilitate the development of flow and reactive transport models and the analysis of model results. Most of the improvements have been carried out in CORE^{2D}V5, although updates have been performed also in other codes such as INVERSE-CORE^{2D}, BIOCORE^{2D} and CORE^{3D} (TRANMEF-3D).

Particularly noteworthy are the improvements implemented in CORE^{2D}V5 dealing with porosity changes and its verification. CORE^{2D}V5 has been extended to take into account porosity changes due to mineral precipitation/dissolution and dynamically update the flow, transport and chemical parameters. The updated version of the code has been extensively verified against analytical solutions (Hayek et al., 2011, 2012) and by comparison with other reactive transport codes (Xie et al., 2015).

A non-isothermal reactive transport model of the interactions of compacted bentonite with the corrosion products of a carbon-steel canister and the concrete liner of the engineered barrier of a HLW in clay reported by Mon et al. (2017) has been performed with the updated version of CORE^{2D}V5. The model results after 40000 years calculated with and without porosity feedback have been compared. The major differences of the porosity computed with and without the porosity feedback are located in the concrete and at the concrete-clay and canister-bentonite interfaces. The thickness of pore clogging in the concrete and in the concrete-clay interface computed with the model with the porosity feedback is smaller than that computed without the porosity feedback.

11.2 Numerical flow and reactive transport models of laboratory experiments with strong porosity changes

Numerical flow and reactive transport models were performed with the updated version of CORE^{2D}V5 to simulate laboratory experiments with strong porosity changes due to dissolution/precipitation reactions carried out at the Paul Scherrer Institut (Switzerland). The following test were simulated with CORE^{2D}V5: 1) A test without chemical reactions and 2) A test focused on the porosity changes caused by precipitation of barium sulphate.

A conservative transport model in an advective regime was performed with CORE^{2D}V5 in Case 1. The tracer breakthrough curves at several ports of the tank, the contour plots of tracer concentrations and velocity profiles along various lines of the tank were computed with CORE^{2D}V5 and compared with the measured data and the model predictions of other reactive transport codes such as TOUGHREACT, OpenGeoSys-GEM, Pflotran and MIN3P. The results obtained with CORE^{2D}V5 agree with the measured data and with the results computed with other reactive transport codes, although there are small differences due to differences in the numerical methods and dispersive parameters of the reactive transport codes.

A reactive transport model focused on porosity changes due to mineral dissolution/precipitation reactions was performed for Case 2. The injection into the tank of $BaCl_2$ enhanced the dissolution of strontium sulphate and the precipitation of barium sulphate. The porosity changed during the experiment due to the difference between strontium sulphate and barium sulphate molar volumes. The total amounts of $BaSO_4$(s) and $SrSO_4$(s) in the tank and the concentrations of Cl^-, Sr^{2+} and Ba^{2+} computed with CORE^{2D}V5 agree with those computed with other reactive transport codes. In addition, the porosity and permeability changes calculated with CORE^{2D}V5 and other codes are in good agreement, although there are slightly differences at the interfaces. A sensitivity analysis to the grid discretization performed with CORE^{2D}V5 for Case 2 confirmed that the differences at the interfaces are due to the differences in the spatial discretization used by the reactive transport codes.

11.3 Caesium migration through Opalinus clay calculated by single-species and multi-species transport models

Single-species and multi-species transport models were performed with CORE^{2D}V5 to simulate the non-linear sorption of caesium (Cs) in Opalinus clay. The numerical models are related to former work carried out by Jakob et al. (2009) and to laboratory diffusion experiments performed at the Paul Scherrer Institut (PSI), Switzerland.

The single-species transport model uses a tabulated non-linear sorption isotherm measured in the laboratory to simulate the non-linear Cs sorption in Opalinus clay (Van Loon et al., 2009). CORE^{2D}V5 was modified to implement the tabulated sorption isotherm in a look-up table form with given values of K_d for pairs of Cs data: Cs in solution versus K_d. The results of the single-species transport model performed with CORE^{2D}V5 were compared with the results of COMSOL Multiphysics and MCOTAC. Cs breakthrough curves were computed at several locations for three Cs boundary concentrations with the three transport codes. The three codes give similar results. However, there are small differences between the results computed with the three codes due to: 1) Differences in the spatial discretization used in the codes, 2) Differences in the implementation of the sorption isotherm and

3) Differences in the interpolation procedures. A sensitivity analysis was performed with CORE^{2D}V5 to evaluate the numerical discretization errors. The computed results confirm that coarse grids lead to numerical dispersion.

The non-linear Cs sorption in Opalinus clay has been simulated also with a multi-species reactive transport model with cation exchange in three sites (Bradbury and Baeyens, 2000). Cs breakthrough curves computed with CORE^{2D}V5 at several locations in the Opalinus clay for three Cs boundary concentrations were compared with those computed with the reactive transport code MCOTAC. The results of both codes generally agree. However, there are slight differences between the results computed with CORE^{2D}V5 and MCOTAC due to the differences in the spatial discretization. In the models carried out with CORE^{2D}V5, the convergence tolerance to solve the chemical reactions had to be reduced to 10^{-7} to minimize the numerical errors.

The Cs breakthrough curves at several locations in the Opalinus clay computed with CORE^{2D}V5 with the single-species and the multi-species transport models using the same finite element mesh generally agree despite the differences in the formulation of the non-linear Cs sorption in Opalinus clay.

11.4 Flow and reactive transport models at the Centralised Temporary Storage for radioactive waste (CTS) at the Villar de Cañas site (Cuenca), Spain

On 30 December 2011, the Government of Spain designated the municipality of Villar de Cañas in Cuenca as the site for the Centralised Temporary Storage (CTS) facility for radioactive waste and its Associated Technological Centre. This facility will provide temporary storage for the spent fuel and high-level radioactive waste from Spanish nuclear power plants. ENRESA (Empresa Nacional de Residuos Radiactivos S.A.) started the site characterization activities early 2012. The *"Agua y Suelo"* Research Group of the University of A Coruña led by Professor Javier Samper has been involved in the numerical groundwater flow modelling of the CTS site since 2013. These numerical flow models constitute a very important part of this PhD Dissertation. The following flow and reactive transport models were performed:

- 2-D horizontal groundwater flow models for the simulation of groundwater pumping at the CTS site to: 1) Interpret a long-term pumping test carried out in June 2016 in the creek located east of the nuclear zone of the CTS site, estimate the hydrogeological parameters of the subsurface and characterize the horizontal and vertical extent of the gypsum affected by dissolution processes within the Balanzas Gypsum Formation; and 2) Simulate the

potential impact of the Chaparral water supply pumping well on the hydrogeological conditions of the nuclear zone of the CTS site.

- 2-D flow models in vertical profiles in East-West and North-South directions at local and site scales to: 1) Test the hydrogeological conceptual model proposed by Suso (2016); 2) Quantify hydraulic heads and groundwater flows; 3) Predict the effects of the construction of the nuclear facilities on the hydraulic heads; and 4) Evaluate the need to place drainage systems north of the nuclear zone of the CTS site.

- A fully 3-D local-scale numerical model at the CTS site to: 1) Test the hydrogeological conceptual model; 2) Quantify hydraulic heads and groundwater flows; and 3) Test the hypotheses of the vertical profile models which assume that groundwater flow occurs mostly within vertical planes.

- Water flow, heat transport, groundwater age, hydrochemical mixing fraction and multicomponent reactive transport models at the CTS site to: 1) Test the validity of the numerical flow models performed at the CTS site; 2) Test the hydrogeochemical conceptual model of the site proposed by CIEMAT (Gómez et al., 2013; 2014a,b; 2016); and 3) Quantify the time evolution of gypsum dissolution at the contact between the YB and UI+LBI formations away from the nuclear zone of the CTS.

The conclusions of the numerical flow and the reactive transport models performed at the CTS site are not included in this reduced version of the dissertation. The numerical models performed during the course of this dissertation at the CTS site are subjected to data protection due to a confidentiality commitment from ENRESA. The conclusions of the numerical flow and the reactive transport models at the CTS site can be found in the full version of the dissertation.

11.5 Parametric/numerical analysis of the estimation of groundwater recharge from water table fluctuations in unconfined aquifers

A parametric and numerical analysis has been performed by means of 1-D and 2-D deterministic and stochastic models and it has allowed to quantify the errors made when the recharge is estimated from the piezometric oscillations recorded in wells in unconfined aquifers. The errors made in the estimation of the recharge depend on the parameters of the aquifer. The parametric and numerical analysis carried out indicates that the estimation of recharge from water table fluctuations (WTF method) may contain large errors, especially near a river with level rises simultaneously during the recharge period of the aquifer or when the recharge is not instantaneous. The results of the 1-D homogeneous

models show that the errors made in estimating the groundwater recharge from a hydrograph of a well located 100 m from a river may be larger than 50% when the recharge is not instantaneous or there are variations of the level of the river.

In heterogeneous and anisotropic aquifers, the hydraulic heads and, consequently, the errors made in estimating groundwater recharge with the WTF method depend on the main direction of anisotropy and the spatial connectivity of the most permeable zones near the river. The errors propagate in the main direction of anisotropy following the most permeable zones connected to the river. In the presence of anisotropy, the estimation errors may be important even at 1800 m from the river.

The errors made in the estimation of the recharge in the numerical models where the main direction of anisotropy is perpendicular to the river are much greater than the errors made in the models in which the main direction of anisotropy is parallel to the river. In addition, in the models simulating a rise of the river stage simultaneously to the recharge period, the distance from the river in which errors are large is smaller than in the case where the heads are only affected by a non-instantaneous recharge.

11.6 Recommendation for future works

This dissertation contains significant contributions within the field of flow and reactive transport modelling of low-permeability structured media. However, there are still challenges to be solved in the future. Recommendations for future research include:

1) Improving the codes of the CORE series by:
    a. Adapting all the codes for the use of available public-domain post-processing tools.
    b. Implementing more efficient numerical algorithms to improve the convergence of the iterative methods and reduce computation times.
    c. Optimizing the management of the memory codes.
    d. Updating all the codes to take into account the feedback effect of the changes in porosity caused by mineral dissolution/precipitation.
    e. Reviewing and extending the thermodynamic, kinetic and microbiological databases of the CORE codes.

2) Model testing and benchmarking:
    a. Testing the improvements implemented in CORE^{2D}V5 with additional laboratory experiments with porosity changes due to mineral dissolution/precipitation and the update of the flow, transport and chemical parameters.
    b. Extending the Cs sorption benchmarking test case to account for mineral phases.

c. Testing the relevance of the changes in porosity and other transport parameters for the long-term predictions of a HLW repository in clay.

3) Improving and extending the numerical models of the CTS site in Villar de Cañas (Cuenca, Spain) by:

   a. Updating and improving the site-scale models in vertical profiles to take into account the additional recent data on hydraulic conductivity and hydraulic heads.

   b. Refining the mesh of the local-scale profile model in E-W direction to improve the simulation of the groundwater ages at the CTS site.

   c. Updating the fully 3-D flow model with more recent data, including hydraulic head data in boreholes where the natural hydraulic heads have not yet reached stabilized values. This model could also be improved by incorporating more details in the zonation of hydraulic conductivities.

   d. Extending the 3-D flow model to transient conditions and analysing the effects of the construction of the nuclear facilities on the hydraulic heads.

   e. Modelling the pumping test carried out on the creek located east of the nuclear zone of the CTS site and analysing the effect of the pumping in the Chaparral well on the hydrogeological conditions in the nuclear zone of the CTS site with the 3-D flow model.

   f. Performing heat transport, groundwater age, hydrogeochemical mixing and reactive transport models of the CTS site with the 3-D model.

CHAPTER 12. REFERENCES

Ackerer, P. (Editor), (2010). Simulations of reactive transport: results of the MoMaS benchmark. Comput. Geosci., vol. 14 (3).

Ahrens, J., Geveci, B., Law, C., (2005). ParaView: An End-User Tool for Large Data Visualization, Visualization Handbook, Elsevier, ISBN-13: 978-0123875822.

Archie, G., (1942). The electrical resistivity log as an aid in determining some reservoir characteristics. Pet. Trans. AIME, 146, 54-62.

Ayachit, U., (2015). The ParaView Guide: A Parallel Visualization Application, Kitware, ISBN 978-1930934306.

Bear, J., (1979). Hydraulics of Groundwater. McGraw-Hill, New York. 569 pp.

Berner, U., Kulik, D.A., Kosakowski, G., (2013). Geochemical impact of a low-pH cement liner on the near field of a repository for spent fuel and high-level radioactive waste. Phys. Chem. Earth, 64, 46-56.

Bradbury, M.H., Baeyens, B., (2000). A generalised sorption model for the concentration dependent uptake of caesium by argillaceous rocks. J. Contam. Hydrol., 42, 141-163.

Carman, P.C., (1937). Fluid through granular beds. Trans. Inst. Chem. Eng., 15, 150-166.

Carnahan, C.L., (1990). Coupling of precipitation/dissolution reactions and mass diffusion via porosity changes. In Chemical Modeling of Aqueous Systems II, edited by D.C, Melchior and R.L. Bassett, American Chemical Society, Washington, D.C. 234-242.

Cederberg, G.A., Street, R., Leckie, J.O., (1985). A groundwater mass transport and equilibrium chemistry model for multicomponent systems. Water Resour. Res., 21(8) 1095-1104.

Dai, Z., Samper, J., (1999). INVERSE-CORE^{2D}: A Code for inverse problem of water flow and reactive solute transport, User's Manual, Version 0, Universidade da Coruña.

Dai, Z., (2000). Inverse problem of water flow and reactive solute transport in variably saturated porous media, Ph.d. dissertation, 334 pp., Universidade da Coruña, A Coruña, Spain.

Dai, Z., Samper, J., (2004). Inverse problem of multicomponent reactive chemical transport in porous media: Formulation and Applications. Water Resources Research, vol. 40 (7).

De Windt, L., Pellegrini, D., Van der Lee, J., (2004). Coupled modeling of cement/claystone interactions and radionuclide migration. J. Contam. Hydrol., 68, 165-182.

De Windt, L., Badredinne, R., Lagneau, V., (2007). Long-term reactive transport modelling of stabilized/solidified waste: from dynamic leaching tests to disposal scenarios. J. Hazard. Mater., 207, 529-536.

Engesgaard, P., Kipp, K.L., (1992). A geochemical transport model for redox-controlled movement of mineral fronts in groundwater flow systems: A case of nitrate removal by oxidation of pyrite. Water Resour. Res., 28(10) 2829-2843.

ENRESA, (1995). TRANQUI User's Manual. Technical report for ENRESA. J. Samper, C. Ayora, T. Xu, N. Cuellar. A Coruña, 1995.

ENRESA, (2004). Evaluación del comportamiento y de la seguridad de un almacén geológico profundo de residuos radiactivos en arcilla. Report ENRESA 49-1PP-M-A1-01.

Gaucher, E.C., Blanc, P., (2006). Cement/clay interaction - a review: experiments, natural analogues, and modelling. Waste Manag., 26, 776-788.

Goode, D.J., (1996). Direct simulation of groundwater age. Water Resources Research, Vol. 32, No. 2, pp 289-296.

Gómez-Hernández, J.J., Journel, A.G., (1993). Joint simulation of multi-Gaussian random variables. In Soares, A., editor, Geostatistics Tróia '92, volume 1, pp. 85-94. Kluwer.

Gómez, P., Peña, J., Garralón, A., Torres, E., Buil, B., Turrero, M.J., Robredo, L.M., Domínguez, R., Durán, J.M., Escribano, A., Sánchez, L., (2013). Estudio hidrogeológico del emplazamiento del Almacén Centralizado Temporal (ATC) en Villar de Cañas (Cuenca). Technical Report for ENRESA. CIEMAT, Madrid, 88 pp.

Gómez, P., Peña, J., Torres, E., Buil, B., Garralón, A., Turrero, M.J., Escribano, A., Domínguez, R., Durán, J.M., Sánchez, L., (2014). Estudio hidrogeológico del emplazamiento del Almacén Centralizado Temporal (ATC) en Villar de Cañas (Cuenca). Technical Report for ENRESA. CIEMAT, Madrid, 90 pp.

Gómez, P., Torres, E., Peña, J., Garralón, A., Turrero, M.J., Buil, B., Durán, J.M., Escribano, A., Sánchez, L., Domínguez, R., (2016). Actualización del Modelo Hidrogeoquímico del ATC (Villar de Cañas, Cuenca). Technical Report for ENRESA. CIEMAT, Madrid, 116 pp.

Hayek, M., Kosakowski, G., Churakov, S., (2011). Exact analytical solutions for a diffusion problem coupled with precipitation–dissolution reaction and feedback of porosity change. Water Resour., 47, W07545. http://dx.doi.org/10.1029/2010WR010321.

Hayek, M., Kosakowski, G., Jakob, A., (2012). A class of analytical solutions for multidimensional species diffusive transport coupled with precipitation–dissolution reactions and porosity changes. Water Resour., 48, W03525. http://dx.doi.org/10.1029/2011WR011663.

Jakob, A., Pfingsten, W., Van Loon, L., (2009). Effects of sorption competition on caesium diffusion through compacted argillaceous rock. Geochimica et Cosmochimica Acta, 73, 2441-2456

Jennings, A.A., Kirkner, D.J. Theis, T.L., (1982). Multicomponent equilibrium chemistry in groundwater quality models. Water Resour. Res., 18(4): 1089-1096.

Juanes, R., (1997). Un código para la modelización tridimensional de flujo y transporte. Technical project, E.T.S.I.C.C.P., Universidade da Coruña.

Juanes, R., Samper, J., (2001). Una formulación general y eficiente de fracturas y condiciones de contorno en el M.E.F.: II. Aplicación a casos sintéticos. Revista Internacional de Métodos Numéricos para Cálculo y Diseño en Ingeniería, 17(1):67-82.

Juanes, R., Samper, J., Molinero, J., (2002). A general and efficient formulation of fractures and boundary conditions in the finite element method. International Journal for Numerical Methods in Engineering, 54, 1751-1774.

Juncosa, R., Navarro, V., Samper, J., (1999) Manual del usuario de FADES-CORE (Versión 0.0.). E. T. S. I. de Canales y Puertos, Universidade da Coruña.

Kirkner, D.J., Theis, T.L., Jennings, A.A., (1984). Multicomponent solute transport with sorption and soluble complexation. Adv. Water Resour., 7: 120-125.

Kirkner, D.C., Reeves, M., (1988). Multicomponent mass transport with homogeneous and heterogeneous chemical reactions: Effect of the chemistry on the choice of numerical algorithm: 1, Theory. Water Resour. Res., vol. 24 (1) 1719-1729.

Kosakowski, G., Berner, U., (2013). The evolution of clay rock/cement interfaces in a cementitious repository for lowand intermediate level radioactive waste. Phys. Chem. Earth, 64, 65-86.

Lensing, H.J., Vogt, M., Herrling, B., (1994). Modeling of biologically mediated redox processes in the subsurface. Journal of Hydrology, 159: 125-143.

Lichtner, P.C., Steefel, S.I., Oelkers, E.H., (1996). Reactive Transport in Porous Media. Reviews in Mineralogy. Mineralogical Society of America, 34:83-100.

Liu, C.W., Narasimhan, T.N., (1989). Redox-controlled multiple species reactive chemical transport, 1. Model development. Water Resour. Res., 25: 869-882.

Mangold, D., Tsang, C., (1991). A Summary of Subsurface Hydrological and Hydrochemical models. Reviews of Geophysics, 29: 51-79.

Mayer, K.U., Frind, E.O., Blowes D.W., (2002). Multicomponent reactive transport modeling in variably saturated porous media using a generalized formulation for kinetically controlled reactions, Water Resour. Res., 38(9), 1174, doi:10.1029/2001WR000862.

Mayer, K.U., MacQuarrie, K.T.B., (2010). Solution of the MoMaS reactive transport benchmark with MIN3P-model formulation and simulation results. Comput. Geosci., Vol 14, 3, pp 405-419.

Miller, C.W., Benson, L.V., (1983). Simulation of solute transport in a chemically reactive heterogeneous system: Model development and application. Water Res. Res., 19: 381-391.

Mon, A., (2017). Coupled thermo-hydro-chemical-mechanical models for the bentonite barrier in a radioactive waste repository. Ph.D. Dissertation, Universidade da Coruña, 483 pp.

Mon, A., Samper, J., Montenegro, L., Naves, A., Fernández, J., (2017). Long-term non-isothermal reactive transport model of compacted bentonite, concrete and corrosion products in a HLW repository in clay. J. Contam. Hydrol., https://doi.org/10.1016/j.jconhyd.2016.12.006

Narasimhan, T.N., White, A.F., Tokunaga, T., (1986). Groundwater Contamination from an inactive uranium mill tailings pile, 2, Application of a dynamic mixing model. Water Resour. Rec., 22(13): 1820-1834.

Parkhurst, D.L., Appelo, C.A.J., (1999). User's guide to PHREEQC (version 2) - A computer program for speciation, batch-reaction, one-dimensional transport, and inverse geochemical calculations, U.S. Geol. Surv. Water Resour. Invest. Rep., 99-4259, 312 pp.

Parkhurst, D.L., Kipp, K.L., Engesgaard, P., Charlton S.R., (2002). PHAST - A program for simulating ground-water flow and multicomponent geochemical reactions, U.S. Geol. Surv., Denver, Col.

Pfingsten, W., (1994). Modular coupling of transport and chemistry: theory and model applications. PSI Bericht No. 94-15. Paul Scherrer Institut, Villigen PSI, Switzerland and Nagra technical report 94-19. Nagra, Wettingen, Switzerland.

Pfingsten, W., (2002). Experimental and modelling indications for self-sealing of a cementitious low- and intermediate-level waste repository by calcite precipitation. Nucl. Technol., 140, 63-82.

Pfingsten, W., (2005). MCOTAC 2005. PSI internal report AN-44-05-07. Paul Scherrer Institut, Villigen PSI, Switzerland (in German).

Pfingsten, W., Jakob, A., (2014). Benchmark for nonlinear sorption processes of Cs migration through Opalinus Clay using a single species (COMSOL) and a multi-species (MCOTAC) reactive transport model. Workshop TRePro III-Transport and Reaction Processes, 5-7 March 2014, Karlsruhe, Germany.

Poonoosamy, J., Kosakowski, G., Van Loon, L.R., Mäder, U., (2015). Dissolution-precipitation processes in tank experiments for testing numerical models for reactive transport calculations: Experiment and modelling. J. Contam. Hydrol., 177-178, 1-17.

Rheinheimer, G., (1992). Aquatic Microbiology. 4th Edition, Published by John Wiley & Sons Ltd.

Rubin, J., James, R.V., (1973). Dispersion-affected transport of reacting solutes in saturated porous media: Galerkin method applied to equilibrium-controlled exchange in unidirectional steady water flow. Water Resour. Res., vol. 9: 1332-1356.

Rubin, J., (1983). Transport of reactive solutes in porous media: relation between mathematical nature of problem formulation and chemical nature of reactions. Water Resources Research, vol. 19 (5) 1231-1252.

Saaltink, M.W., Benet, I., Ayora, C., (1997). RETRASO, Fortran code for solving 2D reactive transport of solutes, user's guide, ETSI Caminos, Canales y Puertos, Universitat Politècnica de Catalanya and Instituto de Ciencias de la Terra, CSIC, Barcelona.

Saaltink, M., (1999). On the approaches for incorporating equilibrium and kinetic chemical reactions in transport models. Ph.D. Dissertation. Universitat Politècnica de Catalunya. Barcelona.

Samper, J., Juncosa, R., Delgado, J., Montenegro, L., (1998). CORE-LE User's Manual. Universidade da Coruña, 207 pp.

Samper, J., Delgado, J., Juncosa, R., Huguet, Ll., (1999). Manual de VISUAL-CORE-LE, Version 1.0. Technical report for ENRESA. E. T. S. Ingenieros de Caminos. Universidade da Coruña.

Samper, J., Juncosa, R., Delgado, J., Montenegro, L., (2000). CORE^{2D}: A code for non-isothermal water flow and reactive solute transport, User's manual version 2, Universidade da Coruña, Publication for ENRESA, 131 pp.

Samper, J., Yang, C., Montenegro, L., (2003). CORE^{2D} version 4: a code for non-isothermal water flow and reactive solute transport. User's Manual. Universidade da Coruña, Spain.

Samper, J., Zhang, G., Montenegro L., (2006). Coupled microbial and geochemical reactive transport models in porous media: Formulation and Application to Synthetic and In Situ Experiments. Journal of Iberian Geology, 32 (2) 2006: 215-231.

Samper, J., Lu, C., Montenegro, L., (2008a). Coupled hydrogeochemical calculations of the interactions of corrosion products and bentonite. Phys. Chem. Earth, 33, S306–S316. http://dx.doi.org/10.1016/j.pce.2008.10.009.

Samper J., Zheng, L., Montenegro, L., Fernández, A.M., Rivas, P., (2008b). Coupled thermo-hydro-chemical models of compacted bentonite after FEBEX in situ test, Appl. Geochem. Vol 23/5: 1186-1201.

Samper, J., Pisani, B., (2009). Aquifer recharge evaluation by a combination of soil water balance and groundwater flow models. Estudios en la Zona no Saturada del Suelo. Vol IX, O. Silva et al. Barcelona, November 18-20, 2009

Samper, J., Xu, T., Yang, C. (2009). A sequential partly iterative approach for multicomponent reactive transport with CORE^{2D}. Comput. Geosci., http://dx.doi.org/10.1007/s10596-008-9119-5.

Samper, J., Yang, C., Zheng, L., Montenegro, L., Xu, T., Dai, Z., Zhang, G., Lu, C., Moreira, S., (2011). CORE^{2D}V4: A code for water flow, heat and solute transport, geochemical reactions, and microbial processes, Chapter 7 of the Electronic book Groundwater Reactive Transport Models, F Zhang, G-T Yeh, C Parker & X Shi (Ed), Bentham Science Publishers, pp 161-186, ISBN: 978-1-60805-029-1.

Samper, J., Naves, A., Montenegro, L., Mon, A., (2016). Reactive transport modelling of the long-term interactions of corrosion products and compacted bentonite in a HLW repository in granite: Uncertainties and relevance for performance assessment. Appl. Geochem. Vol, 67, 42-51.

Samper, J., Fernández, J., Pisani, B., Mon, A., Naves, A., Montenegro, L., (2014a). Modelos matemáticos de flujo subterráneo en el emplazamiento del almacén temporal centralizado (ATC) en Villar de Cañas (Cuenca). Technical report for ENRESA. Universidade da Coruña. June 2014.

Samper, J., Fernández, J., Pisani, B., Mon, A., Naves, A., Montenegro, L., (2014b). Modelos matemáticos de flujo subterráneo en el emplazamiento del almacén temporal centralizado (ATC) en Villar de Cañas (Cuenca). Updated and revised version. Technical report for ENRESA. Universidade da Coruña. December de 2014.

Samper, J., Fernández, J., Pisani, B., Mon, A., Naves, A., Montenegro, L., (2016). Modelo matemático (2D/3D) del flujo de aguas subterráneas en el emplazamiento del ATC. Technical report for ENRESA. E.T.S.I. Caminos, Canales y Puertos. Universidade da Coruña.

Samper, J., Mon, A., Fernández, J., Montenegro, L., (2017). Discretization errors and porosity feedback for the long-term reactive transport model of the interactions of concrete, compacted bentonite and clay in a HLW repository in clay. Proceedings of the Second Annual Workshop of the HORIZON 2020 CEBAMA Project. 16th-19th May 2017 Finland.

Steefel, C.I., Lasaga, A., (1990). Permeability change are to Coupled Flow and Reaction. In: Chemical Modelling of Aqueous Systems II, Am. Chem. Soc. (Chapter 16) 212-225.

Steefel, C.I., MacQuarrie, K.T.B., (1996). Approaches to modeling reactive transport in porous media, in: P.C. Lichtner, C.I. Steefel, E.H. Oelkers (Eds.), Reactive Transport in Porous Media, Reviews in Mineralogy, vol. 34, pp. 83-125.

Steefel, C. I., (2001). CRUNCH: Software for modeling multicomponent, multidimensional reactive transport, user's guide, Rep. UCRL-MA-143182, Lawrence Livermore Nat. Lab., Livermore, Calif.

Suso, J., (2016). Caracterización piezométrica y actualización del modelo conceptual hidrogeológico del ATC (Villar de Cañas, Cuenca). Technical report for ENRESA, ENR-16-IF-01 R01. 39 pp.

Valocchi, A.J., Street, R.L., Roberts, P.V., (1981). Transport of ion-exchanging solutes in groundwater: Chromatographic theory and field simulation. Water Resour. Res., 17(5) 1517-1527.

van der Lee, J., De Windt L., (2001). Present state and future directions of modeling of geochemistry in hydrogeological systems, J. Contam. Hydrol., 47(2-4), 265-282.

van der Lee, J., De Windt L., Lagneau V., Goblet P., (2003). Module-oriented modeling of reactive transport with HYTEC, Comput. Geosci., 29(3), 265-275.

van der Lee, J. (2005). Reactive transport modelling with HYTEC, user's guide and tutorial, Tech. Rep. LHM/RD/05/30, 114 pp., Cent. d'Inf. Géol., École des Mines, Fontainebleau, France.

Van Loon, L.R., Soler, J.M., Bradbury, M.H., (2003a). Diffusion of HTO, $^{36}Cl^-$ and $^{125}I^-$ in Opalinus clay samples from Mont Terri - effect of confining pressure. J. Contam. Hydrol., 61, 73-83.

Van Loon, L.R., Baeyens, B., Bradbury, M.H., (2009). The sorption behaviour of caesium on Opalinus clay: A comparison between intact and crushed material. Appl. Geochem., 24, 999-1004.

Walsh, M.P., Bryant, S.L., Lake, L.W., (1984). Precipitation and dissolution of solids attending flow through porous media. AICHE J., 30 (2): 317-328.

White, A.F., Delany, J.M., Narasimhan, T.N., Smith, A., (1984). Groundwater contamination from an inactive uranium mine tailings pile, 1, Application of a chemical mixing model. Water Resour. Res., 22 (3) 1743-1752.

Wolery, T.J., (1992). EQ3/6, a software package for geochemical modeling of aqueous systems: package overview and installation guide (version 7.0). Technical Report UCRL-MA-110662-Pt 1. Lawrence Livermore National Laboratory, CA, USA.

Wycisk, P., Hubert, T., Gossel, W., Neumann, Ch., (2009). High-resolution 3D spatial modelling of complex geological structures for an environmental risk assessment of abundant mining and industrial megasites. Computers & Geosciences, 35: 165-182

Xie, M., Mayer, K.U., Claret, F., Alt-Epping, P., Jacques, D., Steefel, C., Chiaberge, C., Simunek, J., (2015). Implementation and evaluation of permeability-porosity and tortuosity-porosity relationships linked to mineral dissolution-precipitation. Computat. Geosci., 19, 655-671.

Xu, T., (1996). Modeling Non-isothermal multi-component reactive solute transport through variably saturated porous media. Ph.D. dissertation. Universidade da Coruña. A Coruña.

Xu, T., Samper, J., Ayora, C., Manzano, M., Custodio, E., (1999). Modeling of Non-Isothermal Multi-Component Reactive Transport in Field Scale Porous Media Flow System. J. Hydrol., 214, 144-164.

Xu, T., Sonnenthal E., Spycher N., Pruess K. (2004). TOUGHREACT user's guide: A simulation program for non-isothermal multiphase reactive geochemical transport in variable saturated geologic media, Rep. LBNL-55460, 192 pp., Lawrence Berkeley Natl. Lab., Berkeley, Calif.

Xu, T., Sonnenthal E., Spycher N., Pruess K. (2006). TOUGHREACT - A simulation program for non-isothermal multiphase reactive geochemical transport in variably saturated geologic media: Applications to geothermal injectivity and CO_2 geological sequestration, Comput. Geosci., 32(2), 145-165.

Xu, T., Spycher N., Sonnenthal E., Zhang G., Zheng L., Pruess K., (2011). TOUGHREACT version 2.0: A simulator for subsurface reactive transport under non-isothermal multiphase flow conditions, Comput. Geosci., 37(6), 763-774.

Yang, C., Juanes, R., Samper, J., Molinero, J., Montenegro, L., (2003). User's manual of CORE^{3D}, Technical Report. Universidade da Coruña, Spain.

Yang, C., Samper, J., Montenegro, L., (2008). A coupled non-isothermal reactive transport model for long-term geochemical evolution of a HLW repository in clay. Environ. Geol., 53:1627–1638. http://dx.doi.org/10.1007/s00254-007-0770-2.

Yeh, G.T., Tripathi, V.S., (1989). A critical evaluation of recent developments of hydrogeochemical transport models of reactive multichemical components. Water Resour. Res., vol 25 (1) 93-108.

Yeh, G.T., Tripathi, V.S., (1991). A model for simulating transport of reactive multispecies components: model development and demonstration, Water Resour. Res., 27(12) 3075-3094.

Yeh, G.T. (2000). Computational subsurface hydrology, reactions, transport and fate. Kluwer Academic Publishers, The Netherland, 318p.

Zhang, G., (2001). Nonisothermal hydrobiogeochemical models in porous media. Ph.D. Dissertation. Universidade da Coruña. Spain.

Zhang, G., Samper, J., (2001). BIOCORE^{2D}: A code for non-isothermal hydrobiogeochemical reactive transport. User's Manual V0. Technical report. E.T.S.I. de Caminos, Canales y Puertos. Universidade da Coruña, 244 pp.

Zheng, L., Samper J. (2005). Manual of Inverse FADES-CORE, Technical report, Universidade da Coruna, Spain.

Zheng, L., Samper, J., (2008). Coupled THMC model of FEBEX mock-up test. Phys. Chem. Earth, 33:S486–S498. http://dx.doi.org/10.1016/j.pce.2008.10.023.

Zheng, L., Samper, J., Montenegro, L., Fernández, AM., (2010). A coupled THMC model of a heating and hydration laboratory experiment in unsaturated compacted FEBEX bentonite. J. Hydrol., 386, 80-94. http://dx.doi.org/10.1016/j.jhydrol.2010.03.009.

Zheng, L., Samper, J., Montenegro, L., (2011). A coupled THC model of the FEBEX in situ test with bentonite swelling and chemical and thermal osmosis. J. Contam. Hydrol., 126, 45-60.

Zhou, Y. and Li, W., (2011). A review of regional groundwater flow modeling. Geoscience Frontiers, 2:205-214.

Zysset, A., Stauffer, F., Dracos, T., (1994a). Modeling of chemically reactive groundwater transport. Water Resour. Res., 30 (7) 2217-2228.

Zysset, A., Stauffer, F., Dracos, T., (1994b). Modeling of reactive groundwater transport governed by biodegradation. Water Resour. Res., 30 (8) 2423-2434.

APPENDIX 1. IMPROVEMENTS, UPDATES, CORRECTIONS AND EXTENSIONS OF THE CODES OF THE CORE SERIES

This appendix presents the improvements and the extensions performed in the codes of the CORE series. New features have been implemented in several codes to extend them and enhance their applications. The improvements facilitate the development of reactive transport models and the analysis of model results.

ABSTRACT

This appendix presents the improvements and the extensions implemented in the codes of the CORE series for modelling non-isothermal flow and solute transport coupled with biogeochemical processes in porous and fractured media developed at the University of A Coruña. The improvements introduced facilitate the development of reactive transport models and the analysis of results. Most of the improvements have been performed in CORE^{2D}V5, although updates have been performed also in INVERSE-CORE^{2D}, BIOCORE^{2D} and CORE^{3D} (TRANMEF-3D). The main improvements implemented in the CORE series include:

1) Adaptation of CORE^{2D}V5 to use available public-domain post-processing tools.
2) Adaptation of CORE^{2D}V5 to allow running models with purely conservative transport.
3) Adaptation of CORE^{2D}V5 to compute and print out water velocities and boundary inflows and outflows for several types of boundary conditions.
4) Improvement of CORE^{2D}V5 to improve the convergence criteria for solving flow in variably-saturated porous media.
5) Adaptation of INVERSE-CORE^{2D} to estimate large sets of variables.
6) Development of a database with the microbiological input parameters of BIOCORE^{2D}.
7) Corrections of bugs in the source codes of the CORE series.

A1.1. INTRODUCTION

CORE is a series of reactive transport codes developed at the University of A Coruña. CORE stands for *"a COde for modeling water flow (saturated and unsaturated), heat transport and multi-component REactive solute transport under both local chemical equilibrium and kinetic conditions"*. The reactive transport codes developed since 1991 include: TRANQUI (Xu, 1996; ENRESA, 1995); CORE-LE-2D V0.0a (Samper et al., 1998); FADES-CORE-LE (Juncosa et al., 1999) obtained by coupling the thermo-hydro-mechanical code FADES (Navarro, 1997) and CORE-LE-2D V0.0a; CORE^{2D}V2 (Samper et al., 2000) which was developed from CORE-LE-2D V0.0a; CORE^{2D}V4 (Samper et al., 2003); TRANMEF-3D (Juanes, 1997; Juanes and Samper, 2001); VISUAL-CORE-LE V1.0 (Samper et al., 1999); CORE Graphics (Samper et al., 1999); INVERSE-CORE^{2D} (Dai and Samper, 1999; Dai, 2000); BIOCORE^{2D} (Zhang, 2001; Zhang and Samper, 2001); CORE^{3D} (Yang et al., 2003); INVERSE-FADES-CORE (Zheng and Samper, 2005) and INVERSE-FADES-COREV2 (Mon, 2017).

The first code in the CORE series was TRANQUI (ENRESA, 1995; Xu, 1996). TRANQUI was a reactive transport code dealing with local equilibrium geochemical reactions in two-dimensional non-isothermal saturated/unsaturated porous media. The code accounts for both aqueous chemical reactions and the interactions between dissolved species and solid phases such as dissolution/precipitation, cation exchange and surface complexation reactions. CORE-LE-2D was released in 1998 (Samper et al., 1998). This code could solve simultaneously for groundwater flow, heat transport and multi-components reactive solute transport under the following conditions: 1) 2-D confined or unconfined, saturated or unsaturated steady-state or transient groundwater flow with general boundary conditions; 2) Chemical equilibrium including (a) Acid-base, (b) Redox, (c) Aqueous complexation, (d) Surface sorption, (e) ion exchange, (f) Mineral dissolution-precipitation, and (g) Gas dissolution-exsolution; 3) Transient heat transport considering conduction, heat dispersion and convection processes.

CORE^{2D}V2, which was released in 2000, was an extension of CORE-LE-2D which accounted for kinetics of mineral dissolution/precipitation (Xu et al., 1999). It was widely verified (Montenegro et al., 1999). Several features developed in other CORE codes were incorporated into this version such as automatic time stepping, improved sequential iterative approach (SIA-1) and kinetic aqueous reactions. CORE^{2D}V4 was released in 2003 (Samper et al., 2003). This version includes anisotropic diffusion, isotope transport, mass balance checking and calculation of boundary fluxes.

TRANMEF-3D is a code for solving 3-D flow and transport equations (Juanes, 1997; Juanes and Samper, 2001). However, this code cannot handle complex chemical reactions except simple reactions such as linear adsorption. CORE^{3D} was developed by Yang et al. (2003) by coupling

CORE^{2D}V4 and TRANMEF-3D. CORE^{3D} is a fully 3-D code to simulate non-isothermal groundwater flow, reactive transport and geochemical reactions.

BIOCORE^{2D} is a coupled biogeochemical reactive transport code developed by adding microbiological processes into CORE^{2D}V2 (Zhang, 2001; Zhang and Samper, 2001). Compared to CORE^{2D}V2, BIOCORE^{2D} incorporates also numerical algorithms which improve the overall numerical efficiency. These improvements include: 1) The implementation of a first-order implicit version of the sequential iteration approach (SIA-1) which is unconditionally stable and therefore is better than the standard Sequential Iteration Approach (SIA) implemented in CORE^{2D}V2; and 2) An automatic time stepping algorithm to optimize the time steps, thus overcoming the limitations of the previous algorithms in which the time increments had to be specified in advance.

INVERSE-CORE^{2D} solves inverse problems by minimizing a generalized least squares criterion with a Gauss-Newton-Levenberg-Marquadt method (Dai and Samper, 1999; Dai, 2000). It automatically calibrates the parameters involved in reactive transport models (Dai, 2000; Dai and Samper, 2004). This code enhanced the capabilities of CORE^{2D}V2.

INVERSE-FADES-CORE is the result of coupling the geochemical modules of CORE^{2D}V4, the THM (Thermo-Hydro-Mechanical) code FADES and the inverse subroutines of INVERSE-CORE (Zheng and Samper, 2005). Applications of INVERSE-FADES-CORE are reported by Zheng et al. (2008, 2010, 2011). Mon (2017) developed INVERSE-FADES-COREV2 by adding new features into INVERSE-FADES-CORE.

A1.2. UPDATE OF CORE^{2D}V5 TO USE AVAILABLE PUBLIC-DOMAIN POST-PROCESSING TOOLS

There are two types of output files in the current version of CORE^{2D}V5 (Samper et al., 2009, 2011): 1) Output files for the time evolution results at selected nodes and 2) Output files of computed nodal values in the finite element mesh. The first type of output files provide the time evolution of a variable in selected nodes whereas the second type of output files provide the spatial distribution of a selected variable in the model domain. The code prints out output files for the main output variables such as hydraulic heads, temperatures, concentrations and mineral dissolution/precipitation. The writing output variables and their frequency are indicated by the user in the input files of CORE^{2D}V5.

A post-processing tool known as CORE Graphics was developed in 1999 (Samper et al., 1999). The version of CORE^{2D} of that time provided output files suited for CORE Graphics. The most recent version of CORE^{2D} incorporates important modifications and advances which make CORE Graphics to be outdated. A more efficient post-processing tool for CORE^{2D}V5 was needed.

CORE^{2D}V5 has been updated to allow the use of recent post-processing tools. ParaView is one of the best known and used post-processing tools (Ahrens et al., 2005; Ayachit, 2015). CORE^{2D}V5 has been updated to print out the output files in VTK format so that the files can be opened directly with ParaView. This update of CORE^{2D}V5 greatly facilitates the post-processing of the results of CORE^{2D}V5.

A1.2.1. ParaView

ParaView is an open-source, multi-platform application for the visualization and analysis of scientific datasets, primarily those that are defined natively in a two- or three-dimensional space, including those that extend into the temporal dimension (Ahrens et al., 2005; Ayachit, 2015).

The ParaView project started in 2000 as a collaborative effort between Kitware, Inc. and Los Alamos National Laboratory through funding provided by the US Department of Energy ASCI Views program. ParaView was developed to analyse extremely large datasets by using distributed memory computing resources. It can be run on supercomputers to analyse datasets of petascale size as well as on laptops for smaller data sets. It has become an integral tool in many national laboratories, universities and industry, and has won several awards related to high performance computation.

The front end graphical user interface (GUI) has an open, flexible and intuitive user interface that gives fine-grained and open-ended control of the data manipulation and display processing needed to explore and present complex data.

CORE^{2D}V5 has been modified to post-process CORE output files with ParaView. Models with structured and unstructured grids can be displayed and the results can be analysed quickly. All possible models performed with CORE^{2D}V5 can be displayed in ParaView (one-dimensional vertical and horizontal grids, two-dimensional grids, two dimensional axisymmetric grids and three dimensional axisymmetric grids).

ParaView allows the visualization of model results at a node or along a line. The results are displayed either graphically or as text and can be exported for further analysis. Data can also be extracted over time (including statistical information such as minimum, maximum and standard deviation). Other capabilities of ParaView include: 1) Contour lines and isosurfaces which can be extracted from input data for scalars and vector components, 2) A sub-region of a dataset can be extracted by cutting or

clipping with an arbitrary plane by specifying threshold criteria to exclude cells, 3) The selection mechanism allows the user to focus on an important subset of a dataset by using either interactive selection as well quantitative selection mechanisms, 4) New variables can be computed in ParaView with the array calculator, 5) A large number of scalar and vector operations are supported, 6) Advanced data processing can be done by using filters, 7) ParaView is fully scriptable by using the simple but powerful Python language, 8) Pictures and videos can be created quickly and 9) Users can save the animation to disk either as a series of images or as a movie file and the animation contains all the visible views.

A1.2.2. Update of CORE^{2D}V5 to use ParaView

CORE^{2D}V5 has been updated to allow the use of ParaView for post-processing model results. ParaView input files use the VTK format. CORE^{2D}V5 has been modified to print out the model results in the VTK format supported by ParaView. The updated version of the code allows for the use of the original CORE output files and the VTK format. An additional variable named "*NWRI*" has been defined in the updated version of CORE^{2D}V5 to specify the option for printing out. This variable can take the following values:

- *NWRI = 0* for the original format output files.
- *NWRI = 1* for VTK format output files (that can be opened directly with ParaView).
- *NWRI = 2,* output files are printed out in both formats (original format and VTK format).

The update of CORE^{2D}V5 of output files affects only the output files of nodal values of the finite element mesh. The output files with the time evolution of nodal results have not been modified.

A1.2.2.1. Output files in VTK format

ParaView allows for several types of file formats. However, the VTK file format, along with all of its relatives, is the preferred format in ParaView. CORE^{2D}V5 has been updated to print out the output files in VTK format which is complex, but very powerful. Figure A1.1 shows the nine parts of the output files in VTK format printed out by CORE^{2D}V5.

The first part includes the file version and the identifier. This part contains a single line with the following text: "*# vtk DataFile Version x.x*". This line must be typed exactly as indicated with the exception of the version number *x.x*, which varies with different releases of VTK. The current version number is 4.0. Previous versions are compatible with version 4.0 files.

The second part is the header. The header which consists of a character string terminated by an end-of-line character. The header must be less than 256 characters.

The third part is the file format. The file format describes the type of file, either *ASCII* or *BINARY*. The *ASCII* file format was chosen for CORE^{2D}V5.

The fourth part describes the type of geometry of the model. ParaView supports multiple geometries. An unstructured grid was chosen for CORE^{2D}V5. This option requires defining the topology and the nodal coordinates explicitly. This option requires significantly more memory to represent the mesh. However, it is the best option to deal with all the possible types of the finite element grids considered in CORE^{2D}V5.

The fifth part provides information regarding the time periods and cycles of the simulation. The updated version of CORE^{2D}V5 prints out the simulation time for each output file in VTK format. All model results in a given file correspond to the same time step. CORE^{2D}V5 also writes the cycle of the simulation which corresponds with the output file name. These two variables are transferred to ParaView with the names: *"TIME"* and *"CYCLE"*.

The sixth part includes first a line with the number of nodes of the grid after the keyword *"POINTS"* and then the nodal coordinates *(x, y, z)*.

The seventh part defines the connectivity matrix. The number of elements and the number of components of the connectivity matrix are indicated after the keyword *"CELLS"* in the first line of this part. The first column of the connectivity matrix corresponds to the number of nodes that define an element. In CORE^{2D}V5 there are two possibilities: 1) One-dimensional elements defined by two nodes and 2) Two-dimensional triangular elements defined by three nodes. This way, the first column of the connectivity matrix can take only the values 2 or 3. The following columns of the connectivity matrix indicate the node numbers of the elements of the finite element mesh. It is important to note that the first node number and the first element number in ParaView are equal to "*0*" while in CORE^{2D} they are equal to "*1*". The user must take into account this difference for post processing model results.

The eighth part defines the type of elements. The number of elements is indicated in the first line of this part after the keyword "*CELL_TYPES*". The geometry of the model is defined as an unstructured grid that consists of combinations of possible element types. For this reason, after the first line of this part, the type of element is indicated with a code number. Two types of elements are used in CORE^{2D}V5. Their code numbers are "*3"* and "*5"*. Figure A1.2 shows the types of elements used by CORE^{2D}V5 in 1-D and 2-D models in VTK format.

The last part describes the dataset attributes. This part includes the results computed with CORE^{2D}V5 in nodes and elements of the finite element mesh. This part begins with the keywords *"POINT_DATA"* or *"CELL_DATA"*, followed by an integer number specifying the number of nodes or elements, respectively. All model results are scalars except water velocities which are vectors.

Figure A1.3 shows an example of an output file in VTK format printed out with the updated version of CORE^{2D}V5. These results correspond to a 2-D numerical model performed with a finite element mesh of 4 nodes and 2 elements. The name of the output file is *"PrVw10005"* and the model results are computed for a time t = 10 [T].

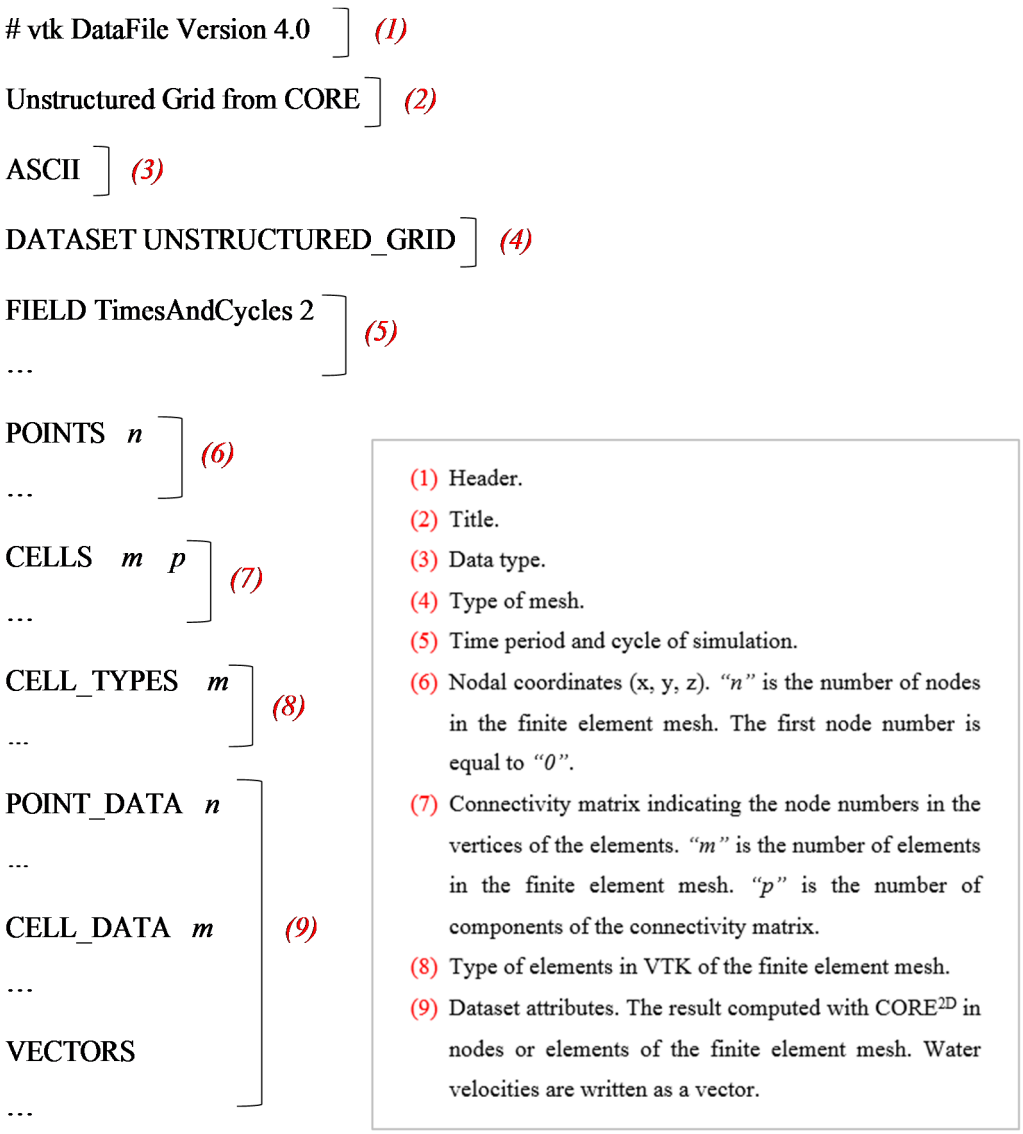

Figure A1.1. Overview of the nine parts of the VTK data file format printed out by CORE^{2D}V5.

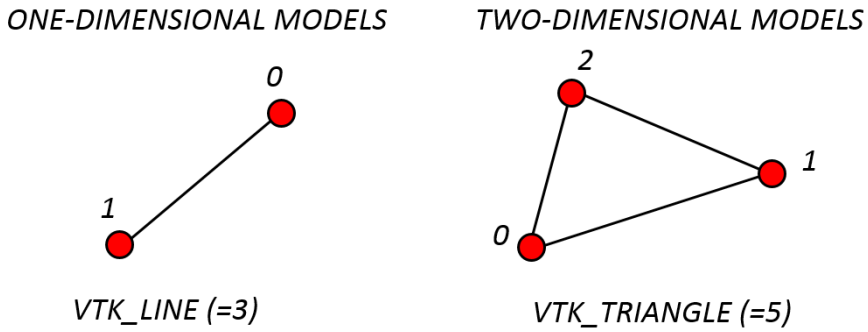

Figure A1.2. Type of elements used by CORE^{2D}V5 in VTK format.

```
# vtk DataFile Version 4.0
Unstructured Grid from CORE
ASCII
DATASET UNSTRUCTURED_GRID
FIELD TimesAndCycles 2
TIME 1 1 double
1.000000000000E+01
CYLCE 1 1 long
10005
POINTS    4 double
0.00E+00    0.00E+00    0.00E+00
0.00E+00    1.00E+01    0.00E+00
1.00E+01    0.00E+00    0.00E+00
1.00E+01    1.00E+01    0.00E+00
CELLS   2    8
3     0    2    1
3     1    2    3

CELL_TYPES   2
5
5

POINT_DATA    4
SCALARS  Hydraulic_Head  double 1
LOOKUP_TABLE default
0.100000E+01
0.100000E+01
0.200000E+01
0.200000E+01
```

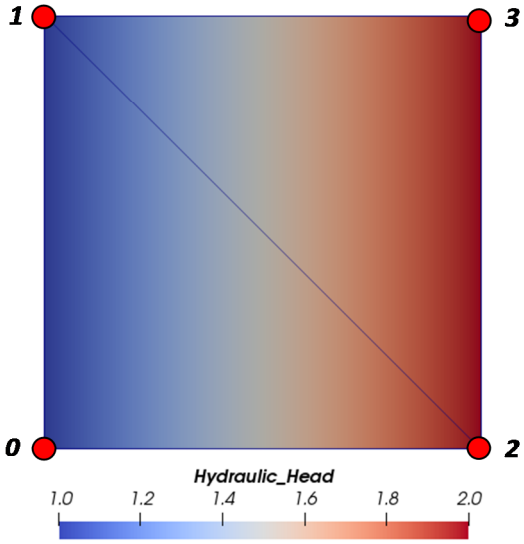

Figure A1.3. Example of an output file in VTK format printed out with the updated version of CORE^{2D}V5 (left) and model results plotted with ParaView (right).

The updated version of CORE^{2D}V5 prints out an output file in VTK format for each one of the time steps selected by the user. CORE^{2D}V5 uses several variables to define the writing frequency. The variable defining the writing frequency in the updated output files is the same that was used in the previous version of the code (*"NWXY"*). The name of the first output file printed out by CORE^{2D}V5 in VTK format is *"PrVw10000"*. The model results computed for $t = 0$ are printed out in this output file. The time step in which CORE^{2D}V5 prints out the model results in the second file depends on the writing frequency, but the name of the file is always *"PrVw10001"*. The sequence of the names of the output files printed by CORE^{2D}V5 in VTK format are: *"PrVw10000"*, *"PrVw10001"*, *"PrVw10002"*, *"PrVw10003"*… The maximum number of output files in VTK format is equal to *"89999"*.

A1.2.2.2. Update of CORE^{2D}V5 to print out the output files in VTK format

CORE^{2D}V5 has been modified to print out the output files in VTK format which can be post-process directly with ParaView. The modifications take into account the different options allowed by the reactive transport code (type of medium or the dimensionality of the model). CORE^{2D}V5 can perform 2-D models, 3-D axisymmetric models with 2-D grids, 1-D horizontal models, 1-D vertical models and 2-D axisymmetric models with 1-D grids. In addition, the code allows also performing 1-D models with 2-D grids with triangular elements. In this case, the results are printed only in alternate nodes.

Subroutines (*"WRITEX2D"* and *"WRITEX1D"*) have been updated to write the output files in VTK format. Subroutine *"WRITEX2D"* prints the results in all nodes of the finite element mesh (both for 1-D and 2-D grids). In this case, the results are written in VTK format only by distinguishing between 1-D and 2-D models (type of elements). Subroutine *"WRITEX1D"* prints the results in alternate nodes (for 2-D grids). In this case, the code has been modified to print the number of nodes, the elements and the connectivity matrix so that in ParaView the results are displayed in 1-D.

The variables defining the geometry of the grid and the time discretization (nodal coordinates, connectivity matrix, simulation time and the type of elements) must be indicated in every output file in VTK format. Model results are printed after this information. The original input file of CORE^{2D} contains the names of the output files which can be printed and the integers indicating which files are printed. A given output file is printed if the corresponding integer is "*1*". The output file is not printed if the integer is "*0*". Output files in VTK format are similar to output files in the original format. The variables that can be printed out include:

1) Nodal hydraulic heads in fully saturated problems or pressure heads and saturation degrees in variably saturated media. These results are printed out if the output file *"OUThx"* is selected by the user.

2) Nodal values of total dissolved concentrations of the selected components. They are printed in in VTK format if the output file *"OUTspx"* is selected by the user.

3) Nodal dissolved concentrations of selected isotopes. They are printed out in VTK format if the output file *"OUTdcx"* is selected by the user.

4) Nodal pH values. They are printed out in VTK format if the output file *"OUTphx"* is selected by the user.

5) Nodal values of cumulative precipitation/dissolution, volume fractions and dissolution/precipitation rates of selected minerals. These results are printed if the output file *"OUTmix"* is selected by the user.

6) Nodal saturation indices of selected minerals. They are printed out in VTK format if the output file *"OUTsix"* is selected by the user.

7) Nodal values of pE, Eh and oxygen concentration. They are printed out in VTK format if the output file *"OUTpex"* is selected by the user.

8) Nodal values of total sorbed concentrations. They are printed out in VTK format if the output file *"OUTadx"* is selected by the user.

9) CEC and the computed nodal concentrations of exchanged species. They are printed out in VTK format if the output file *"OUTexx"* is selected by the user.

10) Nodal values of temperature. They are printed out in VTK format if the output file *"OUTex"* is selected by the user.

11) Water velocities. They are printed out in VTK format as a vector if the output file *"OUTvx"* is selected by the user.

12) The following variables are printed out in VTK format when changes in porosity are taken into account to update flow, transport and chemical parameters (*IMINE* = 1):
    a) Nodal values of porosity and porosity changes with respect to the initial porosity.
    b) Nodal values of the contribution of the minerals to the change in porosity.
    c) Nodal values of the specific surfaces of the selected minerals.
    d) Diffusion coefficients on all the elements of the mesh.
    e) Hydraulic conductivities on all the elements of the mesh.

A1.2.3. Verification of the updated version of CORE^{2D}V5

The updated version of CORE^{2D}V5 which allows the use of the post-processing tools of ParaView has been verified with several types of models. The output files of these models were printed out in two formats (the original and the VTK formats) and both files were compared. In addition, the output files in VTK format were post-processed with ParaView and verified.

It was necessary to verify the modifications performed in CORE^{2D}V5 for all possible models. Five models were performed with the updated version of the code and the results printed out in the output files in VTK format were verified. They include:

1) A 1-D model performed with a row of 2-D triangular elements in the same direction. Model results in ParaView are displayed in 1-D. The results printed out only in alternate nodes in the original format of the output files coincide with the ParaView results.

2) A 2-D model in variably saturated porous media. In this case, the computed pressures, saturation degrees and hydraulic heads were verified.

3) A 2-D model under fully saturated conditions which takes into account the porosity changes. In this case, model results related to the porosity changes (porosity, diffusion coefficients, specific surface of minerals, hydraulic conductivities…) were verified.

4) A 2-D axisymmetric reactive transport model performed with a 1-D mesh. In this case, the results in ParaView are shown in one dimension because the model was performed with a 1-D mesh. Model results for a reactive transport model with cations exchange (concentrations of exchange cations, CEC, temperature, pH, Eh…) were verified.

5) A 3-D axisymmetric reactive transport model performed with a 2-D mesh. In this case, the results in ParaView are shown in two dimensions because the model was performed with a 2-D mesh. Model results of a reactive transport model with adsorption (dissolved concentrations, sorbed concentrations, mineral precipitation …) were verified.

Figure A1.4, Figure A1.5 and Figure A1.6 show the graphical user interfaces of ParaView for some verification cases. Figure A1.4 shows the 2-D model in variably saturated porous media used to verify the post-processing of pressure heads and saturation degrees. Figure A1.5 shows the 2-D model which takes into account the porosity changes. The post-processing variables in this case include porosity, diffusion coefficient and mineral specific surface. Figure A1.6 shows the 3-D axisymmetric reactive transport model used to verify the post-processing of several reactive transport variables such as dissolved, sorbed and precipitated concentrations.

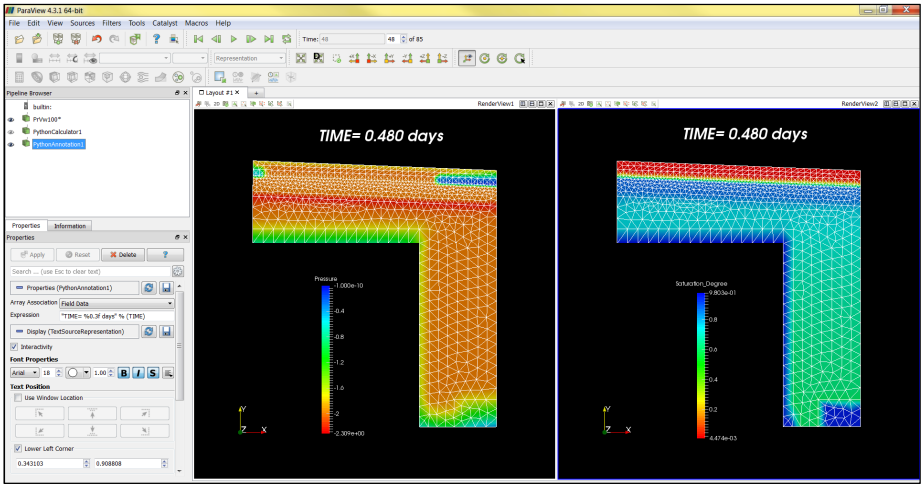

Figure A1.4. Graphical user interface of ParaView for a 2-D model in variably saturated porous medium. This model has been used to verify the modifications performed in the updated version of CORE^{2D}V5.

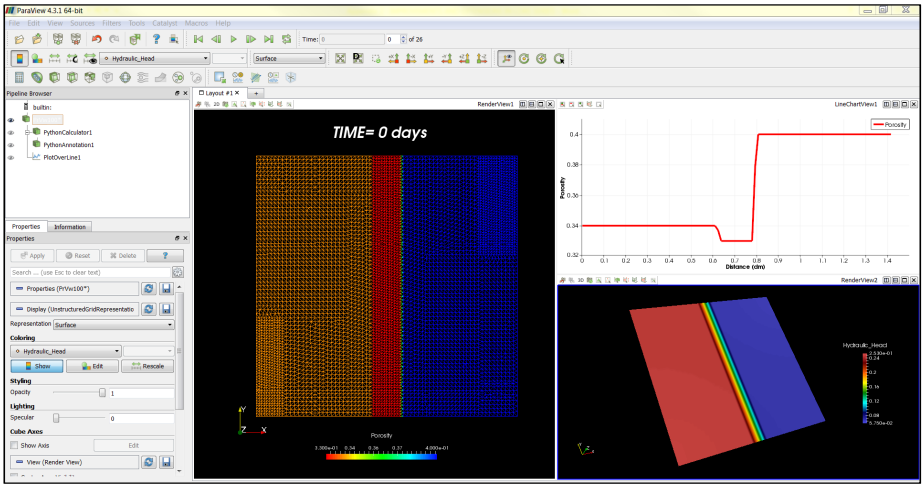

Figure A1.5. Graphical user interface of ParaView for a 2-D model which takes into account the changes in porosity. This case was used to verify the updated version of CORE^{2D}V5.

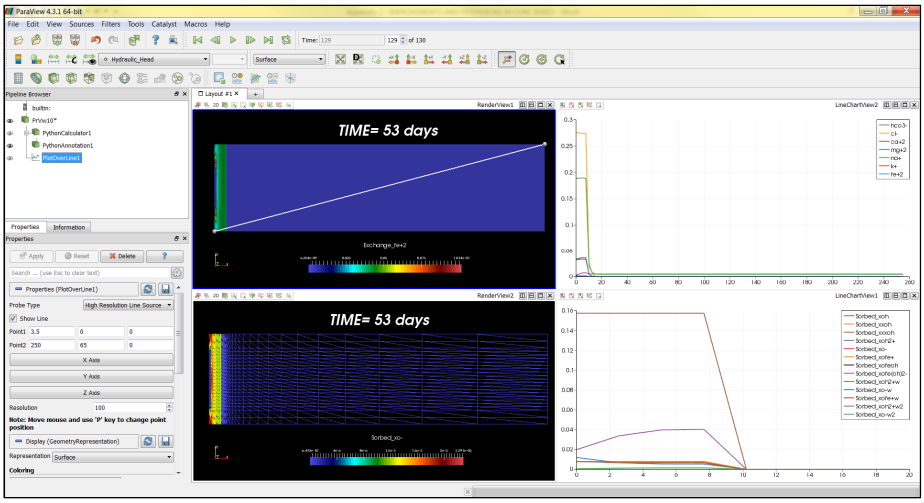

Figure A1.6. Graphical user interface of ParaView for a 2-D axisymmetric reactive transport model performed with a 2-D mesh. This case has been used to verify the updated version of CORE^{2D}V5.

A1.3. UPDATE OF CORE^{2D}V5 TO ALLOW RUNNING MODELS WITH PURELY CONSERVATIVE TRANSPORT

In the absence of chemical reactions with other solutes or interactions with the solid phase, that is to say, for a conservative solute, the spatial and temporal distributions of solute concentrations are controlled by: 1) Advection and 2) Dispersion. For this reason, in order to carry out conservative transport models with a reactive transport code it is only necessary to solve the solute transport equation.

In CORE^{2D}V5, each chemical component has a transport equation which is written in terms of its total solved concentration. There is a mass balance equation for each chemical component at each node. The transport equation of each chemical component has a chemical source/sink term which represents the mass transfer between the aqueous phase and other phases. This source term renders the problem highly non-linear and an iterative procedure between the solution of solute transport and chemical equations is required. In the current version of CORE^{2D}V5, it is possible to indicate in the input files whether a model includes transport simulation or only the flow equation is solved. *"ITRAN"* is the input variable to define this option. *"ITRAN"* is equal to 0 when transport is not simulated whereas if *"ITRAN"* is equal to 1, the transport simulation is considered. However, in the current version of the code, it is not possible to discern between conservative transport and reactive transport. In this way, the code uses the same subroutines for solving conservative and reactive transport problems.

CORE^{2D}V5 has been modified to solve only conservative transport in a more efficient manner. The following options are considered in the updated version of the code:

- Transport simulation is not considered if "*ITRAN"* is equal to *"0"*.
- Reactive transport is performed if "*ITRAN"* is equal to *"1"*.
- Conservative transport is considered if "*ITRAN"* is equal to *"2"*.

The code does not solve the chemical equations when "*ITRAN*" is equal to *"2"* in the updated version of CORE^{2D}V5. The source/sink term included in the transport equation which represents the mass transfer between aqueous and other phases (mineral dissolution/precipitation, cation exchange or adsorption processes) is always equal to 0. This avoids convergence problems and reduces calculation times.

This improvement has been verified for several test cases.

A1.4. UPDATE OF CORE^{2D}V5 TO COMPUTE AND PRINT OUT NEW VARIABLES

CORE^{2D}V5 has been updated to compute and print out new relevant variables for water flow and reactive transport problems such as: 1) Water inflows and outflows for several types of boundary conditions (Dirichlet and Cauchy condition) and 2) Flow velocity vectors.

A1.4.1. Water inflows and outflows through model boundaries

CORE^{2D}V5 considers the following three types of flow boundary conditions:

1) Dirichlet condition:

$$h(x,y,t)|_{\Gamma} = H \tag{1.1}$$

2) Neumann condition:

$$-T\,\nabla h \cdot n|_{\Gamma} = Q \tag{1.2}$$

3) Cauchy or mixed condition:

$$-T\,\nabla h \cdot n|_{\Gamma} = \alpha(H - h) \tag{1.3}$$

where Γ is the boundary of the model, n is a unit vector normal to the boundary pointing outwards, h is the hydraulic head, T is the transmissivity, α is a leakage coefficient and H and Q are specified head and flux, respectively, which may vary in space and time.

Knowing water inflows and outflows through boundary is required for calculating the groundwater balance in the model domain. Water inflows and outflows in Neumann boundaries are prescribed and therefore are known. The current version of CORE^{2D}V5 does not print out inflows and outflows for Dirichlet or Cauchy boundaries. The code computes internally the water inflows and outflows for transient flow, but they are not printed out in the output files. CORE^{2D}V5 has been updated to print out the water inflows and outflows in Dirichlet and Cauchy boundaries in an output file named "*OUTqt.out*". This file contains the following information: 1) Node numbers with Dirichlet and Cauchy boundary conditions, 2) Nodal coordinates, 3) Simulation times, 4) Integers indicating the type of boundary condition (*"1"* for Dirichlet condition and *"3"* for Cauchy condition) and 5) The computed nodal water inflows and outflows. Water inflows are positive and water outflows are negative. The water inflows and outflows in the updated version of CORE^{2D}V5 in nodes with a Dirichlet boundary condition are computed explicitly while they are computed from Equation 1.3 in nodes with a Cauchy boundary

condition. The user can select whether or not to print this output file ("*OUTqt*"). Boundary water inflows and outflows can be printed out for 1-D and 2-D models.

A1.4.1.1. Verification

The capabilities to print out boundary fluxes have been tested and verified with a simple test case. The numerical model has a surface area, *A*, of 100 x 5 m^2 and corresponds to an unconfined aquifer with 10 m initial thickness and a base elevation equal to 0 m. The model has been discretized with a 2-D mesh of triangular finite elements with 202 nodes and 200 elements (Figure A1.7). A Neumann boundary condition was used to specify a water inflow equal to 100 m^3/d (50 m^3/d per node in the left boundary of the model). The hydraulic head is prescribed to 10 m with a Dirichlet condition at the right boundary of the model. The hydraulic conductivity, *K*, is equal to 100 m/d. Groundwater recharge, *R*, is equal to 100 mm/year. The flow is steady.

The model has been calculated with the updated version of CORE^{2D}V5 and the total water outflow computed at the two nodes of the right boundary of the model (printed out in the "*OUTqt.out*" file) is equal to 100.137 m^3/d. The total water inflow into the model is equal to:

$$Q = Q|_{x=0\,m} + R\,A = 100\,m^3/d + \frac{100}{1000 \cdot 365} m/d \cdot 100 \cdot 5\,m^2 = 100.137\,m^3/d \qquad (1.4)$$

The total water outflow computed with the updated version of the code is equal to the true water inflow into the model. A second run was performed with a Cauchy condition at the right boundary with a leakage coefficient, α, equal to 1000 m^2/d. In this run, the total water outflow computed with the code is also equal to the true water inflow.

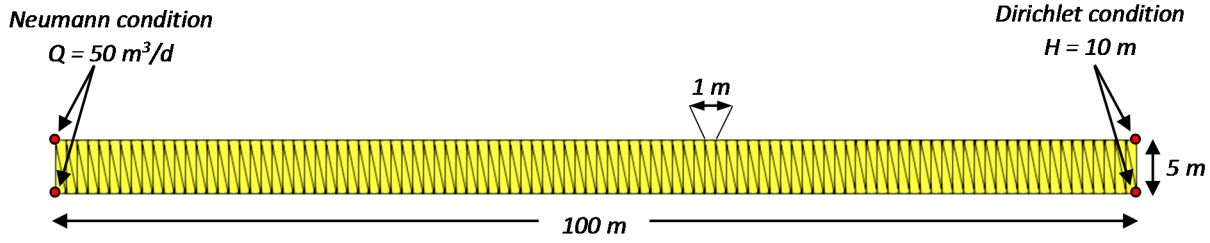

Figure A1.7. 2-D finite element mesh used for the verification of the calculation boundary water inflows and outflows.

A1.4.2. Calculation and print out of the flow velocity vectors

Water flow through porous media is governed by Darcy's Law which can be written in terms of hydraulic head:

$$q = -K\,\nabla h \tag{1.5}$$

where q is the water flux, K is the hydraulic conductivity and h is the hydraulic head.

In the current version of CORE^{2D}V5, flow velocities in transient flow are computed for solving the transport equations, but they are not printed out in the output files. CORE^{2D}V5 has been updated to print out the components of the flow velocities for all elements of the mesh in a file named "*OUTvx.out*". The user can choose whether this output file is printed or not. The x and y components of the flow velocity vector for each element, q_x^e and q_y^e, are computed according to:

$$q_x^e = -\left(K_{xx}^e \sum_{i=1}^{3} h_i^e b_i^e + K_{xy}^e \sum_{i=1}^{3} h_i^e c_i^e \right) \tag{1.6}$$

$$q_y^e = -\left(K_{yy}^e \sum_{i=1}^{3} h_i^e c_i^e + K_{xy}^e \sum_{i=1}^{3} h_i^e b_i^e \right) \tag{1.7}$$

where b_i^e and c_i^e are element coefficients which depend on the geometry of the element, K_{xx}^e, K_{xy}^e and K_{yy}^e are the components of the hydraulic conductivity tensor in the e-th element, h_i^e is the computed head at the i-th node, superscript e denotes element number, subscript i denotes the nodes associated to element e and subscripts x and y are the horizontal and vertical coordinates, respectively.

A velocity vector is computed for each element of the finite element mesh. In 1-D models, the origin of the flow velocity vector is the mid-point of the element while in 2-D triangular elements the origin of the flow velocity vector is the barycentre of the triangle. The following variables are printed out in the output file "*OUTvx.out*" in each time step: 1) The element number, 2) The *(x, y)* coordinates of the origin of the flow velocity vector and 3) The x and y components of the computed flow velocity vector. In addition, the flow velocity vector in each element is printed out in VTK format which can be post-processed with ParaView.

A1.4.2.1. Verification

The updated version of CORE^{2D}V5 has been verified with a synthetic flow model similar to that used to verify the calculation of the boundary inflows and outflows. In this case, the numerical model considers a confined aquifer with a thickness of 5 m. Hydraulic heads are prescribed to 15 m and 10 m at the left and right boundaries of the model, respectively. Figure A1.8 shows the 2-D finite element mesh and the boundary conditions. The hydraulic conductivity, K, equal to 100 m/d. There is no recharge in this case. The flow model was performed in steady state.

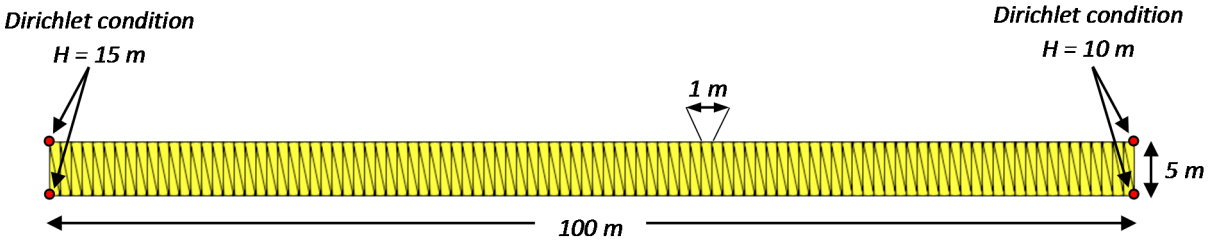

Figure A1.8. 2-D finite element mesh used for the verification of the calculation and printing out of the flow velocity vectors.

Flow velocities are the same in all elements of the finite element mesh because the flow is uniform. The computed *x* and *y* components of the flow velocity vector printed out in the output file "*OUTvx.out*" are equal to 5 m/d and 0 m/d, respectively. The flow velocity can also be calculated analytically from Darcy's law:

$$q_x = -K\,\nabla h = -100\,m/d \cdot \frac{5}{100}\,m/m = 5\,m/d \tag{1.8}$$

The *x* component of the flow velocity vector computed with the updated version of the code is equal to the flow velocity calculated analytically. Figure A1.9 shows the flow velocity vectors computed with the updated version of the code in all elements of the finite element mesh.

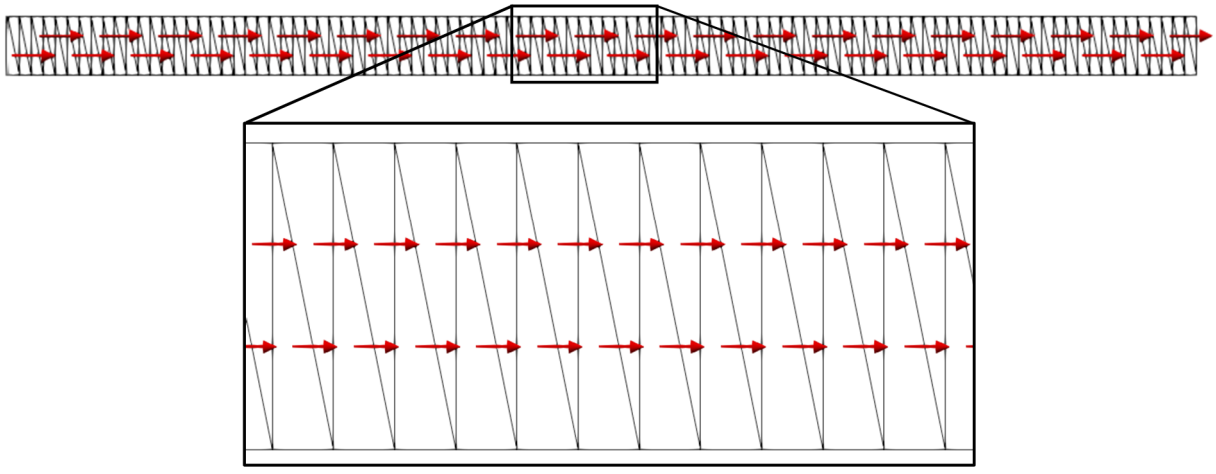

Figure A1.9. Flow velocity vectors computed with the updated version of CORE^{2D}V5.

A1.5. IMPROVEMENT OF CONVERGENCE CRITERIA IN CORE^{2D}V5 TO SOLVE UNSATURATED FLOW

The flow equation for variably saturated media is highly nonlinear. CORE^{2D} solves flow in variably saturated media in terms of pressure heads, ψ, by a Newton-Raphson iterative method. The pressure head takes on positive values in saturated regions and negative values in partly saturated regions. The Newton-Raphson iteration method for solving the system of nonlinear equations is based on the linearization of the problem by using a Taylor series of expansion.

Convergence problems are commonly found with CORE^{2D} when solving unsaturated flow due to the nonlinearity of the flow equation. Convergence problems are often overcome by refining the finite element mesh and reducing the time increments. Figure A1.10 shows the flowchart of the "*FLOW_UNSAT"* subroutine of the previous version of CORE^{2D}V5 which solves the groundwater flow equation in variably saturated porous media. The Jacobian matrix of the Newton-Raphson iterative method is computed first. Then, the changes in pressure heads ($\Delta\psi^{k+1}$) with respect to the previous iteration are calculated. The pressure heads are updated for the next iteration in all nodes of the finite element mesh. The maximum absolute value of the relative change is computed (ε_{max}). The code continues with the iterative process until the maximum absolute value of the relative change is smaller than the tolerance. If the convergence is not achieved with the maximum number of iterations specified by the user ("*MAXITERF"*), the iterative process should be stopped. The previous version of CORE^{2D}V5, however, allowed to continue the calculations even when the maximum relative change in some nodes was greater than the convergence tolerance.

CORE^{2D}V5 has been modified to stop the execution when the iterative algorithm does not converge. Figure A1.11 shows the flowchart of the "*FLOW_UNSAT"* subroutine in the updated version of CORE^{2D}V5 which solves the groundwater flow equation in variably saturated porous media. Similar to the previous version of the code, the changes in the pressure heads ($\Delta\psi^{k+1}$) for all nodes of the mesh are computed. The maximum absolute value of the relative change (ε_{max}) at all nodes of the finite element mesh is computed and compared with the specified convergence tolerance (ω). If the maximum relative change is smaller than the tolerance, the code proceeds to the next time step. Otherwise, the code continues with the iterative process until the relative change is smaller than the convergence tolerance. A new input variable called "*TOLFLFAC*" (*TOLFLFAC* > 1) has been defined in the updated version of CORE^{2D}V5. This variable is used when the maximum number of iterations is exceeded without reaching convergence. In the updated version of the code, the convergence tolerance is increased by a factor (*"TOLFLFAC"*). If the maximum relative change in pressure heads is smaller than the augmented convergence tolerance, the code proceeds to the next time step. Otherwise, the code stops. The use of

the factor *"TOLFLFAC"* provides more flexibility to the user without compromising the numerical accuracy. An additional output file called "*Unsaturated.out*" has been created in which the following information on the iterative process is provided: 1) The node number with the largest relative change (i_{emax}), 2) The maximum relative change in such node and 3) The number of iterations needed to achieve convergence. The code prints in the output file the following message: "*Nº iterations are not enough but continues*" when the maximum number of allowed iterations is reached and the maximum relative error committed is smaller than the convergence tolerance multiplied by the factor "*TOLFLFAC*". On the other hand, the code prints the message: "*Nº iterations are not enough and stop*" when the maximum relative change is greater than the convergence tolerance multiplied by "*TOLFLFAC*".

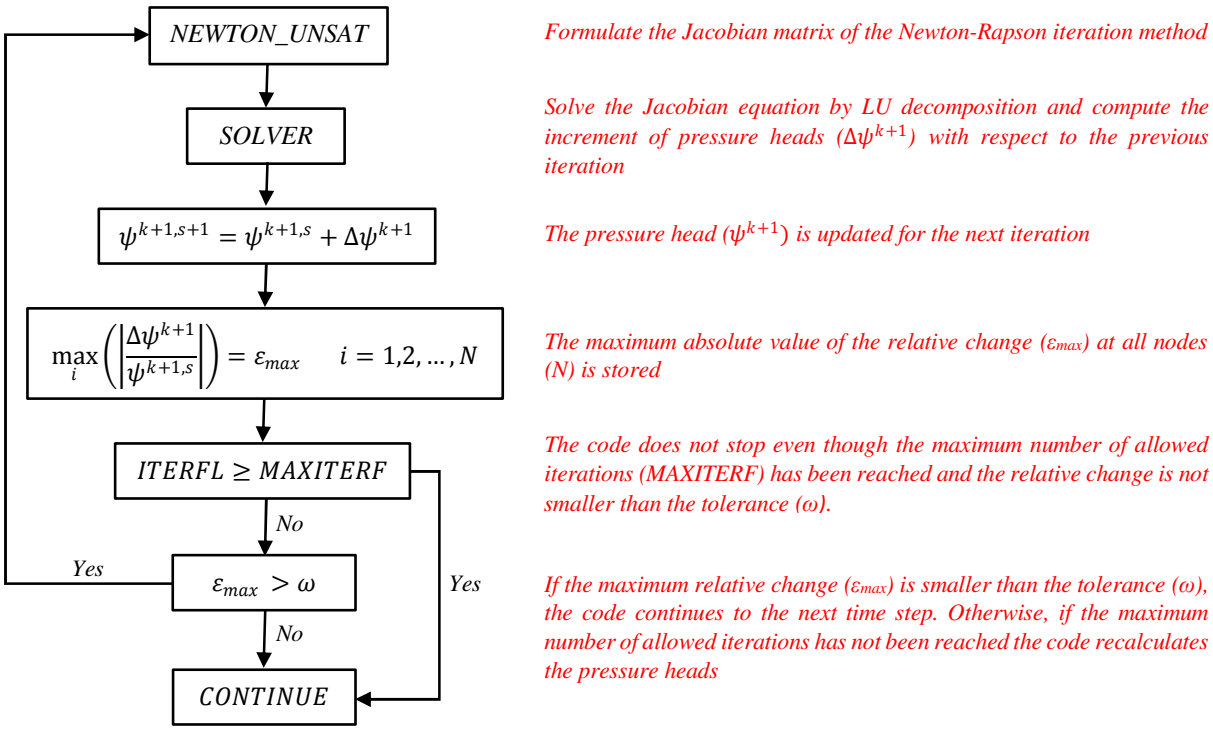

Figure A1.10. Flowchart of the FLOW_UNSAT subroutine in the previous version of CORE^{2D}V5 which solves the groundwater flow equation in variably saturated porous media.

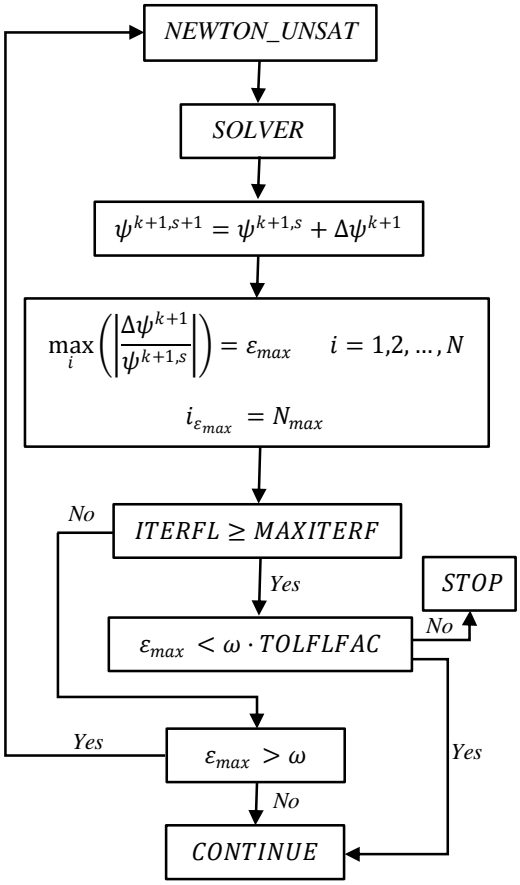

Figure A1.11. Flowchart of the FLOW_UNSAT subroutine in the updated version of CORE^{2D}V5 which solves the groundwater flow equation in variably saturated porous media.

A1.6. UPDATE OF INVERSE-CORE^{2D} TO DEAL WITH LARGER NUMBERS OF PARAMETERS

INVERSE-CORE^{2D} (Dai and Samper, 1999; Dai, 2000) is a reactive transport code of the CORE series to solve inverse problems by minimizing a generalized least squares criterion by means of Gauss-Newton-Levenberg-Marquadt. It calibrates automatically the parameters of reactive transport models (Dai and Samper, 2004; Zheng et al., 2008). The previous version of INVERSE-CORE^{2D} allowed for 10 material zones. The code has been extended to deal with problems with up to 50 material zones. INVERSE-CORE^{2D} uses an identification number for each parameter estimated by the code. These identification numbers have been modified in the updated version of the code. Table A1.1 shows the identification numbers of the water flow and reactive transport parameters in the updated version of INVERSE-CORE^{2D}.

Table A1.1. Identification numbers of water flow and reactive transport parameters (selectivity, initial and boundary concentrations and kinetic reaction parameters) in the updated version of INVERSE-CORE^{2D} (see the list of terms after the index of this dissertation for the definition of the parameters)

Parameter	**Identification numbers for water and solute transport parameter zones**									
	1	**2**	**3**	**4**	**5**	**…**	**25**	**…**	**49**	**50**
ϕ	1	2	3	4	5	…	25	…	49	50
m	51	52	53	54	55	…	75	…	99	100
α	101	102	103	104	105	…	125	…	149	150
n	151	152	153	154	155	…	175	…	199	200
K_1	201	202	203	204	205	…	225	…	249	250
K_2	251	252	253	254	255	…	275	…	299	300
S_S	301	302	303	304	305	…	325	…	349	350
D_x	41000+(number of material zone)*100+(number of primary species)									
D_y	46000+(number of material zone)*100+(number of primary species)									
α_D	51000+(number of material zone)*100+(number of primary species)									
α_L	56000+(number of material zone)*100+(number of primary species)									
α_T	61000+(number of material zone)*100+(number of primary species)									
ϕ_{ac}	66000+(number of material zone)*100+(number of primary species)									
K_d	71000+(number of material zone)*100+(number of primary species)									
CEC	351	/	/	/	/	…	/	…	/	/
Parameter	**Identification numbers for cation selectivities, initial and boundary concentrations**									
	1	**2**	**3**	**4**	**…**	**10**	**11**	**…**	**19**	**20**
K_{sel}	/	352	353	354	…	360	/	…	/	/
C_{O1}	361	362	363	364	…	370	371	…	379	380
C_{O2}	381	382	383	384	…	390	391	…	399	400
C_{B1}	411	412	413	414	…	420	421	…	429	430
C_{B2}	431	432	433	434	…	440	441	…	449	450
Parameter	**Identification number for kinetic parameters**									
	1	**2**	**3**	**4**	**5**	**6**	**7**	**8**	**9**	**10**
A_m	451	452	453	454	455	456	457	458	459	460
E_a	461	462	463	464	465	466	467	468	469	470
f_m	471	472	473	474	475	476	477	478	479	480
$log\ K$	481	482	483	484	485	486	487	488	489	490
k_{mk}	501-510	511-520	521-530	531-540	541-550	551-560	561-570	571-580	581-590	591-600
θ_{mk}	601-610	611-620	621-630	631-640	641-650	651-660	661-670	671-680	681-690	691-700
η_{mk}	701-710	711-720	721-730	731-740	741-750	751-760	761-770	771-780	781-790	791-800
p_{k1}	801-810	811-820	821-830	831-840	841-850	851-860	861-870	871-880	881-890	891-900
p_{k2}	901-910	911-920	921-930	931-940	941-950	951-960	961-970	971-980	981-990	991-1000

A1.6.1. Verification

The following three synthetic 2-D numerical models have been performed to verify the updated version of INVERSE-CORE^{2D}: 1) A steady-state flow model in which the hydraulic conductivity (K_1) has been estimated, 2) A transient-state flow model in which the hydraulic conductivity (K_1) has been estimated and 3) A conservative transport model in which the diffusion coefficient (D_x) has been estimated. The domain of the 2-D numerical models is rectangular with an area of 500 x 50 m^2 and it is the same in the three cases. The models are performed with a row of triangular finite elements with a grid size, Δx, equal to 10 m. The mesh has 102 nodes and 100 elements. The numerical models simulate flow through a confined aquifer with a 1 m thickness. To verify the improvements implemented in INVERSE-CORE^{2D}, 50 uniform material zones are defined in the numerical models (each material zone has a length equal to 10 m in the horizontal direction). Figure A1.12 shows the 2-D finite element mesh used in the three verification cases. Hydraulic heads are prescribed at the left and right boundaries of the model to 10 m and 0 m, respectively. In the second verification case, the hydraulic head at the left boundary of the model varies over time with a time function.

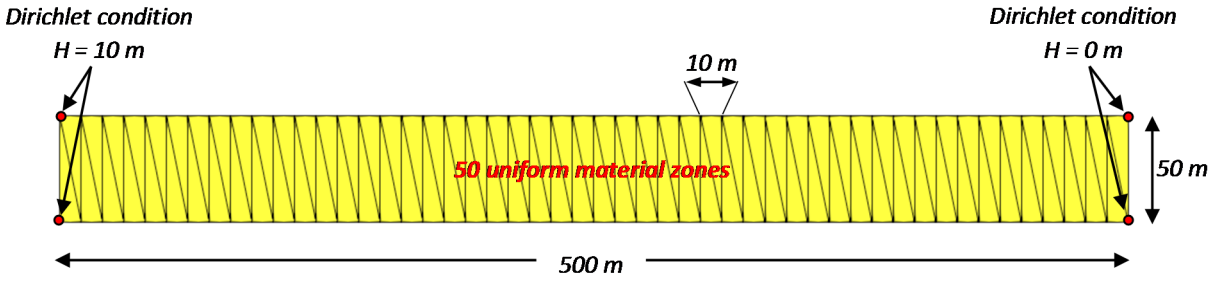

Figure A1.12. 2-D finite element mesh and boundary conditions for the three numerical models performed to verify the updates introduced in INVERSE-CORE^{2D}.

A1.6.1.1. First verification case

A steady-state flow model was performed with the updated version of INVERSE-CORE^{2D} in the first case of verification. The hydraulic conductivity in the 50 material zones defined in the model is equal to 1 m/d in the horizontal direction (K_1) and equal to 10^{-10} m/d in the vertical direction (K_2). Computed hydraulic heads vary linearly along the horizontal direction from H = 10 m (at the left boundary) to H = 0 m (at the right boundary). In order to verify the improvements introduced in INVERSE-CORE^{2D}, a forward model was carried out by reducing the horizontal hydraulic conductivity (K_1) in the material zone number 12 (between x = 110 m and x = 120 m) to 0.01 m/d. The computed hydraulic head at the node 31 (x = 150 m) in this case is equal to 2.36 m. Afterwards, an inverse model

was performed to calibrate the parameter number *"212"* corresponding to the hydraulic conductivity in the material zone number 12 (K_1) such that the hydraulic head is equal to 2.36 m at node 31. The upper and lower bounds of the parameter were taken equal to 10 m/d and 10^{-4} m/d, respectively. The prior estimate of the parameter was equal to 1 m/d. The updated version of the code achieved the optimum K in the material zone number 12 equal to 0.01 m/d after five iterations. Figure A1.13 shows the spatial distribution of the hydraulic heads computed with the inverse model and the location of zone number 12 and node number 31.

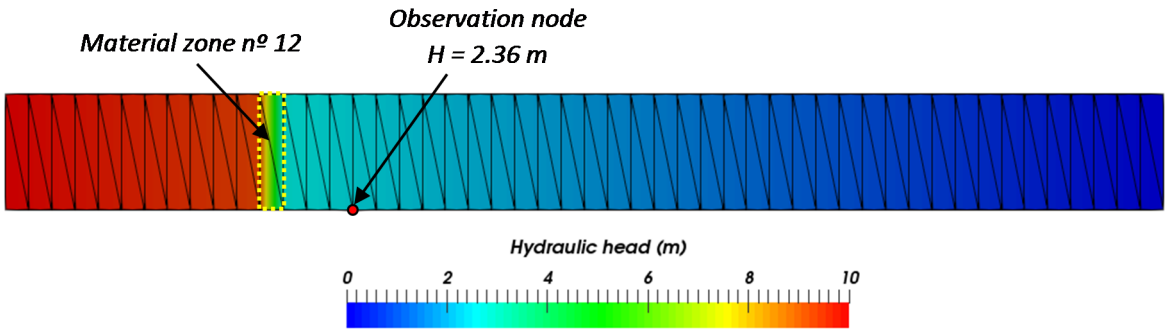

Figure A1.13. Spatial distribution of the hydraulic heads computed with the inverse model performed with INVERSE-CORE^{2D}.

A1.6.1.2. Second verification case

The estimation of the parameters with INVERSE-CORE^{2D} in transient models is more complex than in steady-state models. For this reason, a transient-state flow model was performed with the updated version of the code in the second verification case. The model was performed for a total period of 100 days and the time domain was divided into daily time periods. The hydraulic head at the left boundary of the model varies over time from H =15 m to H = 5 m with the time function shown in Figure A1.14. The hydraulic conductivity in the 50 material zones of the model is equal to 100 m/d in the horizontal direction (K_1) and 10^{-10} m/d in the vertical direction (K_2). Similar to the first verification case, a forward model run was performed. In this case, a run with the forward model was carried out by reducing the horizontal hydraulic conductivity (K_1) to 5 m/d in the material zone 25 (between x = 240 m and x = 250 m). The hydraulic heads computed in this run at node 45 (x = 220 m) were used to solve the inverse model by estimating the parameter number *"225"* corresponding to the hydraulic conductivity in the material zone 25 (K_1). The upper and lower bounds of the parameter are equal to 100 m/d and 10^{-2} m/d, respectively. The initial starting value of the parameter is equal to 100 m/d. The updated version of the code estimated the true hydraulic conductivity in material zone 25 (5 m/d) after eight iterations.

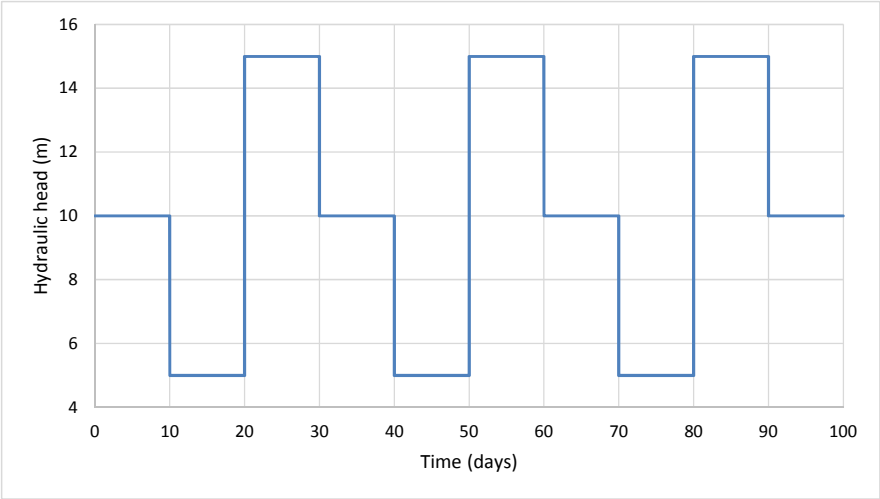

Figure A1.14. Hydrograph of the hydraulic heads at the left boundary of the model performed with INVERSE-CORE^{2D} in the second verification case.

A1.6.1.3. Third verification case

A conservative solute transport model was performed with the updated version of INVERSE-CORE^{2D} in the third verification case in which the diffusion coefficient (D_x) was estimated. The model was performed for a total period of 100 days and the time domain was divided into daily time periods. Hydraulic heads were prescribed to 10 m and 0 m at the left and right boundaries of the model, respectively. The components of hydraulic conductivity in the 50 material zones of the model are equal to 1 m/d in the horizontal direction (K_1) and 10^{-10} m/d in the vertical direction (K_2). The initial concentration of the conservative tracer is uniform and equal to 10^{-10} mol/m^3. The tracer concentration of the water inflow in the left boundary is equal to 1 mol/m^3 during the first 50 days of the simulation. The tracer concentration is equal to 10^{-10} mol/m^3 in the following 50 days of the simulation. The porosity is equal to 0.1. The diffusion coefficient in the pore water is equal to 10^{-6} m^2/d and the dispersivity is equal to 0.1 m. A forward model run was carried out with INVERSE-CORE^{2D} by increasing the horizontal diffusion coefficient (D_x) in the material zone number 1 (between x = 0 m and x = 10 m) to 0.0985 m^2/d. The time evolution of the tracer concentration computed at node 8 (x = 30 m) was used to solve the inverse model. The inverse model was performed by estimating the parameter number *"41101"* corresponding to the horizontal coefficient diffusion in the material zone number 1 (D_x) by using the tracer concentrations at node 8. The upper and lower bounds of the parameter are equal to 1 m^2/d and 10^{-6} m^2/d, respectively. The initial value of the parameter for the iterative estimation was equal to 10^{-6} m^2/d. The updated version of the code provided the optimum estimate of the horizontal diffusion coefficient in material zone number 1 (0.09854 m^2/d) after seven iterations.

A1.7. DEVELOPMENT OF A MICROBIOLOGICAL DATABASE FOR BIOCORE^{2D}

Microbial processes play a major role in controlling geochemical conditions in subsurface systems and their effects on groundwater chemistry are regarded as a new investigation field within hydrogeochemistry. In addition, microbial processes are also relevant for the safety of deep geological high-level radioactive waste (HLW) repositories (McKinley et al., 1997; Pedersen, 1999; Wang and Papenguth, 2001; Wang and Francis, 2005). Various laboratory and *in situ* experiments have been performed to evaluate the relevance of microbial processes and derive key microbial parameters.

Numerical models have been increasingly used to understand how physical, geochemical and biological processes are coupled in groundwater and their effects on groundwater-chemistry evolution and the reactive transport of contaminants and microorganism. Significant efforts have been made during recent years towards the development of such tools (Kirkner et al., 1985; Kaluarachchi and Parker, 1990; Steefel and Van Cappellen, 1990; Lensing et al., 1994; Salvage and Yeh, 1998; Steefel and Lichtner, 1998; Tebes-Stevens et al., 1998; Yabusaki et al., 1998; Chilakapati et al., 2000; Saaltink et al., 2000; Yeh, 2000; Ginn et al., 2001; Regnier et al., 2002; Saaltink et al., 2003; Pruess et al., 2004; Galíndez et al., 2006; Maher et al., 2006; Yang, 2006; Yang et al., 2007; Yang et al., 2008). BIOCORE^{2D} (Zhang, 2001; Zhang and Samper, 2001) is a coupled biogeochemical reactive transport code developed at the University of A Coruña by adding a numerical module for structured and distributed, multiple microbial component ecosystem, into a geochemical reactive transport code, CORE^{2D} (Samper et al., 2003a). BIOCORE^{2D} is a code designed to deal with biogeochemical reactive transport for a diversity of subsurface microbial flora and accounting for biofilms and interactions among microbes. In addition to flow, transport, and geochemical and microbiological processes, BIOCORE^{2D} incorporates a single layer diffusive biofilm model to account for the diffusive resistance, introduced by the attached biomass (immobile), for substrates, electron acceptors and other nutrients species from the solution, while dissolved biomass is considered to be in direct contact with available dissolved substrates, electron acceptors and nutrients.

BIOCORE^{2D} has been used to perform numerical models with microbial processes (Samper et al., 2003; Molinero et al., 2004; Samper et al., 2006; Yang et al., 2007; 2008; Zhang et al., 2008). A brief description of the microbiological processes has been presented in Chapter 2. A microbiological database with the input parameters of BIOCORE^{2D} has been performed in this dissertation.

A1.7.1. Microbiological database used by BIOCORE^{2D}

A microbiological database is attached to the code BIOCORE^{2D} for calculations of microbiological processes. Basic data for kinetic dissolution-precipitation and microbiological metabolism and biotransformation is read from the *"biokindata.dat"* file. The data are arranged in the following three blocks: 1) The first block contains data for kinetic dissolution-precipitation, 2) The second block deals with the parameters for microbiological metabolism and 3) The third block contains information on biotransformation. Blocks 2 and 3 of the microbiological database of BIOCORE^{2D} have been updated in this dissertation. Data on the main microbiological parameters used by the code have been compiled from the microbial models developed with BIOCORE^{2D} at the University of A Coruña in recent years.

The second block of the microbiological database contains parameters of microbiological metabolism. The first line of this block contains: the name of the microbe, the number of substrates on which the microbes can grow, the decay constant, the attachment rate constant, the detachment rate constant, the endogenous respiration rate constant, the pH dependence factor, the preferred pH value, the temperature form factor, the lower temperature limitation, the upper temperature limitation, the number of cometabolism species, the names of cometabolism species, the transformation rate constant of the cometabolism species and clarifying comments. The second line of this block contains: the specific grow rate, the metabolic lag time, the time needed to reach the exponential growth, the name of the substrate, the yield coefficient of the substrate, the half saturation constant for substrate, the inhibition factor of the substrate, the name of electron acceptor, the yield coefficient of the electron acceptor, the half saturation constant for electron acceptor, the name of nutrient, the yield coefficient of the nutrient, the half saturation constant for nutrient, the inhibition factor of the nutrient and the number of competitive bio-species and the competition factors. If the microbe indicated in the first line can grow on several substrates, the second line must repeated as many times as the number of substrates.

The biotransformation processes are defined in the third block of the microbiological database. This blocks includes a line for each species which can be biotransformed. The line contains: the name of the species being biotransformed, the number of the products of the biotransformation, the name of the product and the yield coefficient of the product.

BIOCORE^{2D} has been used to perform a wide range of numerical models involving microbial processes. Microbial data for these models have been compiled. They are discussed next.

The Boom clay formation has been investigated as a geological barrier for high-level radioactive waste (HLW). The CERBERUS experiment (Control Experiment with Radiation of the BElgian

Repository for Underground Storage) was carried out from 1989 to 1994 to study the effects of heating and radiation in the Boom clay formation (Bonne et al., 1992; Beaufays et al., 1994a; Noynaert et al., 2000a,b). This experiment showed that subsurface microbial processes play a major role in controlling groundwater chemistry (Chapelle, 1993; Ehrlich, 1996). Numerical THC and THBC models has been performed with the codes CORE^{2D} and BIOCORE^{2D} (Zhang et al., 2008). The comparison between the computed results and the measured data showed that the concentrations of several species such as SO_4^{2-}, Fe^{+2} or HCO_3^- were affected by microbial processes. Boom clay was isolated from the air after emplacement of the well casing. This way, aerobic biodegradation was inhibited and anaerobic biodegradation by Fe and SO_4^- reducing bacteria became dominant. Iron-reducing bacteria (IRB) and SO_4^- reducing bacteria (SRB) use organic C as a substrate and Fe(III) and dissolved SO_4^2 as an electron acceptor, respectively. IRB and SRB are assumed to grow according to:

$$Organic\ carbon + f_a Fe^{3+} \rightarrow f_a Fe^{2+} + mHCO_3^- + nH^+ + Y_s IRB \quad (1.9)$$

$$Organic\ carbon + f_a SO_4^{2-} \rightarrow f_a HS^- + mHCO_3^- + nH^+ + Y_s SRB \quad (1.10)$$

where Y_s is the yield coefficient of the substrate and f_a is the proportionality coefficient of the electron acceptor and m and n are stoichiometric coefficients equal to 1 and 0.01, respectively. These two microbial processes were compiled in the updated microbiological of BIOCORE^{2D}. The main microbial parameters are listed in Table A1.2.

Table A1.2. Microbial parameters for sulphate and iron reduction bacteria included in the microbial database of BIOCORE^{2D}.

Microbial parameter	Sulphate reduction	Iron reduction
Specific grown rate, G (s^{-1})	$2.53 \cdot 10^{-5}$	$1.54 \cdot 10^{-5}$
Decay constant, K_d (s^{-1})	$5.79 \cdot 10^{-7}$	$5.79 \cdot 10^{-7}$
Yield coefficient of the substrate, Y_s (g/mol)	65.14	65.14
Half-saturation constant of the substrate, K_s (mol/L)	$3.64 \cdot 10^{-4}$	$3.64 \cdot 10^{-4}$
Proportionality coefficient of the electron acceptors, f_a	2.74	24.07
Half saturation constant of the electron acceptor, K_a (mol/L)	$3.25 \cdot 10^{-4}$	$3.04 \cdot 10^{-8}$

The REX project (Redox Experiment in Detailed Scale) was carried out by the Swedish Nuclear Waste Management Company (SKB), JNC and ANDRA at the Äspö Hard Rock Laboratory (HRL) from 1998 to 2001. The REX experiment aimed at evaluating the stability of redox conditions in engineered barriers and the surrounding rock. One of its main objectives was to investigate *in situ* dissolved oxygen depletion after a controlled oxidizing perturbations. Available data from *in situ* experiments indicated that microorganisms play a substantial role in consuming dissolved oxygen and controlling redox

conditions (Bateman et al., 1998; Kotelnikova and Pedersen, 1998; Rivas-Pérez and Banwart, 1998; Kotelnikova and Pedersen, 1999; Puigdomenech et al., 2001; Trotignon et al., 2002; Samper et al., 2003; Molinero et al., 2004). The framework for microbial investigations was named the MICROBE-REX project (Kotelnikova and Pedersen, 1998, 1999). Different microbial groups contribute to oxygen reduction at the Äspö site. However, aerobic respiration of organic matter and methane oxidation are microbially-driven processes most likely responsible for oxygen depletion at the REX experiment. Several hydrobiogeochemical models were performed with BIOCORE^{2D} to evaluate geochemical and microbial consumption of dissolved oxygen (Yang et al., 2007). The models take into account the dissolved organic carbon (DOC) respiration and methane oxidation caused by aerobic heterotrophic bacteria and methanotrophic bacteria, respectively. "DOC respiration" and methane oxidation are assumed to proceed according to:

$$CH_2O + O_2 \rightarrow HCO_3^- + H^+ + Biomass \quad (1.11)$$

$$CH_4 + 2O_2 \rightarrow HCO_3^- + H^+ + H_2O + Biomass \quad (1.12)$$

These two microbial processes were compiled in the updated microbiological database of BIOCORE^{2D}. The microbial parameters are listed in Table A1.3.

Table A1.3. Microbial parameters for DOC respiration and methane oxidation included in the microbial database of BIOCORE^{2D}.

Microbial parameter	DOC respiration	Methane oxidation
Specific grown rate, G (s^{-1})	$1.33 \cdot 10^{-4}$	$2.48 \cdot 10^{-6}$
Decay constant, K_d (s^{-1})	$1.11 \cdot 10^{-5}$	$9.84 \cdot 10^{-7}$
Yield coefficient of the substrate, Y_s (g biomass/g substrate)	0.5	0.41
Half-saturation constant of the substrate, K_s (mol/L)	$1.25 \cdot 10^{-4}$	$1.25 \cdot 10^{-4}$
Half saturation constant of the electron acceptor, K_a (mol/L)	$1.5 \cdot 10^{-6}$	$1.50 \cdot 10^{-6}$

A microbial model of the redox zone experiment of the Äspö Hard Rock Laboratory was also performed with BIOCORE^{2D} (Molinero et al., 2004). This experiment aimed at evaluating the effects of the construction of an access tunnel on the hydrochemical conditions of a fracture zone. The microbial model accounts for the fermentation of particulate organic matter (POC) and the oxidation of DOC. POC containing sulfur compounds ferments in the shallow anaerobic zone, releasing DOC and sulfur compounds. Then, DOC is transported to deeper parts of the fracture zone and is further degraded by heterotrophic bacteria that employ Fe^{3+} as an electron acceptor. Fermentation is carried out by many anaerobic microorganisms. The model uses a generic microbial species representing all possible fermentation workers. POC acts as a substrate for fermenters and the concentrations of electron

acceptors do not limit the growth of POC fermenters. POC fermentation and DOC oxidation are assumed to take place according to:

$$POC \rightarrow f_{DOC}DOC + f_{SO_4}SO_4^{2-} + f_H H^+ \quad (1.13)$$

$$DOC + f_{Fe}Fe^{+3} + f_H H^+ \rightarrow f_{HCO_3}HCO_3^- + f_{Fe}Fe^{+2} + f_H H_2O \quad (1.14)$$

These two microbial processes were compiled in the updated microbiological database of BIOCORE^{2D}. The microbial parameters are listed in Table A1.4.

Table A1.4. Microbial parameters for POC fermentation and DOC oxidation by iron reducing bacteria included in the microbial database of BIOCORE^{2D}.

Microbial parameter	POC fermentation	DOC oxidation
Specific grown rate, G (s^{-1})	$1.94 \cdot 10^{-6}$	$1.75 \cdot 10^{-6}$
Yield coefficient of the substrate, Y_s (g biomass/g substrate)	$3.076 \cdot 10^{-3}$	$8.48 \cdot 10^{-3}$
Half-saturation constant of the substrate, K_s (g/L)	$7.60 \cdot 10^{-3}$	$6.60 \cdot 10^{-3}$
Half saturation constant of the electron acceptor, K_a (mol/L)	-	$3.25 \cdot 10^{-10}$
Proportionality coefficient, f_{DOC}	-0.9 g DOC / g POC	-
Proportionality coefficient, f_{SO_4}	-0.019 mol SO_4^{-2} /g POC	-
Proportionality coefficient, f_H	-0.05 mol H^+ /g POC	0.01 mol H^+ /g DOC
Proportionality coefficient, f_{HCO_3}	-	-0.0606 mol HCO_3^- /g DOC
Proportionality coefficient, f_{Fe}	-	0.021 mol $Fe3^+$ /g DOC

Nitrification is a sequential microbial metabolism series carried out by chemoautotrophic bacteria such as nitrosomonas and nitrobacter. They oxidize ammonia or ammonium into nitrite to gain energy for their metabolism and use inorganic carbon (dissolved CO_2 or HCO_3^-) as carbon source. The final metabolic product of nitrofiers is nitrate. Nitrification is a very important step in the nitrogen cycle and in nitrogen contamination removal. Nitrification takes place under obligate aerobic conditions. The first step of nitrification is the oxidation of ammonium:

$$NH_4^+ + 2O_2 \rightarrow NO_2^- + 2H_2O \quad (Nitrosomas) \quad (1.15)$$

The second step is:

$$NO_2^- + O_2 \rightarrow 2NO_3^- \quad (Nitrobacter) \quad (1.16)$$

Nitrifiers (microorganisms carrying out nitrification processes) are very sensitive to temperature, oxygen content and pH. Their growth rate depends strongly on these environmental

conditions and can show variations of up to 3 orders of magnitude. Wiesmann (1994) reported some values for microbial parameters (at 20ºC and pH = 8) which were used to update the microbiological database of BIOCORE^{2D} according to Table A1.5.

Two microbial models were performed with BIOCORE^{2D} to simulate the nitrification processes carried out in a lab biofilm reactor and an industrial prototype reactor (Zhang, 2001). Although nitrification processes taking place in a biofilm reactor cannot be considered as geological processes, intrinsic biochemical processes are the same as those taking place in a subsurface environments. The numerical models simulated the experiments carried out in laboratory and industrial prototype biofilm reactors (Nogueira et al., 1998; Vieira and Melo, 1999; Lazaro va et al., 1997; Lazaro va et al., 1998). Table A1.6 and Table A1.7 show the calibrated microbial parameters used for modelling the lab experiment and the industrial scale experiment, respectively. Microbial parameters values used to simulate the two experiments are different because the temperatures are slightly different. The industrial scale experiment was carried out at a temperature within the range 16-25ºC whereas in the laboratory experiment the temperature varied between 25ºC and 30ºC. For this reason, the two calibrated nitrification processes were compiled in the update microbiological database of BIOCORE^{2D}.

Table A1.5. Microbial parameters for nitrification processes according to Wiesmann (1994) included in the microbial database of BIOCORE^{2D}.

Microbial parameter	Nitrosomas	Nitrobacter
Specific grown rate, G (s^{-1})	$8.91 \cdot 10^{-6}$	$1.25 \cdot 10^{-5}$
Decay constant, K_d (s^{-1})	$5.55 \cdot 10^{-7}$	$5.55 \cdot 10^{-7}$
Endogenous respiration rate (s^{-1})	$5.79 \cdot 10^{-8}$	$5.79 \cdot 10^{-8}$
Yield coefficient of the substrate, Y_s (mg/mg substrate)	0.147	0.042
Half-saturation constant of the substrate, K_s (mol/L)	$3.88 \cdot 10^{-5}$	$2.83 \cdot 10^{-5}$
Yield coefficient of the electron acceptor , Y_a (mg O_2/ mg NH_4^+)	3.16	1.1
Half saturation constant of the electron acceptor, K_a (mol/L)	$9.38 \cdot 10^{-4}$	$3.44 \cdot 10^{-5}$

Table A1.6. Microbial parameters for nitrification processes used for modelling the lab scale experiment (25-30ºC) included in the microbial database of BIOCORE^{2D}.

Microbial parameter	Nitrosomas	Nitrobacter
Specific grown rate, G (s^{-1})	$5.65 \cdot 10^{-6}$	$1.48 \cdot 10^{-5}$
Decay constant, K_d (s^{-1})	$1.41 \cdot 10^{-6}$	$1.41 \cdot 10^{-6}$
Yield coefficient of the substrate, Y_s (mg/mg substrate)	0.207	0.070
Half-saturation constant of the substrate, K_s (mol/L)	$4.43 \cdot 10^{-5}$	$2.17 \cdot 10^{-5}$
Yield coefficient of the electron acceptor, Y_a (mg O_2/ mg NH_4^+)	3.16	1.1
Half saturation constant of the electron acceptor, K_a (mol/L)	$1.00 \cdot 10^{-5}$	$1.63 \cdot 10^{-5}$

Table A1.7. Microbial parameters for nitrification processes used for modelling the industrial scale experiment (16-25ºC) included in the microbial database used by BIOCORE^{2D}.

Microbial parameter	Nitrosomas	Nitrobacter
Specific grown rate, G (s^{-1})	$2.72 \cdot 10^{-6}$	$1.96 \cdot 10^{-6}$
Decay constant, K_d (s^{-1})	$1.75 \cdot 10^{-6}$	$5.55 \cdot 10^{-7}$
Yield coefficient of the substrate, Y_s (mg/mg substrate)	0.101	0.030
Half-saturation constant of the substrate, K_s (mol/L)	$4.43 \cdot 10^{-5}$	$2.07 \cdot 10^{-5}$
Yield coefficient of the electron acceptor, Y_a (mg O_2/ mg NH_4^+)	0.8	0.95
Half saturation constant of the electron acceptor, K_a (mol/L)	$7.19 \cdot 10^{-6}$	$1.09 \cdot 10^{-5}$

BIOCORE^{2D} was used to simulate the biodegradation of the complex $HNTA^{2-}$ (Samper et al., 2006; Yang et al., 2008). The biodegradation of $HNTA^{2-}$ is given by:

$$HNTA^{2-} + 1.620O_2 + 1.272H_2O + 2.424H^+ \rightarrow 0.576C_5\,H_7O_2N + 3.120H_2CO_3 + 0.424NH_4^+ \quad (1.17)$$

The parameters of the biodegradation of $HNTA^{2-}$ were compiled in the updated microbiological database of BIOCORE^{2D}. The main microbial parameters are listed in Table A1.8.

Table A1.8. Microbial parameters for the biodegradation of the complex $HNTA^{2-}$ included in the microbial database of BIOCORE^{2D}.

Microbial parameter	Biodegradation of $HNTA^{2-}$
Specific grown rate, G (s^{-1})	$2.63 \cdot 10^{-5}$
Decay constant, K_d (s^{-1})	$5.72 \cdot 10^{-7}$
Yield coefficient of substrate, Y_s (g/mol substrate)	65.14
Half-saturation constant of substrate, K_s (mol/L)	$7.64 \cdot 10^{-7}$
Half saturation constant of electron acceptor, K_a (mol/L)	$6.25 \cdot 10^{-6}$

The development of a detailed microbiological database presents many difficulties because microbial metabolism depends strongly on environmental variables such as temperature, pressure, turbidity, pH, Eh, and the concentrations of organic and inorganic compounds. For this reason, most of the data used in the compilation of the microbiological database have been obtained from the microbial models developed with BIOCORE^{2D} in recent years. It is expected that this microbiological database will facilitate future coupled geochemical and microbial models.

A1.8. OTHER IMPROVEMENTS AND CORRECTIONS OF BUGS IN SOURCE CODES OF CORE SERIES

Other minor improvements have been implemented in the codes of the CORE series. Some bugs in the source codes have been corrected also. The following corrections and improvements have been performed:

1) Vectors storing heat parameters such as dry and saturated thermal conductivities had fixed dimensions in the previous version of CORE^{2D}V5. When the number of material zones in a heat transport model was greater than the dimensions of the vectors storing heat parameters, the code could not use the right heat parameters. CORE^{2D}V5 has been corrected so that the vectors that store the heat variables have the same dimensions as the maximum number of material zones (*"MAXQM"*).

2) CORE^{2D}V5 allows for several cation exchange zones. The user specifies the CEC (Cation Exchange Capacity) of each exchange cation zone. The code calculates the sum of the concentrations of the exchanged cations to get the CEC in each zone. There was a bug in calculating the CEC in CORE^{2D}V5 when there were several cation exchange zones. The code has been corrected so that the CEC in each zone is calculated correctly.

3) The CEC (Cation Exchange Capacity) in CORE^{2D}V5 is given in meq/100g of soil. The code calculates internally the concentration of the exchanged cations in mol/L of fluid. The density of the solids is required to transform the concentrations in mol/L to meq/100g of soil. A bug was found in CORE^{2D}V5 because the code always used a constant density equal to 2.65 kg/L. CORE^{2D}V5 has been updated to allow the user to specify in the input files the density of the solids in each material zone.

4) The format for reading the specific surface of the minerals was not fully accurate. The small errors in reading this variable have been fixed by using the *"D0"* format. There was also a bug in the user's manual of CORE^{2D}V5 for the specific surface of the minerals. The specific surface of the mineral in the user's manual was defined as dm^2 of mineral surface per dm^3 of medium. The code, however, considered the surface as mineral surface per unit volume of fluid. The user's manual has been updated.

5) Improvements have been carried out in some output files of CORE^{2D}V5 such as *"OUTspx"*, *"OUTmix"* or *"OUTtexx"*. The number of decimal digits has been increased and the writing frequency of the results in these output files has been improved.

6) The source code of CORE^{2D}V5 has been updated to allow the storage of larger arrays and vectors in dynamic memory. This modification has allowed to perform numerical models with large variables.

7) The previous versions of CORE^{2D}V5 were compiled with Intel Fortran compilers. A revised version of the code has been prepared to be compiled with GNU Fortran (open source). The updated version of CORE^{2D}V5 allows to carry out numerical models with large variables because the Intel Fortran compilers have important limitations of memory (2 GB to store static data). Other codes of the CORE series such as INVERSE-CORE^{2D}, BIOCORE^{2D}, TRANMEF-3D and CORE^{3D} have been adapted also to be compiled with Intel Fortran compilers.

A1.9. DESCRIPTION OF THE INPUT AND OUTPUT FILES OF THE UPDATED VERSION OF CORE^{2D}V5

This section contains the description of the input data and main output files of the updated version of CORE^{2D}V5. Input data of this code have the same structure as those of the previous version of CORE^{2D}V5. The input files for heat transfer, solute transport and chemical data are similar to those of the previous version of CORE^{2D}V5 and therefore they are not presented here. The parts which have been changed or updated are underlined.

Card_1. Title

Card_1.1.
Variable: TITLE
Format: A76
TITLE: Title of the problem, comments and remarks. This title is reproduced in the output files.

Card_1.2.
Variable: Label
Format: A76
TITLE: Comments.

Card_2. General options for flow and transport

Variables:	IOTPA	IOFLU	IODIM	XITA1	XITA2	IHEAT	ITRAN	IRESTART	NWRI
Format:	I5	I5	I5	F10.3	F10.3	I5	I5	I5	I5

IOTPA: integer indicator of the type of medium
0 = confined aquifer
1 = unconfined aquifer
2 = variably saturated flow in vertical cross-sections

IOFLU: integer indicator for flow regime

0 = steady state

1 = transient state

IODIM: integer indicator for problem dimensionality

2 = two-dimensional flow

3 = three-dimensional axisymmetric flow. In this case the X coordinate must be the horizontal (radial) coordinate

4 = one-dimensional horizontal flow. Here 1-d mesh is used

5 = one-dimensional vertical flow. Here 1-d mesh is used (here this option is not implemented)

6 = two-dimensional axisymmetric flow. Here 1-d mesh is used

It is noted that the option 4, 5 and 6 are not implemented for unsaturated flow.

XITA1: coefficient for the type of numerical scheme used for solving the flow equation

1.0 = implicit

0.0 = explicit

between 1.0 and 0.0 = mixed scheme

XITA1=1.0 (implicit) is suggested. If IOFLU=0, XITA1 is not required (leave it blank).

XITA2: coefficient for the type of numerical scheme used for solving transport equations

1.0 = for an implicit scheme (unconditionally stable)

0.0 = for an explicit scheme (conditionally stable)

between 1.0 and 0.0 = mixed scheme

XITA2=1.0 (implicit) is suggested

IHEAT: integer indicator for heat transport simulation

0 = not considered

1 = considered

ITRAN: integer indicator for transport simulation

0 = not considered

1 = considered

IRESTART: indicator for using the restart procedure. Computed results are saved in a file named RESTART.DAT which can be used later to restart the simulation.

0 = not considering the restart option

1 = only write the data to the file of restart. A file is output, restartw.dat.

2 = Restart the run from the time written in the restartw.dat. Take care of that if irestart=2, the restartr.dat should be prepared which modified the name of restartw.dat

NWRI: integer indicator of the output files format

0 = output files in the original format

1 = output files in the VTK format (ParaView)

2 = output files in both formats (in the original format and in VTK format)

Card_3. Options for chemical calculations and coupling reactive transport approaches

Variables:	ISPIA	INIBOUND	NSIA	IASAME	IATIME	IMINE
Format:	I5	I5	I5	I5	I5	I5

ISPIA: indicator for using a sequential partly-iterative approach (SPIA) according to which after one transport iteration, the chemical model is only called for the nodes not satisfying a prescribed convergence tolerance

0 = not using SPIA. In this case the general sequential iteration approach is used.

1 = using SPIA

ISPIA = 0 is suggested

INIBOUND: indicator used for the definition of the chemical composition of boundary and recharge inflows. i.e. chemical initialization of the boundary and recharge waters.

If INIBOUND = 0 the options of Card_37 of the chemical input file are not activated for boundary waters, and therefore chemical speciation of these waters is not performed.

If INIBOUND is different than zero, options of Card_37 are activated and therefore chemical speciation of these waters can be performed. Use of INIBOUND=1 is suggested.

NSIA: indicator for the option of SIA-0 and SIA-1. SIA-0 refers to the general sequential iteration approach and SIA-1 represents the improved sequential iteration approach which uses first order term of Taylor's series extension to linearize the nonlinear kinetics law and causes the equation some implicit behaviour facilitating the iteration progress to reach convergence.

0 = SIA-0

1 = SIA-1

Default value is NSIA=0 (using SIA-0).

Recommended value: solving kinetics problem with a finer mesh (Peclet number smaller than 2) use NSIA=1, other case NSIA=0.

Notice that CORE^{2D} can switch this value between 0 and 1 according to the convergent performance in executions.

IASAME: indicator for the option which all primary species have same or different parameters (including diffusion coefficient, accessible porosity and retard coefficient) for each material zones.

0 = IASAME all primary species have different parameters mentioned above. Card 15_1 in chemical input file must be omitted.

1 = IASAME all primary species have same parameters mentioned above, Card 15_2 in chemical input file must be omitted.

If SIA-1 is used or kinetic adsorption of species is considered, IASAME must be 0.

IATIME: indicator for the option to use automatic time stepping or not.

0 = IATIME Automatic time stepping is used (recommended).

1 = IATIME Automatic time stepping is not used.

IMINE: indicator for the option to consider changeable porosity due to mineral dissolution/precipitation.

0 = changeable porosity is not considered.

1 = changeable porosity is considered and dynamically update the flow and transport and chemical parameters every time step.

Card_4. Input and output file names (except flow and solute transport input and output files)

Variables:

IOWRITE(1), INPUThet	I5, A20
IOWRITE(2), INPUTche	I5, A20
IOWRITE(3), OUTche	I5, A20

Names of files used for input of heat transport data (INPUThet), chemical input data (INPUTche) and chemical output results (OUTche). Each name must be in a separate line.

INPUThet is only needed when IHEAT in Card 2 is equal to 1. This line has to be always present in the input file.

INPUTche is the name of the geochemical input file. This file is always required, therefore a name must be provided always.

OUTche is the name of the geochemical output file. This file is always required, therefore a name must be provided always.

Each line must contain in the first column an integer value which will indicate whether a given file is needed or not. If this integer is 1 the file will be generated otherwise it will not.

Variables:

IOWRITE(4), OUThx: Output of nodal hydraulic head values at specified time steps (which are specified in Card_19): Integer code and file name. (I5, A20).

IOWRITE(5), OUTht: Output of hydraulic head versus time at selected nodes (which are specified in Card_20): Integer code and file name. (I5, A20).

IOWRITE(6), OUTvt: Output of computed volumes of water at selected nodes (which are specified in Card_21) as a function of time: Integer code and file name. (I5, A20).

IOWRITE(7), OUTft, Iflux: Output file name of mass flux versus time at selected nodes (which are specified in Card_21): Integer code and file name. (I5, A20,I5).

If Iflux=0, only total mass flux is printed for all specified nodes.

If Iflux=1, mass flux at each specified node is printed.

If Iflux=2, both of mass flux at each specified node and the total mass flux are printed.

IOWRITE(8), OUTwt: Output file containing the total volume of water stored in selected material zones (which are specified in Card_19) as a function of time: (I5, A20)

IOWRITE(9), OUTtex: Output file name of temperature nodal values at specified time steps (which are specified in Card_19): (I5, A20)

IOWRITE(10), OUTtet: Output file name of temperature versus time at selected nodes (which are specified in Card_20): (I5, A20)

IOWRITE(11), OUTspx: Output file name of nodal values of total dissolved concentrations (molality) of selected components (which are specified in Card_22) at specified time steps (which are specified in Card_19): (I5, A20)

IOWRITE(12), OUTspt: Output file name of total dissolved concentrations (molality) of selected components (which are specified in Card_22) versus time at selected nodes (which are specified in Card_20): (I5, A20)

IOWRITE(13), OUTphx: Output file name of pH nodal values at specified time steps (which are specified in Card_19 (I5, A20)

IOWRITE(14), OUTpht: Output file name of pH values versus time at selected nodes (which are specified in Card_22): (I5, A20)

IOWRITE(15), OUTmix, KLITER: Output file name of nodal values of cumulative precipitation (accumulated from time equal to zero) of selected mineral phases (which are specified in Card_23) at specified times (which are specified in Card_19). In case KLITER equal to 0, the nodal cumulative dissolution/precipitation will be expressed in mol mineral/dm^3 dissolution, which is adequate for saturated conditions. Otherwise in mol mineral/kg dry soil, more appropriate for non-saturated conditions. File OUTmit is congruent with the units specified through KLITER. (I5, A20, I5)

IOWRITE(16), OUTmit: Output file name of cumulative precipitation of selected mineral phases (which are specified in Card_23) versus time at selected nodes (which are specified in Card_20. (I5, A20)

IOWRITE(17), OUTpex: Output file name of pE nodal values at specified times (which are specified in Card_19 (I5, A20)

IOWRITE(18), OUTpet: Output file name of pE value versus time at selected nodes (which are specified in Card_20) (I5, A20)

IOWRITE(19), OUTadx: Output file name of nodal values of total sorbed component concentration at specified times (which are specified in Card_19). (I5, A20)

IOWRITE(20), OUTadt: Output file name of total sorbed component concentration versus time at selected nodes (which are specified in Card_20). (I5, A20).

IOWRITE(21), OUTiter: Output file name containing information on iterative processes. (I5, A20).

IOWRITE(22), OUTcsec, INDCSEC: Output file name of computed concentrations (molality) of dissolved primary, secondary species and selected gases at selected nodes (which are specified in Card_20) versus time. (I5, A20). Notice that for moderately large problems, this file may be exceedingly large. INDCSEC is an indicator to print the results of checking charge balance at selected nodes. In case INDCSEC is equal to 1, results of checking charge balance at selected nodes are outputted, otherwise, results are not printed.

IOWRITE(23), OUT OUTexx: Output file name containing the computed nodal concentrations of exchanged species at selected times (which are specified in Card_19). (I5, A20).

IOWRITE(27), OUT excht: Output file name containing exchanger in the solid versus time at selected nodes (which are specified in Card_20). The unit in this file is meq/100g (CEC) (I5, A20).

IOWRITE(36), OUT OUTdcx: Output file name containing the computed nodal total dissolved concentrations of selected isotopes (which are specified in Card_24) at specified time steps. (I5, A20).

IOWRITE(37), OUT OUTdct: Output file name containing total dissolved concentrations of selected isotopes (which are specified in Card_24) versus time at selected nodes. (I5, A20).

IOWRITE(24), OUTsix: Output file name containing the nodal saturation indices of minerals at selected times (which are specified in Card_19). (I5, A20).

IOWRITE(25), OUTsit: Output file name containing the saturation indices of minerals at selected times for given nodes (which are specified in Card_19). (I5, A20).

The information contained in this file is written in files OUTspx (nodal ionic strength) and OUTcsec (activity coefficients)

IOWRITE(26), OUTmasol, ICHKMS: Output file containing the total mass of dissolved components, total solid mass, the mass inflow and out flow in the whole system versus time. Computed values include the mass of dissolved components. Mass transfer to/from mineral phases or exchange complex is taken into account. The relative error for mass balance, default value is 0, the relative error of the mass balance will not be output;

ICHKMS=2 calculate the relative error for liquid solute, ICHKMS =3 calculate the relative error for total mass in system, ICHKMS =1 output the minimum relative error between the two, ICHKMS =4 output the two relative errors. (I5, A20, I5)

IOWRITE(28), OUTnodbal, INODBAL: Output file containing a summary of solute and water mass (useful for variably saturated media). The file contains: (1) nodal values of mass of aqueous components, (2) total volume of water in the system, (3) total solute mass in the system for selected aqueous components and (4) nodal values of water content, (5) total mass present in the system as minerals, (6) total mass present in the system as exchanged species. For mass balances, units are mol. INODBAL may have values of 0, 1 or 2. In case INODBAL is equal to 0, only total mass balance checks will be printed (total masses of selected components in the water, minerals, and exchanger as well as the amount of mass entering and/or leaving the system within a selected time period). If INODBAL is equal to 1, nodal mass balance is written. In this case, OUTnod can be extremely large. If INODBAL is equal to 2, mass balance is written for each material zone. (I5, A20, I5)

IOWRITE(32), OUTpeclet.OUT: This file contains the maximum dimensionless Peclet and Courant numbers for a given time period. (I5, A20).

IOWRITE(33), Equdb25: This file is an input file which contains the all chemical reaction data at temperature 25ºC and 1 bar. (I5, A20).

IOWRITE(34), Equdbv: This file is an input file which contains the all chemical reaction data at temperature from 0ºC to 300ºC and pressure along the steam saturation curve above 100ºC (I5, A20).

Please note that the equdb25 or equdbv needed depends on the temperature in your system defined. When the temperature in your system is constant and at 25ºC, the Equdb25 is selected, you should set the IOWRITE(33) 1.Otherwise the equdbv should be provided.

IOWRITE(35), Kindb: This file is an input file which contains the all dynamic chemical reaction data. When the kinetics reaction in your system defined, this input file should be provided (I5, A20).

IOWRITE(29), LOG1.OUT, ITERAT, ITERSTOP: This is file is a diagnostic where the values of aqueous species concentrations, activity and activity coefficients are dumped for each chemical iteration for a given node and time step. The file is rewritten for each node and each time step. So, activating this file translates into a really poor performance of CORE^{2D} in terms of time execution. It can be used to identify: (1) species giving problems in terms of chemical convergence; (2) nodes where chemical problems arise; (3) time periods for which chemistry cannot be properly solved. Variables ITERAT and ITERSTOP are provided to indicate the code the number of time period when start writing the LOG1.OUT file and the last time period when this file need to be written. In general, it is easy to identify the time period in which the code crashes. Therefore this time period minus 1 is a good point to start writing this file. ITERAT

may take the value of 0. In this case, the file LOG1.OUT will contain chemical information belonging to time 0 (initial conditions). No matter the filename given to this file, the output file will be called LOG1.OUT. (I5, A20, I5, I5)

IOWRITE(30), LOG2.OUT: In this file are dumped the saturation indices of the minerals of the problem for each chemical iteration in a given node and time period. This file may be as lengthy as the LOG1.OUT file. If the problem does not contain minerals, an error will be generated and, eventually, the execution will crash. Variables ITERAT and ITERSTOP operates over the time periods when this file is going to be generated. General strategy to use this file is similar to that of the LOG1.OUT file. No matter the filename given to this file, the output file will be called LOG2.OUT (I5, A20).

IOWRITE(31), LOG3.OUT, SELECTR: In this file is dumped the incremental value of the sink/source term (R) or the total solute affected by transport (UT), i.e. the value of array R (or UT) at iteration i minus the same value for iteration i-1. This file has as many blocks as transport iterations needed to achieve convergence in all nodes. The whole file is rewritten for each time period. No matter the filename given to this file, the output file will be called LOG3.OUT (I5, A20, 4X, A1).

IOWRITE(38), OUTvx.out: Output of flow velocities at specified time steps (which are specified in Card_19). Flow velocity vector is computed for each element of the finite element mesh. The coordinates of the origin of the flow velocity vector (barycentre of the triangular finite elements in 2-D models) and the x and y components of the flow velocity vector computed by the code are written in the output file. Integer code and file name. (I5, A20).

IOWRITE(39), OUTqt.out: Output of water inflows and outflows versus time at nodes with Dirichlet and Cauchy condition. In the output file an integer is written indicating the boundary condition imposed on the nodes ("1" for nodes with Dirichlet condition and "3" for nodes with Cauchy condition). By convention, the water inflows are positive and the water outflows are negative. Integer code and file name. (I5, A20).

If IMINE = 1 several output files are written automatically:

OUTpox.out: Output of nodal porosity values at specified time steps (Card_19).

OUTpot.out: Output of nodal porosity versus time at selected nodes (Card_20).

contriminx.out: Output of contribution of each existing mineral in the model to the change of nodal porosity at specified time steps (Card_19).

contrimint.out: Output of contribution of each existing mineral in the model to the change of nodal porosity versus time at selected nodes (Card_20).

OUTK.OUT: Output of hydraulic conductivities on all elements of the mesh at specified time steps (Card_19).

OUTDIFF.OUT: Output of diffusion coefficients on all elements of the mesh at specified time steps (Card_19).

OUTAREAM.OUT: Output of nodal specific surfaces of minerals whose dissolution or precipitation is controlled kinetically at specified time steps (Card_19).

Card_5. Dimension variables

Variables:	NNOD	NELE	NMA	NTTIME	TIME_UNIT
Format:	I5	I5	I5	I5	free characters

NNOD: number of nodes in the finite element grid.

NELE: number of triangular elements of the grid.

NMA: number of aquifer material zones (parameter zones).

NTTIME: number of time periods.

TIME_UNIT: time unit used in the practical problem which must be one of:

'second', 'minute', 'hour', 'day', 'month' and 'year'. Notice that writing in Title Type and CAPITAL letters are allowed. The time unit must be consistent between transport and geochemical processes and is free from the time unit used in the kinetics database. The default value of TIME_UNIT is day.

Card_6. Time stepping data

Repeat this card as many times as the number of time periods, NTTIME, defined in Card_5.

Variable: ITI TIMEINT NWRITE NCODE

Format: I5 F10.4 I10 I2

ITI: time period number.

TIMEINT: duration of time period [T].

NWRITE: print number within this time period.

NCODE: base code of variable print intervals. It can be 0 to 9. With different number of NCODE, CORE^{2D} gives different print interval distributions. The duration TIMEINT is divided into NWRITE and NWTI (in Card_19) equal average print interval. IF NCODE=0 or 1, the interval is constant, otherwise the intervals are gradually enlarged or reduced on a given base according to the value of NCODE. Notice that the time increments are given by the automatic time stepping function. Default value of base code NCODE is 0.

Card_7. Number of stepwise time functions for boundary and recharge conditions

Variables: NBOUNDFH NBOUNDFC

Format: I5 I5

NBOUNDFH : number of time functions for groundwater recharge and flow boundary conditions; if boundary parameters do not vary with time, NBOUNDFH is equal to zero. In this case Card_8 is not required.

NBOUNDFC : number of time functions for solute and heat transport boundary conditions. If they are constant in time, NBOUNDFC is equal to zero; in this case, Card_9 is not required.

Card_8. Stepwise time functions for areal recharge and water flow boundary conditions

This card must be omitted if NBOUNDFH=0 in Card_7. Repeat this card NBOUNDFH times, one for each time function.

Variables: I (BOUNDFH(I, J), J=1,NTTIME)

Format: I5 F10.0

BOUNDFH(I, J): value of the *i*-th time function at the *j*-th time period.

Card_9. Stepwise time functions for solute and heat transport

This card must be omitted if NBOUNDFC=0 in Card_7. Repeat this card NBOUNDFC times, one per time function.

Variables: I (BOUNDFC(I, J), J=1,NTTIME)

Format: I5 F10.0

BOUNDFC(I, J): value of the *i*-th function at the *j*-th time period. Use the same format as in Card_8.

Card_10. Parameters of aquifer material zones

Repeat this card NMA times, one per aquifer material zone. A material zone is a set of one or more triangular elements within which the parameters take constant values.

Variables: I PK1(I) PK2(I) ANGLE(I) SS(I) POR(I) DSL(I) DST(I) ITORT(I) TORT(I) DENSEC(I)

Format: I5 7E9.2 I3 2E8.2

I: material zone number

PK1(I): first principal component of the hydraulic conductivity tensor [L/T]

PK2(I): second principal component of the hydraulic conductivity tensor [L/T]

ANGLE(I): Angle (in degrees) between the direction of the first component and the x-coordinate (counter-clock wise)

SS(I): specific storage coefficient for confined (IOTPA=0) or unsaturated flow (IOTPA=2) [1/L]; It is equal to the specific yield for unconfined flow when IOTPA=1 [dimensionless]

POR(I): total transport porosity [dimensionless]

DSL(I): longitudinal dispersivity [L]

DST(I): transverse dispersivity [L]

ITOT(I): Type of law of tortuosity.

If Itort(i)=0, tortuosity constant.

If itort(i)=1, Tortuosity given by Simunek and Suarez's Equation.

If itort(i)=2, cementation.

TORT(I): tortuosity when ITORT=0. For ITORT=1, write 0.

DENSEC(I): dry density [M/L^3]. This datum is used to compute the retardation coefficient. It is only needed for sorbing solutes. Any coherent set of mass units (g, kg) are allowed.

For steady-state flow the storage coefficient SS is not required. One can leave SS blank or assign any value. One must use 'dm' as the unit of length [L]. That is required because concentrations are expressed as mol/L in the chemical model. Notice that for confined flow or unsaturated conditions SS represents the specific storage coefficient. The program computes the storage coefficient by multiplying SS and the thickness of the aquifer. For unconfined aquifers, SS represents the storage coefficient which approximately coincides with specific yield.

Card_11. Unsaturated flow parameters

This card must be provided only when IOTPA = 2 (unsaturated flow), otherwise it must be omitted. Repeat this card NMA times, one per material zone.

Variables:	I	ITPRL	SR(I)	SAS(I)	CM(I)	ALPHA(I)
Format:	2I5	E9.2	E9.2	E9.2	E9.2	

I: material zone number

ITPRL: Integer for relative permeability function:

= 1 for van Genuchten equation

= 2 for Irmay equation

SR(I): residual saturation degree

SAS(I): saturation degree at saturated conditions, normally it is assumed to be equal to 1

CM(I): value of parameter *m* in van Genuchten retention curve

ALPHA(I): value of parameter α in van Genuchten retention curve [L-1]

Card_12. Default values of data defined on triangular elements

Variable:	MATDF	THICKDF	RECHDF	IRECHDF
Format:	I5	F10.3	F10.3	I5

MATDF, THICKDF, RECHDF and IRECHDF are default values of variables MAT, THICK, RECH and IRECH which are defined in the next card, respectively. Default values are assigned to all elements. The next card allows the user to specify different values of these parameters at selected elements.

Card_13. Data for triangular elements

This card is used to provide the values of the parameters and variables that are defined over the elements. These variables include aquifer thickness and areal recharge. Aquifer parameters are assumed constant within material zones. The number of these zones (NMA) is defined in Card_5 and the parameter values of each zone are specified in Card_10. One must indicate the zone number to which a given element belongs to.

One must provide information for all elements (NELE). However, if the properties of the elements (parameters and geometry) is the same for a string of elements, one only has to input the properties of the first element of the string. The properties of the remaining elements are generated automatically by the code. One should always input the information of at least the first and last elements of the grid. The test examples attached to this manual illustrate this feature.

Variable: IE (NODE(IE,I),I=1,3) MAT(IE) THICK(IE) RECH(IE) IRECH(IE)

Format: I5 3I5 I5 F10.0 F10.0 I5

IE: element number

NODE(IE, 3): the three node (vertices) numbers of element IE (in a counter clock wise manner). For the 1-d mesh, blank can be provided as the third number of NODE.

MAT(IE): the number of material zone in which element IE is located

THICK(IE):

= aquifer thickness for flow in 2-D horizontal confined flow

= base elevation for 2-D unconfined flow

= 1 for 2-D vertical confined flow or variably saturated flow

= blank or any value for 3-D axisymmetric flow

RECH(IE): rate of areal recharge (positive for recharge and negative for discharge) [L/T]

IRECH(IE): the number of recharge time function (listed in Card_8) used for element IE. In the program, the amount of recharge is computed as the product of RECH times the time function, BOUNDFH. Leave IREACH blank if areal recharge is constant in time.

Card_14. Default values for nodal data

Variables: IDBHDF HPDF Q1DF ALFADF IQDF H0DF IDBOCDF IIWDF IBWDF IRWDF IMIDF IGSDF IADDF IEXDF IDECF NBDF

Format: I3 3F7.0 I3 F10.0 10I3

IDBHDF, HPDF, Q1DF, ALFADF, IQDF, H0DF, IDBOCDF, IIWDF, IBWDF, IRWDF, IMIDF, IGSDF, IADDF and IEXDF are default nodal values of the variables IDBH, HP, Q1, ALFA, IQ, H0, IDBOC, IZONEIW, IZONEBW, IZONERW, IZONEM, IZONEG, IZONED and IZONEX which are defined in the next card. Default values are assigned automatically to all the nodes of the grid. However, changes to these values can be made with the next card.

Card_15. Nodal data

This card is used to specify the values of properties and parameters which are defined in a nodewise manner. These properties include the nodal coordinates (x,y) as well as nodal boundary conditions and parameters for water flow and solute transport. One must provide these data for all the nodes (NNOD). However, if there is a string of equally spaced nodes having the same properties, the user only has to input the information for the first node of the string. Data for the remaining nodes are generated automatically by the code. Notice that the chemical parameters and properties are defined on a nodewise manner. These properties are assumed constant within zones which consist of a set of grid nodes. There are zones for: initial chemical composition, the chemistry of water flowing into the system along the boundaries, the chemistry of areal recharge water, mineral phases gas phases, sorption processes and properties and ion exchange processes and properties

Variables: IP XX(IP) Y(IP) IDBH(IP) HP(IP) Q1(IP) ALFA(IP) IQ(IP) H0(IP) IDBOC(IP) IZONEIW(IP) IZONEBW(IP) IZONERW(IP) IZONEM(IP) IZONEG(IP) IZONED(IP) IZONEX(IP) IDECA(IP) NBODEC(IP) [PHI(IP)] [PHIFAC(IP)]

Format: I5 2F10.0 I3 F7.0 F12.0 F7.0 I3 F7.0 10I3 [E9.2] [F7.3]

IP: node number

XX(IP): X coordinate of node IP [L]

Y(IP): Y coordinate of node IP [L]

For the 1-d mesh, XX and Y should also be provided.

IDBH(IP): integer indicator of the type of flow boundary condition

1-prescribed head

2-prescribed flux (including no flux). Use this condition for nodes not lying along the boundary.

3-mixed Cauchy condition

4-free drainage (only for variably saturated flow)

HP(IP): when IDBH(IP)=1 represents the prescribed hydraulic head; when IDBH(IP)=3 represents the external reference hydraulic head. Otherwise, HP is not required, and can be left blank

Q1(IP): prescribed water flux [L^3/T], (positive for inflow); only required when IDBH(IP)=2; otherwise leave blank or put any value

ALFA(IP): leakage coefficient [L^2/T]; only required when IDBH(IP)=3, otherwise leave blank or put any value. Notice that ALFA(IP) represents the lumped value of the leakage coefficient for node IP.

IQ(IP): the number of stepwise time function (listed in Card_8) used for the boundary condition of node IP; in the program, BOUNDFH multiplies either HP or Q1 depending on the type of flow boundary condition; if the boundary condition does not change with time, input a zero value

H0(IP): it represents:

= 1: initial hydraulic head for confined flow

= 2: initial pressure head for unsaturated flow

= 3: prior estimation of head for transient unconfined

= 4: steady-state hydraulic heads for steady-state flow

In all other cases, leave it blank or input any value.

IDBOC(IP): integer indicator of the type of solute transport boundary condition

= 1: prescribed concentration

= 2: solute flux associated with water flux (including no flux)

= 3: prescribed solute flux

= 4: evaporation boundary, if this value is 4, you should provide Q1(ip) negative.

IZONEIW(IP): zone number of the initial chemical composition.

IZONEBW(IP): zone number for the chemistry of boundary inflows (including inflows at internal nodes). Leave it blank if there are no inflow zones.

IZONERW(IP): zone number for the chemistry of recharge water. Leave it blank if there is no areal recharge.

IZONEM(IP): mineral zone number to which the node belongs to. Leave it blank if there are no mineral zones.

IZONEG(IP): gas zone number to which the node belongs to. Leave it blank if there are no gas zones.

IZONED(IP): adsorption zone number to which the node belongs to. Leave it blank if there are no sorption zones.

IZONEX(IP): ion exchange zone number to which the node belongs to. Leave it blank if there are no exchange zones.

IDECA(IP): decay zone number to which the node belongs to. Leave it blank if there are no decay zones

NBODEC (IP): boundary number of decay zone to which the node belongs to. Leave it blank if there are no decay zones

[PHI(IP)]: total transport porosity [dimensionless] defined in a nodewise manner. This variable is only necessary when changeable porosity is considered (IMINE = 1 in Card_3). The sum of porosity (PHI) and the volume fractions of minerals associated to one node must be 1 when IMINE = 1.

[PHIFAC(IP)]: factor which is used by CORE^{2D} to compute the accessible porosity associated to the nodes of the mesh. Accessible porosity is computed multiplying the porosity (PHI) by this factor (PHIFAC). PHIFAC can only take values between 0 and 1. This variable is only necessary when changeable porosity is considered (IMINE = 1 in Card_3).

Card_16. Data for free drainage boundary nodes

This card is needed for calculating the free drainage boundary distance. Therefore, it is only needed for unsaturated zones having a free drainage boundary condition. Repeat as many times as nodes having a boundary condition IDBH=4 (see the previous card).

Variables: NODF NODF1 NODF2

Format: I5 I5 I5

NODF: free drainage node number

NODF1: number of the first neighbour node (on the free drainage boundary) of node NODF

NODF2: number of the second neighbour node of node NODF

If one neighbour node is out of the free drainage boundary, input a zero value.

Card_17. Data for convergence criteria

Variables: MAXITPFL TOLFL MAXITPTR TOLTR MAXITPCH TOLCH MAXITPAD TOLAD [TOLFLFAC] [PORMIN]

Format: I5 E10.3 I5 E10.3 I5 E10.3 I5 E10.3 [E10.3] [E10.3]

MAXITPFL: maximum allowed number of iterations for solving the water flow equation. It is needed for unconfined and unsaturated flow.

TOLFL: relative tolerance for convergence of head (or pressure head) values. A value between 10^{-3} and 10^{-6} is suggested.

MAXITPTR: maximum allowed number of iterations for solving transport and geochemistry; set MAXITPTR=1 for the sequential non-iterative approach where transport and chemistry are sequentially solved only once.

TOLTR: relative tolerance for convergence of concentration values during transport calculations. A value between 10^{-3} and 10^{-6} is suggested.

MAXITPCH: maximum allowed number of iterations for solving the geochemical equations.

TOLCH: relative tolerance for convergence of concentration values during the solution of the chemical system. A value between 10^{-3} and 10^{-6} is suggested.

MAXITPAD: maximum allowed number of iterations for solving the equations sorption via surface complexation.

TOLAD: relative tolerance of concentration convergence for solving sorption reactions. A value between 10^{-3} and 10^{-6} is suggested.

[TOLFLFAC]: factor which is used by CORE^{2D} when there are convergence problems in some node of the mesh in variably saturated flow models. This factor is only used by the code when the number of iterations reaches the maximum number of iterations specified without the relative error is smaller than the convergence tolerance. If this occurs, CORE^{2D} compares the maximum relative error committed with the convergence tolerance multiplied by the new factor (TOLFLFAC). If the maximum error committed is smaller than the convergence tolerance multiplied by the factor, the code continues to calculate. Otherwise, the code stops. This variable is only necessary in variably saturated flow models (IOTPA = 2 in Card_2)

[PORMIN]: minimum porosity allowed for reactive transport models (clogging). If the porosity decreases to the minimum porosity, the minerals cannot precipitate more. A value between 10^{-4} and 10^{-10} is suggested. This variable is only necessary when changeable porosity is considered (IMINE = 1 in Card_3).

Card_18. Control variables for Jacobian matrix

Variables: ISWITCH ITEMP NJACOB

Format: I5 I5 I5

ISWICHT: base switch option. ISWICHT = 1 when switching is performed otherwise, leave it blank. Use of ISWICHT = 0 is recommended.

ITEMP: integer for thermal options (= 0 for constant temperature at 25 ºC; = 1 for variable temperature).

NJACOB: the Jacobian matrix for chemical speciation is updated every NJACOB iterations. (Use of NJACOB = 1 is recommended).

Card_19. Control variables for output printout

Variables: NWXY NWDIM NWTI NWNOD NWCOM NWMIN INDMAT NVOL NWTV NWDEC

Format: 10I5

NWXY: time frequency for writing spatial nodal results in CORE^{2D}. CORE^{2D} print spatial nodal results once a time for each time period.

NWDIM: options for spatial results

1 = results versus distance x for 1-D problems

2 = results at all nodes for 2-D problems

NWTI: time frequency for writing the time evolution of results at some selected nodes (NWNOD).

NWNOD: number of nodes at which time evolution will be printed out.

NWCOM: number of chemical components for which results will be printed out, kinetically controlled aqueous species can be ordered following the primary species in the purpose of print out.

NWMIN: number of minerals for which results will be printed out.

INDMAT: aquifer material zone number for which the time evolution of water volume will be printed out.

NVOL: number of nodes for which the time evolution of water content will be printed out.

NWTV: time frequency for writing water content.

NWDEC: number of isotopic components for which results will be printed out.

Card_20. Node numbers at which results are printed out

Variables: (IWNOD(I),I=1,NWNOD)

Format: 15I5

IWNOD(I): Vector of node numbers at which time evolution of results are printed out. Omit this card if NWNOD = 0.

Card_21. Node numbers at which results of water content will be printed out variable

Variable: (INVOL(I), I=1, NVOL)

Format: 15I5

INVOL(I): Vector of node numbers which results of water content will be printed out. Omit this card if NVOL = 0.

Card_22. Components for which results will be printed out

Variable: (IWCOM(I), I=1, NWCOM)

Format: 15I5

IWCOM(I): Vector of chemical component numbers for which results will be printed out. Omit this card if NWCOM = 0.

Card_23. Minerals for which results will be printed out

Variable: (IWMIN(I),I=1,NWMIN)

Format: 15I5

IWMIN(I): Vector of mineral identifiers for which results will be printed out. Omit this card if NWMIN=0.

Card_24. Isotopes for which results will be printed out

Variable: (IWdec (I), I=1,NWDEC)

Format: 15I5

IWdec (I): Vector of isotopes numbers for which results will be printed out. Omit this card if NWDEC=0.

A1.10. REFERENCES

Ahrens, J., Geveci, B., Law, C., (2005). ParaView: An End-User Tool for Large Data Visualization, Visualization Handbook, Elsevier, ISBN-13: 978-0123875822.

Ayachit, U., (2015). The ParaView Guide: A Parallel Visualization Application, Kitware, ISBN 978-1930934306.

Bateman, K., West, J.M., Aoki, K., Yoshida, H., Coombs, P., Gillespie, M.R., Henney, P., Reeder, S., Milodowski, A.E., (1998). Laboratory examination of microbial effects upon redox in a geological disposal site for radioactive waste. In: McKinley, I.G., McCombie, C. (Eds.), Scientific Basis for Nuclear Waste Management XXI. Mat. Res. Soc. Symp. Proc., vol. 506, pp. 1019-1020. Pittsburgh, Penn.

Beaufays, R., De Cannière, P., Fontayne, A., Labat, S., Meynendonckx, L., Noynaert, L., Volckaert, G., Bruggeman, A., Lambrechts, M., Vandervoot, F., (1994). CERBERUS.A demonstration test to study the near-field effects of an HLW canister in an argillaceous formation. SCK - CEN. Activity Report 1990-92. EUR 15718 EN.

Bonne, A., Beckers, H., Beaufays, R., Buyens, M., Coursier, J., De Bruyn, D., Fonteyne, A., Genicot, J., Lamy, D., Meynendonckx, P., Monsecour, M., Neerdael, B., Noynaert, L., Voet, M., Volckaert, G., (1992). The HADES demonstration and pilot project on radioactive waste disposal in a clay formation. SCK - CEN. Final Report. EUR 13851 EN.

Chapelle, F.H., (1993). Groundwater Microbiology and Geochemistry. Wiley, New York.

Chilakapati, A., Yabusaki, S., Szecsody, J., MacEvoy, W., (2000). Groundwater flow, multicomponent transport and biogeochemistry: development and application of a coupled process model. J. Cont. Hydrol., 43 (3-4), 303-325.

Dai, Z., Samper, J., (1999). INVERSE-CORE^{2D}: A Code for inverse problem of water flow and reactive solute transport, User's Manual, Version 0, University of A Coruña.

Dai, Z., (2000). Inverse problem of water flow and reactive solute transport in variably saturated porous media, Ph.D. Dissertation, 334 pp., University of A Coruña, A Coruña, Spain.

Dai Z., Samper, J., (2004). Inverse problem of multicomponent reactive chemical transport in porous media: Formulation and Applications. Water Resources Research, 40, W07407, doi: 10.1029/2004WR003248.

Ehrlich, H.L., (1996). Geomicrobiology. Marcel Dekker, New York.

ENRESA, (1995). TRANQUI User's Manual. Technical report for Empresa Nacional de Residuos Radioactivos (ENRESA). J. Samper, C. Ayora, T. Xu, N. Cuellar. A Coruña, 1995.

Galíndez, J.M., Molinero, J., Samper, J., Yang, C.B., (2006). Simulating concrete degradation processes by reactive transport models. J. Phys., IV France 136, 177-188.

Ginn, T.R., Murphy, E.M., Chilakapati, A., Seeboonruang, U., (2001). Stochastic-convective transport with nonlinear reaction and mixing: application to intermediate-scale experiments in aerobic biodegradation in saturated porous media. J. Cont. Hydrol., 48 (1-2), 121-149.

Juanes, R., (1997). Un código para la modelización tridimensional de flujo y transporte. Technical project, E.T.S.I.C.C.P., Universidade da Coruña.

Juanes, R., Samper, J., (2001). Una formulación general y eficiente de fracturas y condiciones de contorno en el M.E.F.: II. Aplicación a casos sintéticos. Revista Internacional de Métodos Numéricos para Cálculo y Diseño en Ingeniería, 17(1):67-82.

Juncosa, R., Navarro, V., Samper, J., (1999). Manual del usuario de FADES-CORE (Versión 0.0.). E. T. S. I. de Canales y Puertos, Universidade da Coruña.

Kaluarachchi, J.J., Parker, J.C., (1990). Modeling multicomponent organic chemical transport in three-fluid-phase porous media. J. Cont. Hydrol., 5 (4), 349-374.

Kirkner, D.J., Jennings, A.A., Theis, T.L., (1985). Multisolute mass transport with chemical interaction kinetics. J. Hydrol., 76 (1-2), 107-117.

Kotelnikova, S., Pedersen, K., (1998). Microbial oxygen consumption in Äspö tunnel environments. SKB Technical report, PR-HRL- 98-11, Stockholm, Sweden.

Kotelnikova, S., Pedersen, K., (1999). The microbe REX Project: microbial O_2 consumption in the Äspö tunnel. SKB Technical Report, TR-99-17, Stockholm, Sweden.

Lazarova V., Nogueira R., Manem J., Melo L., (1997). Control of nitrification efficiency in a new biofilm reactor. Wat. Sci. Tech. Vol. 36, No. 1, pp. 31-41. Wat. Sci. Tech., 36(1) 31-41.

Lazarova V., Nogueira R., Manem J., Melo L., (1998). Influence of dissolved oxygen on nitrification kinetics in a circulating bed reactor. Wat. Sci. Tech., 37(4-5) 187-193.

Lensing, H.J., Vogt, M., Herrling, B., (1994). Modeling of biologically mediated redox processes in the subsurface. J. Hydrol., 159 (1-4), 125-143.

Maher, K., Steefel, C.I., DePaolo, D.J., Viani, B.E., (2006). The mineral dissolution rate conundrum: insights from reactive transport modeling of U isotopes and pore fluid chemistry in marine sediments. Geochim. et Cosmochim. Acta, 70 (2), 337-363.

McKinley, I.G., Hagenlocher, I., Alexander, W.R., Schwyn, B., (1997). Microbiology in nuclear waste disposal: interfaces and reaction fronts. FEMS Microbiology Reviews 20 (3), 545-556.

Molinero, J., Samper, J., Yang, C., Zhang, G., (2004). Biogeochemical reactive transport model of the Redox zone experiment of the Äspö hard rock laboratory (Sweden). Nuclear Technology, 48 (2), 151-165.

Mon, A., (2017). Coupled thermo-hydro-chemical-mechanical models for the bentonite barrier in a radioactive waste repository. Ph.D. Dissertation, Universidade da Coruña, 483 pp.

Montenegro, L., Zhang, G. Samper, J., Delgado, J., (1999). Documento de Verificación del código CORE^{2D}. Technical report, E.T.S. Ingenieros de Caminos. Universidade da Coruña, 179 pp.

Navarro, V., (1997). Modelo de comportamiento mecánico e hidráulico de suelos no saturados en condiciones no isotermas. Ph.D. Dissertation, Universidad Politécnica de Cataluña, 329 pp.

Nogueira R., Lazarova V., Manem J., Melo L.F., (1998). Influence of dissolved oxygen on the nitrification kinetics in a circulating bed biofilm reactor. Bioprocess Engineering. 19: 441-449.

Noynaert, L., de Cannière, P., De Bruyn, D., Volckaert, G., Put, M., Kursten, B., Sneyers, A., Van Iseghem, P., Beaucaire, C., Pitsch, H., Bouchet, A., Parneix, J.C., Samper, J., Delgado, J., Navarro, V., Montenegro, L., Zhang, G., (2000a). Heat and radiation effects on the near field of a HLW or spent fuel repository in a clay formation (CERBERUS Project). Final Report. EUR 19125 EN.

Noynaert, L., de Cannière, P., Kursten, B., De Bruyn, D., Van Iseghem, P., Volckaert, G., Beaucaire, C., Pitsch, H., Bouchet, A., Parneix, J.C., Samper, J., Delgado, J., Navarro, V., Montenegro, L., Juncosa, R., Zhang, G., (2000b). Study of the effects of heat and radiation on the near field of a HLW or spent fuel repository in clay. The CERBERUS project. In: Euradwaste 1999. Radioactive Waste Management Strategies and Issues, Luxemburg, EUR 19143 EN, 378-381.

Pedersen, K., (1999). Subterranean microorganisms and radioactive waste disposal in Sweden. Engineering Geology, 52, 163-176.

Pruess, K., Garcia, J., Kovscek, T., Oldenburg, C., Rutqvist, J., Steefel, C., Xu, T., (2004). Code intercomparison builds confidence in numerical simulation models for geologic disposal of CO_2. Energy, 29 (9-10), 1431-1444.

Puigdomenech, I., Ambrosi, J.P., Eisenlohr, L., Lartigue, J.E., Banwart, S.A., Bateman, K., Milodowski, A.E., West, J.M., (2001). O_2 depletion in granitic media: The REX project. SKB Technical Report, TR-01-05, Stockholm, Sweden.

Regnier, P., O'Kane, J.P., Steefel, C.I., Vanderborght, J.P., (2002). Modeling complex multi-component reactive-transport systems: towards a simulation environment based on the concept of a knowledge base. Appl. Math. Model., 26 (9), 913-927.

Rivas-Pérez, J., Banwart, S., (1998). Redox experiment in detailed scale (REX). Task 5.1. Laboratory investigations. SKB Technical Report, PR-HRL-98-15, Stockholm, Sweden.

Saaltink, M.W., Carrera, J., Ayora, C., (2000). A comparison of two approaches for reactive transport modelling. J. Geochem. Explor., 97-101.

Saaltink, M.W., Ayora, C., Stuyfzand, P.J., Timmer, H., (2003). Analysis of a deep well recharge experiment by calibrating a reactive transport model with field data. J. Cont. Hydrol., 65 (1-2), 1-18.

Salvage, K.M., Yeh, G.T., (1998). Development and application of a numerical model of kinetic and equilibrium microbiological and geochemical reactions (BIOKEMOD). J. Hydrol., 209 (1-4), 27-52.

Samper, J., Juncosa, R., Delgado, J., Montenegro, L., (1998). CORE-LE User's Manual. Universidade da Coruña, 207 pp.

Samper, J., Delgado, J., Juncosa, R., Huguet, Ll., (1999). Manual de VISUAL-CORE-LE, Versión 1.0. Technical report for ENRESA. E. T. S. Ingenieros de Caminos. Universidade da Coruña.

Samper, F.J., Juncosa, R., Delgado, J., Montenegro, L., (2000) CORE^{2D}: A code for non-isothermal water flow and reactive solute transport, User's manual version 2. Universidade da Coruña. Publ. ENRESA, 131 pp.

Samper, J., Yang, C., Montenegro, L., (2003). CORE^{2D} version 4: a code for non-isothermal water flow and reactive solute transport. User's Manual. University of A Coruña, Spain.

Samper, J., Molinero, J., Yang, C., Zhang, G., (2003). Redox Zone II. Coupled modeling of groundwater flow, solute transport, chemical reactions and microbial process in the Äspö Island. SKB Technical Report, TR-03-16, Stockholm, Sweden.

Samper, J., Zhang, G., Montenegro L., (2006). Coupled microbial and geochemical reactive transport models in porous media: Formulation and Application to Synthetic and In Situ Experiments. Journal of Iberian Geology, 32 (2) 2006: 215-231.

Samper, J., Xu, T., Yang, C., (2009). A sequential partly iterative approach for multicomponent reactive transport with CORE^{2D}. Comput. Geosci., 13:301–316.

Samper, J., Yang, C., Zheng, L., Montenegro, L., Xu, T., Dai, Z., Zhang, G., Lu, C., Moreira, S., (2011). CORE^{2D}V4: A code for water flow, heat and solute transport, geochemical reactions, and microbial processes. Chapter 7 of the Electronic book Groundwater Reactive Transport Models. In: Zhang F., Yeh G.-T., Parker C., Shi X. (Eds.) Bentham Science Publishers, pp 161-186.

Steefel, C.I., Van Cappellen, P., (1990). A new kinetic approach to modeling water-rock interaction: the role of nucleation, precursors, and Ostwald ripening. Geochim. et Cosmochim. Acta, 54 (10), 2657-2677.

Steefel, C.I., Lichtner, P.C., (1998). Multicomponent reactive transport in discrete fractures: II: Infiltration of hyperalkaline groundwater at Maqarin, Jordan, a natural analogue site. J. Hydrol., 209 (1-4), 200-224.

Tebes-Stevens, C., Valocchi, A.J., VanBriesen, J.M., Rittmann, B.E., (1998). Multicomponent transport with coupled geochemical and microbiological reactions: model description and example simulations. J. Hydrol., 209 (1-4), 8-26.

Vieira M.J., Melo L.F., (1999). Intrinsic kinetics of biofilms formed under turbulent flow and low substrate concentrations. Bioprocess Engineering 20: 369-375.

Wang, Y.F., Papenguth, H.W., (2001). Kinetic modeling of microbially-driven redox chemistry of radionuclides in subsurface environments: coupling transport, microbial metabolism and geochemistry. Journal of Contaminant Hydrology, 47 (2–4), 297–309.

Wang, Y.F., Francisb, A.J., (2005). Evaluation of microbial activity for long-term performance assessments of deep geologic nuclear waste repositories. Journal of Nuclear and Radiochemical Sciences, 6 (1), 43-50.

Wiesmann, U., (1994). Biological nitrogen removal from wastewater. In Fietcher A. (ed.), Advances in biochemical engineering biotechnology, vol. 51, p. 113-154, Springer-Verlag, Berlin, Heidelberg, Germany.

Xu, T., (1996). Modeling non-isothermal multi-component reactive solute transport through variably saturated porous media. Ph.D. dissertation. Universidade da Coruña. A Coruña (Spain).

Xu, T., Samper, J., Ayora, C., Manzano, M., Custodio, E., (1999). Modeling of non-isothermal multi-component reactive trasnport in field scale porous media flow systems. J. Hydrol., 214:144-164.

Yabusaki, S.B., Steefel, C.I., Wood, B.D., (1998). Multidimensional, multicomponent, subsurface reactive transport in nonuniform velocity fields: code verification using an advective reactive streamtube approach. J. Cont. Hydrol., 30 (3-4), 299-331.

Yang, C., Juanes, R., Samper, J., Molinero, J., Montenegro, L., (2003). User's manual of CORE^{3D}, Technical Report. Universidade da Coruña, Spain.

Yang, C., (2006). Conceptual and Numerical Coupled Thermal-hydro-bio-geochemical Models for Three-dimensional Porous and Fractured Media. Ph.D. Thesis, University of A Coruña, Spain.

Yang, C., Samper, J., Molinero, J., Bonilla, M., (2007). Modelling geochemical and microbial consumption of dissolved oxygen after backfilling a high level radioactive waste repository. J. Cont. Hydrol., 93, 130-148.

Yang, C., Samper, J., Molinero, J., (2008). Inverse microbial and geochemical reactive transport models in porous media. Physics and Chemistry of the Earth, Volume 33, Issue 14, p. 1026-1034.

Yeh, G.T., (2000). Computational Subsurface Hydrology, Reactions, Transport and Fate. Kluwer Academic Publishers. The Netherland.

Zhang, G., (2001). Nonisothermal hydrobiogeochemical models in porous media. Ph.D. Dissertation. University of A Coruña. Spain.

Zhang, G., Samper, J., (2001). BIOCORE^{2D}: A code for non-isothermal hydrobiogeochemical reactive transport. User's Manual V0. Technical report, E.T.S.I. de Caminos, Canales y Puertos. Universidade da Coruña, 244 pp.

Zhang, G., Samper, J., Montenegro, L., (2008). Coupled thermo-hydro-bio-geochemical reactive transport model of CERBERUS heating and radiation experiment in Boom clay. Applied Geochemistry. Volume 23, Issue 4, pp 932-949.

Zheng, L., Samper J. (2005). Manual of Inverse FADES-CORE, Technical report, University of A Coruna, Spain.

Zheng, L., Samper, J., (2008). A coupled THMC model of FEBEX mock-up test. Physics and Chemistry of the Earth, 33, S486-S498.

Zheng, L., Samper, J., Montenegro, L., (2008). Inverse hydrochemical models of aqueous extract experiments. Physics and Chemistry of the Earth, 33, 1009-1018.

Zheng, L., Samper, J., Montenegro, L., Fernández, A.M., (2010). A coupled THMC model of a heating and hydration laboratory experiment in unsaturated compacted FEBEX bentonite, Journal of Hydrology, Vol 386, Issues 3-4, 80-94.

Zheng, L., Samper, J., Montenegro, L., (2011). A coupled THC model of the FEBEX in situ test with bentonite swelling and chemical and thermal osmosis, J. Cont. Hydrol., 126:45-60.

APPENDIX 2. IMRPOVEMENTS IMPLEMENTED IN CORE^{2D}V5 DEALING WITH POROSITY CHANGES AND FEEDBACK OF TRANSPORT PARAMETERS

This appendix describes the improvements implemented in CORE^{2D}V5 dealing with porosity changes. CORE^{2D}V5 has been extended to take into account the porosity changes due to mineral dissolution/precipitation and update dynamically each time step the flow, transport and chemical parameters. These improvements have been verified with several test cases.

ABSTRACT

This appendix presents the improvements implemented in CORE^{2D}V5 (Samper et al., 2009, 2011) dealing with porosity changes due to mineral precipitation and dissolution. The changes in the porosity in a porous medium due to mineral dissolution/precipitation change the flow, transport and chemical parameters. CORE^{2D}V5 has been extended to take into account the changes in porosity and update each time step the flow, transport and chemical parameters. Porosity changes due to dissolution/precipitation reactions and their feedback on transport and chemical properties are taken into account with empirical formulae such as the Kozeny-Carman equation for porosity/permeability (Carman, 1973) and Archie's law for porosity/diffusivity (Archie, 1942). The improvements implemented in CORE^{2D}V5 to deal with porosity changes have been verified with analytical solutions for diffusion problems coupled with precipitation-dissolution reactions and feedback of porosity changes in one-dimensional (Hayek et al., 2011) and two-dimensional (Hayek et al., 2012) test cases. In addition, a benchmark case has been used to benchmark the improvements of CORE^{2D}V5 with other reactive transport codes such as CrunchFlow, HP1, MIN3P, Pflotran and TOUGHREACT. This benchmark considers advective-dispersive transport in saturated media with kinetically-controlled mineral precipitation and dissolution leading to porosity changes (Xie et al., 2015).

A2.1. INTRODUCTION

Porosity may change due to mechanical deformation, swelling of clay minerals, mineral dissolution/precipitation and thermal deformation. Mineral dissolution and precipitation generally modifies the pore space geometry of rocks, which in turn changes flow and influences transport parameters. Porosity changes induced by mineral dissolution/precipitation are important for the description of various hydrogeological processes and influence the evolution of natural geological environments and underground systems.

Porosity changes in natural porous media occur normally very slowly, but in a long term can be of pivotal importance for the migration of fluids and solutes. If porosity increases substantially, preferential fluid migration pathways may develop, accelerating solute transport. On the other hand, a significant porosity decrease may inhibit fluid and solute transport. When the porosity is close to cero, clogging occurs and the aqueous phase may vanish completely.

Porosity changes due to mineral dissolution/precipitation may alter the behaviour of natural and engineered systems including treatment for contaminated groundwater, CO_2 storage in deep geological formations, CO_2 enhance oil recovery in carbonate reservoirs and also at clay/cement interfaces in high level nuclear waste repositories. In fact, porosity changes are being actively investigated in connection with deep geological disposal of nuclear waste where chemically very different materials such as clays and concretes come into contact with one another (Gaucher and Blanc, 2006).

Reactive transport models are tools that help to understand natural systems as a whole, and to quantify the fate of contaminants as a function of multiple interdependent reactions. Since its inception a few decades ago, the field of reactive transport in the geosciences has evolved to allow for more realistic numerical representations of the complex couplings that exist in nature among physical, chemical and biological processes. Reactive transport modelling aims at a comprehensive, quantitative, and ultimately predictive treatment of chemical transformations and mass transfers within the earth system. It has had a significant impact on the treatment of contaminant retardation in the subsurface, the description of elemental and nutrient fluxed between major earth reservoirs, and in the treatment of deep earth processes (Steefel et al., 2005). Applications of reactive transport models include geothermal systems (Alt-Epping et al. 2013a; 2013b; Wanner et al., 2014; Diamond and Alt-Epping, 2014), nuclear waste repositories (De Windt et al., 2004, 2007; Samper et al., 2008a,b; Zheng et al., 2010, 2011; Kosakowski and Berner, 2013; Berner et al. 2013; Samper et al., 2016), geological carbon dioxide storage (Gauss et al., 2005; Class et al., 2009; Bildstein et al., 2010) and environmental remediation (Wanner et al., 2012; Jamieson-Hanes et al., 2012; Wanner and Sonnenthal, 2013).

Porosity changes due to dissolution/precipitation reactions and their feedback on transport properties, are accounted for in numerical models by considering empirical formulae. The Kozeny-Carman equation is commonly used to describe the changes in permeability as a function of porosity (Carman, 1937). Archie's law is used to update the tortuosity and the pore diffusion coefficient as a function of the porosity (Archie, 1942). These empirical laws need to be parameterised, either experimentally (e.g., Boving and Grathwohl, 2001; Van Loon et al., 2007; Marica et al., 2011) or by up-scaling from micro-scale models (e.g., Liu et al., 2014; Tyagi et al., 2013). Several computers codes dealing with precipitation dissolution reactions and porosity changes in multidimensional reactive transport problems have been developed in the last decades such as HYTEC (van der Lee and De Windt, 2001; van der Lee et al., 2003: van der Lee, 2005), TOUGHREACT (Xu et al., 2004, 2006, 2011), PHREEQC (Parkhurst and Appelo, 1999), MIN3P (Mayer et al., 2002), PHAST (Parkhurst et al., 2002) and CRUNCH (Steefel, 2001).

The verification of computer codes is commonly conducted by comparing numerical results to analytical solutions. For simulations involving porosity evolution, this is only possible for problems with a limited set of reactions with simplifying assumptions. Only a few analytical solutions for problems coupled with porosity changes are available in the literature (Lagneau and van der Lee, 2010; Hayek et al., 2011; 2012). Lagneau and van der Lee (2010) presented an analytical solution for a one-dimensional system containing a single species and a single mineral. The analytical solution was used to verify the implementation of porosity changes in HYTEC (van der Lee et al., 2003). This solution was only valid for small and moderate porosity changes. Hayek et al. (2011) developed analytical solutions for a 1-D coupled diffusion reaction problem with feedback on porosity changes for benchmarking reactive transport. Analytical solutions describing transport of several aqueous species coupled with precipitation and dissolution of a single mineral in two and three dimensions with porosity changes were proposed by Hayek et al. (2012).

Given the complex nature of realistic reactive transport problems, model verification by means of code intercomparisons through well-defined benchmarks is in many cases the only practical method (Xie et al., 2015). Xie et al. (2015) investigated the implementation of the Kozeny-Carman equation and Archie's law in reactive transport codes and evaluated the porosity changes due to mineral precipitation and dissolution. The results obtained with several reactive transport codes were compared (CrunchFlow, HP1, MIN3P, Pflotran and TOUGHREACT).

A series of reactive transport codes were developed at the University of A Coruña with the generic name of CORE ("*COdes for modelling saturated/unsaturated water flow, heat transport and multi-component REactive solute transport under both local chemical equilibrium and kinetic conditions*"). CORE^{2D}V5 is a code for transient saturated and unsaturated water flow, heat transport and

multicomponent reactive solute transport under both local chemical equilibrium and kinetic conditions in heterogeneous and anisotropic media. It can handle microbial processes and abiotic reactions including acid-base, aqueous complexation, redox, mineral dissolution/precipitation, gas dissolution/exsolution, cation exchange, and surface complexation. The flow and transport equations are solved with Galerkin triangular finite elements and an Euler scheme for time discretization (Samper et al., 2009; 2011). The chemical formulation is based on the ion association theory and uses an extended version of Debye-Hückel equation for the activity coefficients of aqueous species. CORE^{2D}V5 is based on the sequential iteration approach to solve for chemical reactive solute transport. Iterations are repeated until prescribed convergence criteria are attained (Samper et al., 2009). The code has been widely used to model laboratory and in situ experiments (Samper et al., 2008b; Zheng and Samper, 2008; Zheng et al., 2010; 2011), model the interactions of corrosion products and bentonite (Samper et al., 2008a) and evaluate the long-term geochemical evolution of repositories in granite and clay (Samper et al., 2016; Mon et al., 2017).

This appendix presents the improvements implemented in CORE^{2D}V5 to deal with porosity changes due to mineral precipitation and dissolution and update the flow, transport and chemical parameters. The improvements of CORE^{2D}V5 have been verified with analytical solutions for diffusion problems coupled with precipitation-dissolution reactions and feedback of porosity changes in one-dimensional (Hayek et al., 2011) and two-dimensional (Hayek et al., 2012) test cases. In addition, a benchmark has been used to verify the improvements of CORE^{2D}V5 with other codes (Xie et al., 2015).

A2.2. MATHEMATICAL FORMULATION

A2.2.1. Porosity, permeability, pore diffusion coefficients and tortuosity

Mineral dissolution and precipitation reactions can have a significant effect on porosity. Furthermore, changes in porosity lead to changes in flow, transport and chemical parameters. The previous version of CORE^{2D}V5 did not considered porosity changes. The time evolution of the porosity was calculated externally from the computed mineral volume fractions. CORE^{2D}V5 has been extended to take into account porosity changes and update each time step flow, transport and chemical parameters.

Reactive transport codes generally use empirical formulations to take into account porosity changes due to dissolution/precipitation reactions and their feedback on transport parameters. Transport properties of the medium such as effective diffusion coefficients or permeabilities are commonly parameterised as a function of porosity. The Kozeny-Carman relationship (Carman, 1937) is commonly

used to describe the changes in permeability while the Archie´s law (Archie, 1942) is often used to update the pore diffusion coefficient.

The capabilities of CORE^{2D}V5 have been extended to take into account the effects of the changes in porosity caused by mineral dissolution/precipitation. The porosity is updated each time step according to the computed changes in the mineral volume fractions. The porosity of the medium, ϕ, is computed from:

$$\phi = 1 - \sum_{m=1}^{N_p} f_m \tag{2.1}$$

where N_p is the number of minerals and f_m is the volume fraction of the m-th mineral. The porosity is recalculated each time step based on the changes in the mineral volume fractions. The porosity is not allowed to be less than a prescribed threshold.

The changes in the permeability in the updated version of CORE^{2D} are calculated from the Kozeny-Carman relation (Carman, 1937). The permeability, k, is related to porosity, ϕ, through:

$$k = k_0 \frac{(1-\phi_0)^2}{(1-\phi)^2}\left(\frac{\phi}{\phi_0}\right)^3 \tag{2.2}$$

where k_0 is the initial or reference permeability and ϕ_0 is the initial or reference porosity.

The pore diffusion coefficients in the revised version of the code are updated based on Archie's law (Archie, 1942) which describes the ratio between the effective diffusivity of a dissolved species in a porous medium and the diffusion coefficient of such species in pure water. This ratio is a function of the tortuosity of the material and its constrictivity, which in turn depend on porosity. Since the tortuosity and the constrictivity are difficult to measure experimentally, their ratio is often described with a geometrical factor. The relationship can be written as follows:

$$\frac{D_e}{D_0} = \frac{\delta}{\tau} = \phi^m \tag{2.3}$$

where D_0 is the pore diffusion coefficient in pure water, D_e is the effective diffusion coefficient, τ is the tortuosity, δ is the constrictivity and m is the cementation factor.

The dispersion coefficient, D, in CORE^{2D}V5 can be defined in the following ways:

1) In terms of the molecular diffusion in pure water, D_0:

$$\theta D = \tau^* D_0 \theta + \alpha|q| \tag{2.4}$$

where τ^* is a tortuosity factor, D_0 is the molecular diffusion in pure water, θ is the water content (or porosity in a saturated porous medium), α is the dispersivity and $|q|$ is the modulus of the Darcy velocity.

2) In terms of the effective molecular diffusion, D_e:

$$\theta D = D_e + \alpha|q| \tag{2.5}$$

3) In terms of the apparent diffusion coefficient, D_a,

$$\theta D = \theta D_a R + \alpha|q| \tag{2.6}$$

where R is the retardation coefficient factor.

CORE^{2D}V5 provides the following options for the tortuosity factor τ^* in Equation 2.4:

1) Constant tortuosity.

2) Tortuosity τ^* depending on water content and porosity (Simunek and Suares, 1993):

$$\tau^* = \frac{\theta^{7/3}}{\phi^2} \tag{2.7}$$

3) Tortuosity factor τ^* in terms of the cementation factor, m (Marsily, 1986):

$$D_e = \frac{D_0}{\phi\ \tau^*} = \frac{D_0}{\phi^{-m}} \tag{2.8}$$

where m is the cementation factor (Dullien, 1979) which ranges from 1.3 to 2.5.

The pore diffusion coefficients, D_0 and D_e, and the tortuosity, τ^*, are updated each time step from the water content and porosity computed in the previous time step (t). In the following time step ($t+1$), the pore diffusion coefficients and the tortuosity are updated.

A2.2.2. Kinetics of dissolution-precipitation and specific surface

The general kinetic rate expression of mineral dissolution/precipitation used in CORE^{2D}V5 is given by:

$$r_m = s_m e^{\frac{-Ea}{RT}} \sum_{K=1}^{N_K} k_{mk} \prod_{i=1}^{N_C+N_X} a_i^{p_{mki}} \left(\Omega_m^{\theta_{mk}} - 1\right)^{\eta_{mk}} \tag{2.9}$$

where r_m is the dissolution/precipitation rate (mol/m^2/s); s_m is a function which can take a value of 1 or -1 depending on the saturation index (it is equal to 1 for dissolution and -1 for precipitation); Ω_m is the ratio between the ionic activity products and the equilibrium constant; $e^{-Eam/RT}$ is a thermodynamic factor which takes into account the apparent activation energy of overall reaction process *Ea* (KJ/mol), the gas constant *R (KJ/mol·K)* and the absolute temperature *T (K)*; N_K is the kinetic reaction number for the *m*-th mineral; k_{mk} is the kinetics rate constant of the *k*-th kinetic reaction of the *m*-th mineral (mol/m^2/s), a^{pmki} is a factor which accounts for the catalytic effect of some species and the exponent p^{mki} is a dimensionless parameter for the *i*-th aqueous species of the *m*-th mineral in the *k*-th kinetic reaction; N_C is the number of primary species; N_X is the number of secondary species and θ_{mk} and η_{mk} are parameters of the *k*-th kinetics reaction for the *m*-th mineral which are usually determined by experiments.

The sink/source term r_i (mol/m^3/s) for the *i*-th primary aqueous species associated kinetically-controlled to mineral dissolution/precipitation reactions is given by:

$$r_i = \sum_{m=1}^{N_p} v_{mi}^p r_m A_m \tag{2.10}$$

where r_m is the *m*-th mineral dissolution/precipitation rate (mol/m^2/s), v^p_{mi} is the stoichiometric coefficient of the *i*-th species in the *m*-th mineral, N_p is the number of minerals and A_m is the specific surface of the *m*-th mineral (expressed as the surface of mineral per unit volume of water).

The specific surface of the mineral in the extended version of CORE^{2D}V5 is updated each time step according to:

$$A_m^{t+1} = A_m^t \frac{\phi^t}{\phi^{t+1}} \tag{2.11}$$

where $A_m{}^{t+1}$ and $A_m{}^t$ are the specific surfaces of the *m*-th mineral at times *t+1* and *t*, respectively, and ϕ^{t+1} and ϕ^t are the porosities corresponding times *t+1* and *t*, respectively.

A2.3. EXTENDING CORE^{2D}V5 TO DEAL WITH POROSITY CHANGES

CORE^{2D}V5 has been extended to compute the porosity changes due to the mineral dissolution/precipitation and update the flow, transport and chemical parameters. Variable *IMINE* allows for the option to account for porosity changes over time. *IMINE* allows also for the calculations with constant porosity (as in the previous version of the code). The extended version of CORE^{2D} has been verified with 1-D and 2-D test cases.

In CORE^{2D}V5 some input parameters are associated to elements while others are defined nodewise. Porosity is an elementwise input parameter. Since the chemical equations are solved nodewise, the porosity has been defined nodewise in the extended version of CORE^{2D}. In this way, the porosity and the mineral volume fractions are input parameters associated to nodes. The code checks that the sum of the porosity and the mineral volume fractions is equal to 1 in all the nodes of the grid. If this condition is not met, it is not possible to use Equation 2.1 to update the porosity each time step.

Two additional input parameters, *"phifac"* and *"pormin"*, are used in the updated version of CORE^{2D}V5. *"Phifac"* is a factor which is multiplied by the porosity to calculate the accessible porosity associated to the nodes of the mesh. *"Pormin"* is the minimum threshold porosity for clogging. If the porosity of a node reaches the minimum porosity, no further mineral precipitation is allowed in such node.

The groundwater flow equation in CORE^{2D}V5 for saturated media is solved in terms of hydraulic heads. In the revised version of the code, the permeability is updated in the flow equation each time step according to the Kozeny-Carman relationship (Equation 2.2). The equation for steady-state flow is solved once only at the first time step when the porosity changes are not considered. When porosity changes are considered, however, the flow equation is solved each time step. An additional output file, *"OUTK.out",* is created to print out the changes in the hydraulic conductivity over time. This file contains the hydraulic conductivity of the elements of the grid for selected time steps. Nodal water volumes of the finite element mesh are updated with the most recent values of the porosities after solving the flow equations.

Groundwater velocities are needed to evaluate advective and dispersive solute and heat fluxes. They are computed from nodal heads by direct application of Darcy's Law to the finite element solution. In the revised version of the code, water velocities are updated every time step because the hydraulic conductivities may change with time.

Pore diffusion coefficients and tortuosity are updated because these parameters depend on porosity according to Archie's law (Equation 2.3). The updated values of the diffusion coefficients are printed out in the file *"OUTDIFF.out"*. This file contains the values of the diffusion coefficients in all elements of the grid for each selected time step.

CORE^{2D}V5 considers the followings chemical reactions: acid-base, aqueous complexation, redox, mineral dissolution/precipitation, gas dissolution/exsolution, cation exchanges and adsorption. Hydrochemical reactions are solved in a nodewise manner. Chemical equilibrium equations are solved with a Newton-Raphson method. Once the concentrations of primary species are obtained, the concentrations of secondary species, the amount of minerals dissolved or precipitated and the

concentration of sorbed and exchanged species are computed in a straightforward manner. The concentrations of dissolved species are calculated in mol per unit volume of water. When the porosity changes, the concentrations have to be updated each time step (*t*). For that purpose, it is necessary to store the values of the nodal water volumes at the previous time step (*t-1*). The updated concentration at time *t*, *c(t)*, is obtained from the concentration at the previous time step, *c(t-1)*, through:

$$c(t) = c(t-1)\frac{V_n(t-1)}{V_n(t)} \tag{2.12}$$

where $V_n(t\text{-}1)$ and $V_n(t)$ are the nodal water volumes at the previous and the current time steps, respectively.

Mineral dissolution/precipitation reactions in CORE^{2D}V5 can be either at local equilibrium or kinetically controlled. Minerals are not allowed to precipitate anymore when the porosity is smaller than a threshold porosity (*"pormin"*). CORE^{2D}V5 has been modified to account for the threshold porosity.

Mineral specific surface is a parameter which is defined as the surface of a mineral per unit volume of water. Minerals specific surfaces are updated each time step according to Equation 2.11. The computed nodal mineral specific surfaces over time are printed out in the output file, *"OUTAREAM.out"*.

Each time step, the porosity is updated according to Equation 2.1. The computed porosity values are printed out in the output files *"OUTPOX.out"* and *"OUTPOT.out"*. File *"OUTPOX.out"* contains the nodal values of the porosity. File *"OUTPOT.out"* contains the time evolution of the porosity in selected nodes.

CORE^{2D}V5 allows for a restart option. The restart option allows to restart the simulation at the time a run was stopped by modifying some parameters such as the maximum number of iterations and the number of time steps in a time period. Poorly-convergent problems can be solved without having to start the run from the beginning. The restart option has been modified in the revised version of CORE^{2D} to take into account the porosity changes. The porosities in the current time step and the porosities in the previous time step are printed and saved in an appropriate manner. The restart option clearly improves the overall efficiency of numerical modelling for complex problems.

Figure A2.1 shows the main flowchart of CORE^{2D}V5 with an indication of the main modifications performed in the code to take into account porosity changes and the update of the flow, transport and chemical parameters.

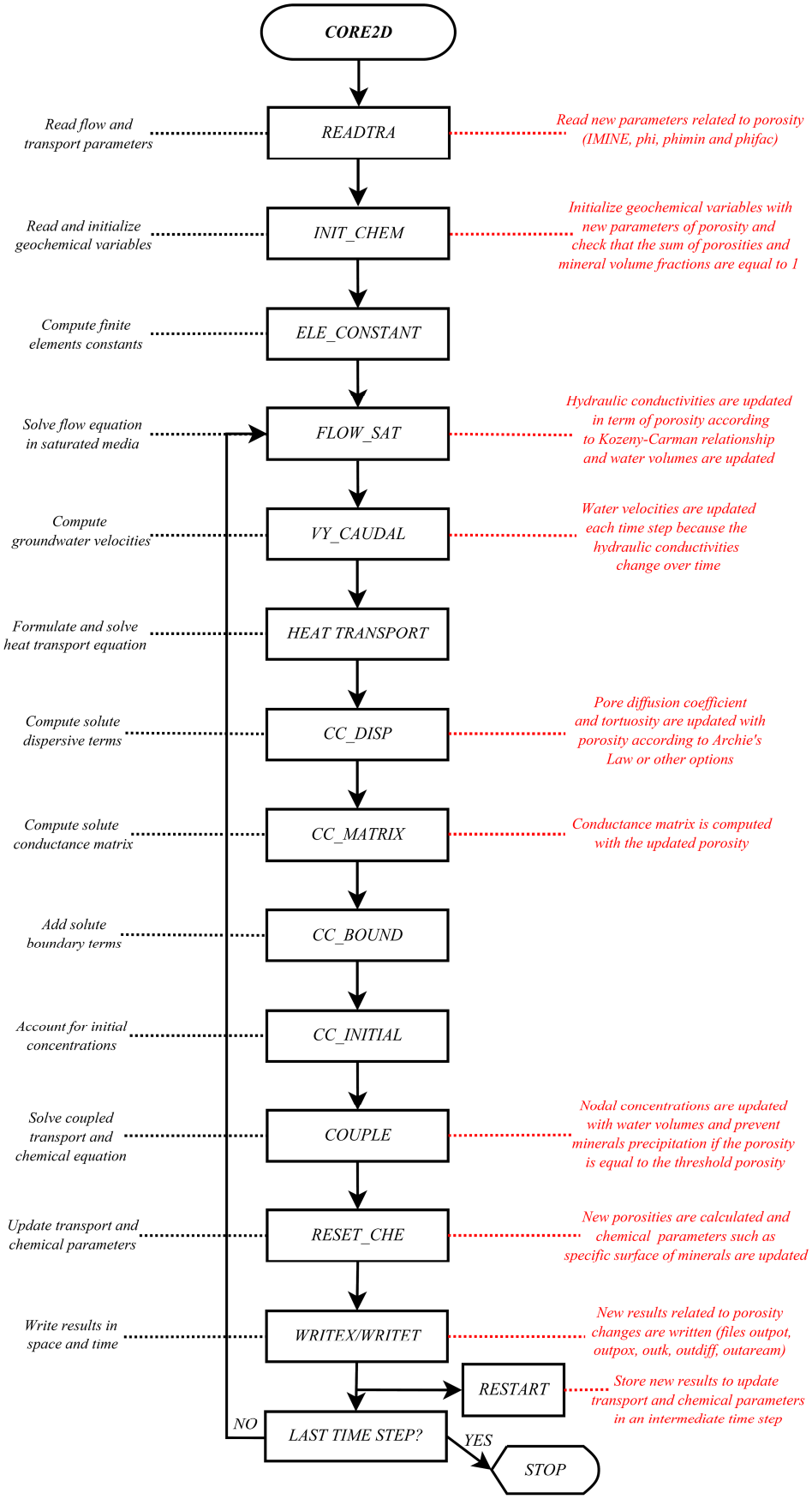

Figure A2.1. Main flowchart of CORE^{2D}V5. Red text shows the main modifications performed in the code to take into account porosity changes and update the flow and transport and chemical parameters.

A2.4. VERIFICATION

The improvements implemented in CORE^{2D}V5 to take into account porosity changes and update flow, transport and chemical parameters have been verified with analytical solutions for diffusion problems coupled with precipitation-dissolution reactions and feedback of porosity change in one-dimension (Hayek et al., 2011) and two-dimensions (Hayek et al., 2012). In addition, a benchmark test case has been used to verify the revised version of the code with other reactive transport codes (CrunchFlow, HP1, MIN3P, Pflotran and TOUGHREACT) (Xie et al., 2015). This benchmark considers advective-dispersive transport in saturated media with aqueous complexation and kinetically-controlled mineral dissolution/precipitation leading to porosity changes.

A2.4.1. Verification with a 1-D analytical solution

The improvements implemented in CORE^{2D}V5 have been verified with the analytical solution reported by Hayek et al. (2011). They presented an analytical solution for 1-D diffusion problem coupled with a precipitation-dissolution reaction with a strong feedback of porosity change for a system of two aqueous species where the concentration of one species if fixed in time. In addition, they also presented two 1-D systems involving transport of a solute through a saturated porous column. These cases were run with the improved version of CORE^{2D}. The numerical results were compared with the analytical solutions.

The analytical solution correspond to a porous column consisting of a reactive mineral phase $M_{(s)}$ in equilibrium with two aqueous species $A_{(aq)}$ and $B_{(aq)}$. The only chemical reaction taking place in the system is:

$$A_{(aq)} + B_{(aq)} \leftrightarrow M_{(s)} \tag{2.13}$$

The concentration of the species *B* is assumed fixed in space and maintained constant throughout the simulation time. Mathematically, the concentration profile of species *B* is defined by a prescribed function *f(x)*. The problem involves only diffusive transport.

The dissolution/precipitation of mineral $M_{(s)}$ is simulated with the following kinetic law:

$$\frac{\partial(\phi P)}{\partial t} = -r_m A_m \left[1 - \frac{f(x)c}{K}\right] \tag{2.14}$$

where ϕ is the porosity, P denotes the concentration of the mineral phase, c is the concentration of the species A, $f(x)$ is the concentration of the species B, K is the solubility constant of the mineral, r_m is the kinetic rate constant, A_m is the reactive surface area of the solid and t is the time.

The general kinetic rate expression of mineral dissolution/precipitation used in CORE^{2D}V5 (Equation 2.9) was modified to be similar to the Equation 2.14. The dissolution/precipitation rate depends on the product $f(x)c$.

The boundary conditions of the problem are given by:

$$c(0,t) = c_0(t) \qquad t > 0 \tag{2.15}$$

$$c(L,t) = c_L(t) \qquad t > 0 \tag{2.16}$$

where L is the length of the porous column, $c_0(t)$ and $c_L(t)$ are prescribed time functions for the concentrations at the boundaries.

The initial solute concentration, c, the porosity, ϕ, and the mineral concentration, P, are given by:

$$c(x,0) = c_i(x) \qquad x \in [0,L] \tag{2.17}$$

$$\phi(x,0) = \phi_0(x) \qquad x \in [0,L] \tag{2.18}$$

$$P(x,0) = P_0(x) \qquad x \in [0,L] \tag{2.19}$$

where $c_i(x)$, $\phi_0(x)$ and $P_0(x)$ are known functions of x.

The verification of the revised version of CORE^{2D} has been performed for two one-dimensional test cases. The first test case deals with mineral precipitation, which leads to a porosity decrease. In this case, clogging is reached and the aqueous phase vanishes. The second test case involves mineral dissolution which leads to an increase in porosity.

A2.4.1.1. 1-D model with mineral precipitation

In order to simplify the analytical solution, the concentration of species B, $f(x)$, is fixed in space and maintained constant in time. In this case, $f(x)$ is constant and equal to 1. Therefore, mineral precipitation occurs only when the concentration of species A, $c(x,t)$, is larger than the solubility constant of the mineral (K) (see Equation 2.14). The initial concentration of species A is given by:

$$c_i(x) = c(x,0) = \frac{1}{V_m} + \alpha^* \exp\left(-\frac{\lambda^* x}{D_0 C_1}\right) \tag{2.20}$$

where V_m denotes the mineral molar volume, D_0 is the pore diffusion coefficient and C_1, α^* and λ^* are constants which are derived after imposing the initial and boundary conditions.

The analytical solution of the solute concentration of species *A* is given by:

$$c(x,t) = \frac{1}{V_m} + \left[c_i(x) - \frac{1}{V_m}\right] \exp\left(\frac{(\lambda^*)^2 t}{D_0 {C_1}^2}\right) \tag{2.21}$$

The porosity is equal to:

$$\begin{aligned} \phi(x,t) = {} & \Phi_1 exp\left\{\frac{r_m A_0 [f(x) - KV_m](C_1 x - \lambda^* t + C_1 x_0 - \xi_1)}{\lambda^* K}\right\} \\ & \cdot exp\left(\frac{r_m A_0 D_0 {C_1}^2 f(x)[1 - V_m c_i(x)]}{(\lambda^*)^2 K}\left\{exp\left(\frac{(\lambda^*)^2 t}{D_0 {C_1}^2}\right)\right.\right. \\ & \left.\left. - exp\left[\frac{\lambda^*(C_1 x + C_1 x_0 - \xi_1)}{D_0 {C_1}^2}\right]\right\}\right) \end{aligned} \tag{2.22}$$

where Φ_1 and ξ_1 are arbitrary constants, A_0 is a constant representing the specific surface area ($A = A_0\phi$) and x_0 is an integration constant.

The analytical solution of the mineral concentration is given by:

$$\begin{aligned} P(x,t) = {} & \frac{1}{\Phi_1 V_m} exp\left\{\frac{r_m A_0 [KV_m - f(x)](C_1 x - \lambda^* t + C_1 x_0 - \xi_1)}{\lambda^* K}\right\} \\ & \cdot exp\left(\frac{r_m A_0 D_0 {C_1}^2 f(x)[V_m c_i(x) - 1]}{(\lambda^*)^2 K}\left\{exp\left(\frac{(\lambda^*)^2 t}{D_0 {C_1}^2}\right)\right.\right. \\ & \left.\left. - exp\left[\frac{\lambda^*(C_1 x + C_1 x_0 - \xi_1)}{D_0 {C_1}^2}\right]\right\}\right) - \frac{1}{V_m} \end{aligned} \tag{2.23}$$

The 1-D model with mineral precipitation was performed with the updated version of CORE^{2D}. The numerical results of solute concentrations, porosity and mineral concentrations were compared with analytical solutions (Equations 2.21, 2.22 and 2.23). The domain of the model has a length *L* equal to 0.05 m and it was discretized with a regular 1-D finite element grid with 50 elements and 51 nodes and grid spacing equal to 10^{-3} m.

The initial porosity and the initial concentration of species *A* in the model are not constants. Each node of the grid has a different initial value. For this reason, it was necessary to define 51 different mineral zones and 51 initial waters in the numerical model.

The numerical model was run for a total period of 10^5 s with 100 time increments of a second. The analytical and the numerical solutions were compared for $2 \cdot 10^4$, $4 \cdot 10^4$, $6 \cdot 10^4$, $8 \cdot 10^4$ and 10^5 s.

Model parameters are listed in Table A2.1. The molar volume is equal to 1, which is highly unrealistic. However, this value does not prevent the use of this test case to verify the updated version of the reactive transport code.

Table A2.1. Parameters of the one-dimensional mineral precipitation verification case.

Parameter	***Value***
D_0 (m^2/s)	10^{-9}
Φ_1	0.2
log(K)	-0.16
r_m ($mol/m^2/s$)	10^{-10}
V_m (m^3/mol)	1
A_0 (m^2/m^3)	$5 \cdot 10^3$
C_1	1
α^*	10
λ^*	$2 \cdot 10^{-7}$
x_0	0
ξ_1	0

The concentration of the species *B, f(x)*, is fixed in the time and maintained constant throughout the simulation time. In this case, *f(x)* is constant and equal to 1. In CORE^{2D}V5, the concentration of a species can be fixed in a node by defining a boundary condition in such node. 51 boundary solutions were defined one per node. The concentration of species *B* was fixed in the time by using a time function associated to the boundary. However, in CORE^{2D}V5, the type of boundary condition is the same for all the species of the chemical system. For this reason, it is not possible to fix in time and space the concentration of species *B* without fixing also the concentration of species *A*. The concentration of species *A* is fixed only at the boundaries of the model (x = 0 and x = 0.05 m), but this is not possible in CORE^{2D}V5. The concentration of species *A* and *B* were fixed in all the nodes of the grid with 51 time functions (one per node).

In spite of the above, a run was performed by fixing the concentrations of species *A* and *B* only at the boundaries of the model (x = 0 and x = 0.05 m). The disadvantage of this run is that the concentration of species *B* is not constant in the internal nodes of the model. Nevertheless, the concentrations of species *A* computed with the numerical model in this run are very similar to those calculated analytically (Equation 2.21). Figure A2.2 shows the comparison of the analytical and numerical solutions of the concentrations profiles of species *A* for several times. The solute concentration increases with time at the left boundary and remains constant at the right boundary. Numerical and analytical solutions generally agree. There are only small differences in the

concentrations calculated from $x = 0$ to $x = 0.01$ m at time $t = 10^5$ s. These small differences are probably due to the fact that the concentration of species *B* in the numerical solution is not constant in the internal nodes.

Although good numerical results were obtained in the run without fixing the concentration of species *B* in all nodes of the grid, it was decided to perform an additional run by fixing the concentration of the two species. In this way, the verification of the code is more realistic.

Figure A2.3 shows the comparison of the computed porosity profiles with the analytical porosity profiles. The porosity was calculated analytically with the Equation 2.22. Numerical and analytical solutions agree completely. The porosity decreases significantly with time at the left boundary whereas a minor decrease of porosity is observed at the right boundary. The porosity near the left boundary of the model reaches very small values (near clogging). In fact, the minimum porosity considered in the numerical model for this case was equal to 10^{-3}. The porosity decreases to this value in the first three nodes of the grid at time $t = 10^5$ s.

Figure A2.4 shows the comparison of the computed mineral concentration (in mol/m^3) with the analytical solution (Equation 2.23). The results computed with the updated version of CORE^{2D} agree with the analytical solution. The precipitation of the mineral occurs at the left boundary of the domain. The concentration of the mineral (in mol/m^3 of fluid) near the left boundary reaches very high values because this concentration increases when the porosity decreases. Figure A2.5 shows the comparison of the computed concentration of the mineral (in mol/m^3 of rock) and the analytical solution. Numerical and analytical solution show a very good agreement. The concentration of the mineral tends to a constant value when the porosity goes to zero.

To illustrate the relevance of the changes in porosity, an additional run was performed in which the feedback effects of the changes in porosity were not taken into account. The porosity and the mineral concentrations were computed with the previous version of CORE^{2D}. Figure A2.6 shows the comparison of the porosity profiles computed with and without considering the feedback effect of porosity changes. The porosity profiles calculated with and without feedback effect are very different and the differences increase with time. The porosity decreases more quickly in the run without the feedback effect. The clogging is also more important in the run without the feedback effect. Figure A2.7 shows the comparison of the mineral concentration profiles (in mol/m^3 of fluid) computed with CORE^{2D} with and without the feedback effect. The mineral concentration profiles computed with and without the feedback effect are different because the porosity is not updated when the feedback effect is not considered. Figure A2.6 and Figure A2.7 show that the improvements implemented in CORE^{2D} are very relevant in problems with mineral dissolution/precipitation leading to strong porosity changes.

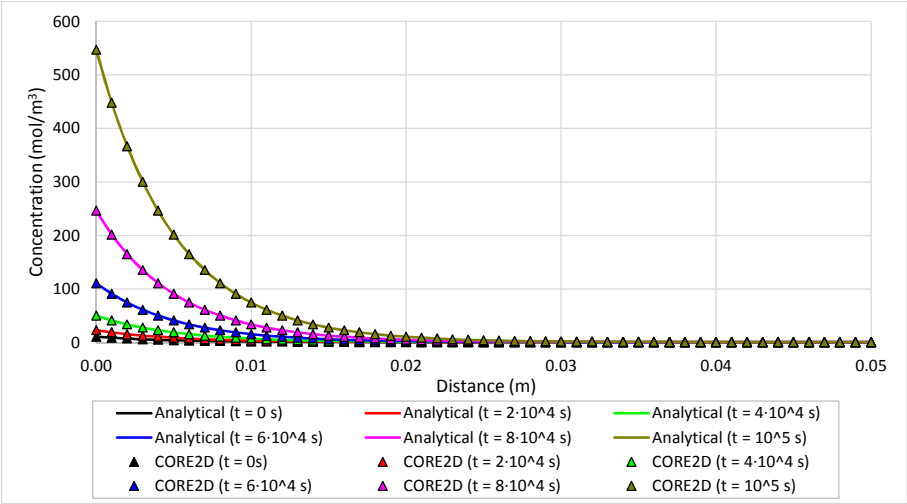

Figure A2.2. Comparison of the numerical and analytical solutions of the concentrations of species *A* for selected times for the case of mineral precipitation.

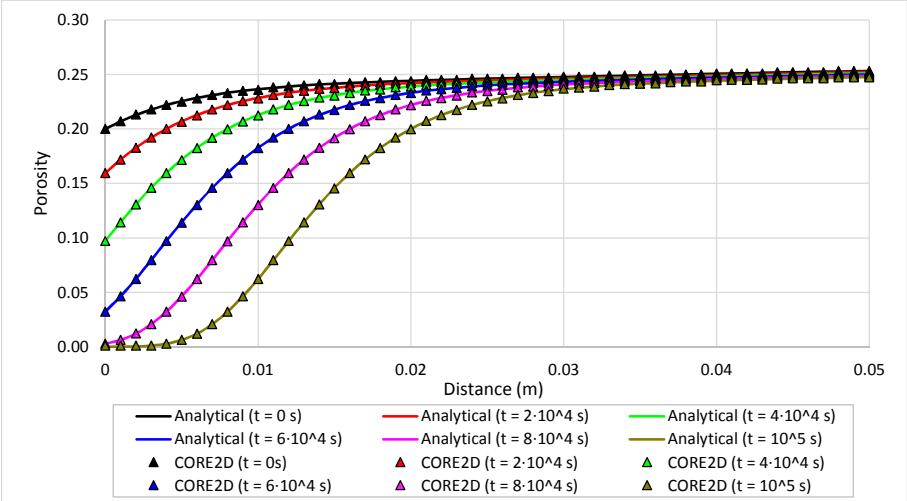

Figure A2.3. Comparison of the computed porosity profiles with the analytical solution at selected times for the case of mineral precipitation.

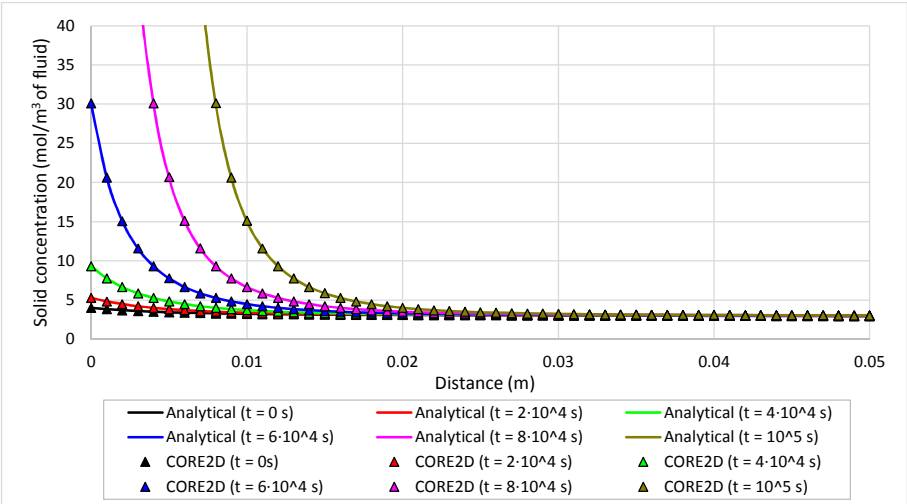

Figure A2.4. Comparison of the mineral concentration profiles (in mol/m^3 of fluid) computed with the numerical and the analytical solutions for selected times for the case of mineral precipitation.

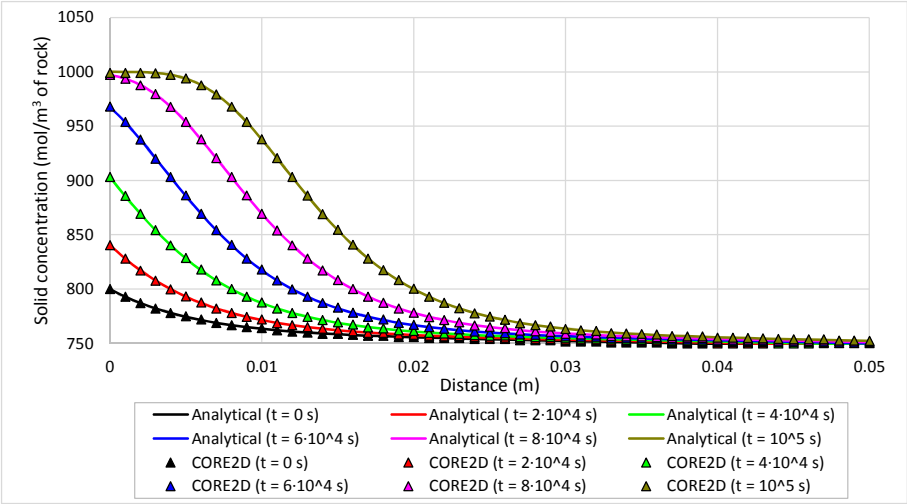

Figure A2.5. Comparison of the mineral concentration profiles (mol/m^3 of rock) computed with the numerical and analytical solutions for selected times for the case of mineral precipitation.

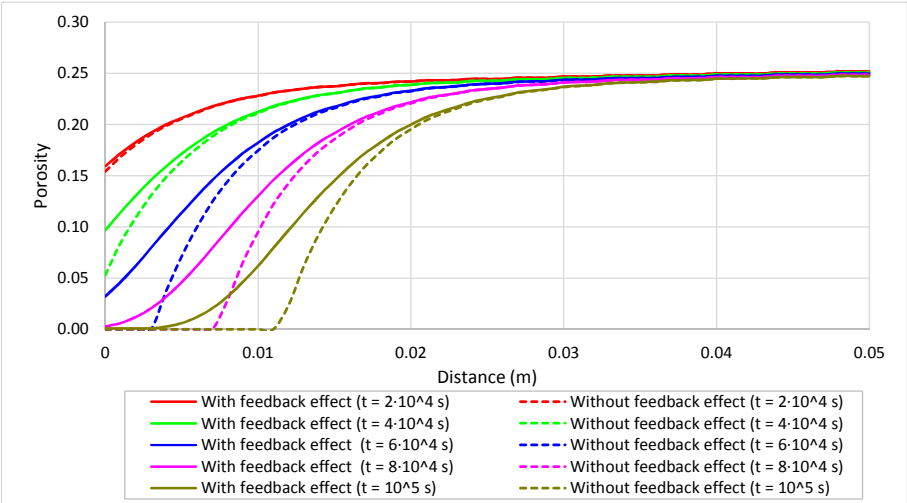

Figure A2.6. Comparison of the computed porosity profiles with and without the feedback effect of the changes in porosity for the case of mineral precipitation.

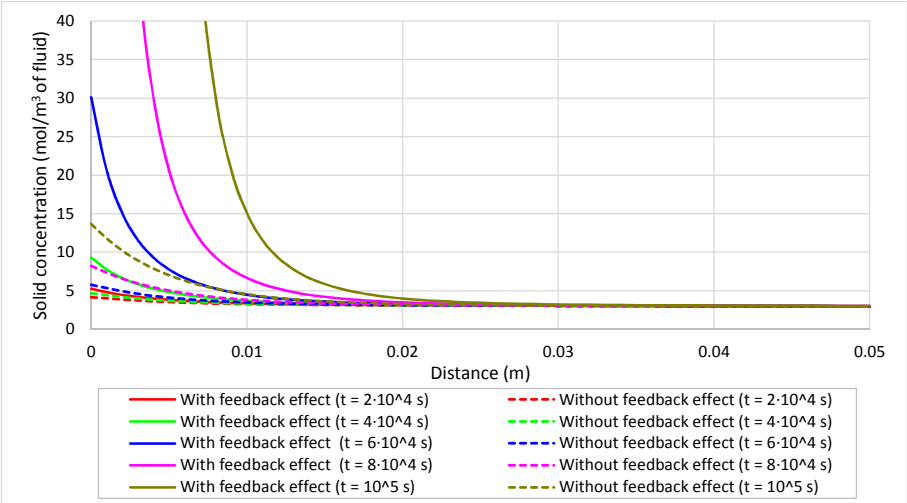

Figure A2.7. Comparison of the computed mineral concentration profiles (in mol/m^3 of fluid) with and without the feedback effect of the changes in porosity for the case of mineral precipitation.

A2.4.1.2. 1-D model with mineral dissolution

This case involves a single mineral which dissolves and then the porosity increases. The initial concentration of species *A* is given by:

$$c_i(x) = \theta^* \exp(-\alpha^* x) \tag{2.24}$$

The concentration of species *B*, *f(x)*, is prescribed and remains constant. Its spatial distribution is given by:

$$f(x) = \frac{\beta^*}{1 + exp[\gamma^*(x - \mu^*)]} \tag{2.25}$$

where are α^*, β^*, γ^*, θ^* and μ^* are arbitrary constants.

The analytical solution of the solute concentration of species *A* is given by:

$$c(x,t) = \frac{K[V_m c_i(x) - 1] - [f(x)c_i(x) - K]exp\left\{-\frac{r_m A_0[f(x) - KV_m]t}{K}\right\}}{f(x)[V_m c_i(x) - 1] - V_m[f(x)c_i(x) - K]exp\left\{-\frac{r_m A_0[f(x) - KV_m]t}{K}\right\}} \tag{2.26}$$

The analytical solution of the porosity is given by:

$$\phi(x,t) = \Phi_1 \left| \frac{f(x)[V_m c_i(x) - 1] - V_m[f(x)c_i(x) - K]exp\left\{-\frac{r_m A_0[f(x) - KV_m]t}{K}\right\}}{f(x)[V_m c_i(x) - 1] - V_m[f(x)c_i(x) - K]exp\left\{-\frac{r_m A_0[f(x) - KV_m](\xi_1 - x_0)}{\lambda^* K}\right\}} \right| \tag{2.27}$$

The analytical solution of the mineral concentration is given by:

$$P(x,t) = \frac{1}{\Phi_1 V_m} \left| \frac{f(x)[V_m c_i(x) - 1] - V_m[f(x)c_i(x) - K]exp\left\{-\frac{r_m A_0[f(x) - KV_m](\xi_1 - x_0)}{\lambda^* K}\right\}}{f(x)[V_m c_i(x) - 1] - V_m[f(x)c_i(x) - K]exp\left\{-\frac{r_m A_0[f(x) - KV_m]t}{K}\right\}} \right| - \frac{1}{V_m} \tag{2.28}$$

The 1-D model with mineral dissolution was performed with the updated version of CORE^{2D}. The computed solute concentrations, porosities and mineral concentrations were compared with the analytical solutions of Equations 2.26, 2.27 and 2.28. The length of the domain *L* is equal to 0.05 m. The model was solved with the same finite element mesh used in the previous case with mineral precipitation. Each node of the grid has a different initial concentration of species *A*. For this reason, it was necessary to define 51 initial waters in the numerical model. The values of the model parameters are listed in Table A2.2.

The reactive transport model was performed for 10^4 s. The time domain was divided into 10^2 time periods. Each time period was subdivided into 100 time increments. The analytical and numerical solutions were compared at $t = 2 \cdot 10^3$, $4 \cdot 10^3$, $6 \cdot 10^3$, $8 \cdot 10^3$ and 10^4 s.

Table A2.2. Model parameters of the one-dimensional model with mineral dissolution.

Parameter	***Value***
D_0 (m^2/s)	10^{-11}
Φ_1	0.5
log(K)	-10.05
r_m ($mol/m^2/s$)	$6 \cdot 10^{-10}$
V_m (m^3/mol)	1
A_0 (m^2/m^3)	$3 \cdot 10^4$
α^*	10^3
β^*	0.1
μ^*	10^{-2}
γ^*	$-5 \cdot 10^{-3}$
θ^*	0.2
x_0	0
ξ_1	0

The concentration of species *B* is simulated with 51 different boundary solutions associated to the 51 nodes of the grid. The concentration of species *A* is also fixed with 51 time functions (one per node). Figure A2.8 shows the analytical and numerical concentration profiles of species *A* for selected times. The analytical solution of the solute concentration of species *A* was calculated with Equation 2.26. The function *f(x)* is also plotted in Figure A2.8. The function *f(x)* has very low values at the left side of the domain. The concentration of species *B* at $x = 0.01$ m increases to 0.1 mol/m^3.

Figure A2.9 shows the comparison of the porosity profiles computed with the numerical and analytical solutions for selected times. The porosity was calculated analytically with the Equation 2.27. The numerical solution matches the analytical solution. There is a 5 mm wide region near the left boundary where the porosity increases with time. The porosity remains constant and equal to 0.5 in the rest of the model domain. Figure A2.10 shows the time evolution of the mineral concentration in mol/m^3 of fluid computed with the analytical (Equation 2.28) and numerical solutions for selected times. The numerical results computed with the updated version of CORE^{2D} reproduce the analytical solution. The mineral concentration decreases with time reaching a minimum value of 0.67 mol/m^3 at $t = 10^4$ s.

To illustrate the relevance of the feedback effect of the changes of the porosity on the model results, an additional run was performed by neglecting the changes in porosity. Porosity and mineral

concentrations were computed with the previous version of the CORE^{2D}. Figure A2.11 shows the comparison of the porosity profiles computed with and without the feedback effect. In the run without the feedback effect, the time evolution of the porosity was calculated from the changes of the mineral volume fractions. The porosity increases more quickly in the run without the feedback effect. The differences between the porosities computed with and without the feedback effect increase with time. Figure A2.12 shows the comparison of the mineral concentration profiles (in mol/m^3 of fluid) computed with CORE^{2D} with and without the changes in porosity. There are important differences between the mineral concentrations computed with and without the feedback effect. These differences increase with time.

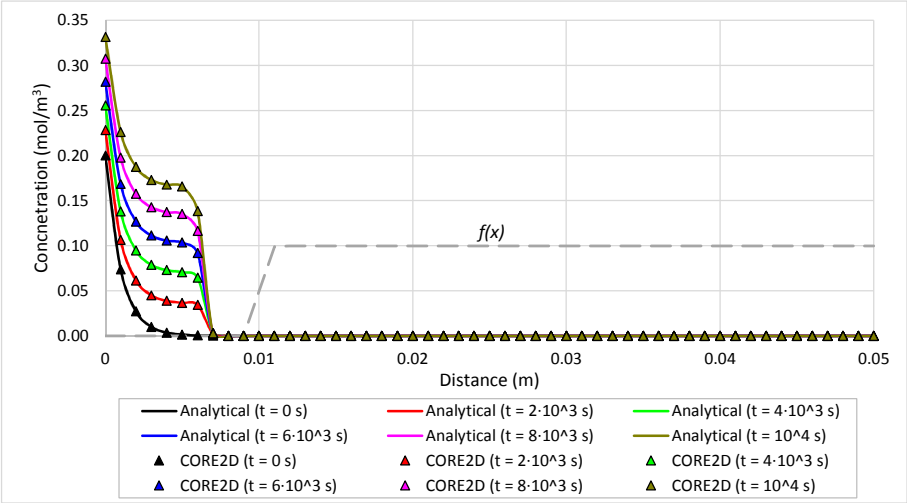

Figure A2.8. Comparison of the concentration profiles of species *A* computed with the numerical and analytical solutions for selected times for the case of mineral dissolution. The dashed line shows the concentration profile of species *B*, *f(x)* which remains constant.

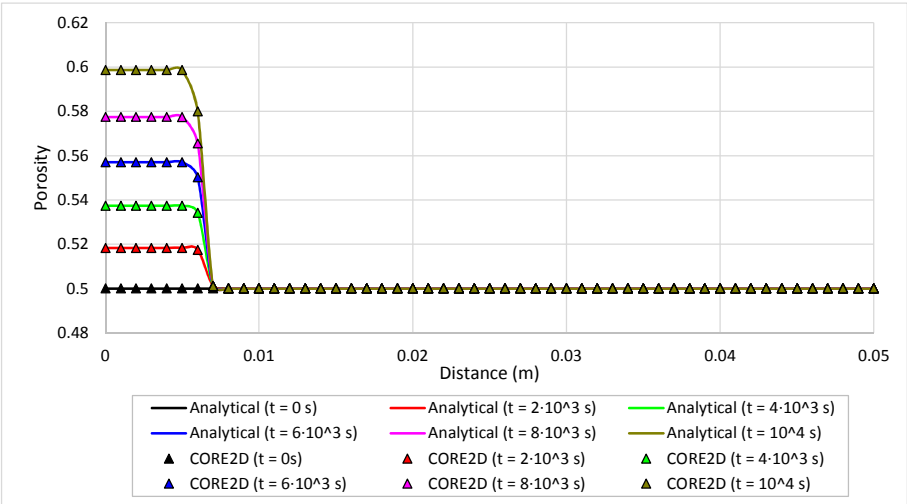

Figure A2.9. Comparison of the porosity profiles computed with the numerical and analytical solutions for selected times for the case of mineral dissolution.

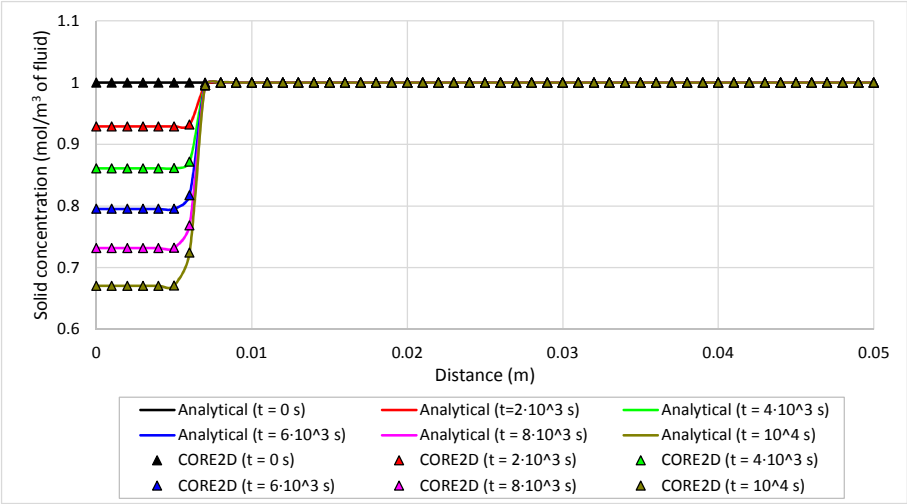

Figure A2.10. Comparison of the mineral concentration profiles (in mol/m^3 of fluid) computed with the numerical and analytical solutions for selected times for the case of mineral dissolution.

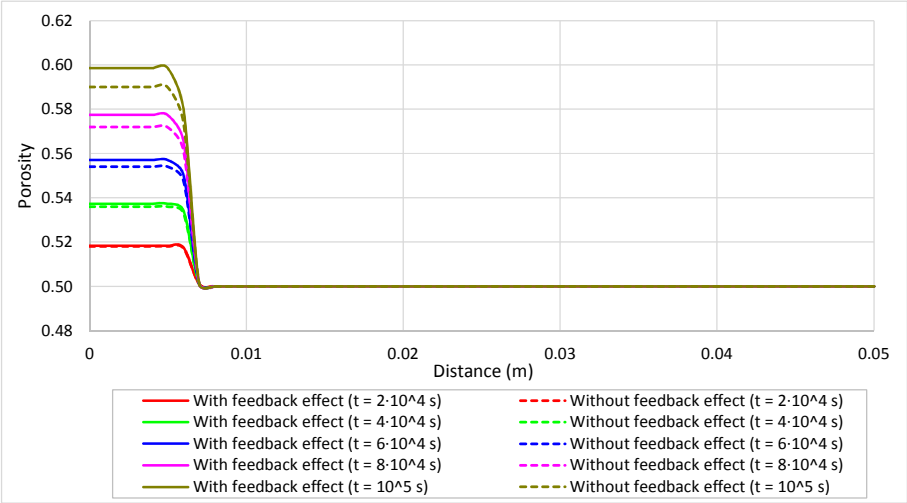

Figure A2.11. Comparison of the numerical porosity profiles computed with CORE^{2D} with and without the feedback effect of the changes in porosity for selected times for the case of mineral dissolution.

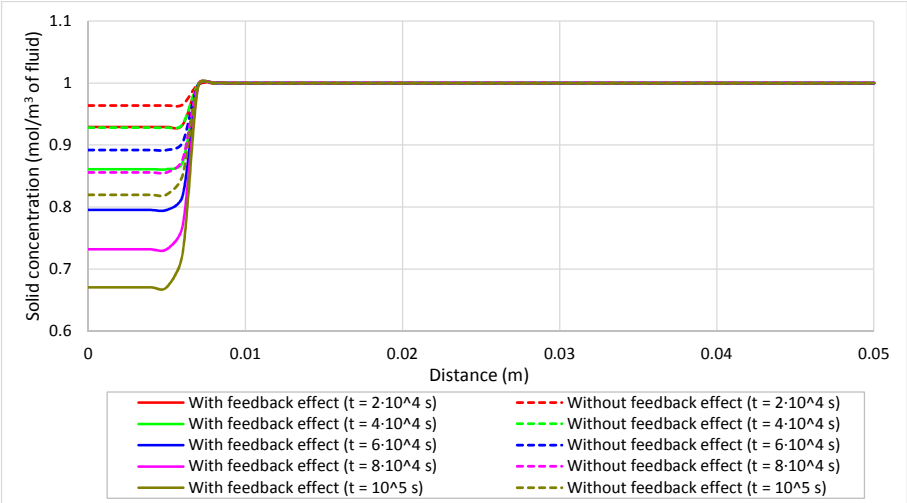

Figure A2.12. Comparison of the computed mineral concentration profiles (in mol/m^3 of fluid) with and without the feedback effect of the changes in porosity for selected times for the case of mineral dissolution.

A2.4.2. Verification with a 2-D analytical solution

The improvements implemented in CORE^{2D}V5 for two-dimensional saturated problems have been verified with an exact analytical solution presented by Hayek et al. (2012). They presented a general methodology to derive the analytical solution for one-, two- and three-dimensional diffusive transport of several aqueous species coupled to dissolution/precipitation of a single mineral with porosity changes. The analytical solution provides the spatial and temporal evolutions of solute concentrations, porosity and mineral concentration for a set of given initial and boundary conditions. This analytical solution is very useful to verify reactive transport codes dealing with strong porosity changes.

The mathematical formulation of the problem was developed by considering a porous medium defined in a bounded domain $\Omega \subset R^d$ with d = 1, 2 or 3. The porous medium consists of a solid phase $O_{(s)}$ reacting with an aqueous solution. Mineral dissolution/precipitation is described with the following reversible reaction:

$$O_{(s)} \leftrightarrow \sum_{i=1}^{N_c} v_i B_i \tag{2.29}$$

where N_c is the total number of solutes, B_i is the i-th solute and v_i is its stoichiometric coefficient.

The analytical solution assumes that solute diffusion is the only transport mechanism. The effective diffusion coefficient is assumed to vary linearly with the porosity with a constant pore diffusion coefficient. All the solute species have the same pore diffusion coefficients.

The rate law of mineral dissolution/precipitation is given by:

$$R_m(x,t) = r_m A_m(x,t)\left[1 - \frac{\prod_{i=1}^{N} c_i(x,t)^{v_i}}{K}\right] \tag{2.30}$$

where $R_m(x,t)$ is the reaction rate, $c_i(x,t)$ denotes the concentration of the i-th species, K is the solubility constant of the mineral, r_m is the kinetic rate constant and A_m is the solid phase reactive surface area per unit volume of rock. The ion activity product $\prod_{i=1}^{N} c_i(x,t)^{v_i}$ is smaller, larger or equal to K when the aqueous solution is undersaturated, supersaturated or in equilibrium, respectively, with respect to the solid. Equation 2.9 shows the general kinetic rate expression of mineral dissolution/precipitation used in CORE^{2D}V5. This equation can be rearranged to be similar to the Equation 2.30.

The initial concentrations are given by:

$$c_i(x,0) = f_i(x) \qquad (i = 1, \ldots, N_c) \tag{2.31}$$

where $f_i(x)$ are spatial functions. The initial porosity is also known and is given by:

$$\phi(x,0) = \phi_0(x) \tag{2.32}$$

The verification of the updated version of CORE^{2D} has been performed by comparing the numerical and the analytical solutions for a two-dimensional model. This verification test case considers two aqueous species B_1 and B_2 in equilibrium with a solid phase $O_{(s)}$ according to Equation 2.29. Clogging is reached and the aqueous phase completely disappears.

The analytical solutions for the solute concentrations of the species B_1 and B_2 are given by:

$$c_1(x_1,x_2,t) = \frac{1}{V_m} + a_1 exp\{a[\alpha_1 x_1 + \alpha_2 x_2 + D_0 a(\alpha_1^2 + \alpha_2^2)t]\} \tag{2.33}$$

$$c_2(x_1,x_2,t) = \frac{1}{V_m} + a_2 exp\{a[\alpha_1 x_1 + \alpha_2 x_2 + D_0 a(\alpha_1^2 + \alpha_2^2)t]\} \tag{2.34}$$

where V_m denotes the mineral molar volume, D_0 is the pore diffusion coefficient and α_1, α_2, a, a_1 and a_2 are arbitrary constants.

The analytical solution of the porosity is:

$$\begin{aligned}\phi(x_1,x_2,t) = \Phi_1 exp\Bigg\{ & -\frac{r_m A_0 (1 - KV_m^2)[\alpha_1 x_1 + \alpha_2 x_2 + D_0 a(\alpha_1^2 + \alpha_2^2)t]}{KV_m D_0 a(\alpha_1^2 + \alpha_2^2)} \\ & - \frac{r_m A_0 (a_1 + a_2)}{KD_0 a^2(\alpha_1^2 + \alpha_2^2)} exp\{a[\alpha_1 x_1 + \alpha_2 x_2 + D_0 a(\alpha_1^2 + \alpha_2^2)t]\} \\ & - \frac{r_m A_0 V_m a_1 a_2}{2KD_0 a^2(\alpha_1^2 + \alpha_2^2)} exp\{2a[\alpha_1 x_1 + \alpha_2 x_2 + D_0 a(\alpha_1^2 + \alpha_2^2)t]\}\Bigg\}\end{aligned} \tag{2.35}$$

where Φ_1 is an arbitrary constant and A_0 is a constant which relates the specific surface area to the porosity ($A = A_0\phi$).

The analytical solution of the mineral concentration is given by:

$$P(x_1,x_2,t) = \frac{1}{V_m}\left[\frac{1}{\Phi_1 exp\left\{\begin{array}{l} -\frac{r_m A_0 (1 - KV_m^2)[\alpha_1 x_1 + \alpha_2 x_2 + D_0 a(\alpha_1^2 + \alpha_2^2)t]}{KV_m D_0 a(\alpha_1^2 + \alpha_2^2)} - \\ \frac{r_m A_0 (a_1 + a_2)}{KD_0 a^2(\alpha_1^2 + \alpha_2^2)} exp\{a[\alpha_1 x_1 + \alpha_2 x_2 + D_0 a(\alpha_1^2 + \alpha_2^2)t]\} - \\ \frac{r_m A_0 V_m a_1 a_2}{2KD_0 a^2(\alpha_1^2 + \alpha_2^2)} exp\{2a[\alpha_1 x_1 + \alpha_2 x_2 + D_0 a(\alpha_1^2 + \alpha_2^2)t]\} \end{array}\right\}} - 1\right] \tag{2.36}$$

A 2-D rectangular domain was considered (1 m x 1 m). A triangular mesh with 406 nodes and 736 elements was used. The mesh was refined at the lower left corner where the concentrations and the porosity are expected to show steep gradients. Figure A2.13 shows the mesh used for the numerical model performed with CORE^{2D}. The numerical and analytical solutions were compared along the diagonal of 2-D domain. The reactive transport model was performed for $1.5 \cdot 10^7$ s. The time domain was divided into 1500 time periods of 10^4 s. Each time period was subdivided into 100 time increments. Analytical and numerical solutions were compared at $t = 5 \cdot 10^6$, $1 \cdot 10^7$ and $1.5 \cdot 10^7$ s.

406 different mineral zones and 406 initial waters were defined in the numerical model (one per node) to define the initial nodal concentrations of species B_1 and B_2 and the initial mineral volume fractions. The solute concentrations are assumed to be known at the boundaries of the model domain (Dirichlet boundary conditions). The following boundary conditions were considered at $x_1 = 0$:

$$c_1(0, x_2, t) = \frac{1}{V_m} + a_1 exp\{a[\alpha_2 x_2 + D_0 a(\alpha_1^2 + \alpha_2^2)t]\} \tag{2.37}$$

$$c_2(0, x_2, t) = \frac{1}{V_m} + a_2 exp\{a[\alpha_2 x_2 + D_0 a(\alpha_1^2 + \alpha_2^2)t]\} \tag{2.38}$$

The conditions at $x_1 = L$ are:

$$c_1(L, x_2, t) = \frac{1}{V_m} + a_1 exp\{a[\alpha_1 L + \alpha_2 x_2 + D_0 a(\alpha_1^2 + \alpha_2^2)t]\} \tag{2.39}$$

$$c_2(L, x_2, t) = \frac{1}{V_m} + a_2 exp\{a[\alpha_1 L + \alpha_2 x_2 + D_0 a(\alpha_1^2 + \alpha_2^2)t]\} \tag{2.40}$$

Similarly, the boundary conditions at $x_2 = 0$ are:

$$c_1(x_1, 0, t) = \frac{1}{V_m} + a_1 exp\{a[\alpha_1 x_1 + D_0 a(\alpha_1^2 + \alpha_2^2)t]\} \tag{2.41}$$

$$c_2(x_1, 0, t) = \frac{1}{V_m} + a_2 exp\{a[\alpha_1 x_1 + D_0 a(\alpha_1^2 + \alpha_2^2)t]\} \tag{2.42}$$

Finally, the conditions at $x_2 = L$ are:

$$c_1(x_1, L, t) = \frac{1}{V_m} + a_1 exp\{a[\alpha_1 x_1 + \alpha_2 L + D_0 a(\alpha_1^2 + \alpha_2^2)t]\} \tag{2.43}$$

$$c_2(x_1, L, t) = \frac{1}{V_m} + a_2 exp\{a[\alpha_1 x_1 + \alpha_2 L + D_0 a(\alpha_1^2 + \alpha_2^2)t]\} \tag{2.44}$$

The parameters of the numerical and the analytical solutions are listed in Table A2.3. The mineral molar volume is equal to 1, which is highly unrealistic. However, this value does not prevent the use of this case for benchmarking CORE^{2D}V5. In fact, this case has already been used to verify OpenGeoSys-GEMS (Shao et al., 2009a, 2009b) and COMSOL Multiphysics (http://www.comsol.com). Both numerical implementations could be verified with the help of the analytical solutions and showed good agreement in terms of spatial and temporal evolution of the concentrations and the porosities.

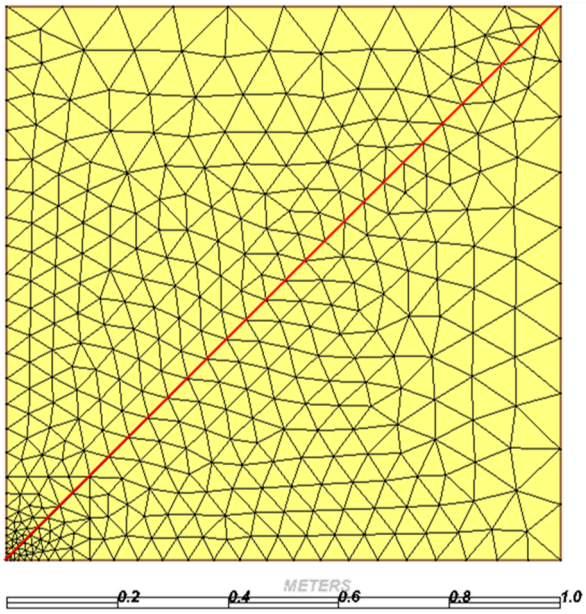

Figure A2.13. Finite element mesh used in CORE^{2D} for the verification against the analytical solution. The analytical and numerical solutions were compared along the main diagonal line (red line).

Table A2.3. Parameters of the two-dimensional numerical and analytical solutions for mineral precipitation.

Parameter	***Value***
D_0 (m^2/s)	10^{-9}
Φ_1	0.210550448
log(K)	-0.41
k ($mol/m^2/s$)	10^{-12}
V_m (m^3/mol)	1
A_0 (m^2/m^3)	10^3
L (m)	1
a	-10
a_1	1
a_2	2
γ^*	1
α_1	1
α_2	1

The two-dimensional model was performed with the updated version of CORE^{2D} by fixing the concentrations of species B_1 and B_2 at the nodes located along the boundaries of the model. Figure A2.14 and Figure A2.15 show the comparison of the analytical and numerical concentration profiles of species B_1 and B_2 along the first 40 cm of the diagonal of the model domain. The concentrations of species B_1 and B_2 increase with the time at the lower left corner and remain constant in the middle part of the domain. The concentration of species B_2 is almost twice the concentration of species B_1 because $a_2 = 2a_1$ (see Table A2.3). The numerical and analytical solutions agree in all cases.

Figure A2.16 shows the comparison of the porosity profiles computed with the numerical and the analytical solutions along the first 40 cm of the main diagonal of the model domain. The porosity at the lower left corner decreases slowly at the beginning and later decreases exponentially. The porosity reaches very low values at $t = 1.5 \cdot 10^7$ s. The minimum porosity considered in the numerical model for this case was equal to 10^{-3}. The porosity decreases to this value at the lower left corner of the model domain at the end of the simulation. Numerical and analytical solutions fully agree.

Figure A2.17 shows 3-D plots of the spatial distribution of the porosity computed with the numerical and analytical solutions at selected times. The main changes in the porosity occur near the origin *(0, 0)* while the porosity remains constant in the rest of the model domain. The 3-D plots calculated with the numerical solutions agree with the plots of the analytical solution.

Figure A2.18 shows the comparison of the analytical and numerical mineral concentration profiles (in mol/m^3 of fluid) along the first 40 cm of the main diagonal of the model domain. The results computed with the updated version of CORE^{2D} generally agree with the analytical solutions. Similar to the decrease of the porosity, the precipitation of the mineral occurs at the lower left corner of the domain. The mineral concentration (in mol/m^3 of fluid) at $t = 1.5 \cdot 10^7$ s reaches very high values because the porosity decreases significantly. As the porosity decreases to very low values (near clogging) at the lower left corner of the domain, the aqueous phase reduces drastically and the mineral concentration reaches very high values.

To illustrate the relevance of the changes in porosity, the two-dimensional model was performed with and without considering the feedback effect of the changes in porosity. Porosity and mineral concentrations were computed also with the previous version of CORE^{2D} which does not account for the feedback effect of the changes in porosity. Figure A2.19 shows the comparison of the porosity profiles computed with and without the feedback effect along the first 40 cm of the main diagonal of the model domain. The porosities computed in the two runs are similar at early times ($t = 5 \cdot 10^6$ s). Later, the differences in porosity increase. The porosity decreases more quickly in the run without the feedback effect ($t = 1 \cdot 10^7$ s and $t = 1.5 \cdot 10^7$ s). The clogging effect is more important in the run without the feedback effect. Figure A2.20 shows the comparison of the mineral concentration profiles (in mol/m^3 of fluid) computed with and without the feedback effect. The mineral concentration profiles computed with and without the feedback effect are very different because the porosity is not updated in the run without the feedback effect. Figure A2.19 and Figure A2.20 show that the improvements incorporated in CORE^{2D} are very relevant in problems with mineral dissolution/precipitation leading to strong porosity changes.

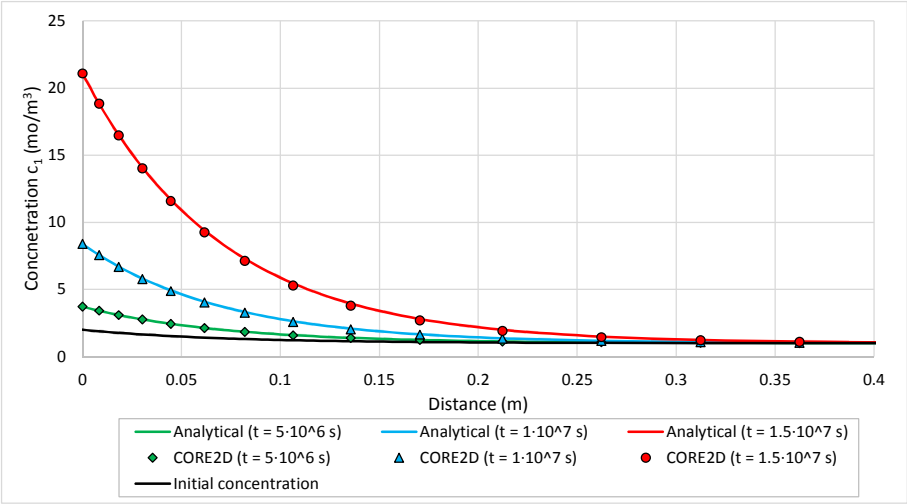

Figure A2.14. Comparison of the analytical and numerical concentration profiles of species B_1 for the two-dimensional model with mineral precipitation.

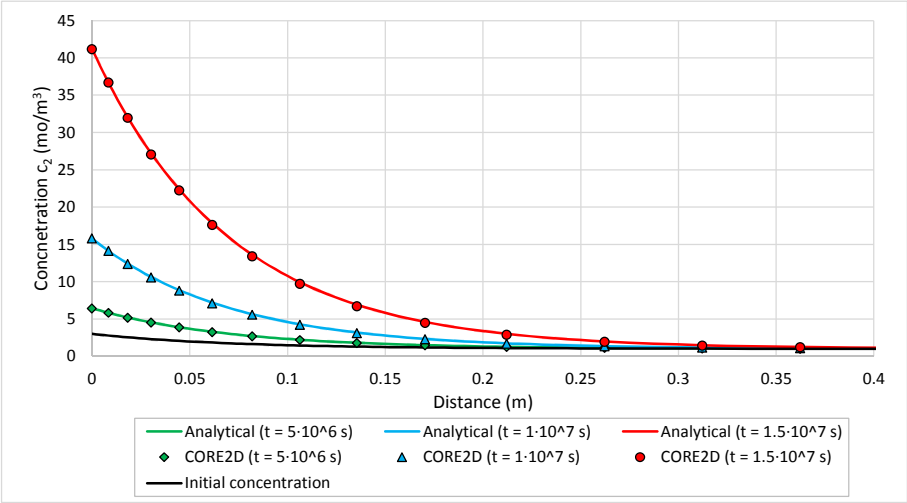

Figure A2.15. Comparison of the analytical and numerical concentration profiles of species B_2 for the two-dimensional model with mineral precipitation.

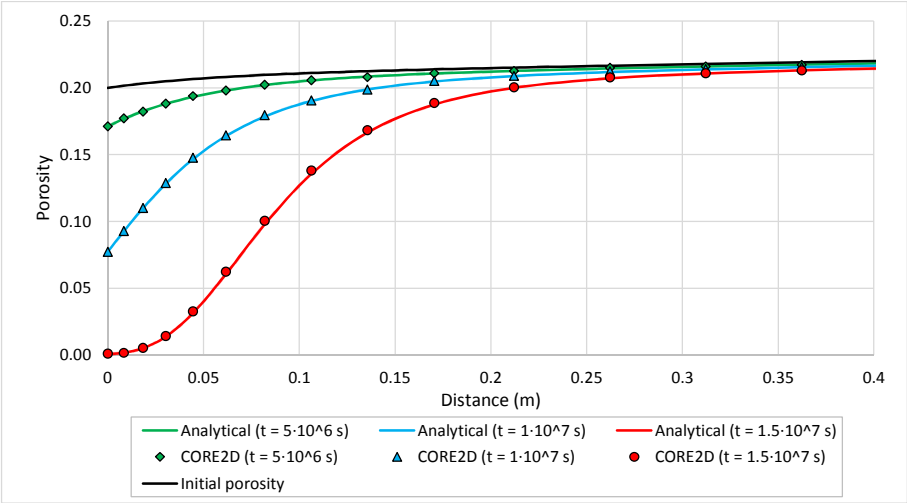

Figure A2.16. Comparison of the analytical and numerical porosity profiles for the two-dimensional model with mineral precipitation.

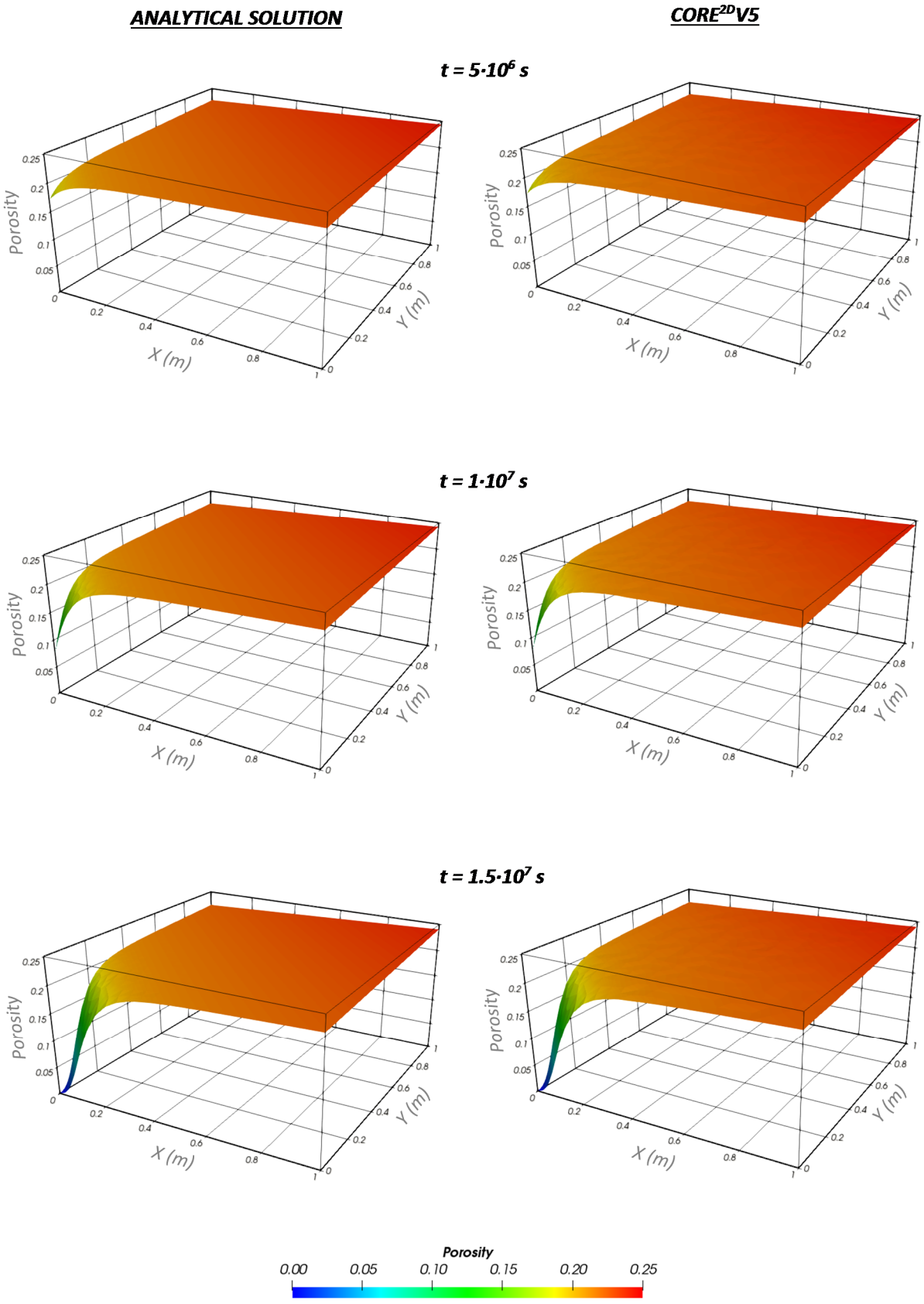

Figure A2.17. 3-D plots of the spatial distribution of the porosity computed with the numerical and analytical solutions at selected times.

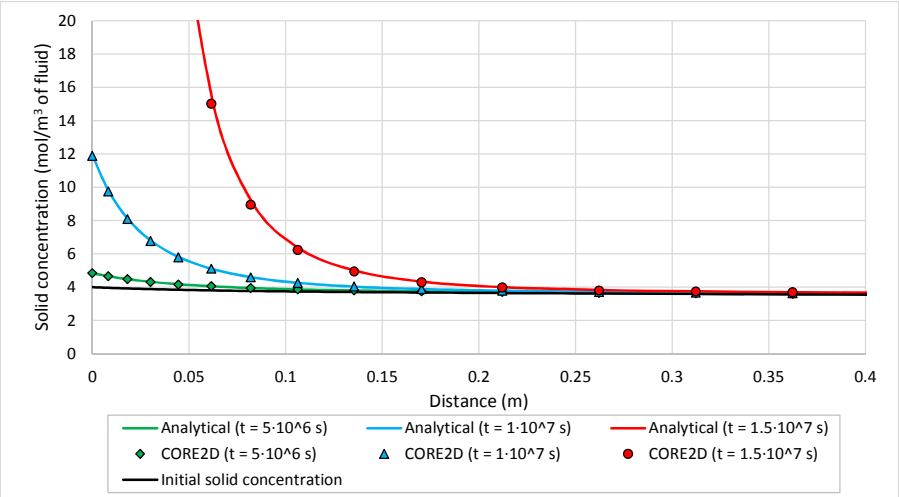

Figure A2.18. Comparison of the analytical and numerical mineral concentration profiles (in mol/m^3 of fluid) for the two-dimensional model with mineral precipitation.

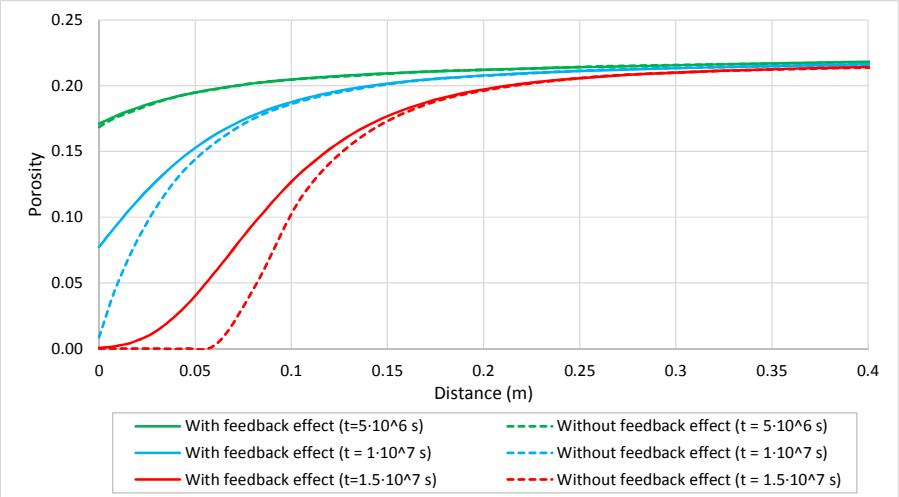

Figure A2.19. Comparison of the porosity profiles computed with CORE^{2D} with and without the feedback effect of the changes in porosity for the two-dimensional model at selected times.

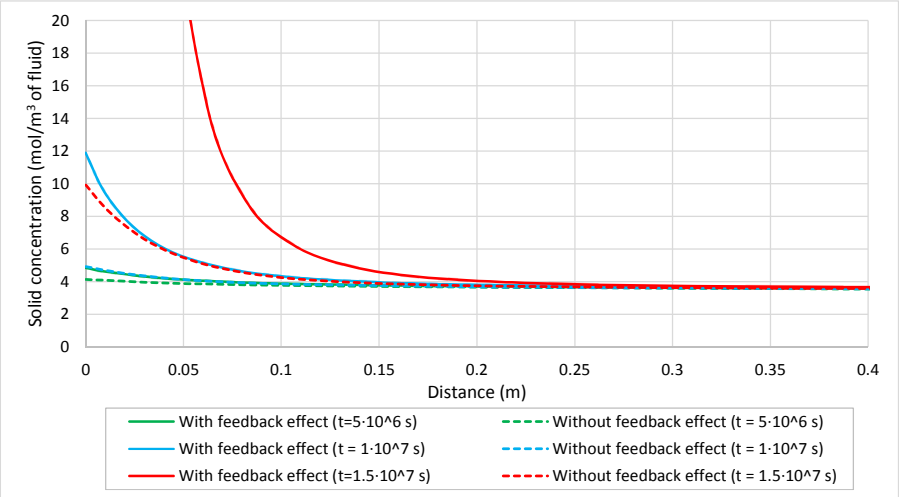

Figure A2.20. Comparison of the mineral concentration profiles (in mol/m^3 of fluid) computed with CORE^{2D} with and without the feedback effect of the changes in porosity for the two-dimensional model with mineral precipitation at selected times.

A2.4.3. Verification by benchmarking

The improvements implemented in CORE^{2D}V5 have been verified also with a benchmark test case entitled "*Implementation and evaluation of permeability-porosity and tortuosity-porosity relationships linked to mineral dissolution-precipitation*" reported by Mingliang Xie, K. Ulrich Mayer, Francis Claret, Peter Alt-Epping, Diederik Jacques, Carl Steefel, Christophe Chiaberge and Jiri Simunek (Xie et al., 2015). This benchmark considers advective-dispersive transport in saturated media, kinetically-controlled mineral precipitation and dissolution and aqueous complexation. Porosity changes due to mineral dissolution/precipitation reactions. The Kozeny-Carman relationship is used to relate permeability to porosity. Archie's law is used to relate the tortuosity and the pore diffusion coefficient to the porosity. Six scenarios or subcases were investigated by using five reactive transport codes: CrunchFlow, HP1, MIN3P, Pflotran and TOUGHREACT. The results of the benchmark show good agreements amongst the codes despite the significant differences in model formulations.

The first two scenarios (*B1* and *B2*) were performed with the updated version of CORE^{2D} and the results were compared with those obtained with other reactive transport codes. The first scenario (*B1*) considers mineral dissolution and the corresponding increase in permeability. The second scenario (*B2*) deals with a precipitation-dominated (clogging) problem. Benchmarks *B1* and *B2* have in common that advection is the only transport process considered. Both simulations were conducted under standard pressure and temperature (25º C) and fully saturated conditions.

The changes in porosity are calculated from the changes in mineral volume fractions. The hydraulic conductivity is updated at the end of each time step according to the Kozeny-Carman relationship. The Archie's law is used to update the tortuosity and the pore diffusion coefficient. Mineral dissolution/precipitation reactions are kinetically-controlled. The reaction rate, R_m, is given by:

$$R_m = -r_m \left[1 - \left(\frac{IAP_m}{K_m}\right)\right] \tag{2.45}$$

where IAP_m is the ion activity product, K_m is the equilibrium constant and r_m is the effective rate constant which varies as a function of mineral abundance at each time step. For primary mineral phases (i.e., the mineral phases which are initially present in the system), a two-third power relationship is used to update the effective rate constant according to:

$$r_m^t = -r_m^0 \left(\frac{f_m^t}{f_m^0}\right)^{\frac{2}{3}} \tag{2.46}$$

where r_m^t and f_m^t are the effective rate constant and mineral volume fraction at time *t*, respectively; and $k_i^{m,0}$ and f_m^0 are the initial rate constant and mineral volume fraction, respectively. The rate constants of secondary minerals (i.e., newly-formed minerals) are assumed to remain constant.

Equation 2.9 shows the general kinetic rate expression of mineral dissolution/precipitation used in CORE^{2D}V5. This equation was rearranged to become similar to the Equation 2.45.

The dimensions of the model and the spatial discretization of the scenarios *B1* and *B2* are described in the benchmark statement (Xie et al., 2015). All the reactive transport codes used the same spatial discretization scheme. It is a one-dimensional saturated test case with a length of 2 m. The domain was discretized with uniform intervals of 0.025 m. The model was solved with CORE^{2D} with a uniform 1-D finite element grid with 80 elements and 81 nodes.

The porous medium is initially homogeneous with an initial porosity of 0.35 and an initial hydraulic conductivity of $1.16 \cdot 10^{-4}$ m/s. Dispersion is neglected in scenarios *B1* and *B2* to minimize the complexity of the problem.

The initial hydraulic head is equal to 0 in all nodes of the finite element grid. A constant hydraulic head equal to 0.007 m is considered for scenarios *B1* and *B2* at the inflow (x = 0 m). The hydraulic head remains constant and equal to 0 m at the outflow (x = 2 m).

The dissolution/precipitation of the minerals in the scenarios *B1* and *B2* are kinetically-controlled. Scenario *B1* involves only calcite while scenario *B2* involves calcite and gypsum. Mineral parameters are listed in Table A2.4.

Table A2.4. Physical and kinetic mineral parameters.

Mineral	r_m^0 (m^2 mineral/L bulk)	Density (g/cm^3)	Mol weight (g/mol)	Molar volume (cm^3/mol)	Update type
Calcite	$5 \cdot 10^{-8}$	2.71	100.09	36.93	Two third
Gypsum	$5 \cdot 10^{-8}$	2.32	172.17	74.21	Constant

A2.4.3.1. Scenario *B1*: changes in porosity and permeability due to dissolution

Scenario *B1* considers the infiltration of a sulfuric acid solution into a rock matrix containing calcite in an otherwise non-reactive (inert) rock matrix. The main processes include: advective transport in saturated media, kinetically-controlled mineral dissolution and aqueous complexation reactions.

The reactive transport model was performed for 500 years. The time discretization is not the same amongst all reactive transport codes. In CORE^{2D}, the time domain was divided into 500 time periods of 1 year. However, an automatic adjustment of the time steps was needed to achieve convergence. The numerical solutions were compared at 10, 100 and 120 years.

Calcite is the only mineral phase considered in scenario *B1*. Its volume fraction is 0.30 m^3/m^3. The remaining fraction of the solid phase is inert. The solution domain is initially occupied by an alkaline solution in equilibrium with calcite. The infiltration water is acidic with a pH of 3 and is undersaturated with respect to calcite. Four primary species are included: H^+, Ca^{2+}, CO_3^{2-} and SO_4^{2-}. The chemical composition of the initial and the boundary waters are listed in Table A2.5.

The four primary species included in the numerical model lead to the formation of 10 aqueous complexes. The chemical reactions and their equilibrium constants at 25ºC for the 10 aqueous complexes and the mineral dissolution/precipitation reaction in the scenario *B1* are listed in Table A2.6. The activity coefficients of the aqueous species in CORE^{2D} are calculated according to the extended Debye-Hückel equation.

Table A2.5. Chemical composition of the initial and the boundary waters in scenario *B1*.

Primary components	Unit	Initial water	Boundary water
pH	[-]	9.38	3.0
Ca^{2+}	[mol/L]	$1.57 \cdot 10^{-4}$	$1.00 \cdot 10^{-4}$
CO_3^{2-}	[mol/L]	$2.57 \cdot 10^{-4}$	$1.00 \cdot 10^{-2}$
SO_4^{2-}	[mol/L]	$1.00 \cdot 10^{-10}$	$6.46 \cdot 10^{-4}$

Table A2.6. Reactions and equilibrium constants for aqueous complexation and mineral dissolution reactions at 25ºC in scenario *B1*.

	Aqueous complexes	Log K
	$CaCO_3(aq) + H^+ \Leftrightarrow Ca^{2+} + HCO_3^-$	7.1100
	$CaHCO_3^+ \Leftrightarrow Ca^{2+} + HCO_3^-$	-1.1100
	$CaOH^+ + H^+ \Leftrightarrow Ca^{2+} + H_2O$	12.7800
	$CaSO_4(aq) \Leftrightarrow Ca^{2+} + SO_4^{2-}$	-2.3090
	$CaHSO_4^+ \Leftrightarrow Ca^{2+} + SO_4^{2-} + H^+$	-3.0680
	$CO_3^{2-} + H^+ \Leftrightarrow HCO_3^-$	10.3300
	$CO_2(aq) + H_2O \Leftrightarrow H^+ + HCO_3^-$	-6.3510
	$OH^- + H^+ \Leftrightarrow H_2O$	13.9980
	$H_2SO_4(aq) \Leftrightarrow SO_4^{2-} + 2H^+$	1.0209
	$HSO_4^- \Leftrightarrow H^+ + SO_4^{2-}$	-1.9870
	Mineral	**Log K**
Calcite	$CaCO_3(s) + H^+ \Leftrightarrow Ca^{2+} + HCO_3^-$	1.8550

This benchmark was simulated with the following five reactive transport codes: CrunchFlow, HP1, MIN3P, Pflotran and TOUGHREACT. For the purpose of verifying the updated version of CORE^{2D}, only the results of MIN3P were used because they are available at the benchmark supplementary material. The benchmarking plots are the same as those reported by Xie et al. (2015).

Figure A2.21 shows the comparison of the porosity profiles computed with MIN3P and CORE^{2D} at 10, 100 and 120 years in scenario *B1*. Initially, the porosity is equal to 0.35 throughout the model domain. However, porosity increases as the sulfuric acid solution advances and calcite dissolves. The porosity increases substantially near the inflow boundary during the first ten years of the simulation. However, after 100 years the porosity is equal to 0.65 in the first meter of the model. Both reactive transport codes give very similar results. There are small differences in the upstream part of the porosity front due to the dispersivity. While MIN3P used a dispersivity equal to 0, a small dispersivity was used in CORE^{2D} to ensure convergence. These differences were reported for other codes.

Figure A2.22 shows the comparison of the profiles of calcite volume fraction computed with MIN3P and CORE^{2D} at 10, 100 and 120 years in scenario *B1*. Model results show that the dissolution front of calcite is initially narrow. Later, the front widens as permeability and flow velocities increase. The initial volume fraction of calcite is equal to 0.3. Calcite dissolves with time until the volume fraction reaches a value of 0 throughout the model domain. The profiles of calcite volume fraction calculated with MIN3P and CORE^{2D} at 10 and 100 years are very similar, despite their differences in transport schemes and coupling methods.

Figure A2.23 shows the comparison of the hydraulic head profiles computed with MIN3P and CORE^{2D} at 10, 100 and 120 years in scenario *B1*. The hydraulic head at the inflow (0.007 m) and at the outflow (0 m) boundaries are constant. The initial hydraulic head shows a linear distribution. The dissolution of calcite causes an increase in the permeability near the inflow boundary and, consequently, the hydraulic head gradient decreases. As calcite dissolves, the computed hydraulic heads increase to values close to 0.007 m. At 120 years, the computed hydraulic heads decrease because the permeability increases near the outflow and the water outflow also increases. The hydraulic head computed with MIN3P and CORE^{2D} coincide always.

Figure A2.24 shows the comparison of the water outflows calculated with MIN3P and CORE^{2D} in scenario *B1*. Although the porosity and the permeability increase substantially near the inflow boundary at early times, the water outflow increases slightly during the first 100 years. The outflow increases sharply when calcite depleted in the entire model domain. The outflows computed with CORE^{2D}V5 fully coincide with those computed with MIN3P.

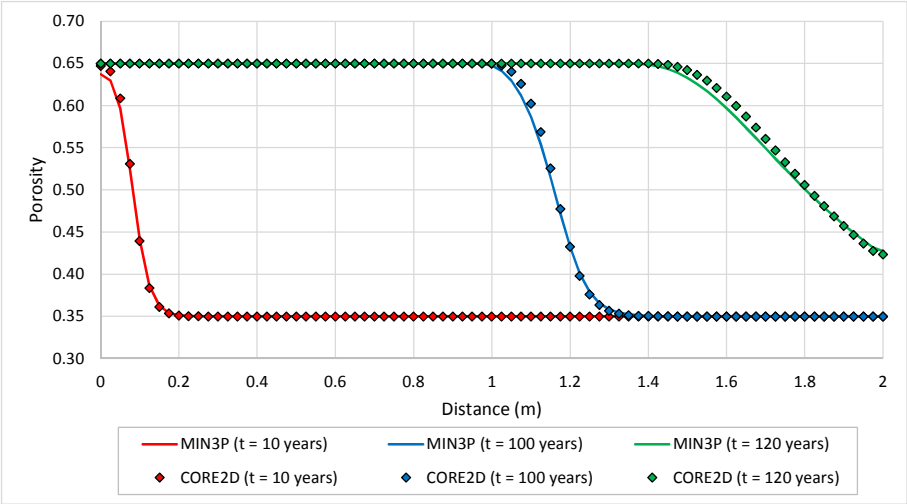

Figure A2.21. Comparison of the porosity profiles computed with MIN3P and CORE^{2D} at 10, 100 and 120 years in scenario *B1*.

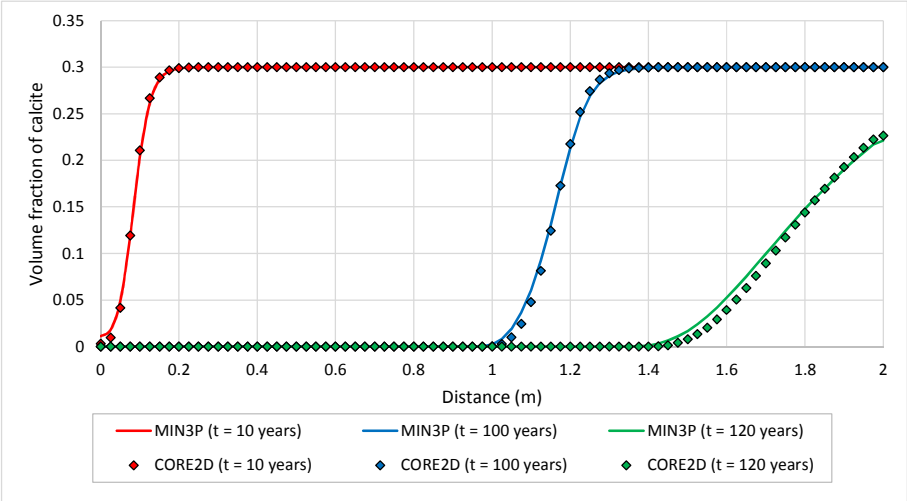

Figure A2.22. Comparison of the calcite volume fraction profiles computed with MIN3P and CORE^{2D} at 10, 100 and 120 years in scenario *B1*.

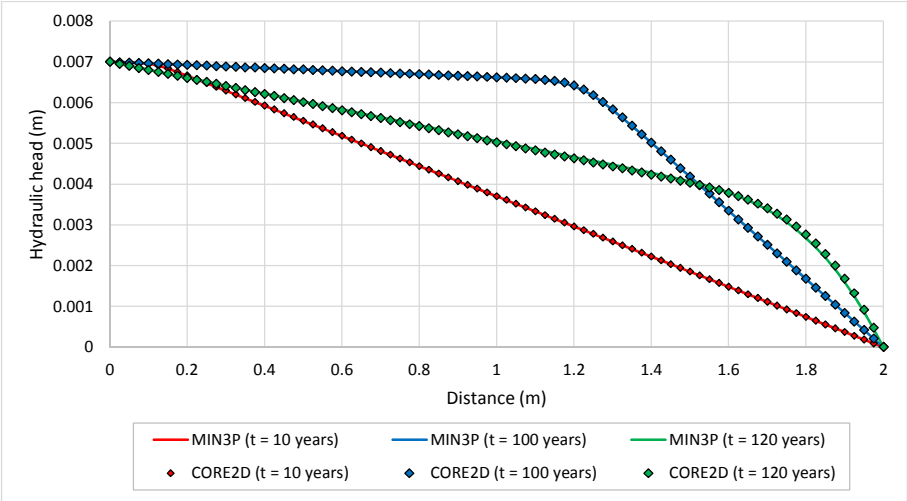

Figure A2.23. Comparison of the hydraulic head profiles computed with MIN3P and CORE^{2D} at 10, 100 and 120 years in scenario *B1*.

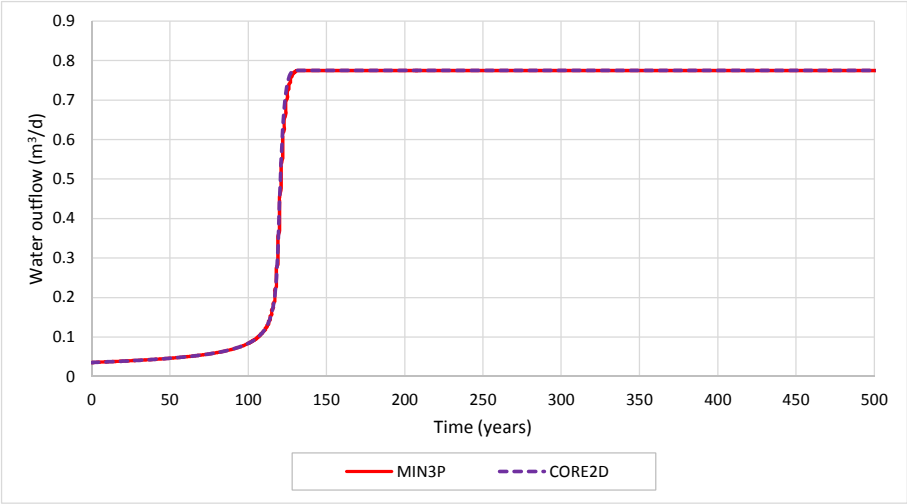

Figure A2.24. Comparison of the time evolution of the water outflow (x = 2 m) computed with MIN3P and CORE^{2D} in scenario *B1*.

A2.4.3.2. Scenario *B2*: clogging due to mineral precipitation

Similar to scenario *B1*, scenario *B2* considers also the infiltration of a sulfuric acid solution into a rock matrix containing calcite in an otherwise non-reactive (inert) rock matrix. However, the boundary solution has a SO_4^{2-} concentration much higher than that of the rock porewater. Consequently, gypsum precipitates and the porosity and the permeability decrease. In this case, clogging occurs and the aqueous phase vanishes.

The hydraulic properties and the model set-up are of scenario *B2* are similar to those of scenario *B1*. The reaction network and the initial and boundary chemical concentrations of scenario *B2*, nevertheless, differ from those of scenario *B1*.

The reactive transport model of scenario *B2* was performed for a total period of 1000 years. The time domain in CORE^{2D} was divided into 1000 time periods of 1 year. However, an automatic adjustment of the time increments was needed to achieve convergence.

Calcite and gypsum are the mineral phases considered in the scenario *B2*. The domain includes initially calcite with a volume fraction of 0.30 m^3/m^3. The resident pore water is in equilibrium with calcite and undersaturated with respect to gypsum. With the infiltration of a sulfuric acid solution, calcite dissolves and gypsum precipitates. At later times, gypsum re-dissolves near the inflow boundary. Mineral dissolution/precipitation is kinetically-controlled. The effective rate constant of calcite is updated with a two-third power relationship (see Equation 2.46) whereas the effective rate constant of gypsum precipitation is assumed constant (see Table A2.4).

The following five primary species were considered: H^+, Ca^{2+}, CO_3^{2-}, SO_4^{2-} and Na^+. The chemical composition of the initial and boundary waters are listed in Table A2.7. The model accounts for 13 aqueous complexes. Their chemical reactions and equilibrium constants at 25 ºC and the mineral dissolution/precipitation reactions are listed in Table A2.8.

Table A2.7. Chemical composition of the initial and boundary waters in scenario *B2*.

Primary components	Unit	Initial condition	Boundary condition
pH	[-]	9.33	3.0
Ca^{2+}	[mol / L]	$1.70 \cdot 10^{-4}$	$1.00 \cdot 10^{-4}$
CO_3^{2-}	[mol / L]	$2.70 \cdot 10^{-4}$	$1.00 \cdot 10^{-2}$
SO_4^{2-}	[mol / L]	$1.70 \cdot 10^{-4}$	$2.00 \cdot 10^{-1}$
Na^+	[mol / L]	$3.20 \cdot 10^{-4}$	$3.96 \cdot 10^{-1}$

Table A2.8. Reactions and equilibrium constants for aqueous complexation and mineral dissolution/precipitation reactions at 25ºC in scenario *B2*.

	Aqueous complexes	Log K
	$CaCO_3(aq) + H^+ \Leftrightarrow Ca^{2+} + HCO_3^-$	7.1100
	$CaHCO_3^+ \Leftrightarrow Ca^{2+} + HCO_3^-$	-1.1100
	$CaOH^+ + H^+ \Leftrightarrow Ca^{2+} + H_2O$	12.7800
	$CaSO_4(aq) \Leftrightarrow Ca^{2+} + SO_4^{2-}$	-2.3090
	$CaHSO_4^+ \Leftrightarrow Ca^{2+} + SO_4^{2-} + H^+$	-3.0680
	$CO_3^{2-} + H^+ \Leftrightarrow HCO_3^-$	10.3300
	$CO_2(aq) + H_2O \Leftrightarrow H^+ + HCO_3^-$	-6.3510
	$OH^- + H^+ \Leftrightarrow H_2O$	13.9980
	$NaSO_4^- \Leftrightarrow Na^+ + SO_4^{2-}$	-0.7000
	$NaCO_3^- \Leftrightarrow Na^+ + CO_3^{-2}$	-1.2680
	$NaHCO_3(aq) \Leftrightarrow Na^+ + HCO_3^-$	-0.2500
	$H_2SO_4(aq) \Leftrightarrow SO_4^{2-} + 2H^+$	1.0209
	$HSO_4^- \Leftrightarrow H^+ + SO_4^{2-}$	-1.9870
	Minerals	**Log K**
Calcite	$CaCO_3(s) + H^+ \Leftrightarrow Ca^{2+} + HCO_3^-$	1.8550
Gypsum	$CaSO_4 \cdot 2H_2O(s) \Leftrightarrow Ca^{2+} + SO_4^{2-} + 2H_2O$	-4.5800

Figure A2.25 shows the comparison of the porosity profiles computed with MIN3P and CORE^{2D} at 10, 100 and 1000 years in scenario *B2*. Initially, the porosity is equal to 0.35 throughout the model domain. However, the porosity changes due to the intrusion of the acid solution which causes the dissolution of calcite and the precipitation of gypsum. During the first ten years of the simulation, porosity increases near the inflow boundary due to the dissolution of calcite and the re-dissolution of gypsum. However, the porosity decreases at x = 0.25 m due to the precipitation of gypsum. After 100 years, the length of the model where the porosity is equal to 0.65 increases. The precipitation of gypsum causes the reduction of porosity and clogging occurs at x = 0.425 m. The minimum porosity computed with MIN3P, PFlotran and TOUGHREACT after 1000 years is equal to 0.0016 at x = 0.425 m. It is equal to 0.003 at x = 0.40 m for HP1 and 0.0018 at x = 0.40 m for CrunchFlow. In CORE^{2D}, the minimum porosity considered is equal to 0.001 and is reached at x = 0.425 m after 1000 years. In general, the porosities computed with CORE^{2D} coincide with those calculated with MIN3P and the other reactive transport codes.

Figure A2.26 shows the comparison of the profiles of the calcite volume fraction computed with MIN3P and CORE^{2D} at 10, 100 and 1000 years in scenario *B2*. The numerical results computed with both codes coincide for the most part. The initial volume fraction of calcite is equal to 0.3. Simulation results show a calcite dissolution front. After 100 years, the dissolution front of calcite does not advance due to the clogging caused by gypsum precipitation.

Figure A2.27 shows the comparison of the profiles of gypsum volume fraction computed by MIN3P and CORE^{2D} at 10, 100 and 1000 years in scenario *B2*. The results of both codes are generally similar. Gypsum is not present initially in the system. It precipitates with the infiltration of the sulfuric acid solution. Although gypsum re-dissolves near the inflow boundary, a narrow region of gypsum accumulation causes clogging. After 10 years, the zone of gypsum accumulation is already visible with a maximum value at x = 0.2 m. In this point, the volume fraction of gypsum computed with CORE^{2D} is higher than that computed with MIN3P. The maximum volume fraction of gypsum calculated with MIN3P after 1000 years is equal to 0.626. The maximum volume fraction of gypsum computed with CORE^{2D} after 1000 years is very similar (0.607).

Figure A2.28 shows the comparison of the hydraulic head profiles computed with MIN3P and CORE^{2D} at 10, 100 and 1000 years in scenario *B2*. The heads computed with both codes generally coincide. After 10 years, calcite dissolves for $0 < x < 0.2$ m, the permeability increases and the hydraulic heads in this zone increase to values close to 0.007 m. After 100 years, clogging is nearly complete and the simulated hydraulic head profile shows a sharp decline at the clogging point. Hydraulic heads computed with CORE^{2D} show a good agreement with the results obtained with the rest of the reactive transport codes.

Figure A2.29 shows the comparison of the hydraulic conductivity profiles computed with MIN3P and CORE^{2D} at 10, 100 and 1000 years in scenario *B2*. The hydraulic conductivities computed with CORE^{2D} are similar to those computed with MIN3P. The precipitation of gypsum after 100 years causes clogging approximately at x = 0.425 m. In this point the computed hydraulic conductivities are drastically reduced.

Figure A2.30 shows the comparison of the time evolution of the water outflow computed with MIN3P and CORE^{2D} in scenario *B2*. Both codes give similar results. The calculated outflow decreases rapidly after 50 years of simulation due to the precipitation of gypsum and porosity clogging. The calculated outflow becomes vanishes to zero after 50 years.

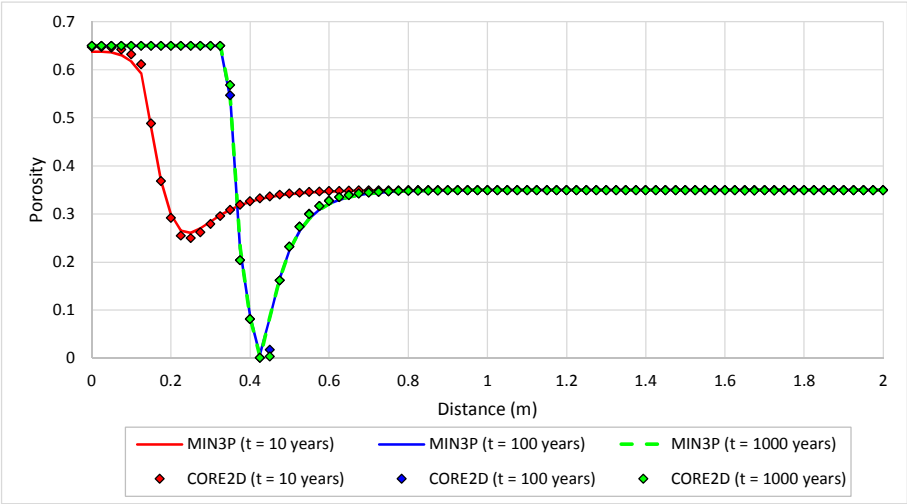

Figure A2.25. Comparison of the porosity profiles computed with MIN3P and CORE^{2D} at 10, 100 and 1000 years in scenario *B2*.

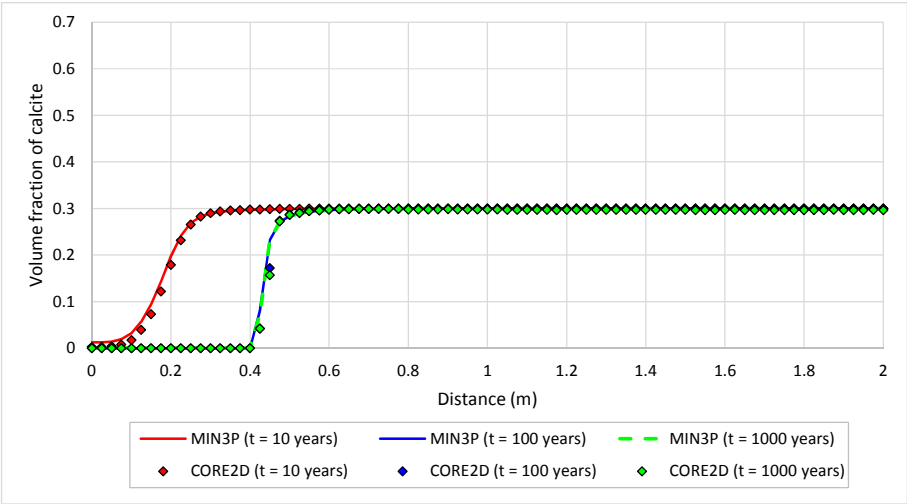

Figure A2.26. Comparison of the calcite volume fraction profiles computed with MIN3P and CORE^{2D} at 10, 100 and 1000 years in scenario *B2*.

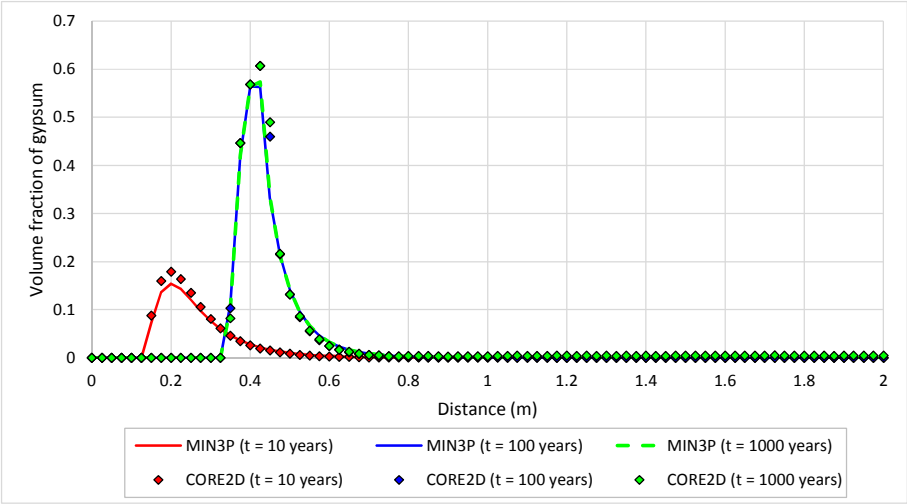

Figure A2.27. Comparison of the gypsum volume fraction profiles computed with MIN3P and CORE^{2D} at 10, 100 and 1000 years in scenario *B2*.

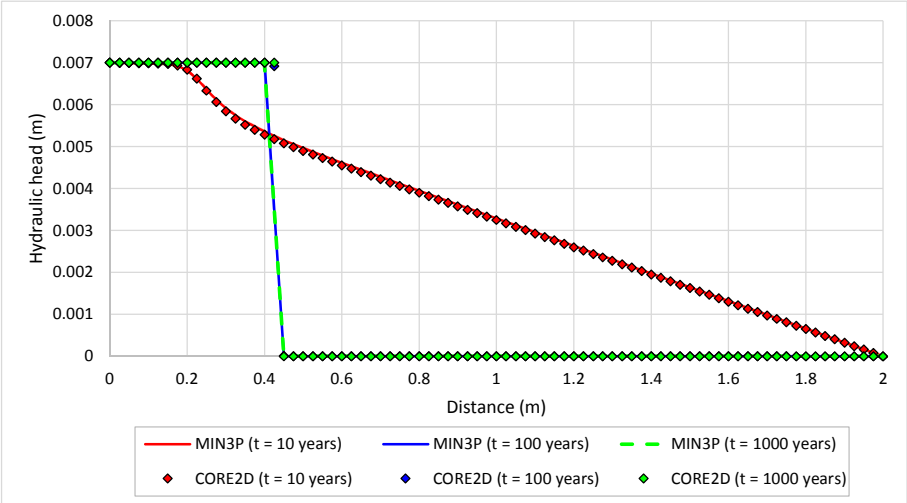

Figure A2.28. Comparison of the hydraulic head profiles computed with MIN3P and CORE^{2D} at 10, 100 and 1000 years in scenario *B2*.

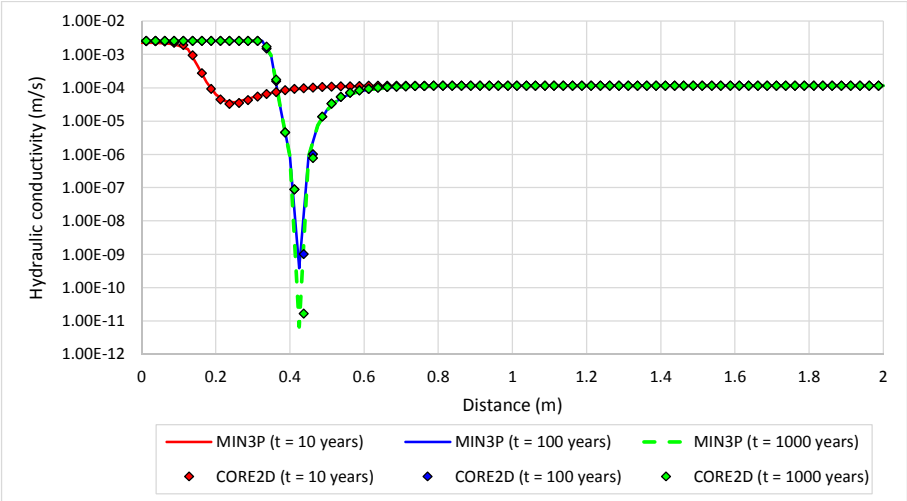

Figure A2.29. Comparison of the hydraulic conductivity profiles computed with MIN3P and CORE^{2D} at 10, 100 and 1000 years in scenario *B2*.

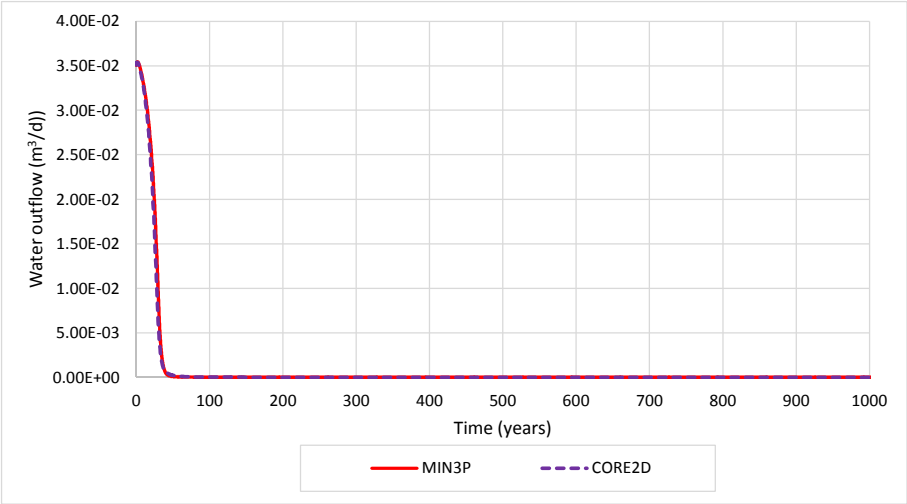

Figure A2.30. Comparison of the time evolution of the water outflow (x = 2 m) computed with MIN3P and CORE^{2D} in scenario *B2*.

A2.5. CONCLUSIONS

Mineral dissolution and precipitation may modify the pore geometry of rocks, which in turn may change flow and transport parameters. Porosity changes induced by mineral dissolution/precipitation therefore can influence the evolution of natural geological environments and underground systems.

CORE^{2D}V5 has been updated to take into account the porosity changes due to mineral dissolution/precipitation and account for their effect on flow, transport and chemical parameters in saturated media in one and two dimensions. The porosity is updated at each time step according to the changes in the volume fractions of the minerals. When the porosity changes, the flow, transport and chemical parameters are updated in the following time step. The changes in permeability are calculated by using a Kozeny-Carman equation. Pore diffusion coefficients and tortuosities are updated according to Archie's law. In addition, other parameters such as water contents, water velocities and mineral specific surfaces are also updated each time step. The changes in time in the hydraulic conductivity, pore diffusion coefficient and mineral specific surfaces are printed out. The restart option of CORE^{2D}V5 has been modified also in the updated version of CORE^{2D} to take into account the porosity changes.

The improvements implemented in CORE^{2D}V5 to take into account the porosity changes and their effects on flow, transport and chemical parameters have been verified with analytical solutions for diffusion problems coupled with dissolution/precipitation reactions and feedback of porosity change in one dimension (Hayek et al., 2011) and two dimensions (Hayek et al., 2012). In addition, the benchmark case study reported by Xie et al. (2015) has been used to verify the updated version of the code with

other reactive transport codes (CrunchFlow, HP1, MIN3P, Pflotran and TOUGHREACT). This benchmark considers advective transport in saturated media, aqueous complexation and kinetically-controlled mineral precipitation and dissolution leading to porosity changes. The model results computed with the updated version of CORE^{2D} reproduce the analytical solutions and the numerical solutions computed with other reactive transport codes.

A2.6. REFERENCES

Archie, G., (1942). The electrical resistivity log as an aid in determining some reservoir characteristics. Pet. Trans. AIME 146, 54-62.

Alt-Epping, P., Diamond, L.W., Häring, M.O., Ladner, F., Meier, D.B., (2013a). Prediction of water-rock interaction and porosity evolution in a granitoid-hosted enhanced geothermal system, using constraints from the 5 km Basel-1 well. Appl. Geochem., 38, 121-133.

Alt-Epping, P., Waber, H.N., Diamond, L.W., Eichinger, L., (2013b). Reactive transport modeling of the geothermal system at Bad Blumau, Austria: Implications of the combined extraction of heat and CO_2. Geothermics, 45, 18-30.

Berner, U., Kulik, D.A., Kosakowski, G., (2013). Geochemical impact of a low-pH cement liner on the near field of a repository for spent fuel and high-level radioactive waste. Phys. Chem. Earth, 64, 46-56.

Bildstein, O., Kervévan, C., Lagneau, V., Delaplace, P., Crédoz A., Audigane, P., Perfetti, E., Jacquemet, N., Jullien, M., (2010). Integrative modeling of caprock integrity in the context of CO_2 storage: Evolution of transport and geochemical properties and impact on performance and safety assessment. Oil Gas Sci. Technol. IFP, 65(3), 485-502.

Boving, T.B., Grathwohl, P., (2001). Tracer diffusion coefficients in sedimentary rocks: correlation to porosity and hydraulic conductivity. J. Contam. Hydrol., 53, 85-100.

Carman, P.C., (1937). Fluid through granular beds. Trans. Inst. Chem. Eng. 15, 150-166.

Class, H., Ebigbo, A., Helmig, R., Dahle, H.K., Nordbotten, J.M., Celia, M.A., Aubigane, P., Darcis, M., Ennis-King, J., Fan, Y., Flemisch, B., Gasda, S.E., Jin, M., Krug, S., Labregere, D., Beni, A.N., Pawar, R.J., Sbai, A., Thomas, S.G., Trenty, L., Wei, L., (2009). A benchmark study problem related to CO_2 storage in geologic formations. Computat. Geosci., 13(4), 409-434.

Marsily, G., (1986). Quantitative Hydrogeology. Academic Press Inc., San Diego, 440 pp.

De Windt, L., Pellegrini, D., van der Lee, J., (2004). Coupled modeling of cement/claystone interactions and radionuclide migration. J. Contam. Hydrol., 68(3-4), 165-182.

De Windt, L., Badredinne, R., Lagneau, V., (2007). Long-term reactive transport modelling of stabilized/solidified waste: from dynamic leaching tests to disposal scenarios. J. Hazard. Mater., 139(3), 529-536.

Diamond, L.W., Alt-Epping, P., (2014). Predictive modelling of mineral scaling, corrosion and the performance of solute geothermometers in a granitoid-hosted, enhanced geothermal system. App. Geochem., 51, 216-228.

Dullien, F.A.L., (1979). Porous Media, Fluid Transport and Pore Structure. Academic Press, New York.

Gaucher, E.C., Blanc, P., (2006). Cement/clay interaction - a review: experiments, natural analogues, and modelling. Waste Manag., 26, 776-788.

Gaus, I., Azaroual, M., Czernichowski-Lauriol, I., (2005). Reactive transport modelling of the impact of CO_2 injection on the clayey cap rock at Sleipner (North Sea). Chem. Geol., 217(3-4), 319-337.

Hayek, M., Kosakowski, G., Churakov, S., (2011). Exact analytical solutions for a diffusion problem coupled with precipitation–dissolution reaction and feedback of porosity change. Water Resour., 47, W07545. http://dx.doi.org/10.1029/2010WR010321.

Hayek, M., Kosakowski, G., Jakob, A., (2012). A class of analytical solutions for multidimensional species diffusive transport coupled with precipitation–dissolution reactions and porosity changes. Water Resour., 48, W03525. http://dx.doi.org/10.1029/2011WR011663.

Jamieson-Hanes, J.H., Amos, R.T., Blowes, D.W., (2012). Reactive transport modeling of Chromium Isotope Fractionation during Cr (IV) Reduction. Environ. Sci. Technol., 46(24), 13311-13316.

Kosakowski, G., Berner, U., (2013). The evolution of clay rock/cement interfaces in a cementitious repository for low and intermediate level radioactive waste. Phys. Chem. Earth, A/B/C, 64, 65-86.

Lagneau, V., van der Lee, J., (2010). Operator-splitting-based reactive transport models in strong feedback of porosity change: The contribution of analytical solutions for accuracy validation and estimator improvement. J. Contam. Hydrol., 112(1-4), 118-129.

Liu, J., Pereira, G.G., Regenauer-Lieb, K., (2014). From characterization of pore-structures to simulations of pore-scale fluid flow and the upscaling of permeability using microtomography: a case study of heterogeneous carbonates. J. Geochem. Explor., 144, 86–96.

Marica, F., Jofre, S.A., Mayer, K.U., Balcom, B.J., Al, T.A., (2011). Determination of spatially-resolved porosity, tracer distributions and diffusion coefficients in porous media using MRI measurements and numerical simulations. J. Contam. Hydrol., 125, 47-56.

Mayer, K.U., Frind, E.O., Blowes D.W., (2002). Multicomponent reactive transport modeling in variably saturated porous media using a generalized formulation for kinetically controlled reactions, Water Resour. Res., 38(9), 1174, doi:10.1029/2001WR000862.

Mon, A., Samper, J., Montenegro, L., Naves, A., Fernández, J., (2017). Long-term non-isothermal reactive transport model of compacted bentonite, concrete and corrosion products in a HLW repository in clay. J. Contam. Hydrol., http://dx.doi.org/10.1016/j.jconhyd.2016.12.006

Parkhurst, D.L., Appelo, C.A.J., (1999). User's guide to PHREEQC (version 2) - A computer program for speciation, batch-reaction, one-dimensional transport, and inverse geochemical calculations, U.S. Geol. Surv. Water Resour. Invest. Rep., 99-4259, 312 pp.

Parkhurst, D.L., Kipp, K.L., Engesgaard, P., Charlton S.R., (2002). PHAST - A program for simulating ground-water flow and multicomponent geochemical reactions, U.S. Geol. Surv., Denver, Col. [Available at http://wwwbrr.cr.usgs.gov/projects/GWC_coupled/phast/index.html.]

Samper, J., Lu, C., Montenegro, L., (2008a). Coupled hydrogeochemical calculations of the interactions of corrosion products and bentonite. Phys. Chem. Earth 33, S306–S316. http://dx.doi.org/10.1016/j.pce.2008.10.009.

Samper J., Zheng, L., Montenegro, L., Fernández, A.M., Rivas, P., (2008b). Coupled thermo-hydro-chemical models of compacted bentonite after FEBEX in situ test, Appl. Geochem., Vol 23/5: 1186-1201.

Samper, J., Xu, T., Yang, C. (2009). A sequential partly iterative approach for multicomponent reactive transport with CORE^{2D}. Comput. Geosci., http://dx.doi.org/10.1007/s10596-008-9119-5.

Samper, J., Yang, C., Zheng, L., Montenegro, L., Xu, T., Dai, Z., Zhang, G., Lu, C., Moreira, S., (2011). CORE^{2D}V4: A code for water flow, heat and solute transport, geochemical reactions, and microbial processes, Chapter 7 of the Electronic book Groundwater Reactive Transport Models, F Zhang, G-T Yeh, C Parker & X Shi (Ed), Bentham Science Publishers, pp 161-186, ISBN: 978-1-60805-029-1.

Samper, J., Naves, A., Montenegro, L., Mon, A., (2016). Reactive transport modelling of the long-term interactions of corrosion products and compacted bentonite in a HLW repository in granite: Uncertainties and relevance for performance assessment. Appl. Geochem., Vol 67, 42-51. http://dx.doi.org/10.1016/j.apgeochem.2016.02.001

Shao, H., Dmytrieva, S. V., Kolditz, O., Kulik, D. A., Pfingsten, W., Kosakowski, G., (2009a). Modeling reactive transport in a non-ideal aqueous-solid solution system. Appl. Geochem., 24(7), 1287-1300.

Shao, H., Kulik D. A., Berner, U., Kosakowski, G., Kolditz, O., (2009b). Modeling the competition between solid solution formation and cation exchange on the retardation of aqueous radium in an idealized bentonite column. Geochem. J., 43(6), e37-e42.

Simunek, J., Suares, D.L., (1993). UNSATCHEM-2D: Code for simulating two-dimensional variably saturated water flow, heat transport, carbon dioxide production and transport, and multicomponent solute transport with major ion equilibrium and kinetic chemistry, User's manual, U.S. Salinity Laboratory, Agricultural Research Service, U.S. Department of Agriculture, Riverside, California.

Steefel, C.I., (2001). CRUNCH: Software for modeling multicomponent, multidimensional reactive transport, user's guide, Rep. UCRL-MA-143182, Lawrence Livermore Nat. Lab., Livermore, Calif.

Steefel, C.I., De Paolo, D.J., Lichtner, P.C., (2005). Reactive transport modeling: an essential tool and a new research approach for earth sciences. Earth Planet. Sci. Lett. 20, 539-558. http://dx.doi.org/10.1016/j.epsl.2005.09.017.

Tyagi, M., Gimmi, T., Churakov, S., (2013). Multi-scale micro-structure generation strategy for upscaling transport in clays. Adv. Water Resour., 59, 181-195.

van der Lee, J., De Windt L., (2001). Present state and future directions of modeling of geochemistry in hydrogeological systems, J. Contam. Hydrol., 47(2-4), 265-282.

van der Lee, J., De Windt L., Lagneau V., Goblet P., (2003). Module-oriented modeling of reactive transport with HYTEC, Comput. Geosci., 29(3), 265-275.

van der Lee, J., (2005). Reactive transport modelling with HYTEC, user's guide and tutorial, Tech. Rep. LHM/RD/05/30, 114 pp., Cent. d'Inf. Géol. École des Mines, Fontainebleau, France.

Van Loon, L.R., Müller, W., Glaus, M.A., (2007). Anion exclusion effects in compacted bentonites: towards a better understanding of anion diffusion. Appl. Geochem., 22, 2536-2552.

Wanner, C., Eggenberger, U., Mäder, U., (2012). A chromate-contaminated site in southern Switzerland -part 2: Reactive transport modeling to optimize remediation options. Appl. Geochem., 27(3), 655-662.

Wanner, C., Sonnenthal, E.L., (2013). Assessing the control on the effective kinetic Cr isotope fractionation factor: A reactive transport modeling approach. Chem. Geol., 337-338, 88-98.

Wanner, C., Peiffer, L., Sonnenthal, E.L., Spycher, N., Iovenitti, J., Kennedy, B.M., (2014). Reactive transport modeling of the Dixie Valley geothermal area: Insights on flow and geothermometry. Geothermics, 51, 130-141. DOI: 10.1016/j.geothermics.2013.12.003.

Xie, M., Mayer, K.U., Claret, F., Alt-Epping, P., Jacques, D., Steefel, C., Chiaberge, C., Simunek, J., (2015). Implementation and evaluation of permeability-porosity and tortuosity-porosity relationships linked to mineral dissolution-precipitation. Computat. Geosci., 19, 655-671.

Xu, T., Sonnenthal, E., Spycher, N., Pruess, K., (2004). TOUGHREACT user's guide: A simulation program for non-isothermal multiphase reactive geochemical transport in variable saturated geologic media, Rep. LBNL-55460, 192 pp., Lawrence Berkeley Natl. Lab., Berkeley, Calif.

Xu, T., Sonnenthal, E., Spycher, N., Pruess, K., (2006). TOUGHREACT - A simulation program for non-isothermal multiphase reactive geochemical transport in variably saturated geologic media: Applications to geothermal injectivity and CO_2 geological sequestration, Comput. Geosci., 32(2), 145-165.

Xu, T., Spycher, N., Sonnenthal, E., Zhang, G., Zheng, L., Pruess, K., (2011). TOUGHREACT version 2.0: A simulator for subsurface reactive transport under non-isothermal multiphase flow conditions, Comput. Geosci., 37(6), 763-774.

Zheng, L., Samper, J., (2008). Coupled THMC model of FEBEX mock-up test. Physs. Chem. Earth., 33, S486-S498. http://dx.doi.org/10.1016/j.pce.2008.10.023.

Zheng, L., Samper, J., Montenegro, L., Fernández, A.M., (2010). A coupled THMC model of a heating and hydration laboratory experiment in unsaturated compacted FEBEX bentonite. J. Hydrol., 386, 80-94. http://dx.doi.org/10.1016/j.jhydrol.2010.03.009.

Zheng, L., Samper, J., Montenegro, L., (2011). A coupled THC model of the FEBEX in situ test with bentonite swelling and chemical and thermal osmosis. J. Contam. Hydrol., 126, 45-60.

APPENDIX 3. NUMERICAL FLOW AND REACTIVE TRANSPORT MODELS OF LABORATORY EXPERIMENTS WITH POROSITY CHANGES DUE TO DISSOLUTION/PRECIPITATION REACTIONS

This appendix presents numerical flow and reactive transport models of laboratory experiments with strong porosity changes due to dissolution/precipitation reactions. These laboratory experiments were carried out at the Paul Scherrer Institut (Switzerland). They were performed with CORE^{2D}V5. The results obtained with CORE^{2D}V5 have been compared with the experimental data reported by Poonoosamy et al. (2015) and the numerical results obtained with other reactive transport codes (benchmarking). A manuscript entitled "*Benchmarking of reactive transport codes for a 2D setup with mineral dissolution/precipitation reactions and feedback of transport parameters*" will be submitted soon to a SCI journal. In addition, the material presented in this appendix has been partly published in the following references:

→ Fernández Águila J., J. Samper, L. Montenegro, A. Mon & B. Pisani, 2015. Modelos numéricos de flujo y transporte de solutos reactivos de experimentos con fuertes cambios de porosidad. In: Jornadas de Zona no Saturada Vol. XII, Silvia Martínez y Antonio Sastre Ed, pp. 243-250. [in Spanish].

→ Poonoosamy J., G. Kosakowski, C. Wanner, P. Alt Epping, J.F. Águila, J. Samper, L. Montenegro, U. Mader & L.R. Van Loon, 2016. Benchmarking of reactive transport codes for a 2D setup with mineral dissolution/precipitation reactions and feedback on transport parameters. In: Book of Abstracts. International Workshop Subsurface Environmental Simulation Benchmarking Workshop V, A Coruña, October 2016, pp. 25-30.

→ Poonoosamy J., G. Kosakowski, C. Wanner, P. Alt Epping, J.F. Águila, J. Samper, L. Montenegro, U. Mader & L.R. Van Loon, 2017. Benchmarking of reactive transport codes for a 2D setup with mineral dissolution/precipitation reactions and feedback of transport parameters (to be submitted to Comput. Geosciences).

ABSTRACT

The dissolution/precipitation of minerals in porous media at the interfaces of materials with different properties modifies the porosity which in turn causes changes in transport parameters such as permeabilities and diffusion coefficients. Nowadays, porosity changes due to mineral dissolution/precipitation are being actively investigated in connection with deep geological disposal of nuclear waste where chemically reactive materials such as clays and concretes come into contact with one another. This appendix presents numerical flow and reactive transport models of laboratory experiments with strong porosity changes due to dissolution/precipitation reactions. The numerical models have been performed with the updated version of CORE^{2D}V5 by taking into account the changes in porosity due to mineral dissolution/precipitation and the feedback effect on flow, transport and chemical parameters (see Appendix 2). The laboratory experiments were performed at the Paul Scherrer Institut (PSI) located in Switzerland and they took place in a tank containing a reactive layer of strontium sulphate ($SrSO_4$(s), celestite), sandwiched between two layers of non-reacting quartz sand (SiO_2(s)). Several types of laboratory tests were performed with the same experimental setup (Poonoosamy et al., 2015). The numerical models have been used to simulate a transport experiment without chemical reactions and other experiments with reactive transport focused on porosity changes caused by the precipitation of barium sulphate ($BaSO_4$(s), barite) after injecting into the tank a solution with high concentration of $BaCl_2$. The injection of $BaCl_2$ into the tank enhanced the dissolution of strontium sulphate and the precipitation of barium sulphate. Changes in the porosity occurred during the experiment due to the difference in the molar volumes of strontium sulphate and barium sulphate. The results obtained with CORE^{2D}V5 have been compared with experimental data and with the numerical results obtained with other reactive transport codes such as TOUGHREACT, OpenGeoSys-GEM, Pflotran and MIN3P. The results obtained with CORE^{2D}V5 agree with the measured data and with the results computed with other codes. CORE^{2D}V5 has been used also to simulate the unsaturated stage of the experiment and evaluate the relevance of the transient saturation stage of the experiment.

A3.1. INTRODUCTION

The changes in porosity due to mineral dissolution/precipitation and the associated changes in transport and chemical parameters are of great interest for natural geological environments and for engineered underground systems. Numerous investigations are being carried out nowadays on porosity changes due to mineral dissolution/precipitation in connection with deep geological disposal of nuclear waste where chemically-different materials such as clays and concretes come into contact one with

another (Gaucher and Blanc, 2006). Porosity changes in natural porous media occur normally at a very slow rate, but in the long term can be of pivotal importance for the migration of fluids and solutes. If the porosity increases substantially, preferential fluid migration pathways may develop, accelerating solute transport. On the other hand, if the porosity decreases significantly, clogging may occur, and fluid and solute migration may be prevented.

Reactive transport models are commonly used to predict the evolution of systems that are not experimentally accessible in space and time. These models solve the set of equations which describe the transport of mobile chemical species together with the geochemical reactions. Reactive transport models can be used to study the behaviour of CO_2 in saline aquifers (Lagneau et al., 2005; Chasset et al., 2011), nuclear waste repositories (De Windt et al., 2004; Gaucher and Blanc, 2006; De Windt et al., 2007; Samper et al., 2008a,b; Zheng et al., 2010, 2011; Kosakowski and Berner, 2013; Berner et al. 2013; Samper et al., 2016), geothermal systems (Alt-Epping et al. 2013a; 2013b; Wanner et al., 2014; Diamond and Alt-Epping, 2014) or environmental remediation (Wanner et al., 2012; Jamieson-Hanes et al., 2012; Wanner and Sonnenthal, 2013).

Porosity changes due to dissolution/precipitation reactions and their feedback on transport parameters are accounted for in numerical models by considering empirical formulae such as the Kozeny-Carman equation for porosity/permeability (Carman, 1937), and the Archie's law for porosity/diffusivity (Archie, 1942). These empirical laws are parameterized either experimentally (e.g., Boving and Grathwohl, 2001; Van Loon et al., 2007; Marica et al., 2011) or by up-scaling from micro-scale models (e.g., Liu et al., 2014; Tyagi et al., 2013). Several numerical codes are able to handle the feedback of chemistry on flow and mass transport such as HYTEC (van der Lee and De Windt, 2001; van der Lee et al., 2003: van der Lee, 2005), TOUGHREACT (Xu et al., 2004, 2006, 2011), PHREEQC (Parkhurst and Appelo, 1999), MIN3P (Mayer et al., 2002, 2010), PHAST (Parkhurst et al., 2002) and CRUNCH (Steefel, 2001). CORE^{2D}V5 (Samper et al., 2009, 2011) has been updated in this dissertation to take into account the feedback effect of the porosity changes on transport and chemical parameters (see Appendix 2).

There is a need to evaluate the capabilities and the correctness of the implemented features and the performance of the reactive transport codes. The results simulated with numerical models for porosity changes depend on the assumed rate laws for reactions kinetics and spatial discretization (Marty et al., 2009). Whenever possible, computer codes are verified by comparing the numerical solutions with analytic solutions. However, available analytical solutions for problems involving porosity changes are limited (Hayek et al 2011, 2012; Lagneau and van der Lee, 2010). Another possibility consists on comparing the results obtained with several reactive transport codes (benchmarking) and comparing the results of laboratory and field experiments with numerical models (Lagneau, 2000; Tartakovsky, 2008;

Katz et al., 2011). Benchmarking cases with porosity enhancement, reduction or clogging are of great interest because the coupling between transport and chemistry is commonly encountered in real geosystems (Xie et al., 2015).

This appendix presents flow and reactive transport numerical models of laboratory experiments with strong porosity changes due to dissolution/precipitation reactions. These laboratory experiments were carried out at the Paul Scherrer Institut (PSI), Switzerland. The models were performed with CORE^{2D}V5. The results obtained with CORE^{2D}V5 have been compared with the experimental data of Poonoosamy et al. (2015) and with the numerical results obtained with TOUGHREACT, OpenGeoSys-GEM, Pflotran and MIN3P for saturated conditions. The model performed with CORE^{2D}V5 has been used to simulate the initial transient stage of the experiment during which the flow was unsaturated.

A3.2. LABORATORY EXPERIMENTS

The laboratory experiments were carried out at the Paul Scherrer Institut (PSI). PSI is the largest research centre for natural and engineering sciences in Switzerland. Cutting-edge research is performed in matter and materials, energy and environment and human health. The experiments aimed at studying the porosity changes due to mineral dissolution/precipitation and testing numerical models with measured data (Poonoosamy et al., 2015). The experiments were conducted in a transparent tank containing a reactive layer of strontium sulphate ($SrSO_4$(s), celestite), sandwiched between two layers of essentially non-reacting quartz sand. The tank is square and its dimensions are 10 x 10 cm. The tank has a thickness of 1 cm and has two holes of 0.033 cm. One of these holes is located 0.965 cm from the bottom of the tank and is the inlet of water into the tank. The other hole is on the opposite corner of the tank and constitutes the outlet of the tank. Figure A3.1 shows the tank in which the experiments were performed (Poonoosamy et al., 2015). The tank has three zones. The first (*Z1)* and the third zones *(Z3*) have a width of 4.5 cm and are made up of non-reacting quartz sand. The sand used in the experiment has a purity of 99.9% and a grain size of 0.1-0.3 mm with a coefficient of variation of 0.96. Zones *Z1* and *Z3* have different degrees of compaction. The porosity in zone *Z1* is equal to 0.34 ± 0.02 while the porosity in zone *Z3* is equal to 0.40 ± 0.02. The second zone *Z2* is a 1 cm wide reactive layer of strontium sulphate and is sandwiched between zones *Z1* and *Z3*. Natural strontium sulphate from Madagascar (purity of 99.7%) was used in the experiments. Particles of different grain sizes were mixed. The strontium sulphate was compacted to a porosity of 0.33 ± 0.02. The permeability of strontium sulphate ranges from 10^{-14} m^2 to $6 \cdot 10^{-14}$ m^2 and is three orders of magnitude smaller than the permeability of the sand layers.

Data were collected at the back of the tank in 4 ports *(a, b, c, d)*. The (*x*, *z*) coordinates in mm of the ports *a*, *b*, *c*, and *d* are (20.00, 20.00), (80.00, 80.00), (80.00, 20.00) and (20.00, 80.00), respectively. In addition, the following three straight lines were selected for the purpose of comparing model results: 1) Line 1 which connects the inlet and the outlet of the tank, 2) A horizontal line at $z = 0.01$ m (line 2) and 3) A vertical line at $x = 0.01$ m (line 3) (see Figure A3.1).

Several types of tests were performed with this experimental setup. The following test were simulated with CORE^{2D}V5: 1) A test without chemical reactions and 2) A test focused on the porosity changes caused by the precipitation of barium sulphate. In the first test without chemical reactions, a conservative tracer was injected at the inlet of the tank. Nevertheless, prior to making the tracer test, a saturated solution of strontium sulphate was injected in the tank for 24 hours to stablish a steady flow field. After that, a pulse (0.5 mL at rate of 20 µL/min) of dye tracer with a concentration of 3 g/L was injected at the inlet followed by a continuous inflow of a saturated solution of strontium sulphate at a flow rate of 20 µL/min. The tracer evolution in the tank was monitored for 20 hours. The experiment was carried out at a temperature of 25 ± 1°C. A barium chloride solution ($BaCl_2$) with a concentration of 0.3 mol/L was injected at the inlet of the tank at a flow rate of 20 µL/min in the reactive transport test. The injection of $BaCl_2$ into the tank enhanced the dissolution of strontium sulphate and the precipitation of barium sulphate. The porosity changed during the experiment because the molar volumes of strontium sulphate and barium sulphate are different. The test lasted 300 hours. The reactive transport test was performed also at 25 ± 1°C.

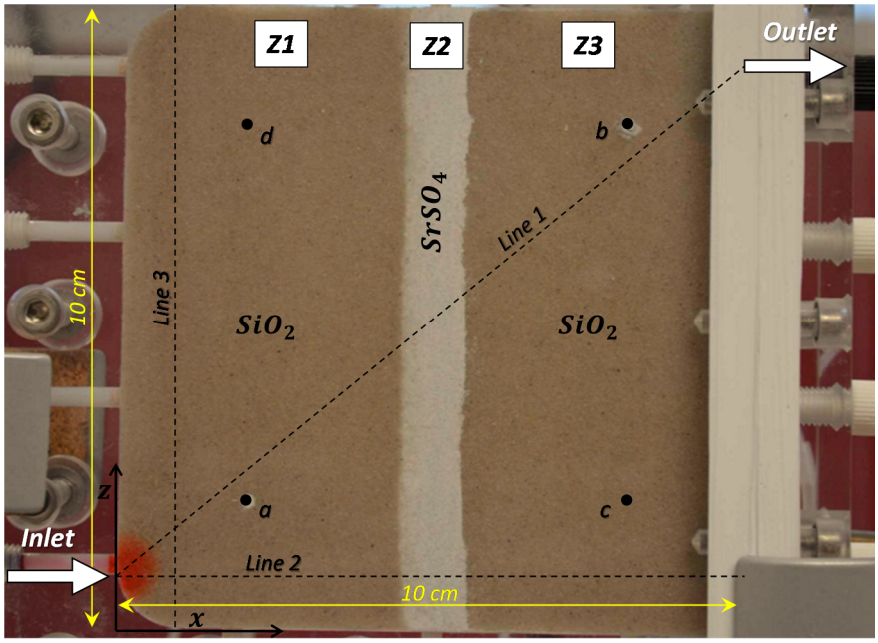

Figure A3.1. Experimental setup of the reactive transport tests. Zones *Z1* and *Z3* are made up of non-reacting quartz sand while zone *Z2* is a reactive layer of strontium sulphate. Data were collected at ports *a*, *b*, *c* and *d*. Lines 1, 2 and 3 were used for comparing model results (Poonoosamy et al., 2015).

A3.3. NUMERICAL MODELS

The laboratory experiments of Poonoosamy et al. (2015) were simulated with 2-D numerical models using the updated version of CORE^{2D}V5 which takes into account the feedback effect of the porosity changes due to mineral dissolution/precipitation on flow and transport parameters. Numerical models were performed for the following tests: 1) Conservative transport (Case 1) and 2) Reactive transport focused on porosity changes (Case 2). Figure A3.2 shows a sketch of the experimental setup used to perform the 2-D numerical models. The model domain was discretized with a 2-D grid of triangular finite elements. Three material zones were defined in the model which coincide with *Z1*, *Z2* and *Z3* zones in Figure A3.2. The triangular finite elements of the grid have a size equal to 1.5 mm, except in zone *Z2* (reactive layer) and near the inlet and outlet of the tank where the grid is refined up to 1 mm. The grid used in the base run has 5815 nodes and 11319 elements. Several runs were performed to evaluate the sensitivity of model results to grid refinement. The following grids were considered: 1) A coarse grid with 1460 nodes and 2790 elements, 2) An intermediate grid with 3631 nodes and 7059 elements, 3) A fine grid with 5815 nodes and 11319 elements and 4) A very fine grid with 10201 nodes and 20000 elements. Figure A3.3 shows the grids used with CORE^{2D}V5 to evaluate the sensibility of model results to numerical discretization.

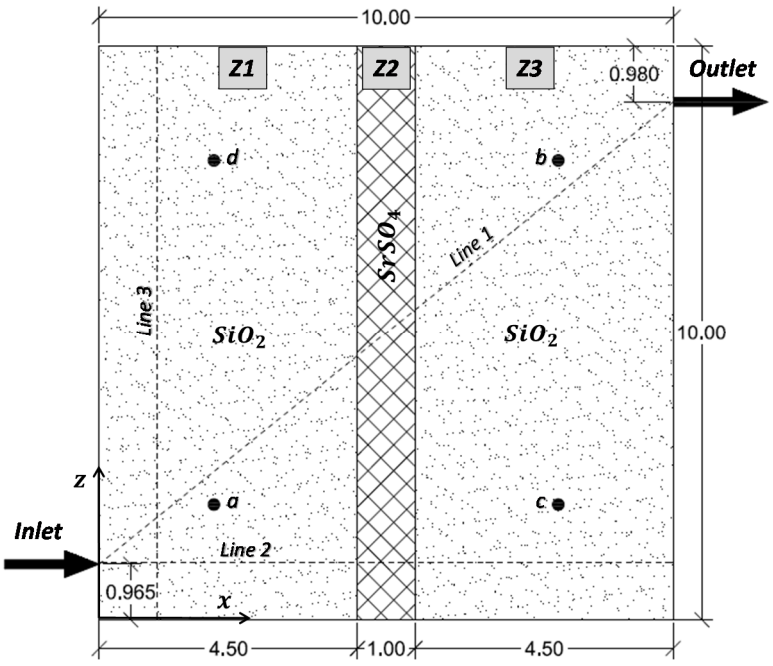

Figure A3.2. Sketch of the experimental setup (dimensions in cm).

The parameters of the three zones used in the numerical models of Cases 1 and 2 are listed in Table A3.1. Case 1 considers the injection of a concentrated non-reacting solution into a saturated porous medium. The water inflow is equal to 20 µL/min. The water inflow and outflow are distributed

in five nodes in the fine and very fine finite element grids and in three nodes in the coarse and intermediate grids (see Figure A3.3). The model was performed for a total period of 24 hours and the time domain was divided into time steps equal to 1 s. The conservative tracer is injected during the first 25 minutes of simulation with a concentration of 3 g/L. The zone *Z2*, composed of $SrSO_4(s)$, is assumed to be nonreactive in this case. The tracer breakthrough curves at ports *c* and *d*, the contour plots of tracer concentrations and the velocity profiles along lines 1, 2 and 3 were computed with CORE^{2D}V5 and compared with the measured data and the model predictions of other reactive transport codes such as TOUGHREACT, OpenGeoSys-GEM, Pflotran and MIN3P.

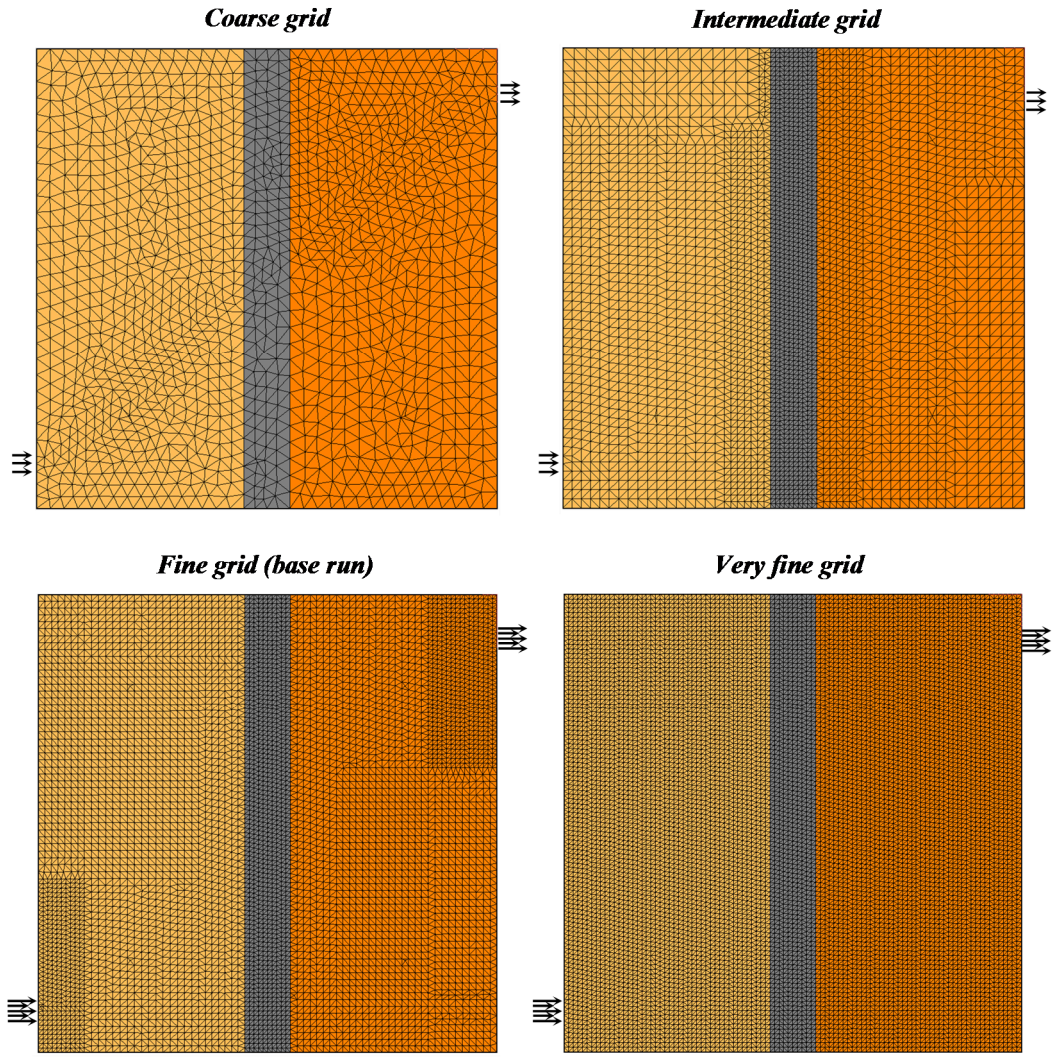

Figure A3.3. Finite element grids used with CORE^{2D}V5 to evaluate the sensitivity of model results to grid refinement.

A reactive transport model was performed with the updated version of CORE^{2D}V5 for Case 2. This case considers mineral dissolution/precipitation with porosity changes. Similar to Case 1, the water inflow is equal to 20 µL/min. However, a highly concentrated solution (0.3 mol/L) of barium chloride

($BaCl_2$) was injected into the tank in Case 2. The injection of barium chloride leads to the precipitation of barium sulphate and the dissolution of strontium sulphate according to:

$$BaCl_{2(aq)} + SrSO_{4(s)} \rightarrow BaSO_{4(s)} + SrCl_{2(aq)} \quad (3.1)$$

This sequence of reactions leads to changes in porosity because the molar volume of $BaSO_4$ is larger than the molar volume of $SrSO_4$. The changes in porosity lead in turn to changes in flow, transport and chemical parameters such as permeability, diffusion coefficient and mineral specific surface. The reactive zone *Z2* has an initial porosity of 0.33 and is composed of small-grain and large-grain celestites.

Barite precipitation is assumed to occur at chemical equilibrium. The dissolution of strontium sulphate, however, is simulated with a kinetic law. The dissolution/precipitation reactions and their equilibrium constants at 25°C are given by:

$$SrSO_4(s) \leftrightarrow Sr^{2+} + {SO_4}^{2-} \qquad logK = -6.63 \quad (3.2)$$

$$BaSO_4(s) \leftrightarrow Ba^{2+} + {SO_4}^{2-} \qquad logK = -9.97 \quad (3.3)$$

The kinetic rate of celestite dissolution at pH = 5.6, r_m, is calculated from:

$$r_m = S\, k_m\, (1 - \Omega_m) \quad (3.4)$$

where S is the reactive surface area of celestite, k_m is the rate constant at 25ºC which is equal to $10^{-5.66}$ mol/m^2/s and Ω_m is the ratio of ion activity product to the equilibrium constant (Dove and Czank, 1995; Palandri and Kharaka, 2004). The reactive surface area is computed from:

$$S = V_m\, A_m \quad (3.5)$$

where V_m is the mineral volume fraction and A_m is the mineral surface area (surface area per unit volume of mineral). Different kinetic rates of dissolution were used for the two grain celestites because small-grain and large-grain celestites have different surface areas. They are equal to 20000 and 100 m^2 of mineral/m^3 of mineral, respectively. The general kinetic rate expression of mineral dissolution/precipitation used in CORE^{2D}V5 was adapted to Equations 3.4 and 3.5.

The geochemical model accounts for the following primary species: H_2O, H^+, Cl^-, SO_4^{2-} Sr^{2+} and Ba^{2+}. The chemical compositions of the initial and the boundary waters are listed in Table A3.2. The total simulation time is equal to 300 hours.

The porosity changes due to mineral dissolution/precipitation. Flow and transport parameters such as permeability and diffusion coefficient were parameterized as a function of porosity in the

updated version of CORE^{2D}V5 (see Appendix 2). Permeability is related to porosity according to the Kozany-Carman equation (Carman, 1937). The following Archie equation was used in all the reactive transport codes to relate the effective diffusion, D_e, to porosity, ϕ, (Archie, 1942):

$$D_e = D_0\, \phi^m \tag{3.6}$$

where D_0 is the pore diffusion coefficient in pure water and m is an empirical coefficient which was assumed equal to 1 in Case 2.

Table A3.1. Parameters of the zones *Z1*, *Z2* and *Z3* used for modelling the laboratory experiments (see Figure A3.1).

Parameters	Z1	Z2	Z3
Width (m)	0.045	0.010	0.045
Initial porosity (ϕ_0)	0.34	0.33	0.40
Initial permeability k_0 (m^2)	$1.82\cdot10^{-11}$	$1.80\cdot10^{-14}$	$1.82\cdot10^{-11}$
Dispersivity α (m) Case 1	10^{-4}	10^{-4}	10^{-4}
Dispersivity α (m) Case 2	$5\cdot10^{-4}$	$5\cdot10^{-4}$	$5\cdot10^{-4}$
Pore diffusion coefficient (m^2/s)	10^{-9}	10^{-9}	10^{-9}
Total volume fraction of $SrSO_4$(s)	0	0.67	0
Volume fraction of small-grain $SrSO_4$(s)	0	0.2233	0
Volume fraction of large-grain $SrSO_4$(s)	0	0.4467	0

Table A3.2. Chemical composition of the initial and boundary waters considered in the numerical model for Case 2.

Species	Initial water	Boundary water
pH	5.6	5.6
Cl (mol/L)	10^{-5}	0.6
SO_4^{2-} (mol/L)	10^{-5}	10^{-5}
Sr^{2+} (mol/L)	10^{-5}	10^{-5}
Ba^{2+} (mol/L)	10^{-5}	$3\cdot10^{-5}$

A3.4. CONSERVATIVE TRANSPORT MODEL RESULTS

The results of the conservative transport model performed with CORE^{2D}V5 (Samper et al., 2009, 2011) were compared with the measured data and the predictions performed with TOUGHREACT (Xu

et al., 2004, 2006, 2011), OpenGeoSys-GEM (Shao et al., 2009; Kosakowski and Wanatabe, 2013), Pflotran (Lichtner et al., 2013) and MIN3P (Mayer et al., 2002, 2010).

The numerical flow model was carried out in saturated conditions because the tank was completely saturated with a strontium sulphate solution before the tracer experiment. In this case, the flow equation was solved with CORE^{2D}V5 only once at the beginning of the simulation because the boundary conditions and the inflow did not change with time during the experiment. Figure A3.4 shows the contour plots of the computed hydraulic heads and the flow velocity vectors computed with CORE^{2D}V5. There is a strong gradient of the hydraulic heads in zone *Z2* because the permeability in this zone is three orders of magnitude smaller than the permeability in zones *Z1* and *Z3*. The water flows from the inlet to the outlet of the tank. The largest flow velocities are located near the inlet and the outlet of the tank while the smallest velocities occur at the upper left and the lower right corners of the model domain which are stagnant zones.

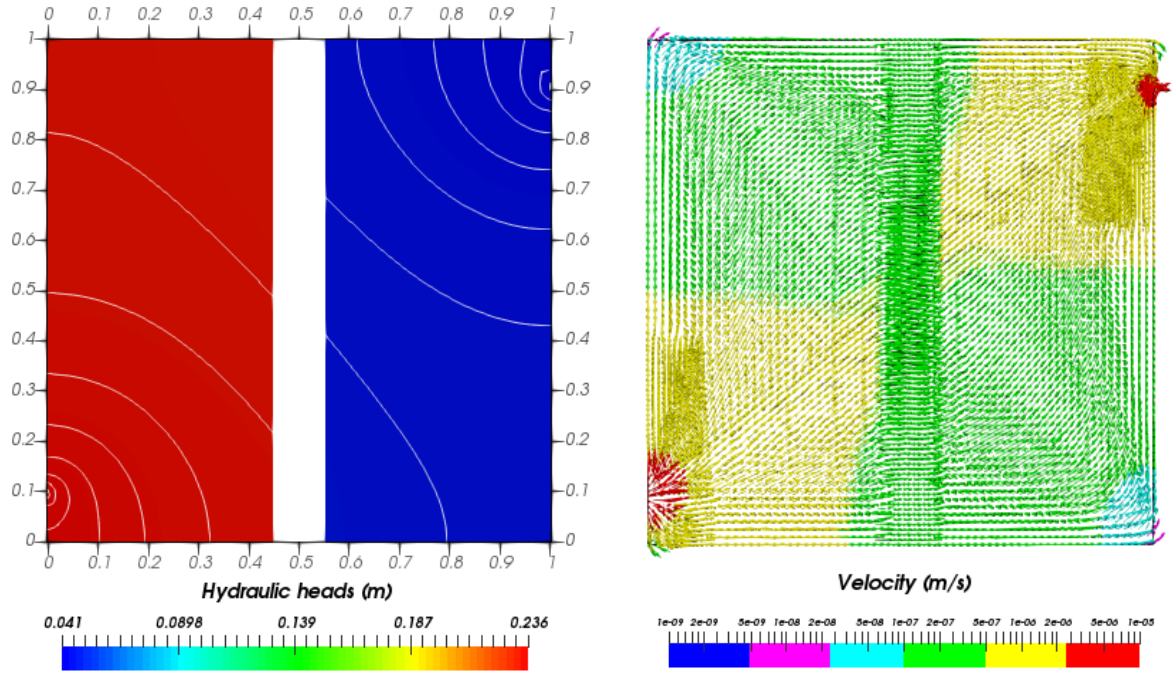

Figure A3.4. Contour plots of the computed hydraulic heads (left) and water velocity vectors (right) computed with CORE^{2D}V5 (dimensions in dm).

Water velocities along lines 1, 2 and 3 were computed with CORE^{2D}V5. Figure A3.5 shows the velocities computed with CORE^{2D}V5, TOUGHREACT, OpenGeoSys-GEM and Pflotran along the main diagonal (line 1). The velocities computed with all the codes agree for the most part. However, there are local differences among the velocities near the inlet and the outlet. These differences are attributed to differences in the numerical implementation of the boundary conditions in the reactive transport codes. The number of nodes considered at the inlet and the outlet are different. CORE^{2D}V5

and OpenGeoSys-GEM distribute the water inflow evenly in 5 nodes and 4 nodes, respectively. TOUGHREACT distributes the inflow in a single element.

Figure A3.6 shows the horizontal component of the velocity (V_x) computed with CORE^{2D}V5, TOUGHREACT, OpenGeoSys-GEM and Pflotran along line 2 which begins at the inlet of the tank. There are differences in the velocities computed with these codes near the inlet. Figure A3.7 shows the vertical component of the velocity (V_z) computed with several reactive transport codes along line 3. The velocities computed with the codes are similar in this case because line 3 is far from the inlet and outlet of the tank.

Figure A3.8 shows the tracer concentration contour plots computed with CORE^{2D}V5 and the tracer images recorded in the lab by Poonoosamy et al. (2015) at 3, 9, 15 and 20 hours. Model results reproduce the patterns of the experimental data. The tracer contour plots describe concentric circles at the beginning of the simulation (t = 3 hours). The circles get slightly distorted as the tracer moves towards the less permeable zone *Z2* (t = 9 hours). The maximum computed tracer concentration decreases with time due to tracer dispersion. The maximum tracer concentrations are smaller than 0.20 g/L after 15 hours.

Figure A3.9 and Figure A3.10 show the tracer breakthrough curves at ports *c* and *d*, respectively, computed with CORE^{2D}V5, TOUGHREACT, OpenGeoSys-GEM, Pflotran and MIN3P. Port *d* is located in zone *Z1* while port *c* is located in zone *Z3* of the tank (see Figure A3.1). The tracer has to travel through the low permeability zone *Z2* to reach port *c*. For this reason, the arrival time of the tracer to port *c* is greater than the time of arrival of the tracer to port *d*. In addition, the maximum computed tracer concentration in port *d* (0.13 g/L) is greater than that in port *c* (0.1 g/L). There are some differences in the tracer breakthrough curves computed with different codes at ports *c* and *d*. The concentrations computed with CORE^{2D}V5 are similar to those computed with OpenGeoSys-GEM. On the other hand, the concentrations computed with TOUGHREACT, Pflotran and MIN3P are similar among them and differ from those computed with CORE^{2D}V5 and OpenGeoSys-GEM. These differences are due to differences in the numerical methods and the dispersion parameters of the reactive transport codes. The longitudinal dispersivity is equal to the transverse dispersivity in OpenGeoSys-GEM and CORE^{2D}V5. PFlotran considered only longitudinal dispersivity with no transversal dispersion. Additional calculations performed with PFlotran with a diffusion coefficient two times larger than the reference diffusion provide breakthrough curves similar to those computed with CORE^{2D}V5 and OpenGeoSys-GEM. In spite of these small differences, all the codes provide similar results for the tracer breakthrough curves and the general evolution of the tracer concentrations.

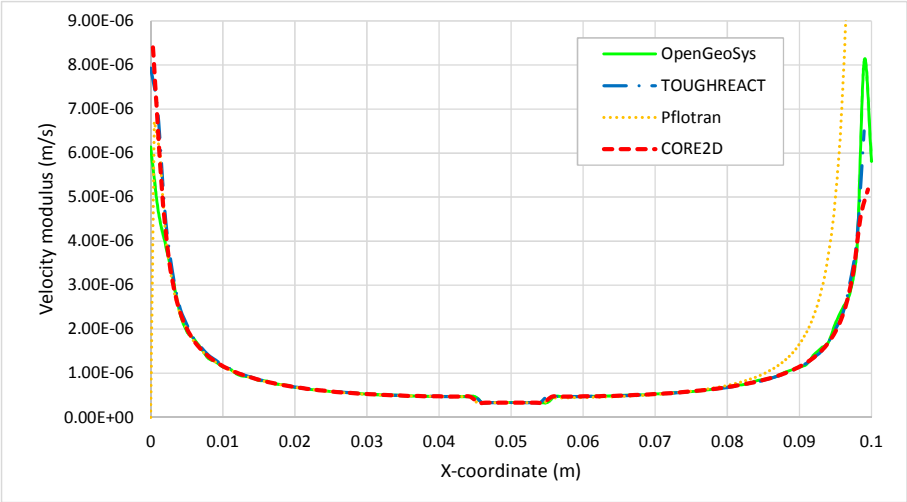

Figure A3.5. Modulus of the velocity vector along line 1 computed with CORE^{2D}V5, TOUGHREACT, OpenGeoSys-GEM and Pflotran.

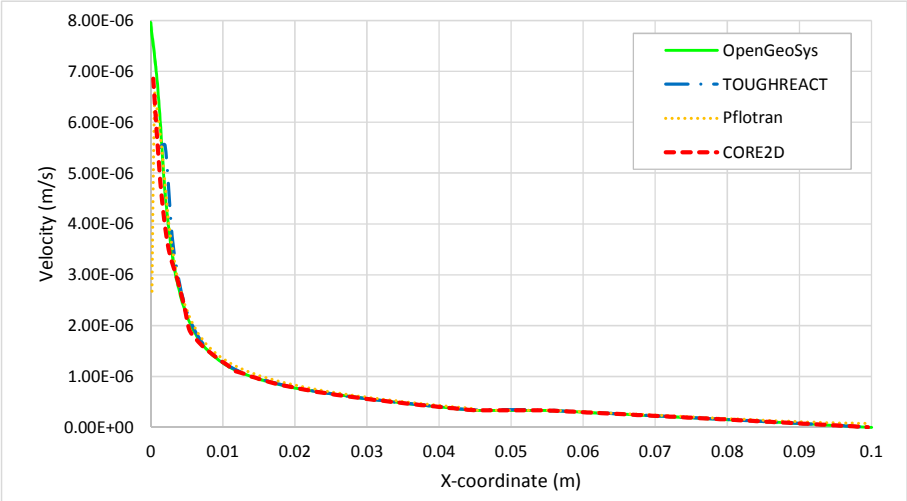

Figure A3.6. Horizontal component of the velocity (V_x) computed with CORE^{2D}V5, TOUGHREACT, OpenGeoSys-GEM and Pflotran along line 2.

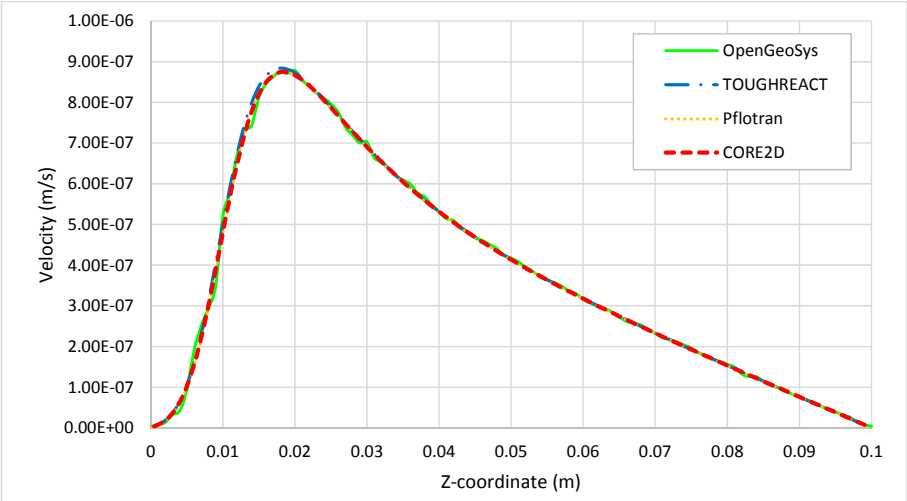

Figure A3.7. Vertical component of the velocity (V_z) computed with CORE^{2D}V5, TOUGHREACT, OpenGeoSys-GEM and Pflotran along line 3.

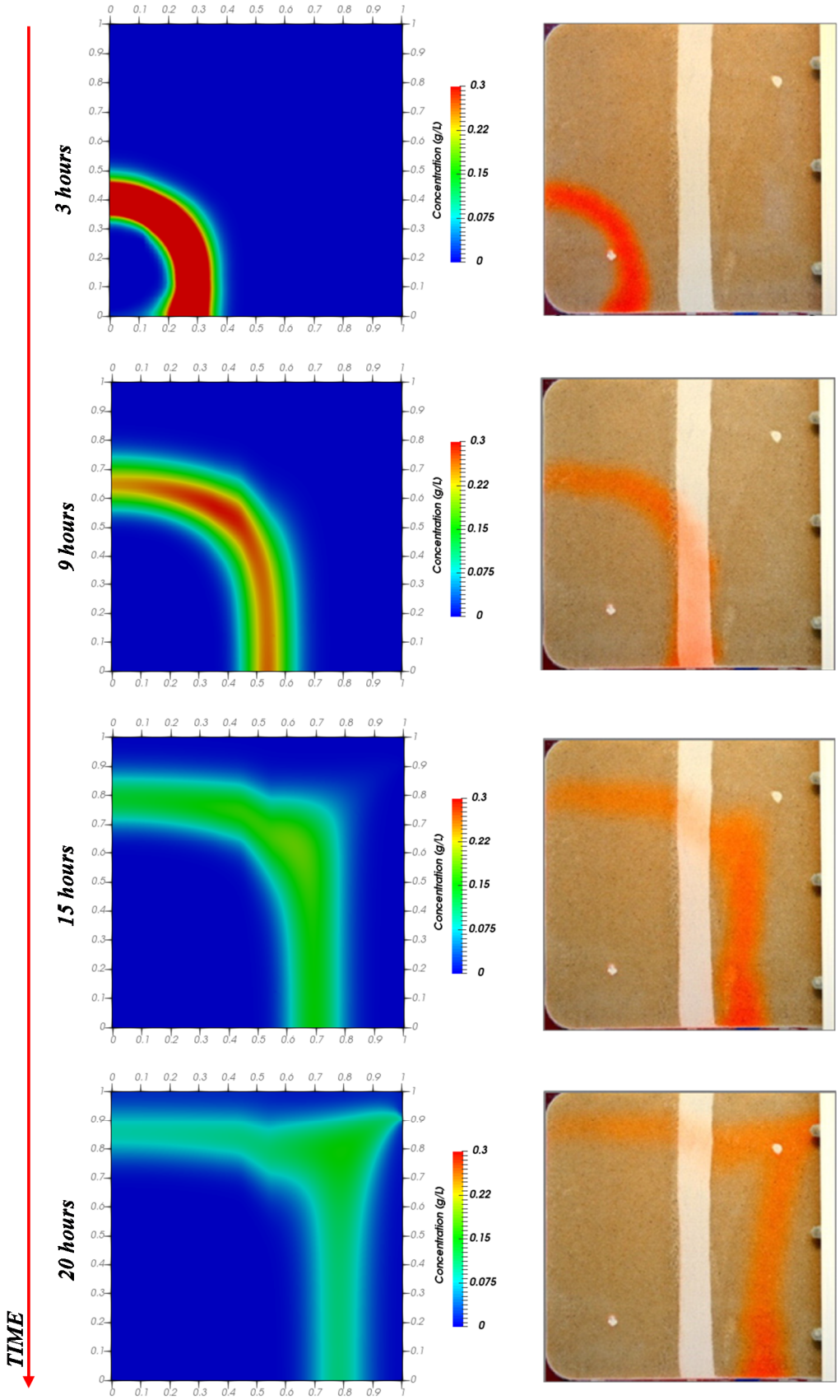

Figure A3.8. Tracer concentration contour plots computed with CORE^{2D}V5 (left) and tracer images recorded in the lab by Poonoosamy et al. (2015) (right) at 3, 9, 15 and 20 hours.

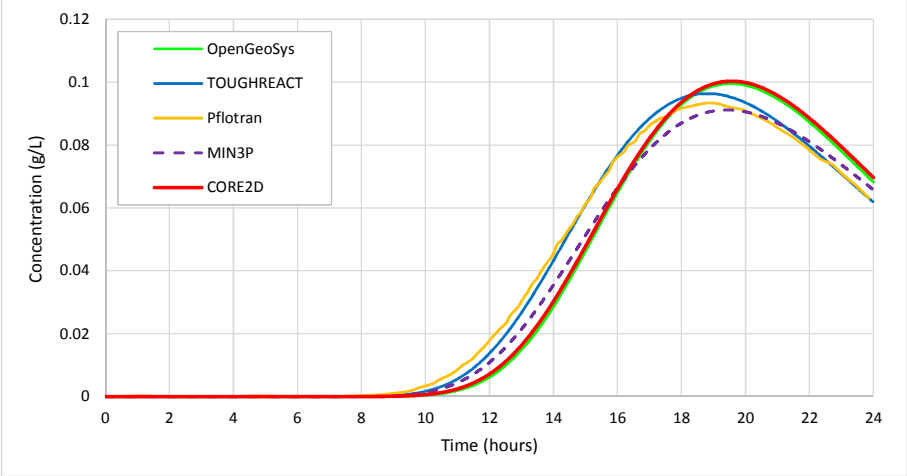

Figure A3.9. Tracer breakthrough curves at port *c* computed with CORE^{2D}V5, TOUGHREACT, OpenGeoSys-GEM, Pflotran and MIN3P.

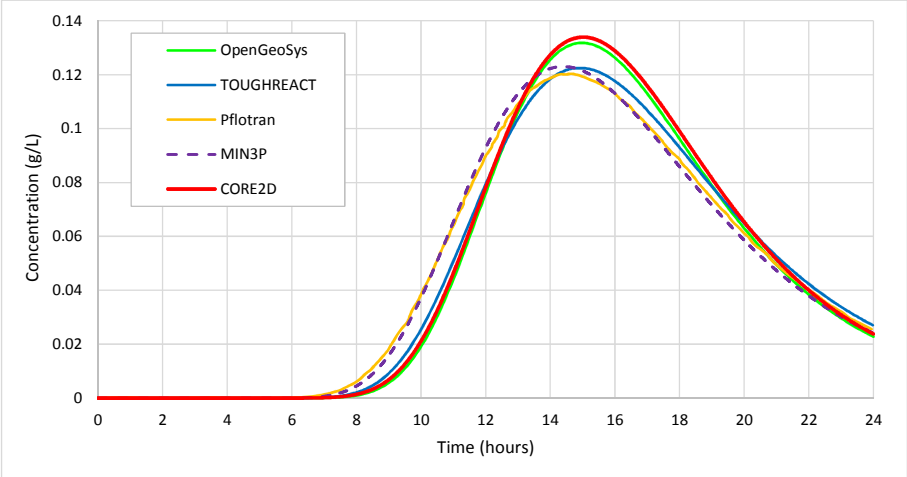

Figure A3.10. Tracer breakthrough curves at port *d* computed with CORE^{2D}V5, TOUGHREACT, OpenGeoSys-GEM, Pflotran and MIN3P.

The discretization errors of the simulations performed with CORE^{2D}V5 have been quantified by performing additional simulations with the following grids: 1) A coarse grid with 1460 nodes and 2790 elements, 2) An intermediate grid with 3631 nodes and 7059 elements, 3) A fine grid with 5815 nodes and 11319 elements and 4) A very fine grid with 10201 nodes and 20000 elements. The number of nodes considered at the inlet and at the outlet of the tank is not the same for all models. The injection of the fluid is evenly distributed in 3 nodes in the coarse and intermediate grids and in 5 nodes in the fine and very fine grids. Similarly, at the outflow boundary, the discharge is distributed in 3 nodes in the coarse and intermediate grids and in 5 nodes in the fine and very fine grids.

Figure A3.11 shows the velocities computed with CORE^{2D}V5 along line 1 (the main diagonal going from the inlet to the outlet of the tank) with finite element grids of increasing refinement. Model results obtained with the four finite element grids are in good agreement, although there are some

differences in the velocities computed near the inlet and the outlet of the tank. These differences are related to the grid size and the number of nodes used to specify the boundary conditions at the inlet and the outlet of the tank. The flow velocity vector in CORE^{2D} is computed for each element of the finite element grid. The origin of the flow velocity vector in a given element is the barycentre of the element. The size of the triangular elements and the distance between the barycentre of the element and the boundary nodes to simulate the inlet and outlet of the tank in the coarse grids are greater than in the refined grids. For this reason, the flow velocities in the elements closest to the inlet and outlet of the tank computed with coarse and intermediate grids are smaller than the flow velocities computed with the fine and very fine grids (Figure A3.11).

Figure A3.12 shows the horizontal component of velocity (V_x) computed with CORE^{2D}V5 along line 2 with grids of increasing refinement. There are some differences between the velocities computed at the inlet of the tank with different grids. Figure A3.13 shows the vertical component of velocity (V_z) computed with CORE^{2D}V5 along line 3 with the four finite element grids. The velocities computed with the intermediate, fine and very fine grids are similar. The velocities computed with the coarse grid, however, are slightly smaller than the velocities computed with the other grids.

Figure A3.14 shows the tracer breakthrough curves at ports *c* and *d* computed with CORE^{2D}V5 with finite element grids of increasing refinement. The numerical dispersion is reduced by refining the grid. In fact, the peak tracer concentrations in both ports are largest for the finest grids.

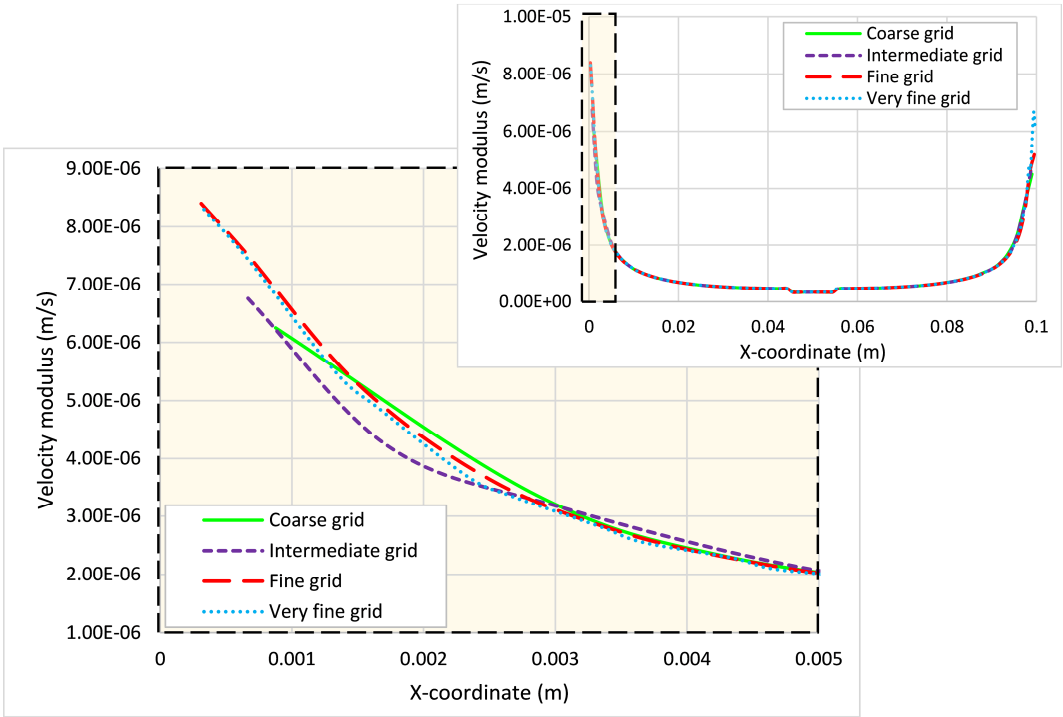

Figure A3.11. Modulus of the velocity vector along line 1 (top) and a zoom near the inlet (bottom) computed with CORE^{2D}V5 with finite element grids of increasing refinement.

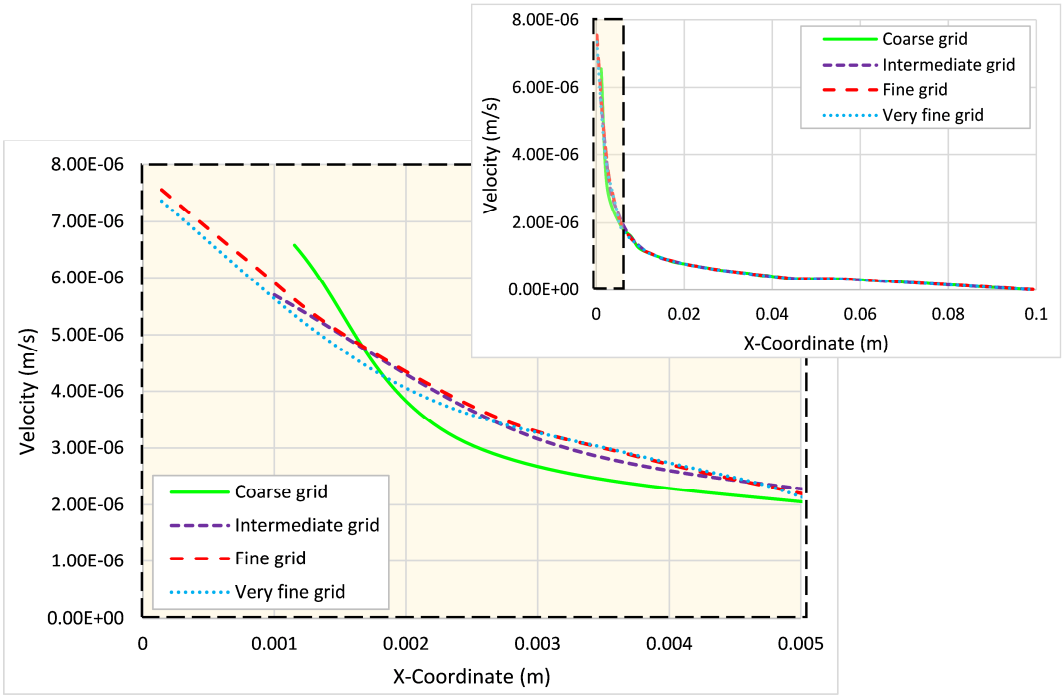

Figure A3.12. Vertical component of the velocity (V_x) computed with CORE^{2D}V5 along line 2 (top) and a zoom near the inlet (bottom) with grids of increasing refinement.

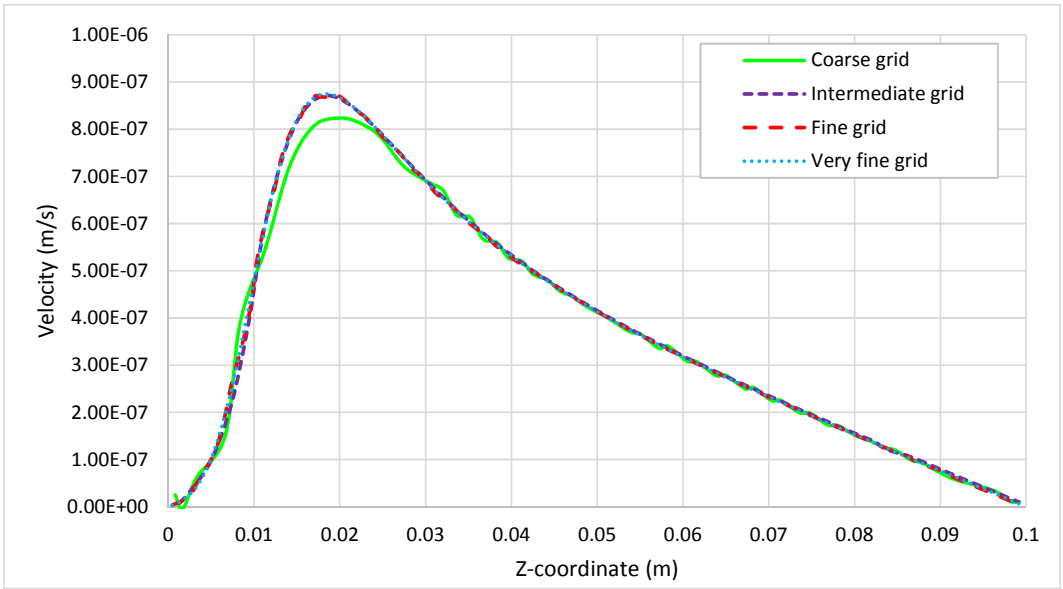

Figure A3.13. Vertical component of the velocity (V_z) computed with CORE^{2D}V5 along line 3 with grids of increasing refinement.

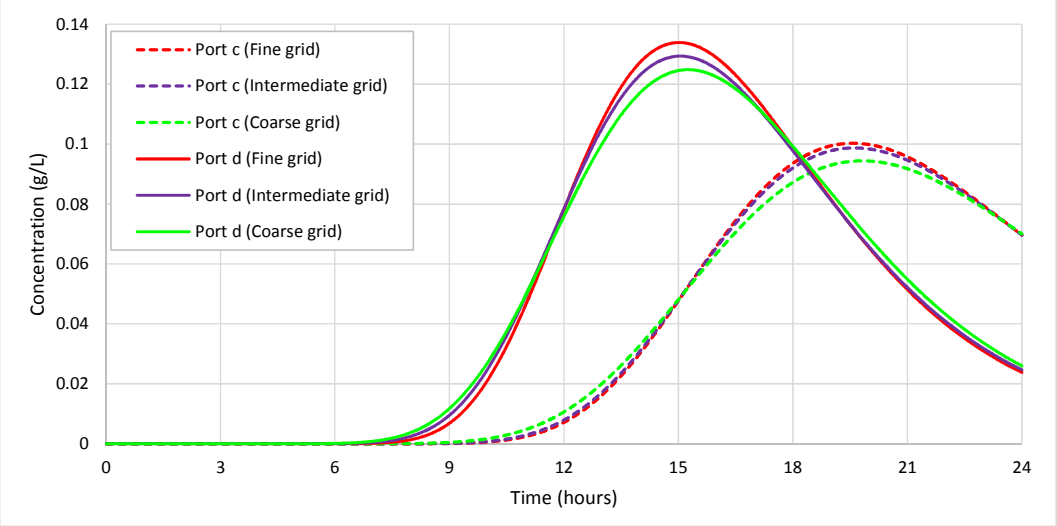

Figure A3.14. Tracer breakthrough curves at ports *c* and *d* computed with CORE^{2D}V5 with finite element grids of increasing refinement.

A3.5. MODEL RESULTS FOR REACTIVE TRANSPORT

A reactive transport model was performed with the updated version of CORE^{2D}V5 by taking into account the porosity changes due to mineral dissolution/precipitation and dynamically updating the flow, transport and chemical parameters. The results obtained with CORE^{2D}V5 were compared with laboratory measured data and with the numerical results of TOUGHREACT, OpenGeoSys-GEM, Pflotran and MIN3P. In Case 2, the flow equation is solved each time step by taking into account the changes in permeability. The numerical model has been performed for a total period of 300 hours and the time domain was divided into time steps ranging from 1 to 3 s.

When a concentrated $BaCl_2$ solution reaches the reactive zone *Z2*, the dissolution of celestite is triggered and barite precipitates. Figure A3.15 shows the time evolution of the total amounts of $BaSO_4$(s) and $SrSO_4$(s) in the tank computed with CORE^{2D}V5, TOUGHREACT, OpenGeoSys-GEM, Pflotran and MIN3P. All the reactive transport codes give similar results. The total amounts of $BaSO_4$(s) and $SrSO_4$(s) change due to mineral dissolution and precipitation. $SrSO_4$(s) dissolves at a constant rate of 0.2 mmol/h during the first 150 hours. Later, the dissolution rate slows down. Similarly, the total amount of precipitated barite increases during the first 150 hours and slowly builds up to 0.043 mol at 300 hours. The precipitation of barite during the first 150 hours is fast due to the dissolution of the small-grain celestite. Once the small-grain celestite is exhausted, the only source of dissolved SO_4^{2-} is the dissolution of large-grain celestite which has a much smaller rate.

Figure A3.16 shows the plots of the volume fractions of small-grain celestite computed with CORE^{2D}V5 at 10, 50, 150 and 300 hours. The initial volume fraction of small-grain celestite is equal to 0.223 in zone *Z2* and 0 in the rest of the model domain. Small-grain celestite dissolves steadily in zone *Z2*. The small-grain celestite begins to dissolve after 10 hours in the left part of zone *Z2*. The dissolution of small-grain celestite after 50 hours of simulation occurs throughout the entire reactive zone. The volume fraction of small-grain celestite is approximately equal to 0.09 in zone *Z2* after 150 hours and approximately equal to 0.03 after 300 hours. The changes in the volume fraction of large-grain celestite during the 300 hours of simulation are extremely small because its reactive surface area is very small. Figure A3.17 shows the plots of the barite volume fraction computed with CORE^{2D}V5 at 10, 50, 150 and 300 hours. Barite precipitates only in zone *Z2*. Precipitation takes place in a small part of zone *Z2* after 10 years. Barite precipitation extends to the entire zone *Z2* after 50 hours. The volume fraction of barite is approximately equal to 0.16 in zone *Z2* after 150 hours and approximately equal to 0.22 after 300 hours.

Figure A3.18 shows the plots of the porosity computed with CORE^{2D}V5 at 10, 50, 150 and 300 hours. Porosity changes only in zone *Z2* where celestites dissolve and barite precipitates. The porosity decreases because the molar volume of barite is larger than that of celestite. The initial porosity in zone *Z2* is equal to 0.33. The porosity hardly changes after 10 hours. The porosity reduces to 0.323 after 50 hours and to 0.311 after 150 hours. The porosity at the end of the simulation is equal to 0.305.

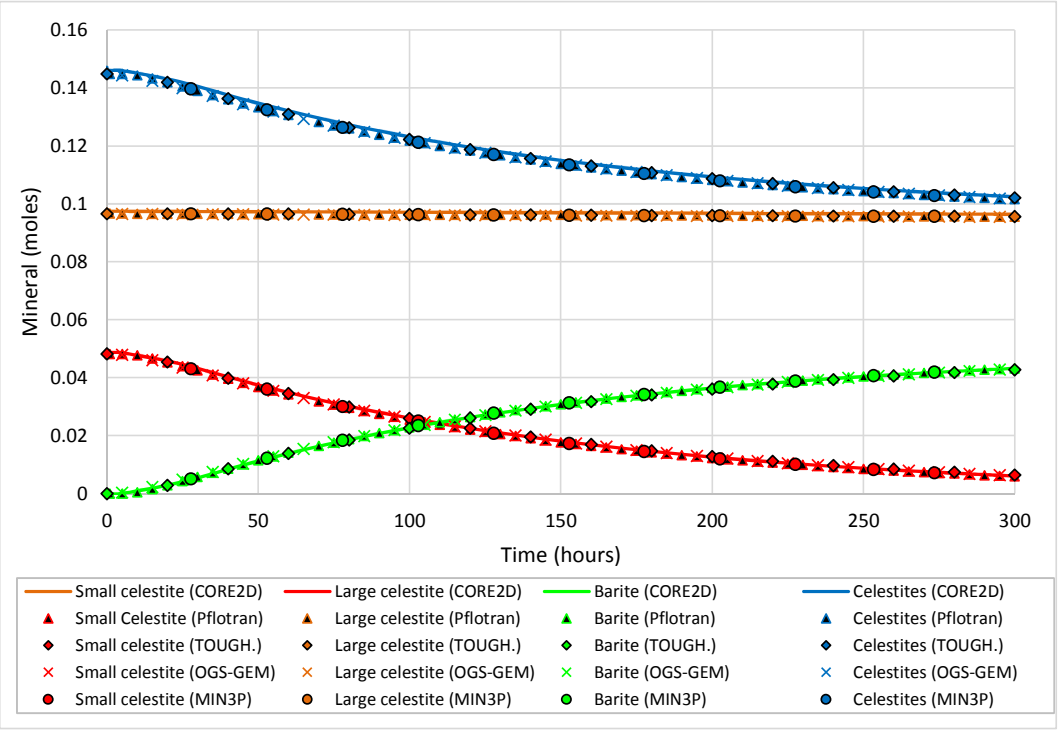

Figure A3.15. Time evolution of the total mass of minerals in the tank computed with CORE^{2D}V5, TOUGHREACT, OpenGeoSys-GEM, Pflotran and MIN3P.

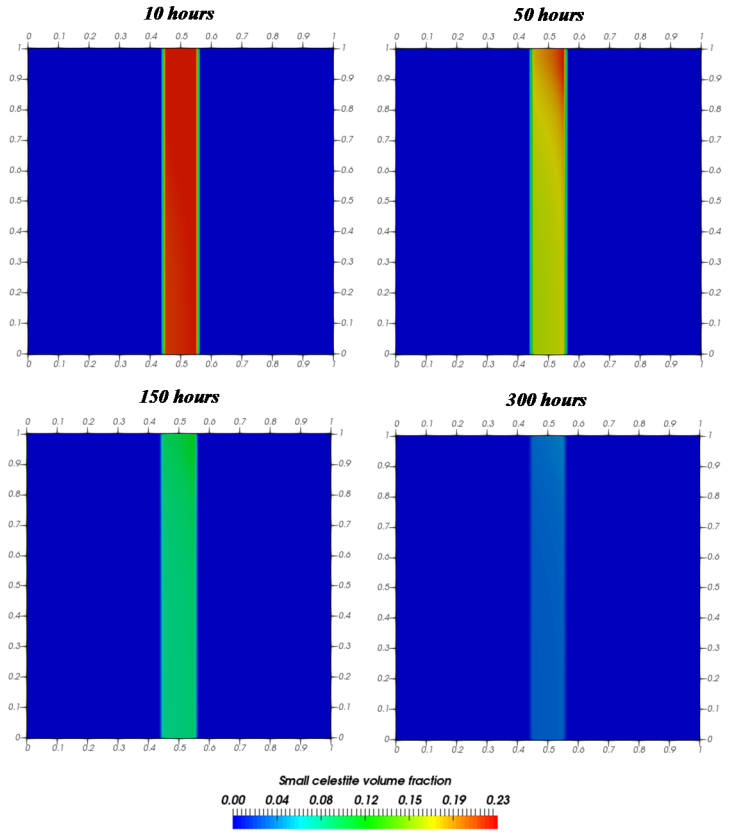

Figure A3.16. Plots of volume fractions of small-grain celestite computed with CORE^{2D}V5 at 10, 50, 150 and 300 hours.

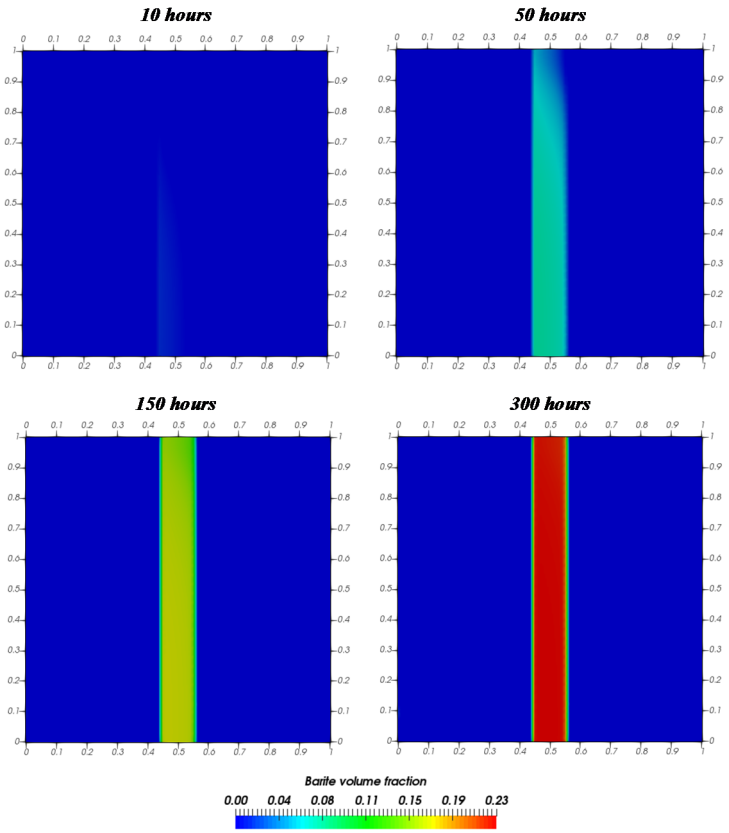

Figure A3.17. Plots of volume fractions of barite computed with CORE^{2D}V5 at 10, 50, 150 and 300 hours.

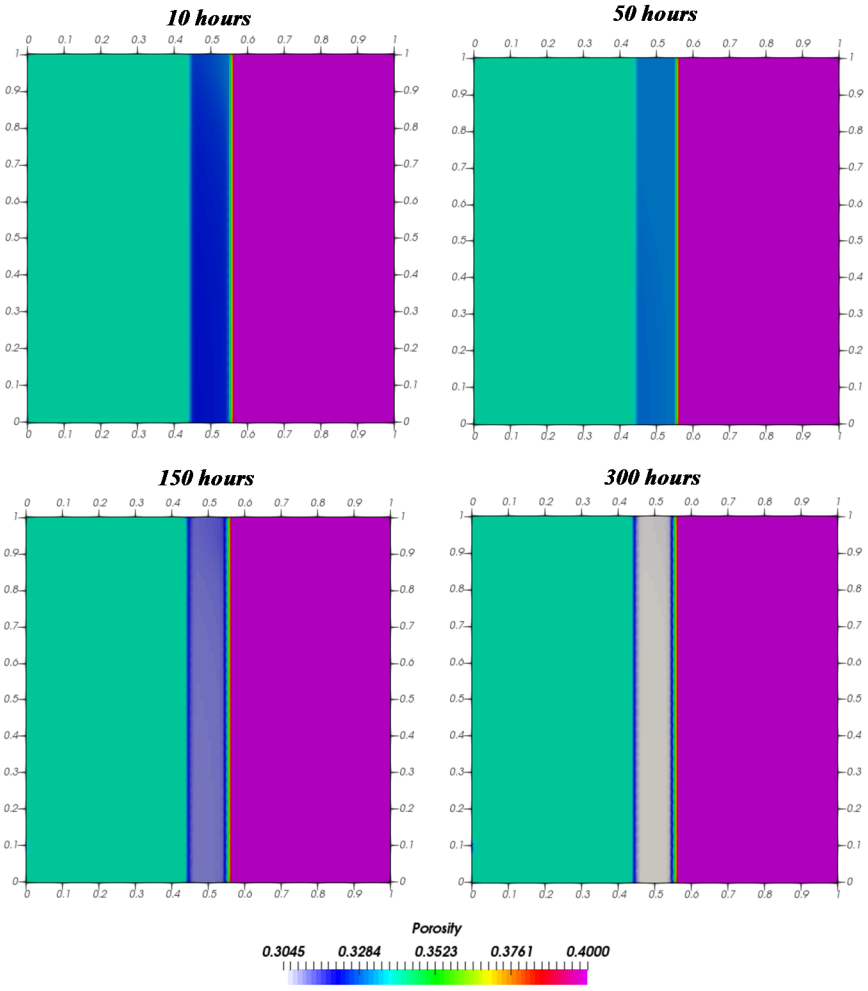

Figure A3.18. Plots of the porosity computed with CORE^{2D}V5 at 10, 50, 150 and 300 hours.

Figure A3.19 and Figure A3.20 show the concentrations of Cl^-, Sr^{2+} and Ba^{2+} along line 2 (z = 0.01 m) computed with CORE^{2D}V5, TOUGHREACT and OpenGeoSys-GEM at 150 hours and 300 hours, respectively. The concentrations computed with CORE^{2D}V5 coincide for the most part with those computed with other two reactive transport codes. The computed concentrations of Cl^- along line 2 after 150 h and 300 h are equal to the Cl^- concentration of the boundary water (0.6 mol/L) because Cl^- is non-reactive species. On the other hand, barite precipitation in the reactive layer causes a decrease of the concentration of dissolved Ba^{2+} in zones *Z2* and *Z3*. The dissolution of celestite in the reactive layer causes an increase of the concentration of dissolved Sr^{2+} in zones *Z2* and *Z3*. The computed concentration of dissolved Ba^{2+} in zone Z3 after 300 hours is higher than that computed after 150 hours while the computed concentration of dissolved Sr^{2+} in zone *Z3* after 300 hours is lower than that computed after 150 hours. This indicates that the rates of barite precipitation and celestite dissolution decrease after 150 hours.

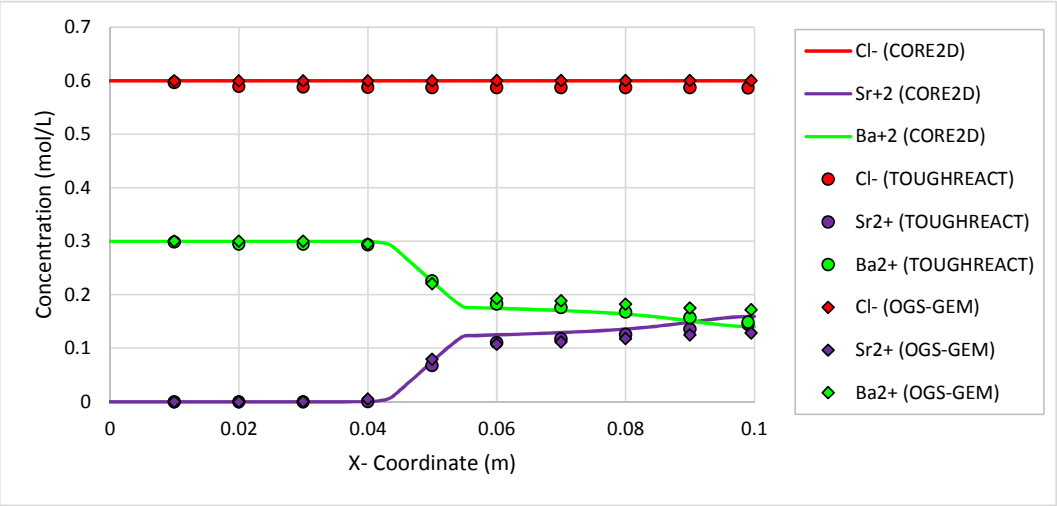

Figure A3.19. Concentrations of dissolved species along line 2 (z = 0.01 m) at 150 hours computed with CORE^{2D}V5 (lines), TOUGHTREACT (circles) and OpenGeoSys-GEM (diamonds).

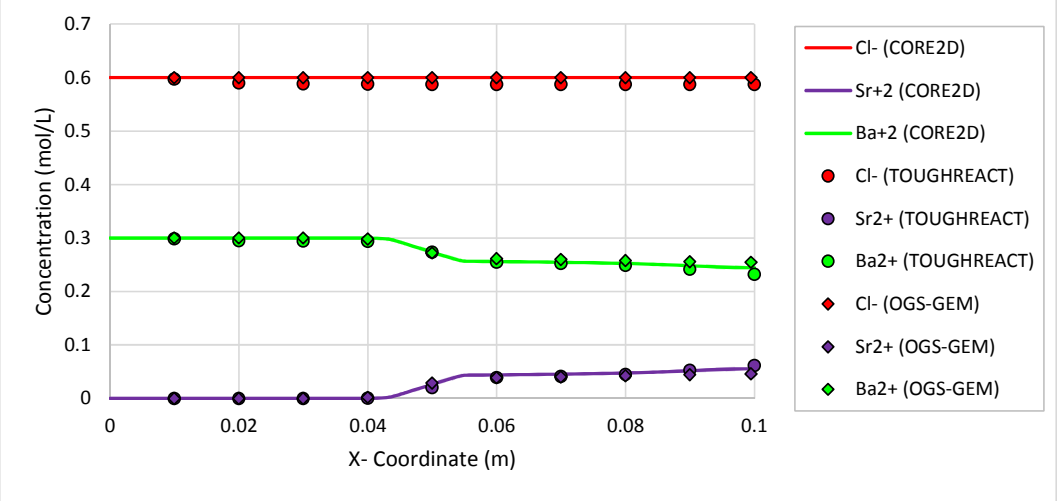

Figure A3.20. Concentrations of dissolved species along line 2 (z = 0.01 m) at 300 hours computed with CORE^{2D}V5 (lines), TOUGHTREACT (circles) and OpenGeoSys-GEM (diamonds).

The simultaneous dissolution of celestite and the precipitation of barite involve an increase in mineral volume fraction of about 0.12. The porosity and the permeability decrease. Figure A3.21 shows the porosity profiles along line 2 after 300 hours computed with CORE^{2D}V5, TOUGHREACT and OpenGeoSys-GEM. The porosities calculated with CORE^{2D}V5 follow a trend similar to those computed with other reactive transport codes. However, there are some differences at the interfaces. These differences are related to the differences in the spatial discretization schemes used by the three reactive transport codes. The numerical model performed with CORE^{2D}V5 uses a finite element grid less refined than those used by the other two reactive transport codes. One the other hand, the processing of the results obtained with TOUGHREACT and OpenGeoSys-GEM has been performed by using the software ParaView (Ahrens et al., 2005; Ayachit, 2015) and the interpolation of the results performed

with this software could contribute to the differences in the computed porosity in the interfaces. The porosities computed directly with CORE^{2D}V5 in the nodes of the finite element grid are shown in Figure A3.21.

Figure A3.22 shows the permeability profiles along line 2 at 300 hours computed with CORE^{2D}V5, TOUGHREACT and OpenGeoSys-GEM. The changes in permeability computed with CORE^{2D}V5 are similar to those calculated with other reactive transport codes. Similar to porosity, there are small differences in the permeability computed with the three reactive transport codes in the interfaces.

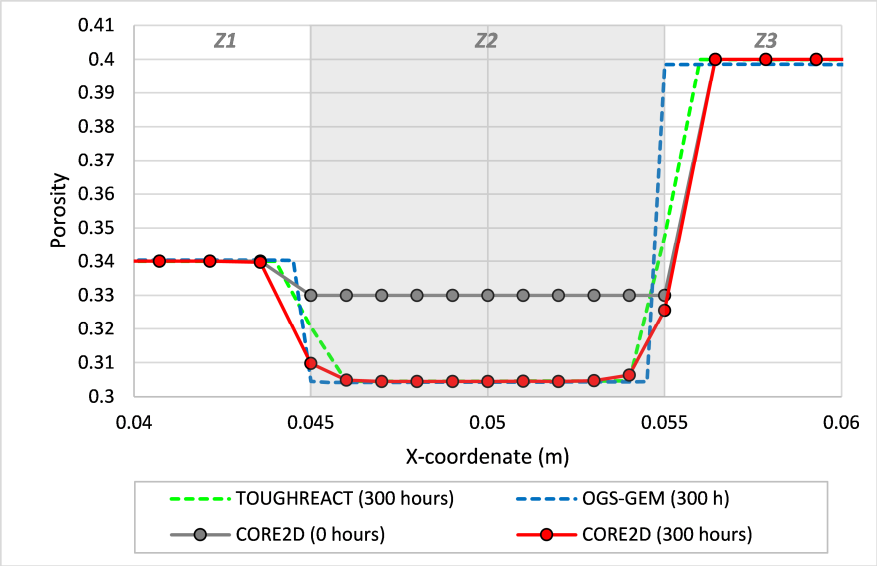

Figure A3.21. Porosity profile along line 2 at 300 hours computed with CORE^{2D}V5, TOUGHREACT and OpenGeoSys-GEM. The grey area indicates the reactive zone *Z2*.

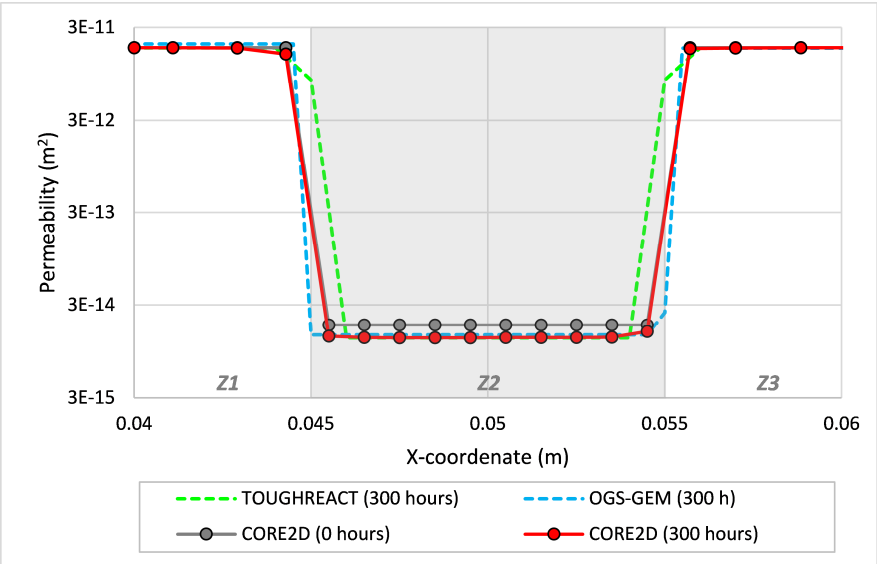

Figure A3.22. Permeability profile along line 2 at 300 hours computed with CORE^{2D}V5, TOUGHREACT and OpenGeoSys-GEM. The grey area indicates the reactive zone *Z2*.

The numerical approaches that are based on the use of a fixed grid of nodes and elements predict discretization-dependent values of porosity, precipitation rates, and eventually the clogging time because of their inability to describe subgrid pore space changes correctly. This was clearly demonstrated by Marty et al. (2009) who showed that the rate of precipitation reactions and the grid size affect clogging times at material interfaces in a diffusive transport regime. Case 2 was solved with the updated version of CORE^{2D}V5 by using several discretization schemes. The following finite element grids were tested: 1) A coarse grid with 1460 nodes and 2790 elements, 2) An intermediate grid with 3631 nodes and 7059 elements and 3) A fine grid 5815 nodes and 11319 elements. Figure A3.23 shows the porosity computed with CORE^{2D}V5 at 300 hours along line 2 with three element grids of increasing refinement. Most of the differences occur at the interfaces of the zones. The results obtained with the coarse grid are the least accurate in the interfaces of the model. The porosities computed with the intermediate and fine grids are similar in the interfaces.

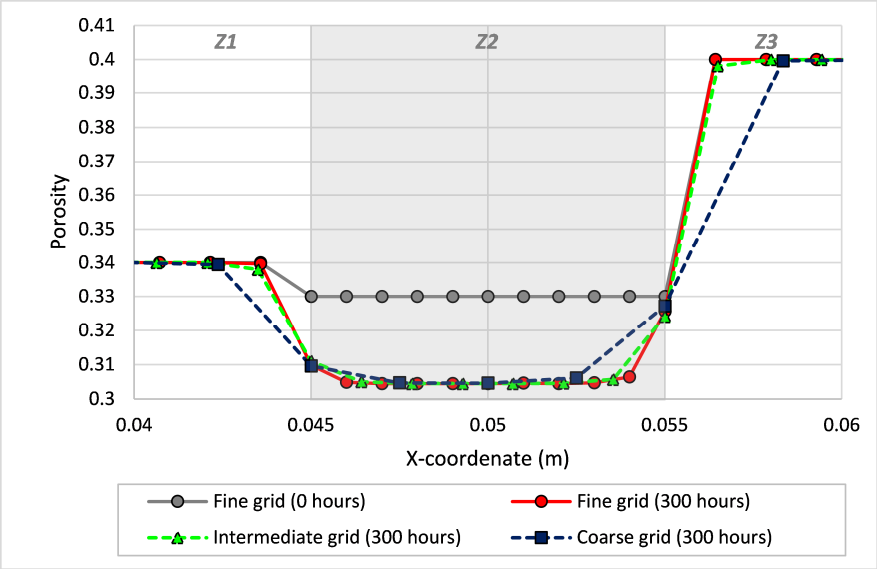

Figure A3.23. Porosity profiles along line 2 at 300 hours computed with CORE^{2D}V5 with three finite element grids of increasing refinement. The grey area indicates the reactive zone *Z2*.

Figure A3.24 shows a comparison of the total mass of barite and celestite in the tank computed with and without the feedback effect of the changes in porosity. Nodal results coincide during the first 50 hours of the simulation. Later, however, the mass of barite and celestite in the tank computed with and without the feedback effect show important differences. The update of the flow, transport and chemical parameters due to the decrease of the porosity in the reactive zone of the tank (zone *Z2*) leads to less celestite dissolution and barite precipitation. The differences in the model results increase with time. A key parameter is the specific surface area of celestite. The previous version of CORE^{2D}V5 considers a constant reactive surface area for small-grain and large-grain celestites. The mass of dissolved small-grain celestite when the decrease of the surface area is not taken into account is greater

than the mass of celestite computed with a variable specific surface. The mass of large-grain celestite computed with the previous and the updated versions of CORE^{2D}V5 are similar because the initial specific surface of this mineral is very small. The results of this comparison illustrates the importance of the reactive surface area for mineral dissolution and precipitation reactions in porous media. The model results obtained with a constant surface area may differ significantly from those obtained with a variable surface area and from the experimental data (Poonoosamy et al., 2015).

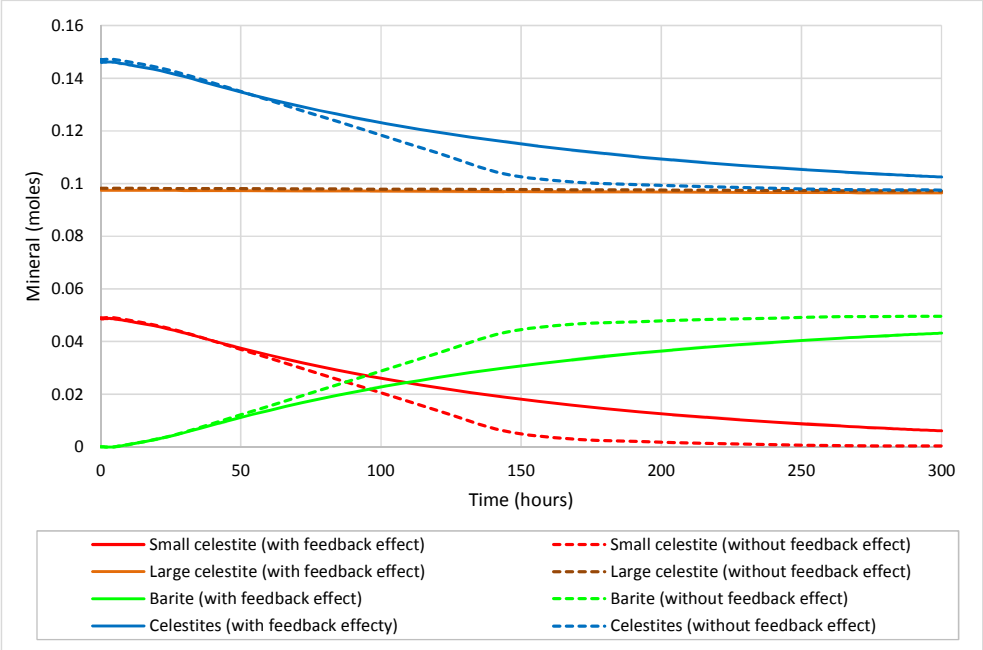

Figure A3.24. Time evolution of the mass of mineral composition in the tank computed with the updated version of CORE^{2D}V5 (with the feedback effect of the porosity changes) and the previous version of CORE^{2D}V5 (without the feedback effect of the porosity changes).

A3.6. MODEL RESULTS IN UNSATURATED CONDITIONS

The tank was flushed with carbon dioxide (CO_2) to remove the air from the pores before performing the laboratory tests. The high solubility of CO_2 enabled the whole porous medium to be completely saturated with a saturated solution of strontium sulphate. A saturated solution of strontium sulphate was used instead of pure water to avoid mineral dissolution. For this reason, the simulation was carried out in saturated conditions. Anyway, a numerical model was performed with CORE^{2D}V5 to simulate the transient unsaturated stage of the laboratory test.

In order to simplify the unsaturated model, the same characteristic curves were used for the entire domain. The following van Genuchten equations were used (Carrera et al., 1992):

$$S_l = \frac{1}{[1 + (12.3 \cdot \psi)^{2.5}]^{0.6}} \tag{3.7}$$

$$k_{rl} = \sqrt{S_l} \cdot \left[1 - \left(1 - {S_l}^{1/0.6}\right)^{0.6}\right]^2 \tag{3.8}$$

where ψ (Pa) is the pressure head, S_l is the saturation degree and k_{rl} is the relative permeability.

An initial saturation degree of 40% was assumed. The tank is saturated after about 17 hours. The numerical model under unsaturated conditions was performed for: 1) Conservative transport (Case 1) and 2) Reactive transport (Case 2). The parameters of the models in unsaturated conditions are similar to those of the models in saturated conditions. However, the outflow of the tank was not simulated in the unsaturated models.

The conservative transport model in unsaturated conditions (Case 1) was performed for a total period of 16 hours. Figure A3.25 shows the contour plots of the tracer concentrations computed with the unsaturated and the saturated models at 2, 4, 8 and 16 hours. The most important differences in the time evolution of the tracer in the tank are located in the lower part of the tank where the tracer front moves faster in the unsaturated model than in the saturated model. In addition, the maximum tracer concentrations computed with the unsaturated model are also higher than those computed with the saturated model.

The tracer breakthrough curves at ports *a, b*, *c* and *d* computed with the models in saturated and unsaturated conditions are shown in Figure A3.26. Tracer concentrations at ports *a* and *c* computed with the unsaturated model are greater than those computed with the model in saturated conditions. However, the opposite occurs at ports *b* and *d*. This is due to the fact that ports *a* and *c* are located in the lower part of the tank while ports *b* and *d* are located in the upper part of the tank. The saturation degree in the lower part of the tank increases more quickly and, for this reason, the maximum tracer concentrations computed with the unsaturated model at the ports located in the lower part of the tank are higher than those computed with the model in saturated conditions.

The reactive transport model in unsaturated conditions (Case 2) was performed for a total period of 8 hours. Figure A3.27 shows a comparison of the contour plots of the concentration of dissolved Ba^{2+} and precipitated barite computed with the unsaturated and the saturated models after 8 hours of simulation. The main differences in the concentrations of dissolved Ba^{2+} are located in the reactive zone *Z2*. The front of dissolved Ba^{2+} computed with the unsaturated model after 8 hours penetrates into the lower part of the reactive zone more than the front computed with the saturated model. The area of the reactive zone where barite precipitates depends on the front of dissolved Ba^{2+}. Barite precipitation in the lower part of the reactive zone in the unsaturated model is larger than that in the saturated model.

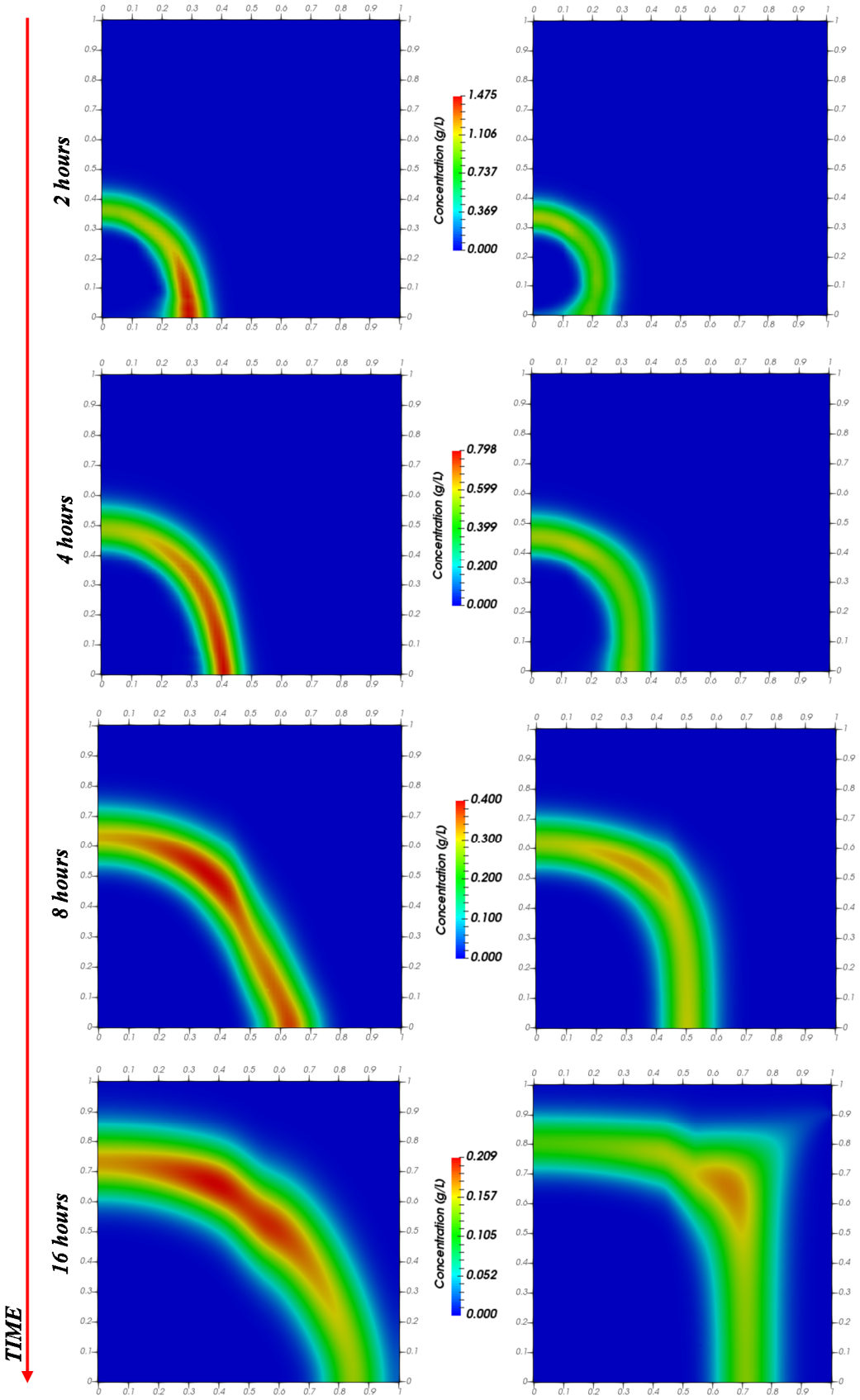

Figure A3.25. Tracer concentration plots computed with the unsaturated (left) and the saturated (right) models for Case 1 at selected times (2, 4, 8 and 16 hours).

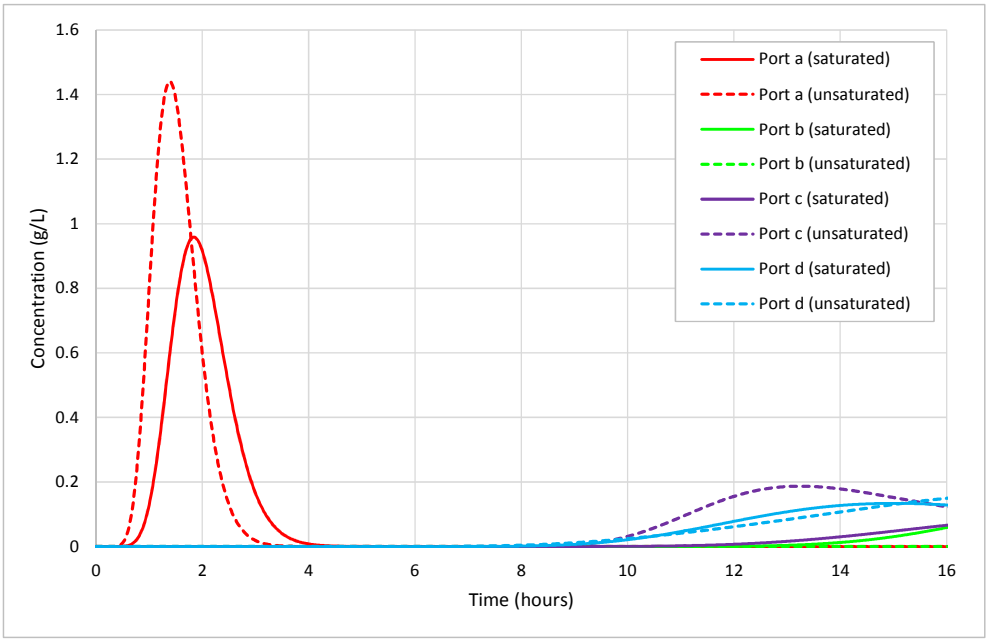

Figure A3.26. Tracer breakthrough curves at ports *a*, *b*, *c* and *d* computed with the saturated and unsaturated models for Case 1.

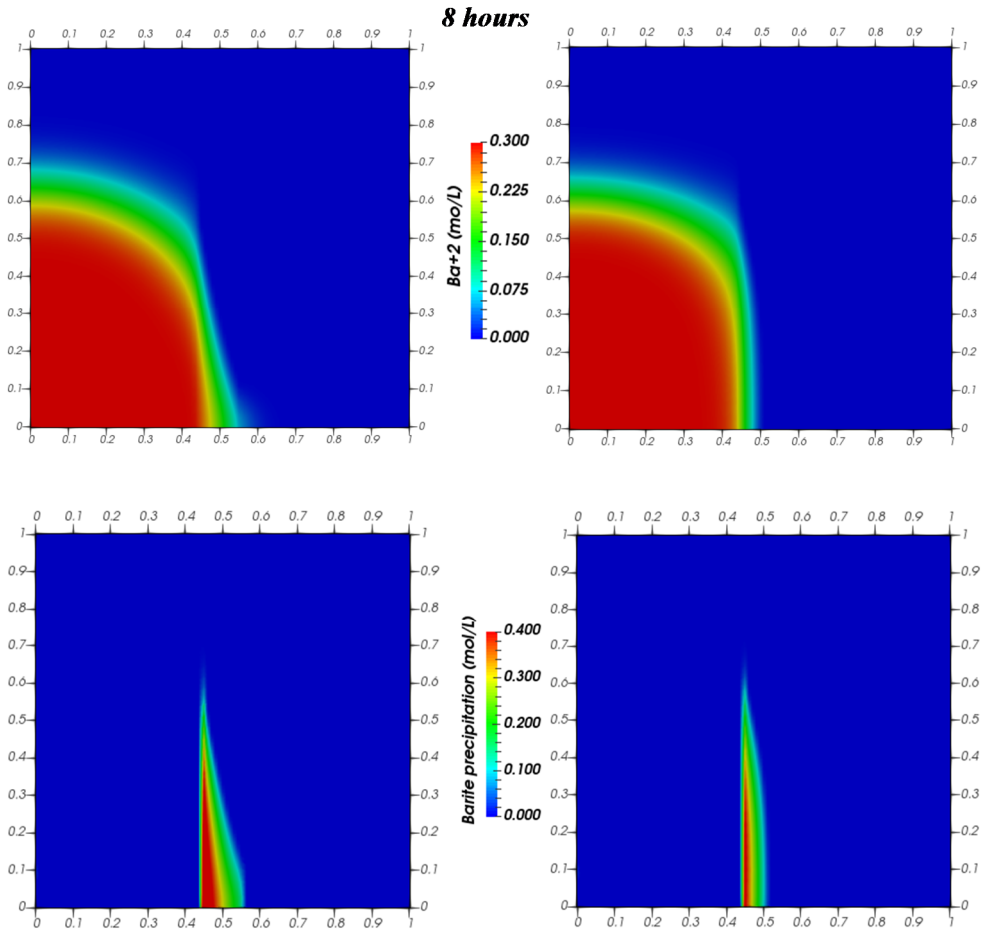

Figure A3.27. Contour plots of the concentrations of Ba^{2+} (top) and precipitated barite (bottom) computed with the unsaturated (left) and saturated (right) models at 8 hours for Case 2.

A3.7. CONCLUSIONS

Chemical processes involving mass transfer from a solid phase to a liquid phase can produce changes in the physical and hydrodynamic properties of porous media. Mineral dissolution/precipitation can increase/decrease the porosity. Porosity changes can in turn produce changes in flow and transport parameters such as permeability, diffusion coefficient and mineral specific surface.

Numerical flow and reactive transport models performed with CORE^{2D}V5 to simulate laboratory experiments with strong porosity changes due to dissolution/precipitation reactions have been presented. The laboratory experiments were carried out at the Paul Scherrer Institut (PSI), Switzerland. The experiments were performed in a tank containing a reactive layer of strontium sulphate ($SrSO_4$(s), celestite), sandwiched between two layers of non-reacting quartz sand (SiO_2). Several types of laboratory tests were performed with the same experimental setup (Poonoosamy et al., 2015). Two of the laboratory experiments were simulated with two 2-D numerical models performed with CORE^{2D}V5: 1) A conservative transport model (Case 1) and 2) A reactive transport models focused on porosity changes (Case 2).

A conservative transport model in an advective regime was performed with CORE^{2D}V5 in Case 1. This case considers the injection of a concentrated non-reacting solution into a porous medium completely saturated. Tracer breakthrough curves at several ports of the tank, temporal tracer plots and seepage velocity along several lines of the tank were computed with CORE^{2D}V5 and compared with experimental data and with the numerical results obtained with TOUGHREACT, OpenGeoSys-GEM, Pflotran and MIN3P. The velocities computed with all codes agree, except near the inlet and the outlet of the tank due to differences in the numerical schemes used by the reactive transport codes.

The computed tracer plots with CORE^{2D}V5 were compared with experimental tracer plots (Poonoosamy et al., 2015) at several times. Model results agree with the experiment data and the numerical results of other codes for Case 1. There are some differences between the tracer breakthrough curves computed with different reactive transport codes due to differences in the implementation of diffusive-dispersive transport. A sensitivity analysis to grid size has been performed for Case 1. Numerical dispersion is greatly reduced when the grid is sufficiently refined.

A reactive transport model focused on porosity changes caused by mineral dissolution/precipitation was performed with the updated version of CORE^{2D}V5 that takes into account the porosity changes and the update of flow, transport and chemical parameters. A barium chloride solution was injected at the inlet of the tank in Case 2. The injection of $BaCl_2$ into the tank leads to the dissolution of strontium sulphate and the precipitation of barium sulphate. The porosity changes due to

the difference in the molar volumes of strontium sulphate and barium sulphate. The total amounts of barite and celestite in the tank computed with CORE^{2D}V5 agree with those computed with TOUGHREACT, OpenGeoSys-GEM, Pflotran and MIN3P. The concentrations of Cl^-, Sr^{2+} and Ba^{2+} along line 2 computed with CORE^{2D}V5 also agree with those calculated with TOUGHREACT and OpenGeoSys-GEM.

The transformation of celestite to barite involves a decrease of porosity of 0.12. At the end of simulation, the porosity and permeability computed with CORE^{2D}V5 along line 2 were compared with those calculated with other reactive transport codes. The results computed with all the reactive transport codes agree, although there are small differences at the interfaces due to the differences in the spatial discretization. A sensitivity analysis to grid size was performed for Case 2 with CORE^{2D}V5. Model results show that the main differences are located at the interfaces of the model and that numerical dispersion is reduced by refining the grid.

Case 2 has been simulated with the previous version of CORE^{2D}V5 with constant porosity and the updated version of CORE^{2D}V5 with variable porosity. The numerical results computed with the two versions of CORE^{2D}V5 show a good agreement during the first 50 hours of simulation. The amounts of $BaSO_4$(s) and $SrSO_4$(s) in the tank computed with the two versions of the code show differences after 50 hours. This comparison stresses the importance of updating the mineral reactive surface area during the simulation. The results obtained with a constant surface area are significantly different from the experimental data reported by Poonoosamy et al. (2015).

Numerical models for Cases 1 and 2 have been performed also in unsaturated conditions. There are important differences between the results obtained with the unsaturated and the saturated models, especially in the lower part of the tank. However, these differences should be taken with caution because the unsaturated model has been performed in a simplified way.

A3.8. REFERENCES

Ahrens, J., Geveci, B., Law, C., (2005). ParaView: An End-User Tool for Large Data Visualization, Visualization Handbook, Elsevier, ISBN-13: 978-0123875822.

Ayachit, U., (2015). The ParaView Guide: A Parallel Visualization Application, Kitware, ISBN 978-1930934306.

Alt-Epping, P., Diamond, L.W., Häring, M.O., Ladner, F., Meier, D.B., (2013a). Prediction of water-rock interaction and porosity evolution in a granitoid-hosted enhanced geothermal system, using constraints from the 5 km Basel-1 well. Appl. Geochem., 38, 121-133.

Alt-Epping, P., Waber, H.N., Diamond, L.W., Eichinger, L., (2013b). Reactive transport modeling of the geothermal system at Bad Blumau, Austria: Implications of the combined extraction of heat and CO_2. Geothermics, 45, 18-30.

Archie, G., (1942). The electrical resistivity log as an aid in determining some reservoir characteristics. Pet. Trans. AIME, 146, 54-62.

Berner, U., Kulik, D.A., Kosakowski, G., (2013). Geochemical impact of a low-pH cement liner on the near field of a repository for spent fuel and high-level radioactive waste. Phys. Chem. Earth, 64, 46-56.

Boving, T.B., Grathwohl, P., (2001). Tracer diffusion coefficients in sedimentary rocks: correlation to porosity and hydraulic conductivity. J. Contam. Hydrol., 53, 85-100.

Carman, P.C., (1937). Fluid through granular beds. Trans. Inst. Chem. Eng., 15, 150-166.

Carrera, J., Alfageme, H., Galarza, G., Medina, A., (1992). Estudio de la infiltración a través de la cobertera de la FUA (Study on the infiltration through the FUA cover). Technical Publication 02/92, ENRESA, Madrid (in Spanish).

Chasset, C., Jarsjo, J., Erlstroem, M., Cvetkovic, V., Destouni, G., (2011). Scenario simulations of CO_2 injection feasibility, plume migration and storage in saline aquifer, Scania, Sweden. Int. J. Greenh. Gas Control, 5, 1303-1318.

De Windt, L., Pellegrini, D., Van der Lee, J., (2004). Coupled modeling of cement/claystone interactions and radionuclide migration. J. Contam. Hydrol., 68, 165-182.

De Windt, L., Badredinne, R., Lagneau, V., (2007). Long-term reactive transport modelling of stabilized/solidified waste: from dynamic leaching tests to disposal scenarios. J. Hazard. Mater., 207, 529-536.

Diamond, L.W., Alt-Epping, P., (2014). Predictive modelling of mineral scaling, corrosion and the performance of solute geothermometers in a granitoid-hosted, enhanced geothermal system. App. Geochem., 51, 216-228.

Dove, P.M., Czank, C.A., (1995). Crystal chemical controls on the dissolution kinetics of the isostructural sulfates: Celestite, anglesite, and barite. Geochim. Cosmochim. Acta, 56(10), 4147-4156.

Gaucher, E.C., Blanc, P., (2006). Cement/clay interaction - a review: experiments, natural analogues, and modelling. Waste Manag., 26, 776-788.

Hayek, M., Kosakowski, G., Churakov, S., (2011). Exact analytical solutions for a diffusion problem coupled with precipitation–dissolution reaction and feedback of porosity change. Water Resour., 47, W07545. http://dx.doi.org/10.1029/2010WR010321.

Hayek, M., Kosakowski, G., Jakob, A., (2012). A class of analytical solutions for multidimensional species diffusive transport coupled with precipitation–dissolution reactions and porosity changes. Water Resour., 48, W03525. http://dx.doi.org/10.1029/2011WR011663.

Jamieson-Hanes, J.H., Amos, R.T., Blowes, D.W., (2012). Reactive transport modeling of Chromium Isotope Fractionation during Cr (IV) Reduction. Environ. Sci. Technol., 46(24), 13311-13316.

Katz, G.E., Berkowitz, B., Guadagnini, A., Saaltink M.W., (2011). Experimental and modeling investigation of multicomponent reactive transport in porous media. J. Contam. Hydrol., 120-121, 27-44.

Kosakowski, G., Berner, U., (2013). The evolution of clay rock/cement interfaces in a cementitious repository for low and intermediate level radioactive waste. Phys. Chem. Earth, 64, 65-86.

Kosakowski, G., Wanatabe, N., (2013). OpenGeoSys-Gem: a numerical tool for calculating geochemical and porosity changes in saturated and partially saturated media. Phys. Chem. Earth, 70-71. http://dx.doi.org/10.1016/j.pce. 2013.11.008.

Lagneau, V., (2000). Influence des processus géochimiques sur le transport en milieu poreux: application au colmatage de barrières de confinement potentielles dans un stockage en formation géologique. PhD Thesis, Ecole des Mines de Paris.

Lagneau, V., Pipart, A., Catalette, H., (2005). Reactive transport modelling of CO_2 sequestration in deep saline aquifers. Oil Gas Sci. Technol. Rev. IFP 60, 231–247.

Lagneau, V., van der Lee, J., (2010). Operator-splitting-based reactive transport models in strong feedback of porosity change: The contribution of analytical solutions for accuracy validation and estimator improvement. J. Contam. Hydrol., 112(1-4), 118-129.

Lichtner, P.C., Hammond, G.E., Lu, C., Karra, S., Bisht, G., Andre, B., Mills, R.T., Kumar, J., (2013). PFLOTRAN User manual: A Massively Parallel Reactive Flow and Transport Model for Describing Surface and Subsurface Processes (2013).

Liu, J., Pereira, G.G., Regenauer-Lieb, K., (2014). From characterization of pore-structures to simulations of pore-scale fluid flow and the upscaling of permeability using microtomography: a case study of heterogeneous carbonates. J. Geochem. Explor., 144, 86-96.

Marica, F., Jofre, S.A., Mayer, K.U., Balcom, B.J., Al, T.A., (2011). Determination of spatially-resolved porosity, tracer distributions and diffusion coefficients in porous media using MRI measurements and numerical simulations. J. Contam. Hydrol., 125, 47-56.

Marty, N.C., Tournassat, C., Burmol, A., Giffaut, E., Gaucher, E., (2009). Influence of reaction kinetics and mesh refinement on the numerical modelling of concrete/clay interactions. J. Hydrol., 364, 58-72. http://dx.doi.org/10.1016/j.jhydrol.2008.10.013

Mayer, K.U., Frind, E.O., Blowes D.W., (2002). Multicomponent reactive transport modeling in variably saturated porous media using a generalized formulation for kinetically controlled reactions, Water Resour. Res., 38(9), 1174, doi:10.1029/2001WR000862.

Mayer, K.U., MacQuarrie, K.T.B., (2010). Solution of the MoMaS reactive transport benchmark with MIN3P-model formulation and simulation results. Comput. Geosci. (2010). doi:10.1007/s10596-009-9158-6.

Palandri, J.L., Kharaka, Y.K., (2004). A compilation of rate parameters of water mineral interaction kinetics for application to geochemical modelling. US Geological Survey, Menlo Park, California.

Parkhurst, D.L., Appelo, C.A.J., (1999). User's guide to PHREEQC (version 2) - A computer program for speciation, batch-reaction, one dimensional transport, and inverse geochemical calculations, U.S. Geol. Surv. Water Resour. Invest. Rep., 99-4259, 312 pp.

Parkhurst, D.L., Kipp, K.L., Engesgaard, P., Charlton S. R., (2002). PHAST - A program for simulating ground-water flow and multicomponent geochemical reactions, U.S. Geol. Surv., Denver, Col. [Available at http://wwwbrr.cr.usgs.gov/projects/GWC_coupled/phast/index.html.]

Poonoosamy, J., Kosakowski, G., Van Loon, L.R., Mäder, U., (2015). Dissolution-precipitation processes in tank experiments for testing numerical models for reactive transport calculations: Experiment and modelling. J. Contam. Hydrol., 177-178, 1-17.

Samper, J., Lu, C., Montenegro, L., (2008a). Coupled hydrogeochemical calculations of the interactions of corrosion products and bentonite. Phys. Chem. Earth, 33, S306-S316. http://dx.doi.org/10.1016/j.pce.2008.10.009.

Samper J., Zheng, L., Montenegro, L., Fernández, A.M., Rivas, P., (2008b). Coupled thermo-hydro-chemical models of compacted bentonite after FEBEX in situ test, Appl. Geochem., Vol 23/5: 1186-1201.

Samper, J., Xu, T., Yang, C., (2009). A sequential partly iterative approach for multicomponent reactive transport with CORE^{2D}. Comput. Geosci., http://dx.doi.org/10.1007/s10596-008-9119-5.

Samper, J., Yang, C., Zheng, L., Montenegro, L., Xu, T., Dai, Z., Zhang, G., Lu, C., Moreira, S., (2011). CORE^{2D}V4: A code for water flow, heat and solute transport, geochemical reactions, and microbial processes, Chapter 7 of the Electronic book Groundwater Reactive Transport Models, F Zhang, G-T Yeh, C Parker & X Shi (Ed), Bentham Science Publishers, pp. 161-186, ISBN: 978-1-60805-029-1.

Samper, J., Naves, A., Montenegro, L., Mon, A., (2016). Reactive transport modelling of the long-term interactions of corrosion products and compacted bentonite in a HLW repository in granite: Uncertainties and relevance for performance assessment. Appl. Geochem., Vol 67, 42-51. http://dx.doi.org/10.1016/j.apgeochem.2016.02.001

Shao, H., Dmytrieva, S.V., Kolditz, O., Kulik, D.A., Pfingsten, W., Kosakowski, G., (2009). Modeling reactive transport in non-ideal aqueous–solid solution system. Appl. Geochem., 24(7), 1287-1300.

Steefel, C.I., (2001). CRUNCH: Software for modeling multicomponent, multidimensional reactive transport, user's guide, Rep. UCRL-MA-143182, Lawrence Livermore Nat. Lab., Livermore, Calif.

Tyagi, M., Gimmi, T., Churakov, S., (2013). Multi-scale micro-structure generation strategy for upscaling transport in clays. Adv. Water Resour., 59, 181-195.

Tartakowsky, A.M., Redden, G., Lichtner, P.C., Scheibe, T.D., Meakin, P., (2008). Mixing-induced precipitation: experimental study and multiscale numerical analysis. Water Resour. Res., 44, 1-19.

van der Lee, J., De Windt L., (2001). Present state and future directions of modeling of geochemistry in hydrogeological systems, J. Contam. Hydrol., 47(2-4), 265-282.

van der Lee, J., De Windt L., Lagneau V., Goblet P., (2003). Module-oriented modeling of reactive transport with HYTEC, Comput. Geosci., 29(3), 265-275.

van der Lee, J., (2005). Reactive transport modelling with HYTEC, user's guide and tutorial, Tech. Rep. LHM/RD/05/30, 114 pp., Cent. d'Inf. Géol., École des Mines, Fontainebleau, France.

Van Loon, L.R., Müller, W., Glaus, M.A., (2007). Anion exclusion effects in compacted bentonites: towards a better understanding of anion diffusion. Appl. Geochem., 22, 2536-2552.

Wanner, C., Eggenberger, U., Mäder, U., (2012). A chromate-contaminated site in southern Switzerland -part 2: Reactive transport modeling to optimize remediation options. Appl. Geochem., 27(3), 655-662.

Wanner, C., Sonnenthal, E.L., (2013). Assessing the control on the effective kinetic Cr isotope fractionation factor: A reactive transport modeling approach. Chem. Geol., 337-338, 88-98.

Wanner, C., Peiffer, L., Sonnenthal, E.L., Spycher, N., Iovenitti, J., Kennedy, B.M., (2014). Reactive transport modeling of the Dixie Valley geothermal area: Insights on flow and geothermometry. Geothermics, 51, 130-141. DOI: 10.1016/j.geothermics.2013.12.003.

Xie, M., Mayer, K.U., Claret, F., Alt-Epping, P., Jacques, D., Steefel, C., Chiaberge, C., Simunek, J., (2015). Implementation and evaluation of permeability-porosity and tortuosity-porosity relationships linked to mineral dissolution-precipitation. Computat. Geosci., 19, 655-671.

Xu, T., Sonnenthal E., Spycher N., Pruess K., (2004). TOUGHREACT user's guide: A simulation program for non-isothermal multiphase reactive geochemical transport in variable saturated geologic media, Rep. LBNL-55460, 192 pp., Lawrence Berkeley Natl. Lab., Berkeley, Calif.

Xu, T., Sonnenthal E., Spycher N., Pruess K., (2006). TOUGHREACT - A simulation program for non-isothermal multiphase reactive geochemical transport in variably saturated geologic media: Applications to geothermal injectivity and CO_2 geological sequestration, Comput. Geosci., 32(2), 145-165.

Xu, T., Spycher N., Sonnenthal E., Zhang G., Zheng L., Pruess K., (2011). TOUGHREACT version 2.0: A simulator for subsurface reactive transport under non-isothermal multiphase flow conditions, Comput. Geosci., 37(6), 763-774.

Zheng, L., Samper, J., Montenegro, L., Fernández, AM., (2010). A coupled THMC model of a heating and hydration laboratory experiment in unsaturated compacted FEBEX bentonite. J. Hydrol., 386, 80-94. http://dx.doi.org/10.1016/j.jhydrol.2010.03.009.

Zheng, L., Samper, J., Montenegro, L., (2011). A coupled THC model of the FEBEX in situ test with bentonite swelling and chemical and thermal osmosis. J. Contam. Hydrol., 126, 45-60.

APPENDIX 4. CAESIUM MIGRATION THROUGH OPALINUS CLAY CALCULATED BY A SINGLE-SPECIES TRANSPORT MODEL USING A MEASURED NON-LINEAR SORPTION ISOTHERM AND A MULTI-SPECIES TRANSPORT MODEL

This appendix presents single-species and multi-species transport models performed with CORE^{2D}V5 to simulate the non-linear sorption and transport of caesium through Opalinus clay. The single-species model uses a non-linear sorption isotherm measured in batch sorption experiments (Van Loon et al., 2009). The multi-species transport model simulates the non-linear Cs sorption in Opalinus clay with cation exchange in three sites (Bradbury and Baeyens, 2000). The results obtained with CORE^{2D}V5 have been compared with those obtained with other reactive transport codes (benchmarking). The results of this benchmarking are expected to be published in a manuscript to be submitted to a SCI journal. Some parts were published in the following reference:

→ Fernández J., W. Pfingsten, J. Samper & L. Montenegro, 2016. Benchmarking of caesium migration through Opalinus clay calculated by a single-species model using a measured non-linear sorption isotherm and a multi-species transport model. In: Book of Abstracts. International Workshop Subsurface Environmental Simulation Benchmarking Workshop V, A Coruña, October 2016, pp. 17-30.

ABSTRACT

The Opalinus clay is currently under investigation as a potential host rock for a high-level radioactive waste repository in Switzerland. Due to the absence of fractures even on a microscopic scale and due to the low hydraulic permeability of the Opalinus clay (10^{-14} - 10^{-13} m/s), diffusion is the main transport mechanism for radionuclides released from a repository. Diffusion and sorption coefficients are commonly derived from small-scale through diffusion experiments. This appendix presents single-species and multi-species reactive transport models performed with CORE^{2D}V5 to simulate non-linear sorption of caesium (Cs) in Opalinus clay. Cs diffusion through Opalinus clay is relevant for the performance assessment of nuclear waste repositories and, in addition, Cs is a key radionuclide showing non-linear sorption behaviour in clay. The non-linear Cs sorption in Opalinus clay is simulated first with a single-species transport model by using a tabulated non-linear sorption isotherm. This isotherm was measured in batch sorption experiments (Van Loon et al., 2009). Then, the non-linear Cs sorption in Opalinus clay is simulated with a multicomponent reactive transport model with cation exchange in three sites (Bradbury and Baeyens, 2000). Cs breakthrough curves computed with CORE^{2D}V5 at several locations in the Opalinus clay have been compared with those computed with other reactive transport codes (benchmarking) such as COMSOL Multiphysics and MCOTAC. The calculations were performed over a wide range of dissolved Cs concentrations of four orders of magnitude (10^{-7} to 10^{-3} mol/L). The three codes give similar result, although there are small differences caused by differences in the spatial discretization. In addition, the Cs breakthrough curves computed with the single-species and the multi-species transport models at several locations in the Opalinus clay agree for the most part.

A4.1. INTRODUCTION

Clay formations are being considered as potential host rocks for deep geological disposal of radioactive waste repositories because these rocks have very low hydraulic conductivity and large sorption capacity for many radionuclides. Diffusion is the main transport mechanism through clay formations. The performance assessment of such host rocks as geological barriers requires understanding and quantifying radionuclide diffusion and sorption from laboratory experiments, field studies and numerical modelling. Radionuclide diffusion and sorption are key processes for the safety of underground radioactive waste repositories. Selecting the appropriate sorption conceptual model is at least as important as estimating the optimum sorption parameters.

Diffusion coefficients and sorption parameters are usually derived from small-scale through-diffusion experiments (Rosanne et al., 2003; Van Loon et al., 2003a,b; Van Loon and Soler, 2004; Van Loon et al., 2004; Melkior et al., 2005) and in situ diffusion tests (Palut et al., 2003; Tevissen et al., 2004; Cartalade et al., 2007). These test are often interpreted with a simple K_d-approach (Shackelford, 1991; Eriksen and Jansson, 1996; Kau et al., 1999; Ochs et al., 2001; Xia et al., 2006). More complex models are applied, especially when the single-species model fails (Malusis and Shackelford, 2002; Bourg et al., 2006; Appelo and Wersin, 2007).

Various experimental programs are being carried out at the Mont Terri Underground Research Laboratory (URL) in Switzerland to study the feasibility of the Opalinus clay formation to host a radioactive waste repository. The Opalinus clay is located in the northern part of Switzerland and was deposited about 180 million years ago as a marine sediment consisting of fine mud particles. It has a thickness of ~ 100 m and contains between 40 and 80% clay minerals with 10% of swelling clays (Gautschi, 1997). The in situ diffusion and retention (DR) experiment was performed at the Mont Terri URL in the Opalinus clay to: 1) Obtain diffusion and retention data for moderately and strongly sorbing tracers, 2) Improve the estimation of diffusion anisotropy and 3) Quantify the effects of the borehole disturbed zone for non-reactive tracers.

Caesium (Cs) diffusion through Opalinus clay is relevant for the performance assessment of nuclear waste repositories. Cs is a key radionuclide showing a non-linear sorption in clay (Van Loon et al., 2009). Extensive modelling and experimental studies have been performed to understand and quantify Cs diffusion in clay (Jakob et al., 2009; Suzuki et al., 2007; Kosakowski et al., 2008; Maes et al., 2008; Van Loon et al., 2003a,b; Wersin et al., 2008). Empirical laws have been used to interpret diffusion experiments in specific experimental set-ups (diffusion parallel or perpendicular to layering, see e.g. Van Loon et al., 2004), but these laws are only applicable to such set-ups. Other experimental Cs diffusion results have been explained with rather strange assumptions on the presence of dead-end pores in the clay with size extensions even larger than the whole sample (Appelo et al., 2010). Consequently, Cs transport and sorption is yet an interesting topic for code benchmarking.

This appendix presents numerical models performed with CORE^{2D}V5 to simulate non-linear Cs sorption in Opalinus clay with: 1) A single-species transport model and 2) A multi-species transport model. The non-linear Cs sorption in Opalinus clay is simulated first with a single-species transport model by using a tabulated non-linear sorption isotherm measured in laboratory batch experiments (Van Loon et al., 2009). Then, the non-linear sorption of Cs in Opalinus clay is simulated with a multicomponent reactive transport model with cation exchange in three sites (Bradbury and Baeyens, 2000). The results obtained with CORE^{2D}V5 were compared with those obtained with COMSOL Multiphysics and MCOTAC.

A4.2. LABORATORY EXPERIMENTS

The numerical models performed to simulate the non-linear sorption of caesium in Opalinus clay are related to former work carried out by Jakob et al. (2009) and to laboratory diffusion experiments performed at the Paul Scherrer Institut (PSI), Switzerland. Opalinus clay samples from the Mont Terri Underground Research Laboratory were used in the diffusion experiments. A high-pressure through diffusion cell was designed for the diffusion studies. The cell was loaded with a cylindrical sample of Opalinus clay and it was sandwiched between two stainless steel filter plates. The diffusion cell used in the experiments is described in detail by Van Loon et al. (2003a).

The experimental set-up includes a diffusion cell, an 8-channel peristaltic pump, two containers of $5.0 \cdot 10^{-4}$ m^3 and $1.0 \cdot 10^{-4}$ m^3 and two circuits. The first circuit connects the cell to a large container (high-concentration loop) and the second circuit connects the opposite boundary of the cell to the small container (low-concentration loop). Before performing the experiment, the samples were saturated for 5 weeks. Cs concentration in the large container was much greater than that in the small container. The tracer diffused through the cell from the boundary with high Cs concentration to the boundary with low Cs concentration. The solution in the small container was regularly replaced in order to maintain the concentration of caesium in the container as low as possible, i.e. <1% of the concentration in the high-concentration container. At the end of the through-diffusion experiment, the solutions in both containers were replaced by artificial pore water without tracer and an out-diffusion experiment was carried out afterwards. All the experiments were performed at 23 ± 2 ºC.

Batch sorption experiments were performed by Van Loon et al. (2009) on crushed and intact Opalinus clay samples. The results demonstrated that sorption of Cs on crushed and intact Opalinus clay are essentially identical. Figure A4.1 shows the distribution coefficient of Cs in Opalinus clay as a function of dissolved Cs concentration measured in batch experiments.

A4.3. NUMERICAL MODELS

This section describes the two numerical models performed with CORE^{2D}V5 to simulate the non-linear sorption of caesium in Opalinus clay: 1) A single-species transport model and 2) A multi-species transport model.

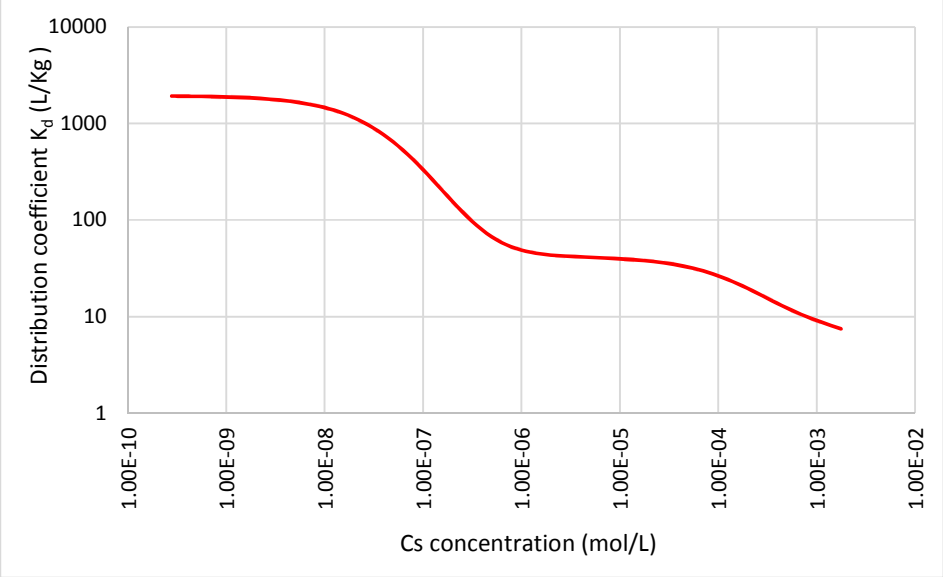

Figure A4.1. Distribution coefficient of caesium measured on crushed and compacted Opalinus clay samples from the Mont Terri Laboratory (Van Loon et al., 2009).

A4.3.1. Single-species transport model

The model geometry corresponds to that of the clay samples from the Mont Terri Rock Laboratory used in the small-scale laboratory diffusion experiments (Jakob et al., 2009). The samples are cylindrical with a diameter of 25.7 mm, a cross-sectional area of 518.7 mm^2 and a length L of 1 cm. For the sake of simplicity, the filters were neglected for numerical modelling. The Opalinus clay is assumed homogeneous and isotropic. The bulk density of the clay samples is equal to 2400 kg/m^3.

The domain of the numerical model performed with CORE^{2D}V5 was discretized with a uniform 2-D mesh of triangular finite elements with a size, Δx, equal to 0.02 cm. The mesh has 102 nodes and 100 elements. The single-species transport model assumes an equilibrated clay porewater (Mont Terri PI-Water) with "high" Cs concentration ranging from 10^{-7} to 10^{-3} M at x = 0 and an equilibrated clay porewater with 10^{-10} M Cs concentration at x = 1 cm ("low" Cs concentration). The solution in both containers of the laboratory experiments are assumed to behave as concentration boundary conditions. The initial Cs concentration is uniform and equal to 10^{-10} mol/L. Figure A4.2 shows the finite element mesh and the boundary conditions of the numerical model.

The main transport parameters include: porosity, ϕ = 0.15; pore diffusion coefficient, $D_0 = 10^{-10}$ m^2/s; and effective diffusion coefficient, $D_e = D_0\,\phi = 1.5 \cdot 10^{-11}$ m^2/s. Transport calculations were performed for a time of 10 years. The time domain was divided into daily time periods which, in turn, were subdivided into 100 time increments. The non-linear sorption of Cs in Opalinus clay was

simulated with a tabulated list of distribution coefficients measured in the laboratory (Van Loon et al., 2009). Sorption modelling with the K_d approach assumes: 1) An instantaneous chemical equilibrium between dissolved and sorbed species; and 2) A linear relationship between the concentrations of sorbed, s, and dissolved species, c, according to:

$$s = K_d\, c \tag{4.1}$$

CORE^{2D}V5 has been modified and updated to allow the use of a tabulated K_d. The K_d values are updated each time step according to the dissolved Cs concentration. The sorption isotherm has been implemented in the code in the form of a look-up table with given K_d values for pairs of Cs data. The non-linear list of K_d values as a function of Cs concentration implemented in CORE^{2D}V5 is shown in Table A4.1.

The K_d values in CORE^{2D}V5 are associated to the elements of the finite elements mesh, whereas the concentrations are computed in a nodewise manner. A sensitivity analysis with two different mesh discretization ($\Delta x = L/50$ and $\Delta x = L/2000$) was performed to evaluate discretization errors.

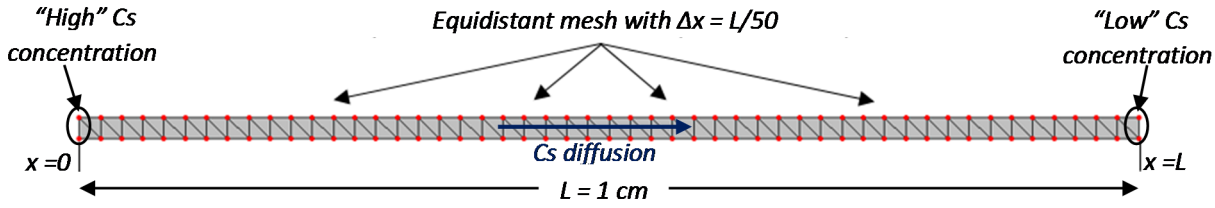

Figure A4.2. Finite element mesh and boundary conditions of the numerical model.

A4.3.2. Multi-species transport model

A multi-species transport model with cation exchange in three sites was performed with CORE^{2D}V5 to simulate the non-linear sorption of Cs through Opalinus clay. The model geometry, spatial discretization, transport parameters and boundary conditions for caesium used in the multi-species transport model are similar to those used in the previous single-species model.

Ten primary species and 22 aqueous complexes were considered in the multicomponent reactive transport model. Table A4.2 shows the initial chemical composition of the Opalinus clay porewater. The equilibrium constants for aqueous complexes are listed in Table A4.3. The sorption model of Bradbury and Baeyens (2000) was used to simulate the non-linear sorption of Cs on Opalinus clay. This model assumes the following three different cation exchange sites: s_{plan} ("planar cation exchange sites"), $s_{Type\text{-}II}$ ("higher affinity sites") and s_{FES} ("frayed edge sites"). These three cation exchange sites were

implemented in the multi-species transport model performed with CORE^{2D}V5 to simulate the non-linear of Cs on Opalinus clay. The Gaines-Thomas convention (Gaines and Thomas, 1953) was used for cation exchange reactions. Table A4.4 lists the cation exchange capacity (CEC) of the three cation exchange sites. Cation exchange reactions and their selectivity coefficients constants for the three cation exchange sites are listed in Table A4.5.

Table A4.1. List of K_d values as a function of dissolved Cs concentration implemented in CORE^{2D}V5.

Cs concentration (mol/L)		***K_d = s/c***
Minimum value	Maximum value	***(L/kg)***
$1.76 \cdot 10^{-3}$	∞	$7.46 \cdot 10^{0}$
$1.11 \cdot 10^{-3}$	$1.76 \cdot 10^{-3}$	$8.76 \cdot 10^{0}$
$7.00 \cdot 10^{-4}$	$1.11 \cdot 10^{-3}$	$1.05 \cdot 10^{1}$
$4.42 \cdot 10^{-4}$	$7.00 \cdot 10^{-4}$	$1.30 \cdot 10^{1}$
$2.79 \cdot 10^{-4}$	$4.42 \cdot 10^{-4}$	$1.65 \cdot 10^{1}$
$1.76 \cdot 10^{-4}$	$2.79 \cdot 10^{-4}$	$2.08 \cdot 10^{1}$
$1.11 \cdot 10^{-4}$	$1.76 \cdot 10^{-4}$	$2.54 \cdot 10^{1}$
$7.00 \cdot 10^{-5}$	$1.11 \cdot 10^{-4}$	$2.97 \cdot 10^{1}$
$4.42 \cdot 10^{-5}$	$7.00 \cdot 10^{-5}$	$3.33 \cdot 10^{1}$
$2.79 \cdot 10^{-5}$	$4.42 \cdot 10^{-5}$	$3.61 \cdot 10^{1}$
$1.76 \cdot 10^{-5}$	$2.79 \cdot 10^{-5}$	$3.80 \cdot 10^{1}$
$1.11 \cdot 10^{-5}$	$1.76 \cdot 10^{-5}$	$3.94 \cdot 10^{1}$
$7.00 \cdot 10^{-6}$	$1.11 \cdot 10^{-5}$	$4.04 \cdot 10^{1}$
$4.42 \cdot 10^{-6}$	$7.00 \cdot 10^{-6}$	$4.13 \cdot 10^{1}$
$2.79 \cdot 10^{-6}$	$4.42 \cdot 10^{-6}$	$4.23 \cdot 10^{1}$
$1.76 \cdot 10^{-6}$	$2.79 \cdot 10^{-6}$	$4.39 \cdot 10^{1}$
$1.11 \cdot 10^{-6}$	$1.76 \cdot 10^{-6}$	$4.75 \cdot 10^{1}$
$7.00 \cdot 10^{-7}$	$1.11 \cdot 10^{-6}$	$5.54 \cdot 10^{1}$
$4.42 \cdot 10^{-7}$	$7.00 \cdot 10^{-7}$	$7.28 \cdot 10^{1}$
$2.79 \cdot 10^{-7}$	$4.42 \cdot 10^{-7}$	$1.09 \cdot 10^{2}$
$1.76 \cdot 10^{-7}$	$2.79 \cdot 10^{-7}$	$1.78 \cdot 10^{2}$
$1.11 \cdot 10^{-7}$	$1.76 \cdot 10^{-7}$	$2.97 \cdot 10^{2}$
$7.00 \cdot 10^{-8}$	$1.11 \cdot 10^{-7}$	$4.76 \cdot 10^{2}$
$4.42 \cdot 10^{-8}$	$7.00 \cdot 10^{-8}$	$7.06 \cdot 10^{2}$
$2.79 \cdot 10^{-8}$	$4.42 \cdot 10^{-8}$	$9.61 \cdot 10^{2}$
$1.76 \cdot 10^{-8}$	$2.79 \cdot 10^{-8}$	$1.21 \cdot 10^{3}$
$1.11 \cdot 10^{-8}$	$1.76 \cdot 10^{-8}$	$1.42 \cdot 10^{3}$
$7.00 \cdot 10^{-9}$	$1.11 \cdot 10^{-8}$	$1.58 \cdot 10^{3}$
$4.42 \cdot 10^{-9}$	$7.00 \cdot 10^{-9}$	$1.70 \cdot 10^{3}$
$2.79 \cdot 10^{-9}$	$4.42 \cdot 10^{-9}$	$1.78 \cdot 10^{3}$
$1.76 \cdot 10^{-9}$	$2.79 \cdot 10^{-9}$	$1.84 \cdot 10^{3}$
$1.11 \cdot 10^{-9}$	$1.76 \cdot 10^{-9}$	$1.87 \cdot 10^{3}$
$7.00 \cdot 10^{-10}$	$1.11 \cdot 10^{-9}$	$1.90 \cdot 10^{3}$
$4.42 \cdot 10^{-10}$	$7.00 \cdot 10^{-10}$	$1.91 \cdot 10^{3}$
$2.79 \cdot 10^{-10}$	$4.42 \cdot 10^{-10}$	$1.92 \cdot 10^{3}$
$-\infty$	$2.79 \cdot 10^{-10}$	$1.92 \cdot 10^{3}$

Table A4.2. Initial chemical composition of the Opalinus clay porewater.

	Concentration	Units
Ca^{2+}	$2.60 \cdot 10^{-2}$	[mol/L]
Mg^{+2}	$1.70 \cdot 10^{-2}$	[mol/L]
Sr^{2+}	$4.49 \cdot 10^{-4}$	[mol/L]
K^{+}	$1.60 \cdot 10^{-3}$	[mol/L]
Na^{+}	$2.40 \cdot 10^{-1}$	[mol/L]
CO_3^{2-}/HCO_3^{-}	$4.57 \cdot 10^{-4}$	[mol/L]
SO_4^{2-}	$1.39 \cdot 10^{-2}$	[mol/L]
Cl^{-}	$3.00 \cdot 10^{-1}$	[mol/L]
Cs^{+}	$1.00 \cdot 10^{-10}$	[mol/L]
pH	7.6	[----]
I	0.36	[mol/L]

Table A4.3. Chemical reactions and equilibrium constants for aqueous complexes at 25ºC.

Aqueous complexes	Log K
$CaCO_3(aq) + H^+ \Leftrightarrow Ca^{2+} + HCO_3^-$	7.1050
$CaHCO_3^+ \Leftrightarrow Ca^{2+} + HCO_3^-$	-1.1060
$CaOH^+ + H^+ \Leftrightarrow Ca^{2+} + H_2O$	12.7800
$CaSO_4(aq) \Leftrightarrow Ca^{2+} + SO_4^{2-}$	-2.3000
$CO_3^{2-} + H^+ \Leftrightarrow HCO_3^-$	10.3290
$KSO_4^- \Leftrightarrow K^+ + SO_4^{2-}$	-0.8500
$NaHCO_3(aq) \Leftrightarrow Na^+ + HCO_3^-$	0.2500
$NaSO_4^- \Leftrightarrow Na^+ + SO_4^{2-}$	-0.7000
$NaOH(aq) + H^+ \Leftrightarrow Na^+ + H_2O$	14.1800
$NaCO_3^- \Leftrightarrow Na^+ + CO_3^{-2}$	-1.2700
$OH^- + H^+ \Leftrightarrow H_2O$	14.0000
$MgSO_4(aq) \Leftrightarrow Mg^{2+} + SO_4^{2-}$	-2.3700
$MgHCO_3^+ \Leftrightarrow Mg^{2+} + HCO_3^-$	-1.0680
$MgOH^+ \Leftrightarrow Mg^{2+} + OH^-$	-2.5600
$MgCO_3(aq) \Leftrightarrow Mg^{+2} + CO_3^{-2}$	-2.9800
$KOH(aq) + H^+ \Leftrightarrow K^+ + H_2O$	14.4600
$SrSO_4(aq) \Leftrightarrow Sr^{2+} + SO_4^{2-}$	-2.2900
$SrHCO_3 \Leftrightarrow Sr^{2+} + HCO_3^-$	-1.1810
$SrCO_3(aq) \Leftrightarrow Sr^{2+} + CO_3^{-2}$	-2.8100
$SrOH^+ + H^+ \Leftrightarrow Sr^{2+} + H_2O$	13.2900
$H_2CO_3(aq) \Leftrightarrow CO_3^{2-} + H^+$	-16.6810
$HSO_4^- \Leftrightarrow H^+ + SO_4^{2-}$	1.9880

Table A4.4. Cation exchange capacity (CEC) values for the three cation exchange sites.

Cation exchange sites	CEC (meq/100 g)
First (planar)	16.216
Second (higher affinity)	1.201
Third (frayed edge)	0.016

Table A4.5. Cation exchange reactions and selectivity coefficients for the three cation exchange sites.

Reaction	$K_{Na\text{-}cation}$
First sites (planar sites)	
$Na^+ + X\text{-}K \Leftrightarrow K^+ + X\text{-}Na^+$	$1.99 \cdot 10^{-1}$
$Na^+ + 0.5\ X_2\text{-}Ca \Leftrightarrow 0.5\ Ca^{2+} + X\text{-}Na$	$4.62 \cdot 10^{-1}$
$Na^+ + 0.5\ X_2\text{-}Mg \Leftrightarrow 0.5\ Mg^{2+} + X\text{-}Na$	$5.07 \cdot 10^{-1}$
$Na^+ + X\text{-}Cs \Leftrightarrow Cs^+ + X\text{-}Na$	$2.51 \cdot 10^{-2}$
Second sites (high affinity sites)	
$Na^+ + X\text{-}K \Leftrightarrow K^+ + X\text{-}Na$	$7.94 \cdot 10^{-3}$
$Na^+ + X\text{-}Cs \Leftrightarrow Cs^+ + X\text{-}Na$	$6.31 \cdot 10^{-4}$
Third sites (frayed edge sites)	
$Na^+ + X\text{-}K \Leftrightarrow K^+ + X\text{-}Na$	$3.98 \cdot 10^{-3}$
$Na^+ + X\text{-}Cs \Leftrightarrow Cs^+ + X\text{-}Na$	$1.00 \cdot 10^{-7}$

A4.4. MODEL RESULTS

A4.4.1. Single-species model

The results obtained with the single-species transport model performed with CORE^{2D}V5 (Samper et al., 2009, 2011) were compared with those obtained with other reactive transport codes (benchmarking). In this case, two other codes were used to perform the single-species transport model: MCOTAC (Pfingsten 1994, 2002, 2005) and COMSOL Multiphysics (http://www.comsol.com). Dissolved Cs concentrations were calculated with the three transport codes at x = 1, 5, 7 and 9 mm. Figure A4.3 shows the Cs breakthrough curves calculated with the three transport codes with the single-species transport model at x = 1, 5, 7 and 9 mm for Cs concentrations at the "high" concentration container equal to 10^{-3}, 10^{-5} and 10^{-7} mol/L. The arrival of the Cs concentration front for a boundary Cs concentration equal to 10^{-3} mol/L is faster than the arrival for Cs concentrations equal to 10^{-5} and 10^{-7} mol/L. The Cs retardation is stronger in the models with lower Cs boundary concentrations due to the non-linear Cs sorption in Opalinus clay (the K_d of Cs decreases with increasing dissolved Cs

concentration). In fact, Cs does not breakthrough at x = 7 and 9 mm even after 10 years when the boundary Cs concentration is equal to 10^{-7} mol/L.

The computed Cs concentrations with the three codes for the three Cs boundary concentrations (10^{-3}, 10^{-5} and 10^{-7} mol/L) agree for the most part. However, there are mild differences at x = 1 mm. The steady Cs concentration plateaus computed with the three codes at late times are similar. Possible reasons for the small differences between the Cs concentrations computed with the three codes include:

- The differences in the spatial discretization of the model domain. A coarse mesh with 50 nodes was used in MCOTAC calculations. An intermediate grid with 102 nodes was used in CORE^{2D}V5 calculations. A fine logarithmically-expanding mesh with more than 500 nodes was used in COMSOL calculations. The Cs breakthrough curves computed with MCOTAC show slightly more dispersion than those computed with CORE^{2D}V5 and COMSOL. In addition, the tracer arrival times computed with MCOTAC are always smaller than those computed with the other transport codes.

- The differences in the implementation of the sorption isotherm and the calculation of the K_d for each Cs concentration interval. The derivative of the sorption isotherm as a function of dissolved Cs concentration was implemented in COMSOL. CORE^{2D}V5 and MCOTAC, however, used directly the measured K_d. The K_d values were assumed constant for the selected intervals of Cs dissolved concentrations.

- The Cs concentrations at individual locations were obtained with the help of a discretization volume in MCOTAC where an average concentration was calculated. For CORE^{2D}V5 and COMSOL the Cs concentrations were obtained by a more appropriate interpolation procedure. These differences contribute to the fact that the tracer arrival times in the models performed with MCOTAC are earlier than those computed with CORE^{2D}V5 and COMSOL.

A sensitivity analysis was performed with CORE^{2D}V5 to analyse the numerical discretization errors. Sensitivity runs were carried out by using a very fine grid with 2002 nodes (Δx = 0.001 cm) for the three Cs boundary concentrations. These sensitivity runs were used also to quantify the errors caused by the fact that K_d values are defined elementwise in CORE^{2D}V5, whereas the concentrations are computed at the nodes of the mesh. The numerical errors decrease by using a very fine grid. Figure A4.4 shows the Cs breakthrough curves calculated with CORE^{2D}V5 at x = 1, 5, 7 and 9 mm for grids with 102 nodes (Δx = 0.02 cm) and with 2002 nodes (Δx = 0.001 cm) for Cs boundary concentrations equal to 10^{-3}, 10^{-5} and 10^{-7} mol/L. The Cs breakthrough curves computed with the very fine grid show a smaller dispersion than those computed with the coarse mesh. The results of the sensitivity runs confirm that the use of a coarse mesh in MCOTAC introduces numerical dispersion.

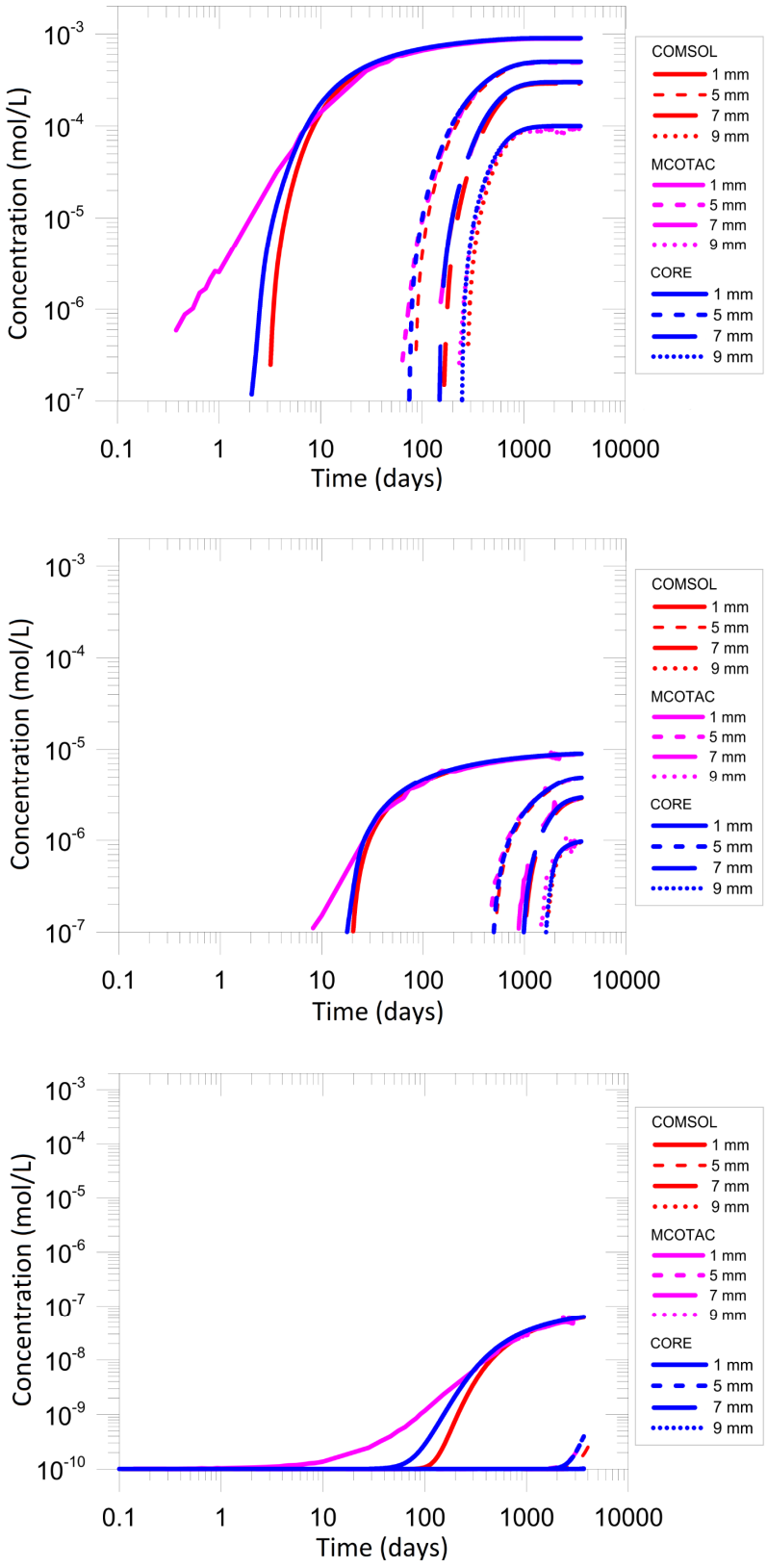

Figure A4.3. Cs breakthrough curves calculated with the single-species transport models at x = 1, 5, 7 and 9 mm with CORE^{2D}V5, MCOTAC and COMSOL. The Cs concentration in the "high" concentration container is equal to 10^{-3} mol/L (top), 10^{-5} mol/L (intermediate) and 10^{-7} mol/L (bottom).

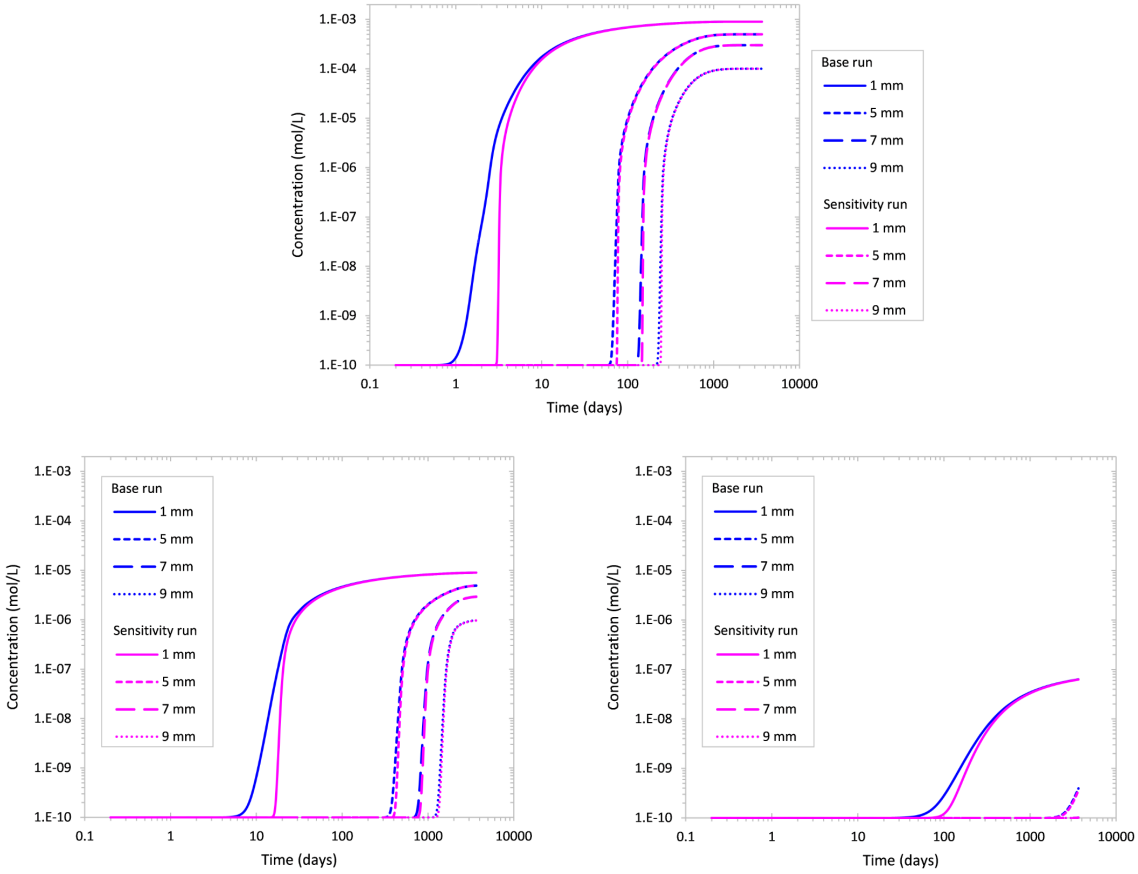

Figure A4.4. Cs breakthrough curves calculated with CORE^{2D}V5 at x = 1, 5, 7 and 9 mm for grids with 102 nodes (Δx = 0.02 cm) and 2002 nodes (Δx = 0.001 cm). The Cs boundary concentrations at the "high" concentration container are equal to 10^{-3} mol/L (top), 10^{-5} mol/L (bottom left) and 10^{-7} mol/L (bottom right).

A4.4.2. Multi-species model

The results obtained with the multi-species transport models performed with CORE^{2D}V5 were compared with those obtained with MCOTAC. Figure A4.5 shows the Cs breakthrough curves calculated with CORE^{2D}V5 and MCOTAC at x = 1, 5, 7 and 9 mm for Cs boundary concentrations at the "high" concentration container equal to 10^{-3}, 10^{-5} and 10^{-7} mol/L. The results computed with CORE^{2D}V5 and MCOTAC with the multi-species transport models performed for several Cs boundary concentrations generally agree. However, there are slight differences in the Cs breakthrough curves calculated with the two codes near the "high" Cs concentration boundary (x = 1 mm) for the three Cs boundary concentrations. These differences are due to the differences in the spatial discretization. Similar to the single-species transport model, the meshes used with MCOTAC has 50 nodes while the mesh used with CORE^{2D}V5 has 102 nodes. The results computed with MCOTAC show slightly more dispersion than those computed with CORE^{2D}V5. The Cs breakthrough curves calculated with the two reactive transport codes are very similar at x = 5, 7 and 9 mm for the three Cs boundary concentrations levels.

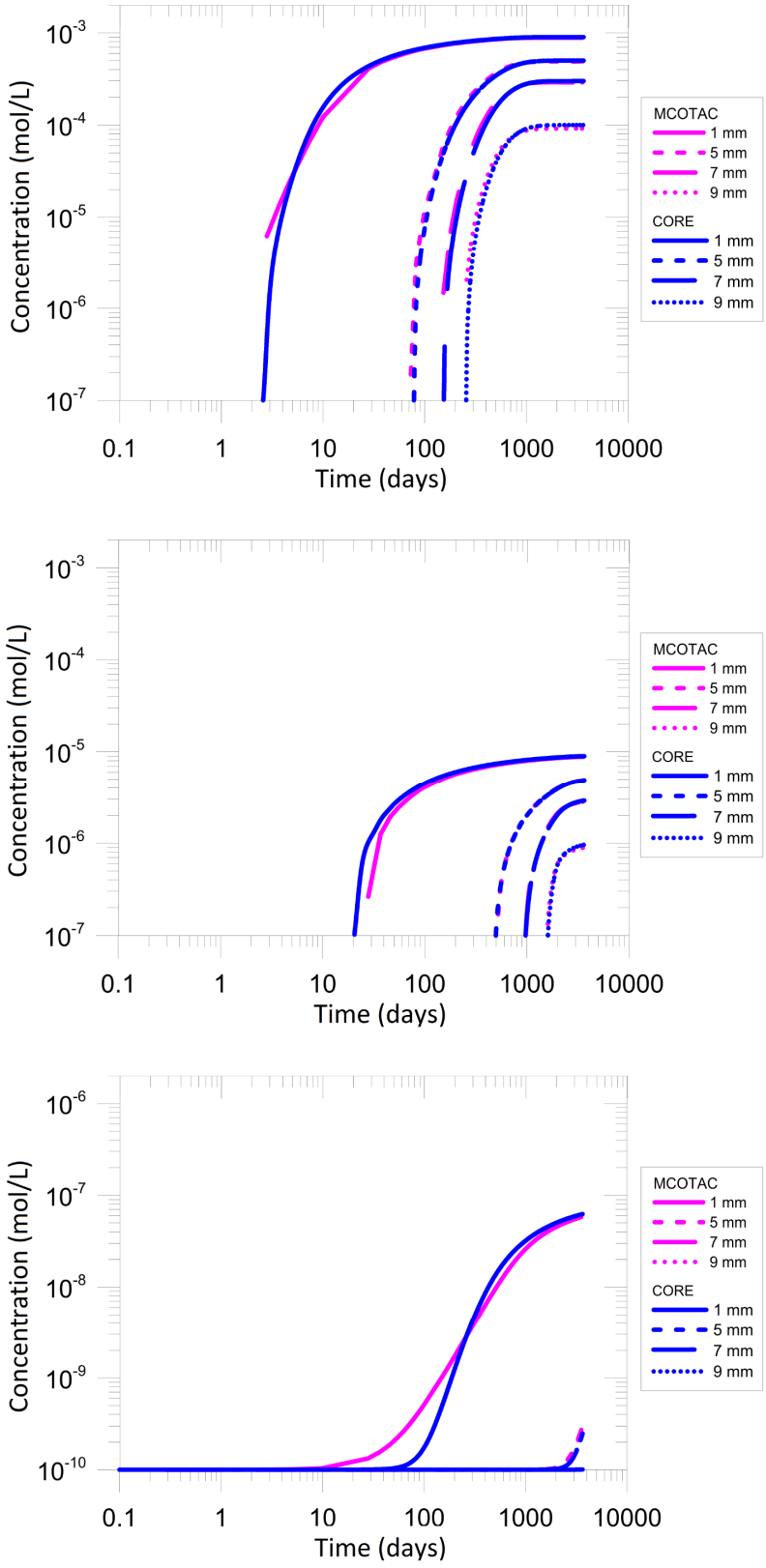

Figure A4.5. Cs breakthrough curves calculated with the multi-species transport models at x = 1, 5, 7 and 9 mm with CORE^{2D}V5 and MCOTAC. The Cs concentration at the "high" concentration container was equal to 10^{-3} mol/L (top), 10^{-5} mol/L (intermediate) and 10^{-7} mol/L (bottom).

Several sensitivity runs were performed with CORE^{2D}V5 to analyse the influence in the model results of the convergence tolerance (ω) for solving the nonlinear set of chemical reactions. The computed dissolved Cs concentrations are very sensitive to the convergence tolerance, especially for a Cs boundary concentration equal to 10^{-7} mol/L. Figure A4.6 shows the Cs breakthrough curves calculated with CORE^{2D}V5 at x = 1 and 5 mm for convergence tolerances equal to 10^{-3}, 10^{-5}, 10^{-6}, 10^{-7} and 10^{-11} for a Cs boundary concentration equal to 10^{-7} mol/L. The convergence tolerance usually is within the range from 10^{-6} to 10^{-3}. However, when a tolerance value between 10^{-6} and 10^{-3} is used in the multi-species transport model, the Cs breakthrough curves computed with CORE^{2D}V5 change significantly. In this case, it was necessary to use a convergence tolerance equal to 10^{-7} to achieve very small differences in the computed Cs concentrations.

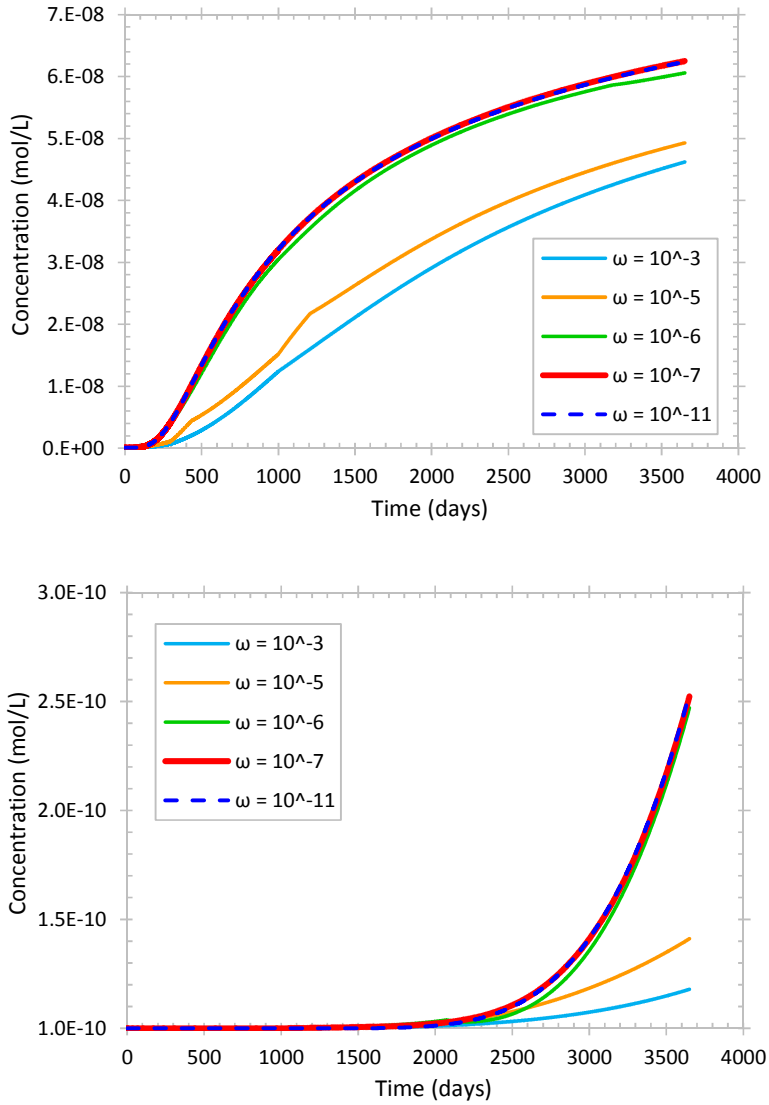

Figure A4.6. Sensitivity of the Cs breakthrough curves computed with CORE^{2D}V5 at x = 1 mm (top) and at x = 5 mm (bottom) to changes in the convergence tolerance (ω) used to solve the set of chemical reactions. The Cs concentration at the "high" concentration container is equal to 10^{-7} mol/L.

Figure A4.7 shows the time evolution of the concentrations of exchanged cations in the first cation exchange site computed with the multi-species transport model in the middle of the sample (x = 5 mm) for a Cs boundary concentration equal to 10^{-3} mol/L. The concentrations of exchanged K^+, Na^+, Mg^{2+} and Ca^{2+} decrease slightly when the concentration of exchanged Cs^+ increases. The concentration of exchanged Cs^+ increases quickly at x = 5 mm after approximately 100 days when Cs reaches this point by diffusion from the "high" concentration boundary. Dissolved Cs^+ exchanges with other cations in the first sorption site type after 100 days. The concentrations of exchanged K^+, Na^+, Mg^{2+} and Ca^{2+} change slightly during the first 100 days of simulation at x = 5 mm, but these changes play a minor role.

Figure A4.8 shows the time evolution of the concentrations of exchanged cations in the second cation exchange site in the middle of the sample (x = 5 mm) for a Cs boundary concentration equal to 10^{-3} mol/L. Na^+ exchanges with K^+ during the first 100 days of the simulation at x = 5 mm. The concentration of exchanged K^+ increases while the concentration of exchanged Na^+ decreases. After approximately 100 days, Cs^+ exchanges with both K^+ and Na^+ in the second type of cation exchange sites.

Figure A4.9 shows the time evolution of the concentrations of the exchanged cations in the third type of cation exchange sites in the middle of the sample (x = 5 mm) for a Cs boundary concentration equal to 10^{-3} mol/L. Similar to the second type of cation exchange sites, Na^+ is exchanged with K^+ during the first 100 days of the simulation at x = 5 mm. When Cs reaches by diffusion this point, both K^+ and Na^+ exchange with dissolved Cs^+. The computed exchanged concentrations were analysed in the middle of the sample of Opalinus clay (x = 5 mm). The patterns of exchanged concentrations at other locations are similar to those computed at x = 5 mm.

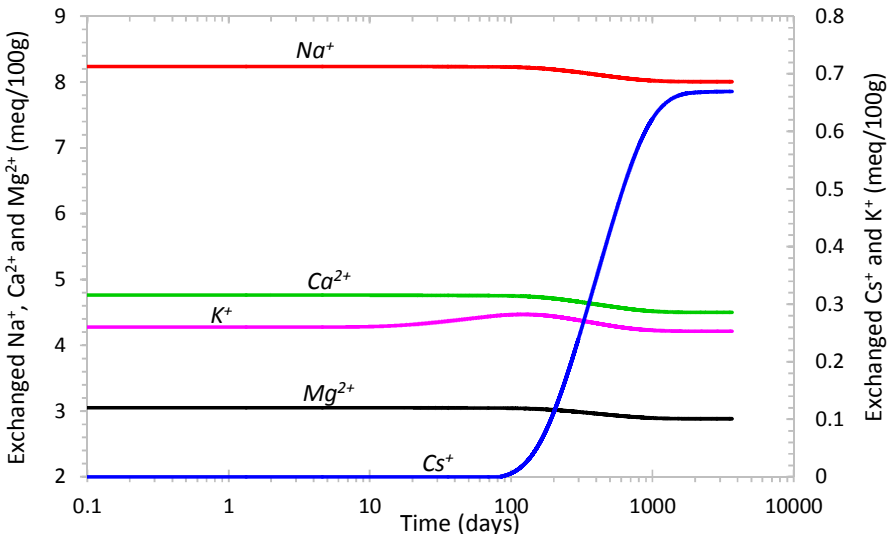

Figure A4.7. Time evolution of the computed concentrations of exchanged cations in the first type of cation exchange sites at x = 5 mm. The Cs concentration at the "high" concentration container is equal to 10^{-3} mol/L.

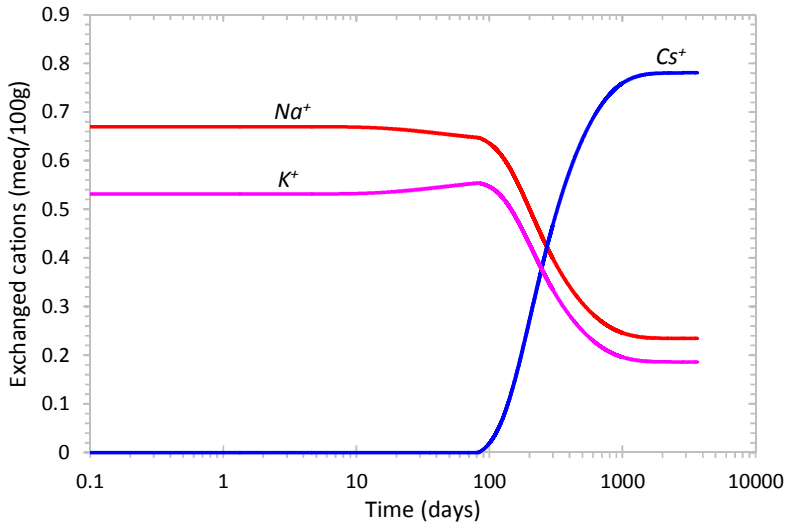

Figure A4.8. Time evolution of the computed concentrations of exchanged cations in the second type of cation exchange sites at x = 5 mm. The Cs concentration at the "high" concentration container is equal to 10^{-3} mol/L.

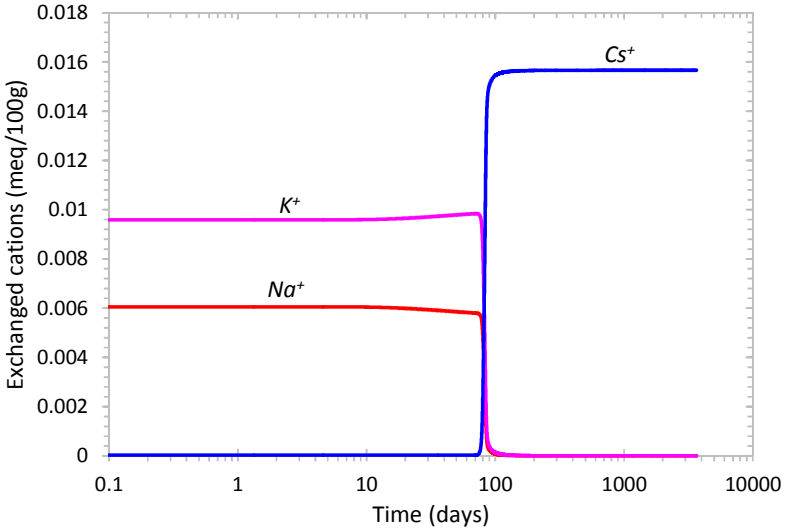

Figure A4.9. Time evolution of the computed concentrations of exchanged cations in the third type of cation exchange sites at x = 5 mm. The Cs concentration at the "high" concentration container is equal to 10^{-3} mol/L.

Figure A4.10 shows the time evolution of the computed concentrations of dissolved Na^+, Ca^{2+}, Mg^{2+}, K^+ and Cs^+ at x = 5 mm for a Cs boundary concentration equal to 10^{-3} mol/L. The concentration of dissolved Cs^+ increases after approximately 100 days due to the Cs diffusion from the "high" concentration boundary. The concentrations of other cations such as Na^+, Ca^{2+}, Mg^{2+}, K^+ remain more or less constant during the simulation time (Figure A4.10). However, from the time evolution of the concentration of dissolved cations, one can see that the concentrations of dissolved K^+, Na^+, Mg^{2+} and Ca^{2+} vary slightly over time. Figure A4.11 shows the time evolution of the computed concentration of dissolved K^+ and Cs^+ at x = 1, 5 and 9 mm for a Cs boundary concentration equal to 10^{-3} mol/L. The

time evolution of the concentration of dissolved K^+ correlates well to that of the dissolved Cs^+. The concentration of dissolved K^+ increases with time. The increase in K^+ concentration is greater at points located near the "high" concentration boundary (x = 1 mm). When the concentration of dissolved Cs^+ begins to increase due to Cs diffusion from the "high" concentration boundary, the concentration of dissolved K^+ decreases. Finally, the computed concentration of dissolved K^+ decreases to its initial value ($1.60 \cdot 10^{-3}$ mol/L).

Cs migration in the multi-species transport is non-linear because sorption depends on the local availability of all the other competing cations. In this test, the Cs breakthrough curves is mainly linked to K^+ and Na^+ distribution. Other cations such as Ca^{2+} or Mg^{2+} play a minor role. Figure A4.12 shows the time evolution of the computed concentration of dissolved Na^+ and Cs^+ at x = 1, 5 and 9 mm for a Cs boundary concentration equal to 10^{-3} mol/L. The time evolution of the concentration of dissolved Na^+ is not as closely correlated with that of dissolved Cs^+ as in the case of K^+. The concentration of dissolved Na^+ increases with time and subsequently decreases to its initial value (0.24 mol/L). However, the decrease of the concentration of Na^+ begins before the concentration of dissolved Cs^+ begins to increase. Despite this, the decrease of Na^+ is faster when the concentration of dissolved Cs^+ increases.

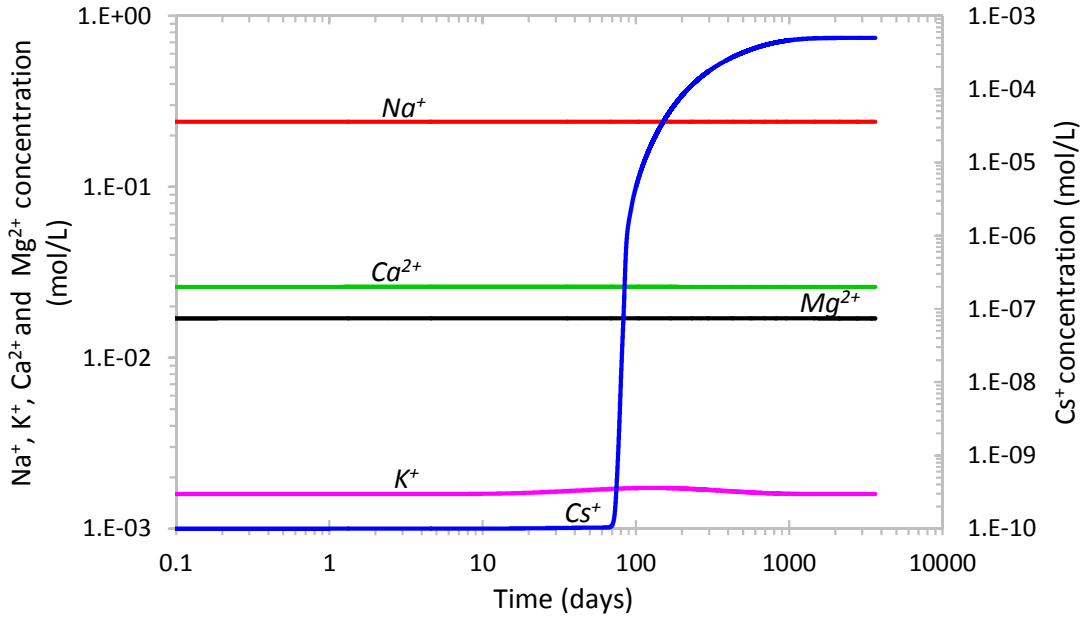

Figure A4.10. Time evolution of the concentrations of dissolved Na^+, Ca^{2+}, Mg^{2+}, K^+ and Cs^+ computed with CORE^{2D}V5 at x = 5 mm. The Cs boundary concentration at the "high" concentration container is equal to 10^{-3} mol/L.

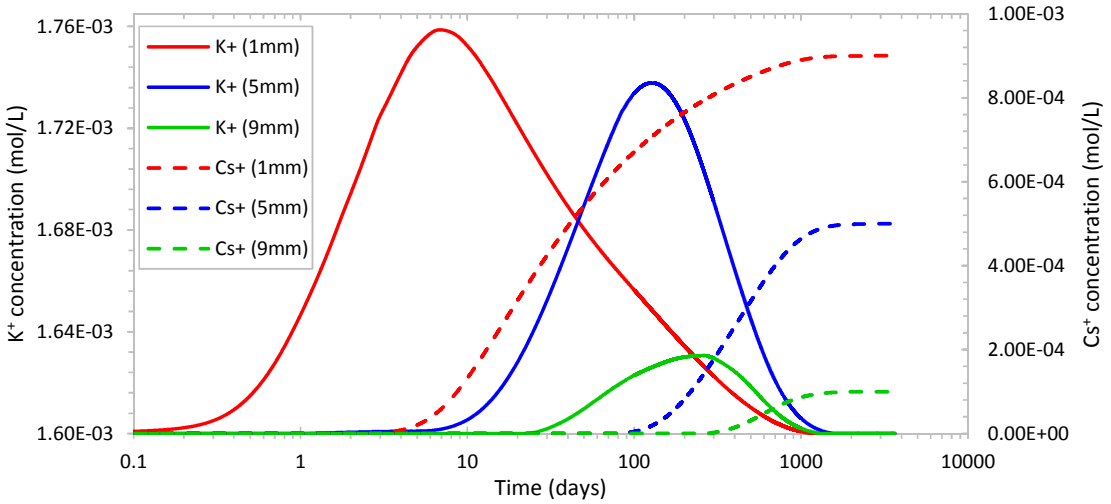

Figure A4.11. Time evolution of the concentrations of dissolved K^+ and Cs^+ computed with CORE^{2D}V5 at x = 1, 5 and 9 mm. The Cs boundary concentration at the "high" concentration container is equal to 10^{-3} mol/L.

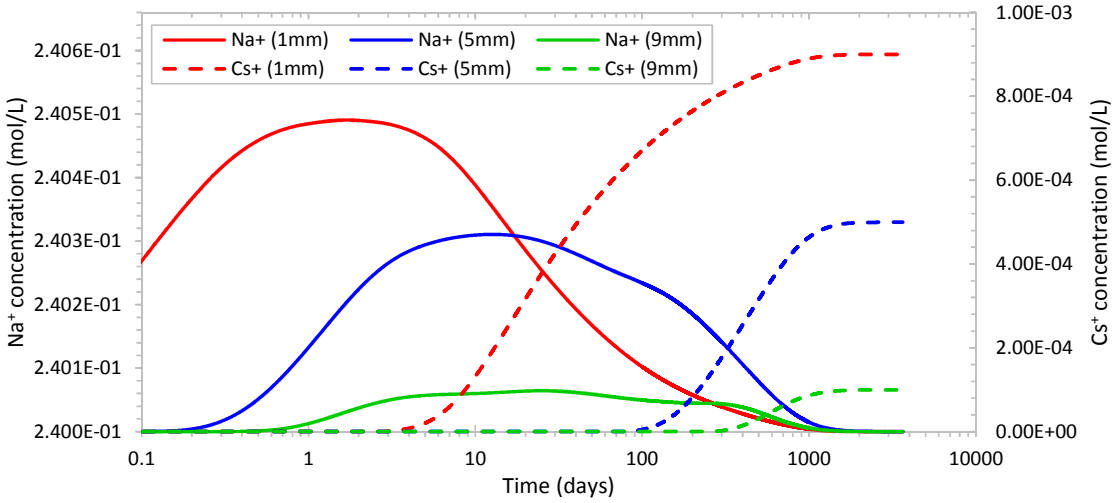

Figure A4.12. Time evolution of the concentrations of dissolved Na^+ and Cs^+ computed with CORE^{2D}V5 at x = 1, 5 and 9 mm. The Cs boundary concentration at the "high" concentration container is equal to 10^{-3} mol/L.

A4.5. COMPARISON OF SINGLE-SPECIES AND MULTI-SPECIES MODELS

Cs breakthrough curves at x = 1, 5, 7 and 9 mm computed with CORE^{2D}V5 with the single-species and the multi-species transport models for Cs boundary concentrations equal to 10^{-3}, 10^{-5} and 10^{-7} mol/L were compared (Figure A4.13). These results were computed with the finite element mesh with 102 nodes. The results computed with the two numerical models are similar for the three Cs concentrations despite the differences in the formulations of the non-linear Cs sorption in Opalinus Clay.

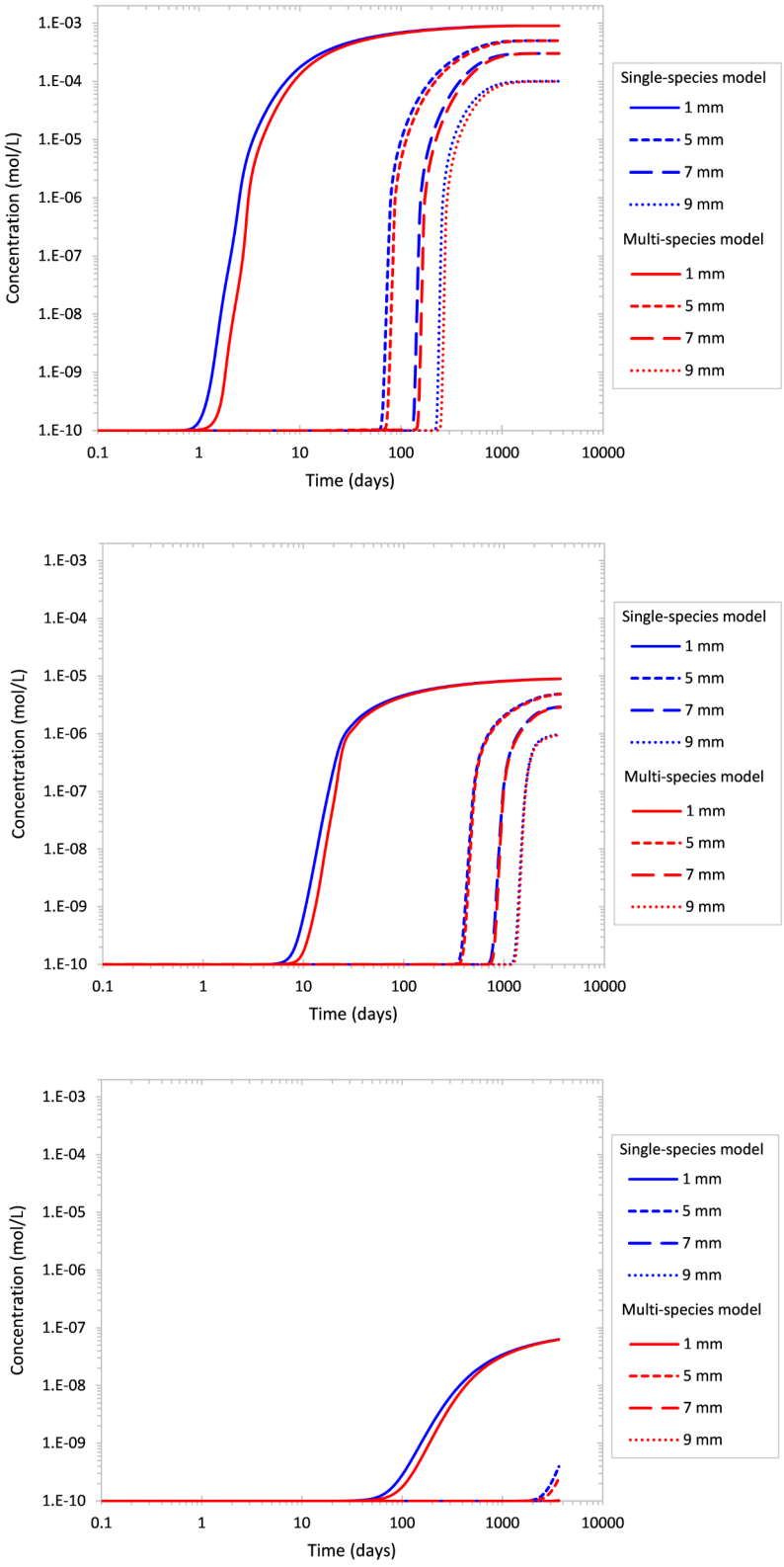

Figure A4.13. Cs breakthrough curves calculated with CORE^{2D}V5 with the single-species and the multi-species transport models at x = 1, 5, 7 and 9 mm. The Cs concentration at the "high" concentration container was assumed to be 10^{-3} mol/L (top), 10^{-5} mol/L (intermediate) and 10^{-7} mol/L (bottom)

A4.6. SUMMARY AND CONCLUSIONS

Clay formations are being considered as potential host rocks for the disposal of radioactive waste in deep geological repositories. Cs is a key radionuclide showing non-linear sorption in clay. Numerical models performed with CORE^{2D}V5 to simulate the non-linear Cs sorption in Opalinus clay have been presented.

A single-species transport model which uses a tabulated non-linear sorption isotherm measured in laboratory was used first to simulate the non-linear Cs sorption in Opalinus clay (Van Loon et al., 2009). CORE^{2D}V5 was modified to implement the tabulated sorption isotherm in form a look-up table with given values for pairs of Cs data: Cs in solution versus K_d. The results of the single-species transport model performed with CORE^{2D}V5 were compared with the results of other numerical transport codes: COMSOL Multiphysics and MCOTAC. The Cs breakthrough curves computed with the three transport codes at several locations for three Cs boundary concentrations are similar. However, there are mild differences due to: 1) Differences in the spatial discretization used in the codes, 2) Differences in the implementation of the sorption isotherm in the transport codes and 3) Differences in the interpolation procedures. A sensitivity analysis was performed with CORE^{2D}V5 to evaluate the discretization errors. The computed results confirm that the use of coarse grids leads to numerical dispersion.

The non-linear Cs sorption in Opalinus clay was simulated also with a multi-species reactive transport model with cation exchange in three sites (Bradbury and Baeyens, 2000). Cs breakthrough curves computed with CORE^{2D}V5 at several location in the Opalinus clay for three Cs boundary concentrations were compared with those computed with the reactive transport code MCOTAC. The results of both codes generally agree. However, there are slight differences between the results of the two codes due to the differences in the spatial discretization. The convergence tolerance to solve the chemical reactions in CORE^{2D}V5 was reduced to 10^{-7} to minimize numerical errors.

The computed exchanged concentrations with the multi-species transport model performed with CORE^{2D}V5 were analysed. Cs^+ exchanges with other cations in the cation exchange sites (K^+, Na^+, Mg^{2+} and Ca^{2+} in the first type of cation exchange sites and K^+ and Na^+ in the second and third types of sites). On the other hand, the time evolution of the concentrations of dissolved K^+ and Cs^+ correlate well. The concentration of dissolved K^+ increases with time throughout the Opalinus clay sample. The concentration of dissolved K^+ begins to decrease when the concentration of dissolved Cs^+ begins to increase. Later, the computed concentration of dissolved K^+ decreases to its initial value.

Cs breakthrough curves at several locations in the Opalinus clay computed with CORE^{2D}V5 with the single-species and the multi-species transport models using the same finite element mesh generally agree despite the differences in the formulation of the non-linear Cs sorption in Opalinus clay.

A4.7. REFERENCES

Appelo, C.A., Wersin, P., (2007). Multicomponent diffusion modelling in clay systems with application to the diffusion of tritium, iodide, and sodium in Opalinus clay. Environ. Sci. Technol., 41, 5002-5007.

Appelo, C.A., Van Loon, L.R., Wersin, P., (2010). Multicomponent diffusion of a suite of tracers (HTO, Cl, Br, I, Na, Sr, Cs) in a single simple of Opalinus Clay. Geochim Cosmochim Acta, 74:1201-1219.

Bradbury, M.H., Baeyens, B., (2000). A generalised sorption model for the concentration dependent uptake of caesium by argillaceous rocks. J. Contam. Hydrol., 42, 141-163.

Bourg, I.C., Sposito, G., Bourg, A.C.M., (2006). Tracer diffusion in compacted, water-saturated bentonite. Clays Clay Mineral, 54, 363-374.

Cartalade, A., Montarnal, P., Filippi, M., Mugler, C., Lamoureux, M., Martinez, J.M., Clément, F., Wileveau, Y., Coelho, D., Tevissen, E., (2007). Application of inverse modeling methods to thermal and diffusion experiments at Mont Terri Rock laboratory. Phys. Chem. Earth, 32, 491-506.

Eriksen, T.E., Jansson, M., (1996). Diffusion of I^-, Cs^+ and Sr^{2+} in compacted bentonite - anion exclusion and surface diffusion. SKB technical report 96-16, Swedish Nuclear Fuel and Waste Management Co., Stockholm, Sweden.

Gaines, L.G., Thomas, C.H., (1953). Adsorption studies on clay minerals. II. A formulation of the thermodynamics of exchange adsorption. J. Chem. Phys., 21:714-718.

Gautschi, A., (1997). Hydrogeology of the Opalinus Clay. Implications for radionuclide transport. Nagra Bulletin, 31, 24-32.

Jakob, A., Pfingsten, W., Van Loon, L., (2009). Effects of sorption competition on caesium diffusion through compacted argillaceous rock. Geochimica et Cosmochimica Acta, 73, 2441-2456.

Kau, P.M.H., Binning, P.J., Hitchcock, P.W., Smith, D.W., (1999). Experimental analysis of fluoride diffusion and sorption in clays. J. Contam. Hydrol., 36, 131-151.

Kosakowski, G., Churakov, S., Thoenen, T., (2008). Diffusion of Na and Cs in montmorillonite. Clays and Clay Minerals, 56(2), 190-206.

Maes, N., Salah, S., Jacques, D., Aertsens, M., Van Gompel, M., De Cannière, P., Velitchkova, N., (2008). Retention of Cs in Boom Clay: Comparison of data from batch sorption tests and diffusion experiments on intact clay cores. Physics and Chemistry of the Earth, Parts A/B/C, 33(Supplement 1): p. S149-S155.

Malusis, M.A., Shackelford, C.D., (2002). Theory for reactive solute transport through clay membrane barriers. J. Contam. Hydrol., 59, 291-316.

Melkior, T., Yahiaoui, S., Motellier, S., Thoby, D., Tevissen, E., (2005). Cesium sorption and diffusion in Bure mudrock samples. Appl. Clay Sci., 29, 172-186.

Ochs, M., Lothenbach, B., Wanner, H., Sato, H., Yui M., (2001). An integrated sorption-diffusion model for the calculation of consistent distribution and diffusion coefficients in compacted bentonite. J. Contam. Hydrol., 47, 283-296.

Palut, J.M., Montarnal, P., Gautschi, A., Tevissen, E. Mouche, E., (2003). Characterisation of HTO diffusion properties by an in situ tracer experiment in Opalinus clay at Mont Terri. J. Contam. Hydrol., 61, 203-218.

Pfingsten, W., (1994). Modular coupling of transport and chemistry: theory and model applications. PSI Bericht No. 94-15. Paul Scherrer Institut, Villigen PSI, Switzerland and Nagra technical report, 94-19. Nagra, Wettingen, Switzerland.

Pfingsten, W., (2002). Experimental and modelling indications for self-sealing of a cementitious low- and intermediate-level waste repository by calcite precipitation. Nucl. Technol., 140, 63-82.

Pfingsten, W., (2005). MCOTAC 2005. PSI internal report AN-44-05-07. Paul Scherrer Institut, Villigen PSI, Switzerland (in German).

Rosanne, M., Mammar, N., Koudina, N., Prunet-Foch, B., Thovert, J.F., Tevissen, E., Adler, P.M., (2003). Transport properties of compacted clays-II. Diffusion. J. Colloid Interface Sci., 260, 195-203.

Samper, J., Xu, T., Yang, C., (2009). A sequential partly iterative approach for multicomponent reactive transport with CORE^{2D}. Comput. Geosci., http://dx.doi.org/10.1007/s10596-008-9119-5.

Samper, J., Yang, C., Zheng, L., Montenegro, L., Xu, T., Dai, Z., Zhang, G., Lu, C., Moreira, S., (2011). CORE^{2D}V4: A code for water flow, heat and solute transport, geochemical reactions, and microbial

processes, Chapter 7 of the Electronic book Groundwater Reactive Transport Models, F Zhang, G-T Yeh, C Parker & X Shi (Ed), Bentham Science Publishers, pp 161-186, ISBN: 978-1-60805-029-1.

Shackelford, C.D., (1991). Laboratory diffusion testing for waste disposal - a review. J. Contam. Hydrol., 7, 177-217.

Suzuki, S., Haginuma, M., Suzuki, K., (2007). Study of Sorption and Diffusion of ^{137}Cs in Compacted Bentonite Saturated with Saline Water at 60ºC. Nuclear Science and Technology. 44, 81-89.

Tevissen, E., Soler, J.M., Montarnal, P., Gautschi, A., Van Loon, L.R., (2004). Comparison between in situ and laboratory diffusion studies of HTO and halides in Opalinus clay from the Mont Terri. Radiochim. Acta, 92, 781-786.

Van Loon, L.R., Soler, J.M., Bradbury, M.H., (2003a). Diffusion of HTO, $^{36}Cl^-$ and $^{125}I^-$ in Opalinus clay samples from Mont Terri - effect of confining pressure. J. Contam. Hydrol., 61, 73-83.

Van Loon, L.R., Soler, J.M., Jakob, A., Bradbury, M.H., (2003b). Effect of confining pressure on the diffusion of HTO, $^{36}Cl^-$, and $^{125}I^-$ in a layered argillaceous rock (Opalinus clay): diffusion perpendicular to the fabric. Appl. Geochem., 18, 1653-1662.

Van Loon, L.R., Soler, J.M., (2004). Diffusion of HTO, $^{36}Cl^-$, $^{125}I^-$ and $^{22}Na^+$ in Opalinus clay: effect of confining pressure, sample orientation, sample depth and temperature. PSI Bericht, No. 04-03. Paul Scherrer Institut, Villigen PSI, Switzerland.

Van Loon, L.R., Soler, J.M., Müller, W., Bradbury, M.H., (2004). Anisotropic diffusion in layered argillaceous rocks: a case study with Opalinus clay. Environ. Sci. Technol., 38(21), 5721-5728.

Van Loon, L.R., Baeyens, B., Bradbury, M.H., (2009). The sorption behaviour of caesium on Opalinus clay: A comparison between intact and crushed material. Appl. Geochem., 24, 999-1004.

Wersin, P., Soler, J.M., Van Loon, L., Eikenberg, J., Baeyens, B., Grolimund, D., Gimmi, T., Dewonck, S., (2008). Diffusion of HTO, Br^-, I^-, Cs^+, $^{85}Sr^{2+}$ and $^{60}Co^{2+}$ in a clay formation: Results and modelling from an in situ experiment in Opalinus Clay. Applied Geochemistry, 23(4): p. 678-691.

Xia, X., Iijima, K., Kamei, G., Shibata, M., (2006). Comparative study of cesium sorption on crushed and intact sedimentary rock. Radiochim. Acta, 94, 683-687.

APPENDIX 5. NUMERICAL FLOW MODELS OF GROUNDWATER PUMPING AT THE CENTRALISED TEMPORARY STORAGE (CTS) FACILITY OF RADIOACTIVE WASTE AT THE VILLAR DE CAÑAS SITE (CUENCA), SPAIN

This appendix presents numerical 2-D horizontal groundwater flow models for the simulation of groundwater pumping at the Centralised Temporary Storage facility of radioactive waste (CTS) at Villar de Cañas site (Cuenca), Spain. These models were performed within the framework of several projects funded by ENRESA. This material was partly published in the following references:

→ Samper J. & J. Fernández, 2016. Modelo matemático de flujo subterráneo del ensayo de interferencia en la vaguada situada al este de la zona nuclear del emplazamiento del Almacén Temporal Centralizado (ATC) en Villar de Cañas (Cuenca). Technical report for ENRESA. E.T.S.I. Caminos, Canales y Puertos. Universidade da Coruña. May 2016. 87 pp. [in Spanish].

→ Samper J., J. Fernández, B. Pisani, A. Mon, A. Naves & L. Montenegro, 2016. Modelo matemático (2D/3D) del flujo de aguas subterráneas en el emplazamiento del ATC. Final technical report for ENRESA. E.T.S.I. Caminos, Canales y Puertos. Universidade da Coruña. October 2016. 410 pp. [in Spanish].

ABSTRACT

On 30 December 2011, the Government of Spain designated the municipality of Villar de Cañas in Cuenca as the site for the Centralised Temporary Storage (CTS) facility of radioactive waste and its Associated Technological Centre. This facility will provide temporary storage for the spent fuel and high-level radioactive waste from Spanish nuclear power plants. ENRESA (Empresa Nacional de Residuos Radiactivos S.A.) started the site characterization activities in early 2012. The *"Agua y Suelo"* Research Group of the University of A Coruña led by Professor Javier Samper has been involved in the numerical groundwater flow modelling of the CTS site since 2013. These numerical flow models constitute a very important part of this PhD Dissertation.

2-D horizontal groundwater flow models for the simulation of groundwater pumping at the Centralised Temporary Storage (CTS) facility of radioactive waste at Villar de Cañas (Cuenca, Spain) site were performed to:

1) Interpret a long-term pumping test carried out in June 2016 in the creek located east of the nuclear zone of the CTS site, estimate the hydrogeological parameters of the subsurface and characterize the horizontal and vertical extent of the Balanzas Gypsum Formation affected by dissolution. The model of the pumping test takes into account the delayed drainage from the unsaturated zone and the water table evapotranspiration. The numerical model was successful in reproducing the measured drawdowns in the observation wells during the pumping test, estimating the hydrodynamic parameters of the Balanzas Gypsum Formation and characterizing the horizontal and vertical extent of the Balanzas Gypsum Formation affected by dissolution.

2) Simulate the potential impact of the Chaparral water supply pumping well on the hydrogeological conditions of the nuclear zone of the CTS site. These simulations were performed for several hypothesis and pumping schemes. Model results show that the drawdown of the water table produced by the Chaparral pumping well in the nuclear zone of the CTS site will be on the order of 0.4 m and will be much smaller than the changes in hydraulic heads caused by other planned actions such as the excavations of the basements of the nuclear buildings and the waterproofing of the built-up area.

The full version of Appendix 5 is not included in this reduced version of the dissertation. The numerical models performed during the course of this dissertation at the site of the Centralised Temporary Storage (CTS) located in Villar the Cañas (Cuenca, Spain) are subject to data protection due to a confidentiality commitment from ENRESA. The full content of the Appendix 5 can be found in the full version of the dissertation.

APPENDIX 6. 2-D LOCAL-SCALE FLOW MODEL IN A VERTICAL PROFILE FOR THE CENTRALISED TEMPORARY STORAGE (CTS) FACILITY OF RADIOACTIVE WASTE AT THE VILLAR DE CAÑAS SITE (CUENCA), SPAIN

This appendix presents a 2-D local-scale flow model in a vertical profile in East-West direction for the Centralised Temporary Storage (CTS) facility of radioactive waste at the Villar de Cañas site (Cuenca), Spain. This numerical model was performed within the framework of the characterization activities of the CTS site. The material presented in this appendix has been published in the following technical reports:

→ Samper J., J. Fernández, B. Pisani, A. Mon, A. Naves & L. Montenegro, 2014. Modelos matemáticos de flujo subterráneo en el emplazamiento del Almacén Temporal Centralizado (ATC) en Villar de Cañas (Cuenca). Technical report for ENRESA. E.T.S.I. Caminos, Canales y Puertos. Universidade da Coruña. December 2014. 261 pp. [in Spanish].

→ Samper J., J. Fernández, B. Pisani, A. Mon, A. Naves & L. Montenegro, 2016. Modelo matemático (2D/3D) del flujo de aguas subterráneas en el emplazamiento del ATC. Final technical report for ENRESA. E.T.S.I. Caminos, Canales y Puertos. Universidade da Coruña. October 2016. 410 pp. [in Spanish].

ABSTRACT

The construction of a Centralised Temporary Storage (CTS) facility to store the spent fuel from Spanish nuclear power plants and high-level radioactive waste for 60 years requires a detailed characterization of the site where this facility will be built. As part of the characterization work, several numerical groundwater flow models were performed at the CTS site. This appendix presents a 2-D local-scale flow model in a vertical profile in East-West direction of the CTS site located in Villar de Cañas (Cuenca, Spain). The numerical model has a length of 6045 m and extends from the Záncara River to the west to the Mesozoic limestones to the east. The upper boundary of the model coincides with the estimated water table under natural conditions. The bottom boundary of the model is located at an elevation of 450 masl. The numerical model was calibrated in steady-state condition. The computed heads match the measured head data with calibration errors being smaller than 1 m. The numerical model was later extended to transient conditions. The computed hydrographs reproduce the measured fluctuations of the piezometric data, although there is time-lag in the maximum hydraulic heads. The numerical model confirms the hydrogeological conceptual model of the site and ratifies that the flows and volumes of water drained from (to) the Mesozoic formations to (from) the Tertiary materials are very small. The groundwater flow system includes a regional component from the Lower Tertiary Formation (UI+LBI) to the creek located in the vicinity of borehole SVC-8, the creek located to the east of the CTS site and the alluvial of the Záncara River. In addition, there are local flows which are controlled by the topography. The nuclear zone of the CTS site is located in a recharge area where groundwater percolates first vertically down. Later, some groundwater flows towards the west to the Záncara River and its alluvial and some groundwater recharge flows to the creek located to the east of the CTS site. The Balanzas Gypsum Formation (YB) behaves as a semi-confined layer which separates the groundwater local flow from the deep regional groundwater flow.

The 2-D local-scale flow model in a vertical profile in East-West direction of the CTS site has been useful to confirm the hydrogeological conceptual model and quantify hydraulic heads, groundwater flows and groundwater balance.

The full version of Appendix 6 is not included in this reduced version of the dissertation. The numerical models performed during the course of this dissertation at the site of the Centralised Temporary Storage (CTS) located in Villar the Cañas (Cuenca, Spain) are subjected to data protection due to a confidentiality commitment from ENRESA. The full content of the Appendix 6 can be found in the full version of the dissertation.

APPENDIX 7. 2-D FLOW MODELS IN VERTICAL PROFILES AT SITE SCALE FOR THE CENTRALISED TEMPORARY STORAGE (CTS) FACILITY OF RADIOACTIVE WASTE AT THE VILLAR DE CAÑAS SITE (CUENCA), SPAIN

This appendix presents two numerical flow models in vertical profiles at site scale for the Centralised Temporary Storage (CTS) facility in Villar de Cañas (Cuenca, Spain). The first flow model was performed in a vertical profile in East-West direction. Predictions of the effects of the construction of the nuclear facilities on the hydraulic heads were carried out with this numerical model. The second flow model was performed in a vertical profile in North-South direction. The need to place a drain to the north of the nuclear zone of the CTS site was evaluated with this numerical model. Both numerical models were part of the works for the characterization of the CTS site which will store the spent fuel and high-level radioactive waste from Spanish nuclear power plants. The material presented in this appendix has been published in the following technical reports:

→ Samper J., J. Fernández, B. Pisani, A. Mon, A. Naves & L. Montenegro, 2014. Modelos matemáticos de flujo subterráneo en el emplazamiento del Almacén Temporal Centralizado (ATC) en Villar de Cañas (Cuenca). Technical report for ENRESA. E.T.S.I. Caminos, Canales y Puertos. Universidade da Coruña. June 2014. 99 pp. [in Spanish].

→ Samper J., J. Fernández, B. Pisani, A. Mon, A. Naves & L. Montenegro, 2014. Modelos matemáticos de flujo subterráneo en el emplazamiento del Almacén Temporal Centralizado (ATC) en Villar de Cañas (Cuenca). Technical report for ENRESA. Updated and revised version. E.T.S.I. Caminos, Canales y Puertos. Universidade da Coruña. December 2014. 261 pp. [in Spanish].

ABSTRACT

Two numerical flow models in vertical profiles at site scale were performed at the Centralised Temporary Storage (CTS) site located in the municipality of Villar de Cañas in Cuenca (Spain). These groundwater flow models were used for predicting the future conditions at the CTS site. The first numerical model was performed in a vertical profile in East-West direction at site scale. The flow model was calibrated in steady-state conditions. The computed hydraulic heads reproduce the measured head data. Predictions of the effects of the construction of the nuclear facilities on the hydraulic heads were carried out with this numerical model in transient conditions. The effects of the decrease of the groundwater recharge in the nuclear zone of the CTS site and the changes of the hydrodynamic parameters caused by the decompression of the rock because of the excavations were simulated in a simplified manner. Moreover, simulations for a total period of 50 years were carried out with the numerical model by assuming two possible scenarios: 1) No placement of drains in the excavations of the nuclear facilities and 2) Placement of drains in the excavations of the nuclear facilities. The model provides reasonable estimates of the changes in water pressures, the drawdown of the water table and the groundwater flows collected at the drains.

The second numerical flow model was performed in a vertical profile in North-South direction at site scale. The flow model was calibrated in steady-state conditions and good agreements were achieved between the measured and computed hydraulic heads. The need to place a drain to the north of the nuclear zone of the CTS site was evaluated with this numerical model in transient conditions. Simulation for a time period of 50 years were performed by taking into account and without taking into account the placement of the drain. In addition, the waterproofing of the built-up area and the effects of excavations were also simulated with the numerical model. According to the model, the placement of the drain will not affect the water table calculated in the long-term and the flow captured by the drain will always be very small.

The full version of Appendix 7 is not included in this reduced version of the dissertation. The numerical models performed during the course of this dissertation at the site of the Centralised Temporary Storage (CTS) located in Villar the Cañas (Cuenca, Spain) are subjected to data protection due to a confidentiality commitment from ENRESA. The full content of the Appendix 7 can be found in the full version of the dissertation.

APPENDIX 8. 3-D LOCAL-SCALE FLOW MODEL FOR THE CENTRALISED TEMPORARY STORAGE (CTS) FACILITY OF RADIOACTIVE WASTE AT THE VILLAR DE CAÑAS SITE (CUENCA), SPAIN

This appendix presents a fully 3-D local-scale flow model at the Centralised Temporary Storage (CTS) site located in Villar de Cañas (Cuenca, Spain). This numerical model has been performed to test the hydrogeological conceptual model and extend the capabilities of the 2-D flow models in vertical profiles carried out at the CTS site. The material presented in this appendix has been published in the following technical report:

→ J. Samper J., J. Fernández, B. Pisani, A. Mon, A. Naves & L. Montenegro, 2016. Modelo matemático (2D/3D) del flujo de aguas subterráneas en el emplazamiento del ATC. Final technical report for ENRESA. E.T.S.I. Caminos, Canales y Puertos. Universidade da Coruña. October 2016. 410 pp. [in Spanish].

ABSTRACT

The groundwater flow at the site of the Centralised Temporary Storage (CTS) in the municipality of Villar de Cañas in Cuenca (Spain) has a three-dimensional nature. A fully 3-D local-scale numerical flow model was carried out as part of the characterization of the CTS site. The 3-D flow model was performed to test the hydrogeological conceptual model and extend the capabilities of the previous 2-D flow models in vertical profiles. The 3-D model covers an area of 16.7 km^2 and extends from the Záncara River (west) to the Mesozoic limestones (east). The north and south boundaries of the model are far enough away from the nuclear zone so that the boundary conditions imposed on these boundaries do not affect the computed results at the CTS site. The upper boundary of the model coincides with the water table under natural conditions estimated by using the Kriging interpolation method and the bottom boundary of the model is located at 450 masl. The model domain was discretized with a 3-D finite element mesh of parallelepipedic elements which accurately reproduces the complex geology at the CTS site. Additional geological profiles parallel to the profile model in East-West direction at local scale were carried out to define the geology in the 3-D model. The numerical model was calibrated in steady-state conditions and the agreements between the measured and computed hydraulic heads are acceptable. The 3-D local-scale flow model confirms the hydrogeological conceptual model. There is a groundwater flow from the outcrops of the Lower Tertiary Formation (UI+LBI) to the creek located east of the CTS site and to the Záncara River and its alluvial. The groundwater flow is modified by relatively high hydraulic heads in the Upper Balanzas Lutites Formation (LBS) in the nuclear zone of the CTS site where part of the groundwater flow is directed towards the Záncara River and its alluvial and another part flows to the creek located east of the CTS site. The results obtained with the 3-D flow model are consistent with those obtained with the 2-D horizontal models and the numerical models performed in vertical profiles. In addition, the 3-D model confirms that the hypothesis assumed in the profile models that the groundwater flow occurs entirely within vertical planes is especially true in the models carried out in East-West direction.

The full version of Appendix 8 is not included in this reduced version of the dissertation. The numerical models performed during the course of this dissertation at the site of the Centralised Temporary Storage (CTS) located in Villar the Cañas (Cuenca, Spain) are subjected to data protection due to a confidentiality commitment from ENRESA. The full content of the Appendix 8 can be found in the full version of the dissertation.

APPENDIX 9. WATER FLOW, HEAT TRANSFER, GROUNDWATER AGE, HYDROCHEMICAL MIXING AND MULTICOMPONENT REACTIVE TRANSPORT MODELS AT THE CENTRALISED TEMPORARY STORAGE (CTS) FACILITY OF RADIOACTIVE WASTE AT THE VILLAR DE CAÑAS SITE (CUENCA), SPAIN

This appendix presents water flow, heat transfer, groundwater age and reactive transport simulations performed with CORE^{2D}V5 at the Centralised Temporary Storage (CTS) site located in Villar de Cañas (Cuenca, Spain). Numerical models include: 1) A heat transport local-scale model in the vertical profile in East-West direction; 2) A local-scale flow and transport model in the vertical profile in East-West direction to simulate groundwater age; 3) A hydrochemical mixing model to quantify mixing fractions; 4) A 1-D multicomponent reactive transport model to test the hydrochemical conceptual model of the site performed by CIEMAT (Madrid); and 5) A 2-D multicomponent reactive transport model to quantify the gypsum dissolution in the contact between the YB and UI+LBI formations located away of the future nuclear zone of the CTS. All these numerical models have been used to test the flow models of the CTS site.

ABSTRACT

The characterization of the site where the Centralised Temporary Storage (CTS) of Villar de Cañas (Cuenca) is planned to be built has required a lot of studies and technical reports on a wide variety of topics. This way, there is good scientific understanding at the CTS site on different areas of knowledge (geology, hydrogeology, topography, meteorology, geotechnical or geochemical). This information was used to carry out several numerical models with the flow, heat transport and reactive transport code CORE^{2D}V5 at the CTS site. A heat transport model was performed in the vertical profile in East-West direction at local scale (see Appendix 6). The computed temperatures generally agree with the measured temperatures at several depths in boreholes drilled at the CTS site. The profile model in East-West direction was also used to simulate groundwater age. The groundwater age was estimated with two methods: 1) Injecting a pulse of a conservative tracer to groundwater recharge and analysing the tracer breakthrough curves at several locations of the model domain and 2) Simulating groundwater age with a unit source term in the solute transport equation and assigning zero age at inflow boundaries of the model. The groundwater ages calculated with the numerical model with both methods agree with the measured water ages with CFCs (chlorofluorocarbons) and ^{14}C. A mixing fraction model was also carried out to quantify the water mixing fractions at several locations of the model domain. Finally, two multicomponent reactive transport models were also performed. The first one is a 1-D model which was used to confirm the main chemical reactions of the hydrogeochemical conceptual model of the CTS proposed by CIEMAT. The second model is a 2-D reactive transport model which was carried out to study and quantify the mechanisms of gypsum dissolution at the contact between the YB and UI+LBI formations away of the nuclear zone of the CTS.

The full version of Appendix 9 is not included in this reduced version of the dissertation. The numerical models performed during the course of this dissertation at the site of the Centralised Temporary Storage (CTS) located in Villar the Cañas (Cuenca, Spain) are subject to data protection due to a confidentiality commitment from ENRESA. The full content of the Appendix 9 can be found in the full version of the dissertation.

APPENDIX 10. PARAMETRIC AND NUMERICAL ANALYSIS OF THE ESTIMATION OF GROUNDWATER RECHARGE FROM WATER TABLE FLUCTUATIONS IN UNCONFINED AQUIFERS WITH 1-D AND 2-D DETERMINISTIC AND STOCHASTIC MODELS

This appendix presents a parametric and numerical analysis of the estimation of groundwater recharge from water table fluctuations in unconfined aquifers using 1-D and 2-D deterministic and stochastic numerical models. The material has been partly published in the following references:

→ Fernández Águila J., J. Samper, B. Pisani & A. Naves, 2016. Análisis paramétrico numérico de las oscilaciones piezométricas en acuíferos libres y su relevancia para la estimación de la recarga a partir de datos piezométricos. In: Congreso Hispano-Luso sobre las aguas subterráneas en el segundo ciclo de planificación hidrológica, AIH-GE, Madrid, November 2016, pp. 219-226. [in Spanish].

→ Fernández Águila J., J. Samper Calvete & B. Pisani Veiga, 2017. Análisis paramétrico/numérico de la estimación de la recarga a partir de las oscilaciones piezométricas en acuíferos libres mediante modelos unidimensionales y bidimensionales determinísticos y estocásticos. In: Jornadas de Zona no Saturada Vol XIII, Zaragoza, 8-10 November, 8 pp. [in Spanish].

→ Samper J., B. Pisani, J. Fernández & A. Naves. Trabajos adicionales de modelización del flujo y transporte de uranio del acuífero de la FUA: Informe de la Actividad nº 1: Actualización de los intervalos de tiempo y de las condiciones de contorno del modelo de flujo y transporte de uranio. Technical report for ENRESA. E.T.S.I. Caminos, Canales y Puertos. Universidade da Coruña. March 2016. [in Spanish].

ABSTRACT

The groundwater recharge produced by discrete precipitation events in unconfined aquifers is often estimated from data of the water table rises recorded in shallow wells (WTF method) when aquifer recharge is instantaneous and concentrated and the response of the hydraulic heads to the rainfall event is fast. These conditions usually occur in areas where the water table is shallow. However, this method for estimating aquifer recharge may present large uncertainties because recharge is not instantaneous and there may be other processes that can produce fluctuations of groundwater levels. In this work, these uncertainties are numerically quantified by means of a numerical/parametric analysis of the water table fluctuations caused by groundwater recharge and by the variation of the level of a river in an unconfined aquifer. This analysis has been performed with 1-D and 2-D numerical flow models in homogeneous and heterogeneous aquifers. 1-D models have been used to assess the sensitivity of hydraulic heads hydrographs to changes in the length of aquifer perpendicular to the river, aquifer parameters (hydraulic conductivity, storage coefficient and thickness) and the river stage. 2-D numerical models have been used to compare and verify the results obtained with the 1-D models and to compute the hydrographs in heterogeneous aquifers with a stochastic structure of hydraulic conductivity generated by geostatistical simulations. The logarithm of the hydraulic conductivity is assumed to be a Gaussian random field with a spherical semivariogram. Computed hydraulic heads are sensitive to the temporal distribution of the recharge (instantaneous or distributed) and variations of the river stage. The results of the parametric and numerical analysis show that the estimation of groundwater recharge from the water table rises may contain errors that are especially important in points located near a river when the water level rises simultaneously during the recharge period of the aquifer. Errors that can be committed in very heterogeneous media depend on the variance of the logarithm of the hydraulic conductivity, i.e., the degree of heterogeneity, and the spatial connectivity of most permeable areas in the vicinity of the river.

Key words: groundwater recharge, water table, numerical modelling, unconfined aquifer, spherical semivariogram.

A10.1. INTRODUCTION

Recharge is the entry of water into the saturated zone made available at the water-table surface (Freeze and Cherry, 1979). Recharge is commonly expressed as a volume (L^3) although sometimes the term "recharge" refers to "recharge rate" which expresses either a flux (L^3T^{-1}) into a specified portion of aquifer or a flux density (LT^{-1}) into an aquifer at a point (volume per unit surface area). Groundwater recharge is a fundamental component in the water balance of any watershed and in the groundwater flow and transport models. Quantification of rates of recharge is necessary, among many other applications, to evaluate the groundwater resources, to know the aquifer vulnerability to contamination and for

efficient groundwater management (Lerner et al., 1990). Recharge is usually difficult to estimate, especially when it involves unsaturated flow, because of the extreme variability of recharge rates and the fact that many relevant processes cannot be directly observed.

Various techniques are available to quantify recharge. Determining which of a wide variety of techniques is likely to provide reliable recharge estimates is often difficult. The selection of the method for estimating recharge depends on several factors such as available data, local geographic and topographic conditions, spatial and temporal scale required and the reliability of results obtained by different methods (Scanlon et al., 2002).The space/time scales of recharge estimates are important because different study goals require recharge estimates over different space and/or time scales. Whereas some studies focus on recharge estimates for water-resource assessment (Luckey et al., 1986; Kearns and Hendrickx, 1998), others concentrate on estimates for contaminant transport or aquifer vulnerability to contamination (Egboka et al., 1983; Flury et al., 1994; Scanlon and Goldsmith, 1997). The most used methods to estimate the groundwater recharge are the following: 1) Water Table Fluctuations (WTF) method which assumes that the rise in the groundwater level in unconfined aquifer is only due to recharge water arriving at the water table; 2) Water budget methods that estimate the recharge from the water budget equation; 3) Methods based on Darcy's law which use the Darcy's law to calculate the recharge; 4) Methods based on empirical relationships relating groundwater recharge and rainfall based on seasonal groundwater balance studies (Kumar and Seethapathi, 2002); 5) Groundwater models which can be used to predict the distribution of recharge in temporal and spatial scales based on the hydrogeological properties and 6) Tracer techniques which are applied by adding chemical or isotopic tracers as a pulse at the soil surface or at some depth within the soil profile to estimate recharge (Athavale and Rangarajan, 1988; Sharma, 1989). Because of uncertainties associated with each approach for estimating recharge, the use of many different approaches is recommended to constrain the recharge estimates. In many cases, different approaches complement each other and help refine the conceptual model of recharge processes.

The groundwater recharge produced by discrete precipitation events in unconfined aquifers is often estimated from data of the water table rises recorded in shallow wells (WTF method) when aquifer recharge is instantaneous and concentrated and the response of the hydraulic heads to the rain is fast. However, this method has considerable uncertainties. In this work, these uncertainties are quantified by means of a numerical/parametric analysis of the water table fluctuations caused by the groundwater recharge and by the variation of the level of a river in an unconfined aquifer. This analysis has been performed with 1-D and 2-D numerical flow models in homogeneous and heterogeneous aquifers with a stochastic hydraulic conductivity field generated by geostatistical simulations.

A10.2. WATER TABLE FLUCTUATION METHOD (WTF)

Techniques based on the rise of groundwater levels are among the most widely-applied methods for estimating recharge rates. This is likely due to the abundance of available groundwater-level data and the simplicity of estimating recharge rates from temporal fluctuations or spatial patterns of groundwater levels. The Water Table Fluctuation (WTF) method for estimating groundwater recharge was applied as early as the 1920s (Meinzer, 1923; Meinzer and Stearns, 1929) and since then it has been used in numerous studies.

The WTF method is only applicable to unconfined aquifers and it is based on the premise that rises in groundwater levels are due to an instantaneous pulse of recharge water arriving at the water table. The recharge rate R is calculated as:

$$R = S_y \frac{\partial h}{\partial t} \cong S_y \frac{\Delta h}{\Delta t} \qquad (10.1)$$

where S_y is the specific yield, h is water table height and t is time. Figure A10.1 shows the hydrograph in a monitory piezometer in Oia (Galice) which illustrates the water level rise in response to rainfall. The water level rise caused by the recharge (Δh) is equal to 0.45 m. Assuming a specific yield equal to 0.1, the estimated recharge by the WTF method in this period of recharge is equal to 45 L/m^2.

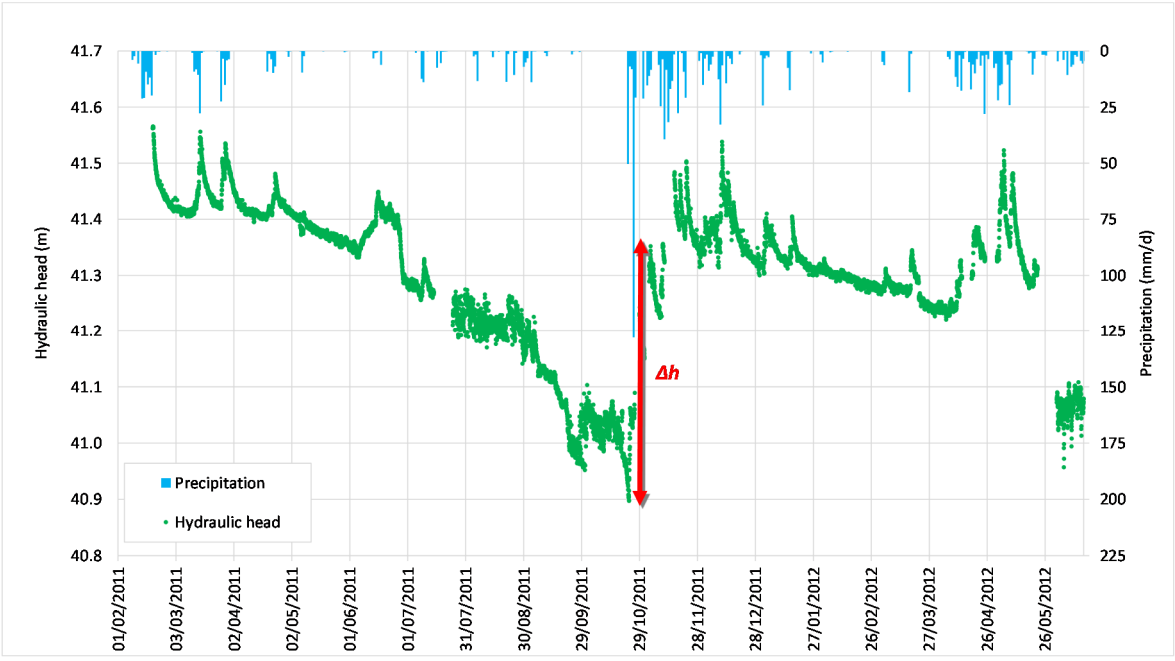

Figure A10.1. Hydrograph of the Oia monitoring piezometer (Galice) showing the water level rise in response to rainfall (Samper et al., 2017). Δh is equal to the difference between the low hydraulic head and the peak of the rise caused by recharge. Precipitation is represented in the secondary axis.

The WTF method assumes that water arriving at the water table goes immediately into storage. The WTF method is most appropriate over short periods of time (hours or a few days) and for shallow water tables that display sharp water-level rises. If water is transported away from the water table at a rate that is not significantly slower than the rate at which recharge water arrives at the water table, then the method is of little value.

The main advantage of the WTF method is its simplicity and ease of use. Preferential flow paths within the unsaturated zone does not restrict its application because this method does not take into account water travels through the unsaturated zone. However, the WTF method has several limitations (Healy and Cook, 2002): 1) The application of the WTF method for estimating recharge requires the proper identification of the process causing water-level rises because other phenomena such as evapotranspiration, changes in atmospheric pressure, the presence of entrapped air ahead of a wetting front, extraction or injection of water by pumping, temperature effects and tidal effects can induce fluctuations in the water table (Todd, 1989); 2) The choice of the wells used to estimate the recharge by the WTF method is very important because recharge rates vary substantially within a basin, owing to differences in elevation, geology, land surface slope, vegetation and other factors. Selected wells should be located such that the monitored water levels are representative of the catchment as a whole; 3) The WTF method should not be applied to deep aquifers because wetting fronts tend to disperse over long distances and the response of the hydraulic heads to rainfall is not fast enough; 4) The method cannot account for steady rate of recharge because if the rate of recharge from an area is constant and equal to rate of drainage away from the water table, water levels will not change and WTF method will predict no recharge and 5) Application of the WTF method requires determining a proper value for specific yield. However, it is a difficult endeavor because specific yield may vary in space and time and methods for estimating it present significant uncertainties (values of specific yield determined from laboratory or field tests are usually dependent on the duration of the test, with longer times corresponding to greater values).

The WTF method is a gross simplification of a very complex phenomenon, movement of water to and from the water table. However, this method has been applied over a wide variety of climatic conditions due to its simplicity. Recharge rates estimated by this technique range from 5 mm/year in the Tabalah Basin of Saudi Arabia (Abdulrazzak et al., 1989) to 247 mm/year in a small basin in a humid region of the eastern US (Rasmussen and Andreasen, 1959). Water-level fluctuations occur in response to spatially averaged recharge. The area represented by the recharge rates ranges from tens of square meters to several hundred or thousand square meters. Time periods represented by the recharge estimates range from event scale to the length of the hydrographic record.

A10.3. DESCRIPTION OF THE NUMERICAL MODELS

A numerical/parametric analysis of the water table fluctuations caused by groundwater recharge and by the change of the level of a river in an unconfined aquifer has been performed. To quantify the uncertainties of the WTF method, 1-D and 2-D numerical flow models in homogeneous and heterogeneous aquifers with a spatial structure of the hydraulic conductivity generated by geostatistical simulations have been performed. The flow models have been solved with the flow and reactive transport code CORE^{2D}V5 (Samper et al. 2003; 2009; 2011). The conceptual model has been inspired by the hydrogeological conditions of the Guadalquivir River alluvial aquifer in Andújar (Jaén, Spain) (Samper and Pisani, 2009). Figure A10.2 shows a conceptual scheme of the numerical flow models. The presence of a river has been simulated in one of the contours of the model to quantify the simultaneous effect on the hydraulic heads of the groundwater recharge and the variations of the river stage.

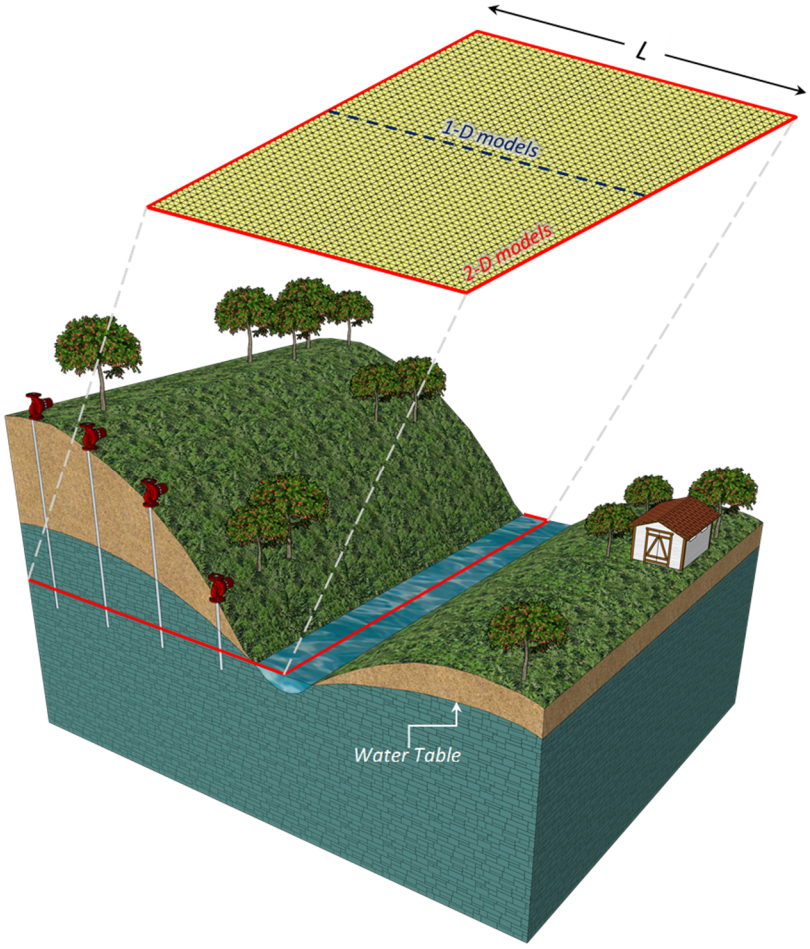

Figure A10.2. Conceptual scheme of the 1-D and 2-D numerical models in which the presence of a river has been assumed in one of contours of the models. "*L*" is the length of the unconfined aquifer.

A10.3.1. 1-D numerical models

1-D numerical flow models have been performed to study the fluctuations of the hydraulic heads caused by groundwater recharge and by the variation of the river stage in an unconfined aquifer. 1-D models have been used to study the sensitivity of the hydrographs to changes in: 1) The hydraulic parameters of the aquifer such as the hydraulic conductivity (K), the specific yield (S_y) and the aquifer thickness (e), 2) The length of the aquifer (L) perpendicular to the river, 3) The temporal distribution of the recharge, 4) Variations of the river stage and 5) The grid size of the finite element mesh (Δx). Moreover, a 1-D flow model has been performed with actual hydrogeological parameters of the Guadalquivir River alluvial aquifer in Andújar (Jaén, Spain). In this model, real time functions have been used to simulate the recharge and the time variability of the river stages.

The aquifer thickness is equal to 2 m and the base elevation is 190.27 m. The left boundary of the model is impermeable. The right boundary is a river simulated with a Dirichlet condition in which the prescribed head is equal to 192.27 m. Figure A10.3 shows the 1-D finite element mesh and the boundary conditions. There is a single zone of material with a hydraulic conductivity, K, equal to 50 m/d and a specific yield, S_y, equal to 0.1. Groundwater recharge, R, is equal to 100 mm/year. The flow model have been solved for a total period of one year with daily time increments. Initially all nodes of the finite element mesh have the same level as the river (H = 192.27 m). In the base run of the model, the length of the aquifer, L, is equal to 1000 m and the grid size, Δx, is equal to 50 m.

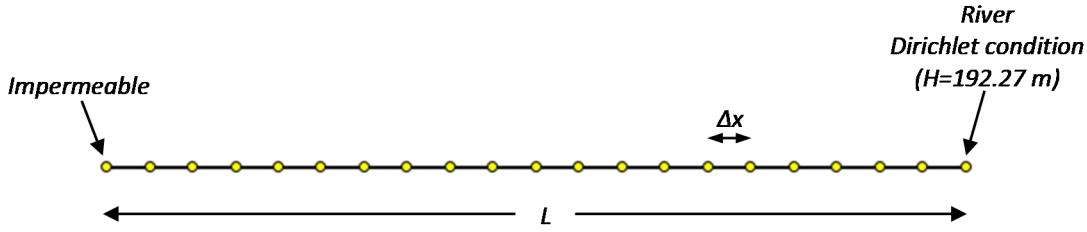

Figure A10.3. 1-D finite element mesh and boundary conditions for the 1-D numerical models.

A10.3.2. 2-D numerical models

2-D flow models have been performed to compare and verify the results obtained with the 1-D models and to study the variations of the hydraulic heads caused by groundwater recharge and the rises of the river stage in homogeneous and heterogeneous aquifers. The spatial structure of K has been generated by geostatistical simulations by assuming that the natural logarithm of the hydraulic conductivity is a Gaussian random field with a spherical semivariogram. The generation of K fields has been performed with GCOSIM3D (Gómez-Hernández and Journel, 1993).

The flow domain is rectangular with a surface of 2 x 3 km. It has been discretized with a uniform 2-D mesh of rectangular triangles finite elements with Δx = 50 m. The mesh has 2501 nodes and 4800 elements. Similar to the 1-D models, an unconfined aquifer has a thickness of 2 m and a base elevation of 190.27 m is considered. At the right boundary of the model (the longest side), a river is simulated with a Dirichlet condition in which the head is equal to 192.27 m. The rest of the boundaries of the model are impermeable. Figure A10.4 shows the 2-D finite element mesh and boundary conditions. The hydraulic parameters for homogeneous 2-D models are the same as those used in the 1-D models (K = 50 m/d, S_y = 0.1 and R = 100 mm/year). In the heterogeneous aquifers a spatial distribution of K has been generated by geostatistical simulations by maintaining the values of S_y and R. The total period of the simulations is a year with daily increments of time. The initial head, h_0, is constant and equal to 192.27 m.

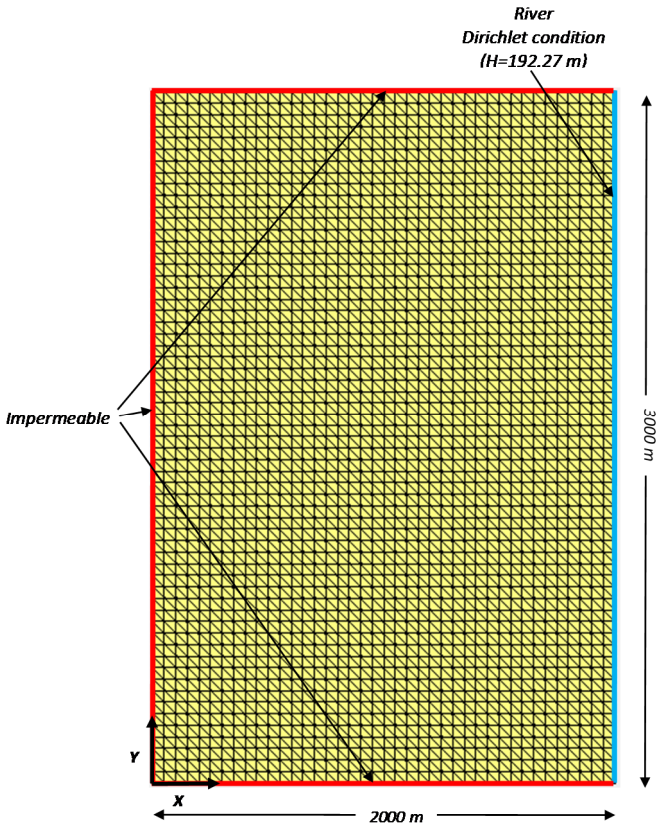

Figure A10.4. 2-D finite element mesh and boundary conditions for the 2-D numerical models.

A10.4. 1-D MODEL RESULTS

The errors made when the groundwater recharge is estimated with the WTF method are quantified analyzing the hydrographs. The variable evaluated in the parametric and numeric analysis are

the following: 1) Hydraulic parameters of the aquifer, 2) Aquifer length, 3) Temporal distribution of the recharge, 4) Variations of the river stage and 5) The grid size. In addition, a sensitivity run using the real hydrogeological parameters of the Guadalquivir River alluvial in Andújar (Jaén, Spain) has been performed with a 1-D model.

A10.4.1. Sensitivity aquifer parameters

Several sensitivity runs has been performed to analyze the sensitivity of the hydrographs at several locations to changes in the hydraulic parameters of the aquifer. The hydraulic conductivity was increased by a factor of 2 (K = 100 m/d), the specific yield was reduced by a factor of 2 (S_y = 0.05) and the aquifer thickness (e) was increased from 2 m (base run) to 10 m. A groundwater recharge, R, equal to 100 mm is assumed to occur during the first day.

Figure A10.5 shows the time evolution of the computed level rises, $s(t)$, at various distances from the river (100, 400 and 800 m) for the base run and two sensitivity runs varying the hydraulic conductivity and the aquifer thickness. The level rises, $s(t)$, is equal to the computed hydraulic head, $h(t)$, minus the initial hydraulic head, $h_0(t)$. Initially, the level rise is equal to 1 m in the base and sensitivities runs because the recharge is instantaneous. When the recharge ceases (t > 1 day) the level rise decreases to zero. The increase in the hydraulic conductivity does not affect the maximum level rise. The recovery of levels after the recharge period is faster when K increases. Increasing the aquifer thickness has a similar effect to the increasing of the hydraulic conductivity. The recovery of levels is slower in the sensitivity run in which the hydraulic conductivity was increased than in sensitivity run increasing the aquifer thickness due to hydraulic conductivity was increased by a factor of 2 whereas the aquifer thickness was increased from 2 m to 10 m (a factor of 5). After a year of simulation, the level rises have decreased to zero throughout the model domain in the sensitivity run with 10 m thickness.

Figure A10.6 shows the sensitivity of the time evolution of the computed level rises at various distances from the river (100, 400 and 800 m) to a reduction of the specific yield by a factor of 2. By reducing the specific yield, the maximum rises of the hydraulic heads in the sensitivity run are doubled. In addition, the recovery of the levels is faster when the specific yield is reduced. The hydraulic heads are very sensitive to variations in the specific yield. For the estimation of the groundwater recharge with the WFT method it is very important to know proper values for specific yield of the aquifer. However, specific yield may vary in space and time and methods for estimating it present significant uncertainties. It is an important disadvantage of the WFT method which can lead to significant errors when the groundwater recharge is estimated by this method.

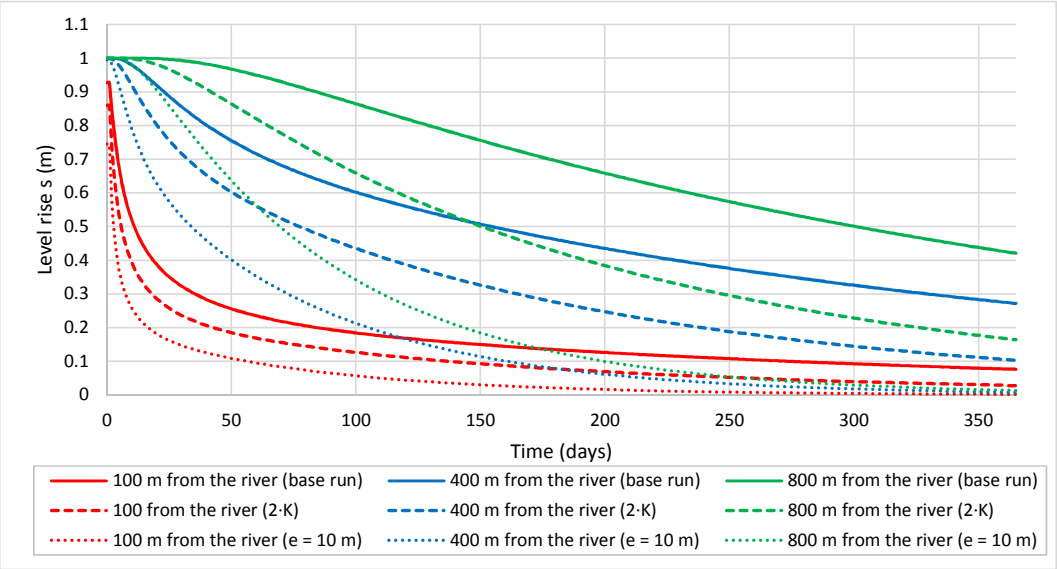

Figure A10.5. Sensitivity of the time evolution of the level rises at 100, 400 and 800 m from the river to changes in the hydraulic conductivity (dashed lines) and the aquifer thickness (dotted lines).

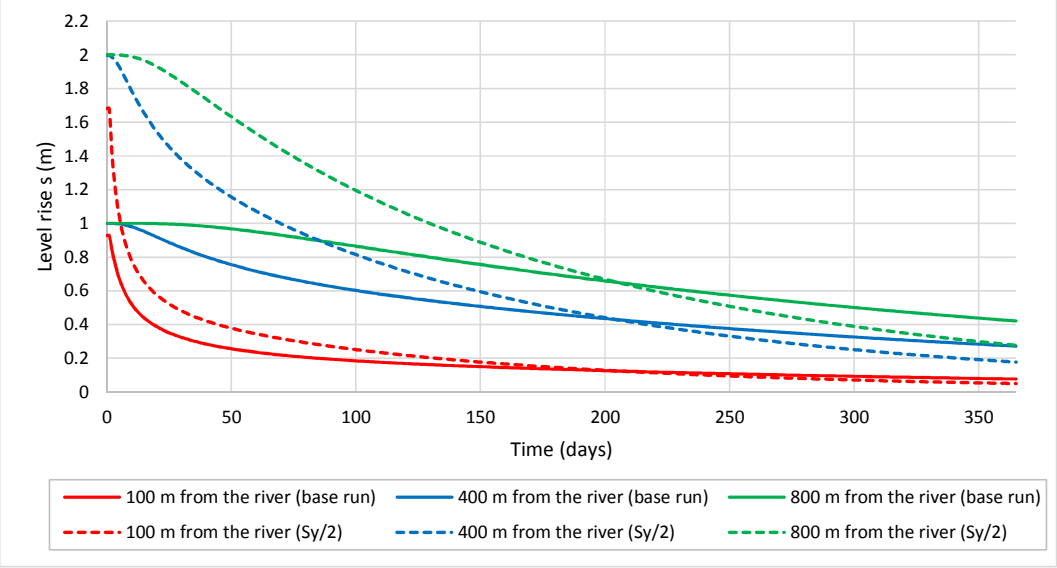

Figure A10.6. Sensitivity of the time evolution of the level rises at 100, 400 and 800 m from the river to changes in the specific yield (dashed lines).

A10.4.2. Aquifer length

The aquifer length in the base run is equal to 1000 m. Sensitivity were performed for lengths equal to 500 and 2000 m. The sensitivity runs were performed with the same grid space (50 m) and groundwater recharge (100 mm in a day) as those of the base run. Figure A10.7 shows the sensitivity of the time evolution of the level rises at 100, 200, 400 and 800 m from the river to changes in aquifer

length. The maximum level rises of the hydraulic heads do not depend on the aquifer length. However, the aquifer length affects the way in which the rises decrease after the recharge period. The recovery of the hydraulic heads is faster when the aquifer length is shorter. The differences between the sensitivity runs are more relevant at the points located farther away from the river.

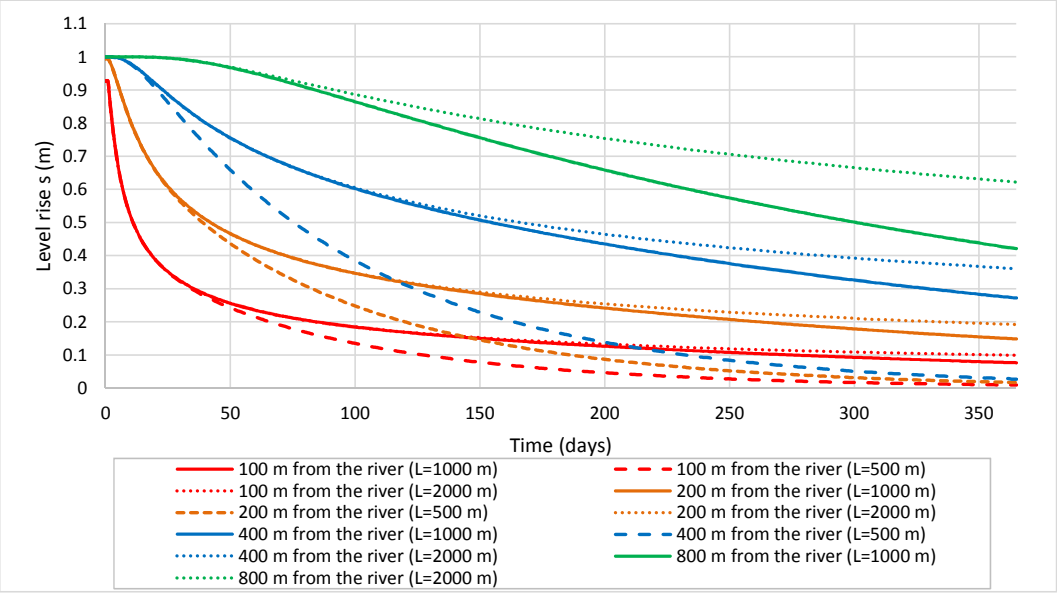

Figure A10.7. Sensitivity of the time evolution of the level rises at 100, 200, 400 and 800 m from the river to changes in the aquifer length.

A10.4.3. Time distribution of groundwater recharge

Groundwater recharge in the base run is equal to 100 mm and is assumed to be concentrated in the first day. Sensitivity runs were performed for the following cases: 1) Recharge distributed uniformly during at month and 2) Variably distributed recharge with 20% in the first 10 days, 60% in the following 10 days and the remaining 20% in the last 10 days. In all cases the total recharge is equal to 100 mm. Figure A10.8 shows the time functions used in the base run and in the sensitivity runs.

Figure A10.9 shows the sensitivity of the time evolution of the level rises at 100, 200, 400 and 800 m from the river to the time distribution of groundwater recharge. The maximum rises of the hydraulic heads computed in the sensitivity runs with variably distributed recharge are significantly smaller than those computed in the base run with the recharge concentrated in a day. Although the total recharge is the same in the three runs, the recharge estimates by WTF method in the runs with distributed recharge is smaller than the recharge estimated in the base run with instantaneous recharge. The maximum level rise at 100 m from the river when the recharge is variably distributed is approximately equal to a 0.5 m. Therefore, the recharge that would be estimated from a well hydrograph located

100 m from the river would be less than 50% of the actual recharge. At 200 m from the river, the estimation error of the WTF method is about 25%. At 400 m from the river, the error is about 5%. At 800 m from the river the error is negligible. Accordingly, it ca be concluded that near the river the maximum rises for variably distributed recharge are much smaller than those corresponding to instantaneous recharge.

The recession curves of the hydrographs once the recharge has ceased are similar in all the cases. In addition, the hydraulic heads computed in the sensitivity runs with non-instantaneous recharge are also very similar.

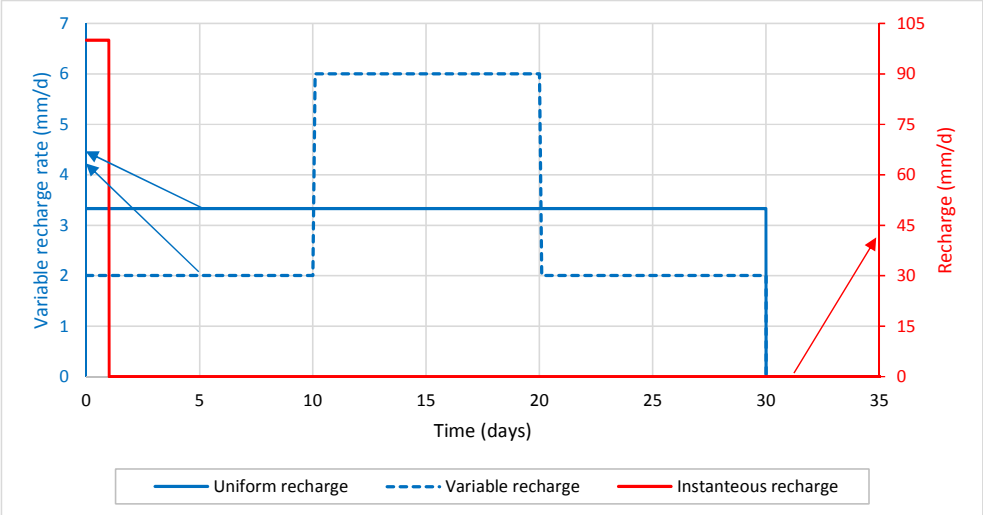

Figure A10.8. Time functions used to simulate variably distributed recharge. The recharge concentrated in a day is represented in the right axis.

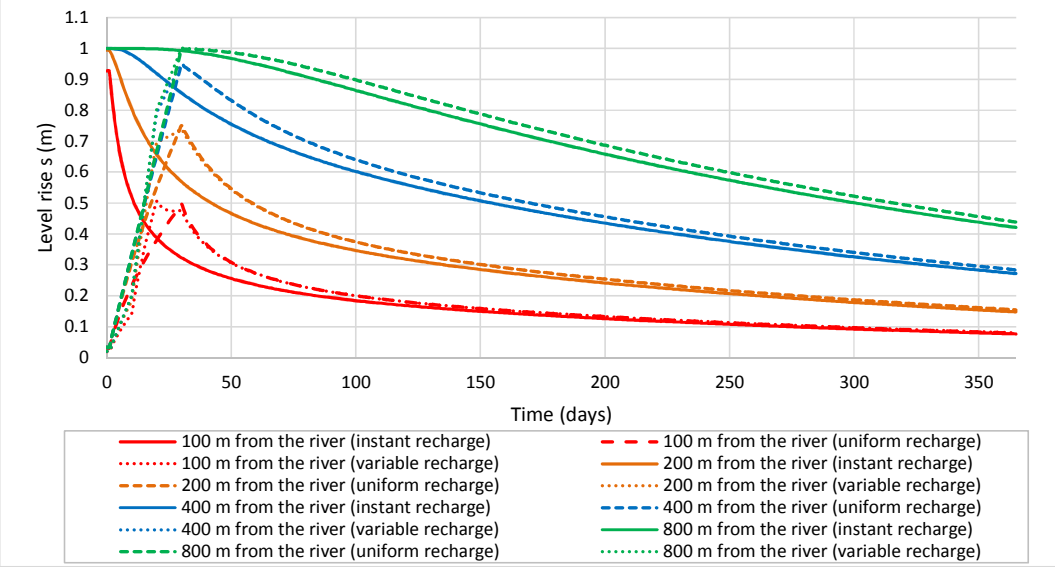

Figure A10.9. Sensitivity of the time evolution of the level rises at 100, 200, 400 and 800 m from the river to the time distribution of the recharge.

A10.4.4. Changes in the river stage

A sudden rise of the river stage of 2 m which remains during the first week of the simulation has been considered. The stages rises from 192.27 m to 194.27 m. Figure A10.10 shows the sensitivity of the time evolution of the computed level rises at 100, 200, 400 and 800 m from the river for the base run with constant stage and the sensitivity run with a river rise of 2 m during the first week. The groundwater recharge (R = 100 mm) has been considered instantaneously during the first time period in the two runs. The hydraulic heads in the points located near the river (100 and 200 m) are more influenced by variations of the level of the river. The maximum level rises in a point 100 m from the river is approximately equal to 1.5 m in the sensitivity run with a rise of the river stage. Therefore, the recharge that would be estimated from the hydrograph of a well located 100 m from the river would be greater than 50% of the actual recharge because the hydraulic heads near the river increase due to combined effect of groundwater recharge and the rise of the river stage. At 200 m from the river, the error is about 20% of the recharge estimated with the WTF method. The error in the estimation of the recharge at 400 m from the river is about 5% while at 800 m from the river the error is negligible. Therefore, the estimates of groundwater recharge with the WTF method can be large near river with large rises in water level.

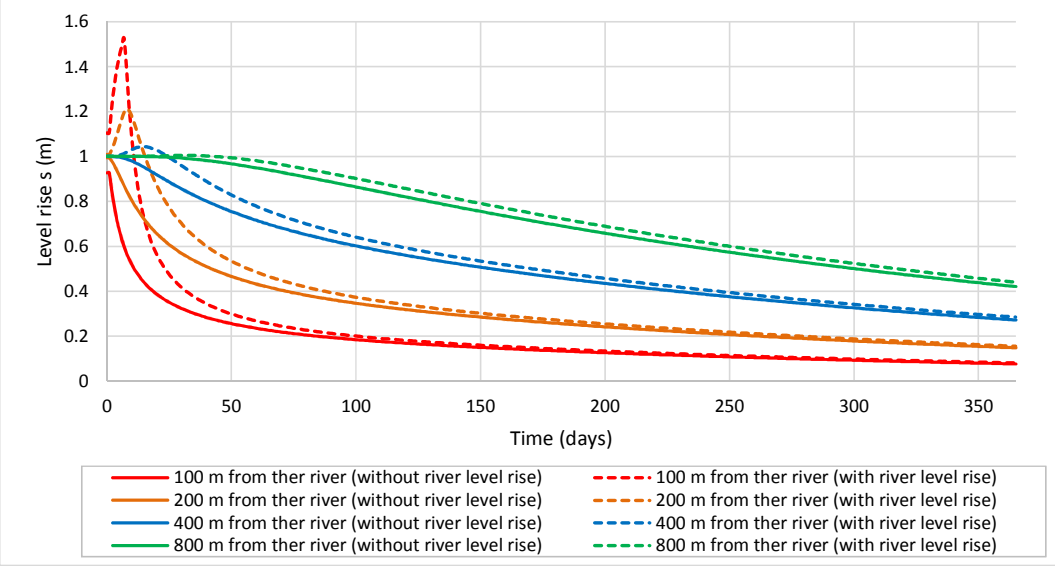

Figure A10.10. Sensitivity of the time evolution of the level rises at 100, 200, 400 and 800 m from the river in the base run with constant river stage (continuous lines) and the run with a river stage rise of 2 m during the first week of the simulation (dashed lines).

A10.4.5. Finite element grid size

All the previous simulation runs were performed with a finite element grid size (Δx) equal to 50 m. To analyze the numerical discretization errors, the finite element mesh was refined by using a grid size equal to 10 m. A rise of the river stage equal to 2 m during the first week and a variably distributed recharge during the first month has been considered in two runs using different grid size. The hydraulic heads computed in the two runs are very similar. The maximum differences occur near the river and are smaller than 0.041 m. Discretization errors were also computed with other sensitivity runs and the errors are always smaller than 0.041 m. It can be concluded that the discretization errors are always very small.

A10.4.6. Model with parameters of the Guadalquivir River alluvial aquifer

A 1-D flow model has been performed by using actual hydrogeological parameters of the Guadalquivir River alluvial aquifer in Andújar (Jaén, Spain) (Samper and Pisani, 2009). The initial aquifer thickness is equal to 2 m. The elevation of the bottom of this aquifer is 188.56 m. The left boundary of the model is impermeable. The Guadalquivir River at the right boundary is simulated with a Cauchy condition. This boundary condition states that the flux, Q, is equal to:

$$Q = \alpha(H - h) \tag{10.2}$$

where H is the specified head, h is the computed hydraulic head and α is a leakage coefficient (m^2/d). The leakage coefficient used in the model is equal to 1.36 m^2/d.

Figure A10.11 shows the 1-D finite element mesh, the material zones and the boundary conditions. The length of the model domain, L, is equal to 1000 m and the grid size, Δx, is equal to 10 m. Five material zones have been defined based on the geological data and measured hydrodynamic parameters. The hydraulic conductivity, specific yield and the location of material zones are listed in Table A10.1. The duration of the simulation is equal to a year and the time domain was divided into daily time periods. The initial head, h_0, is uniform and equal to 190.56 m. Figure A10.12 shows the daily values of groundwater recharge and river stage from 01/10/2009 to 30/09/2010, used for the numerical model. These values were taken from Samper and Pisani (2009).

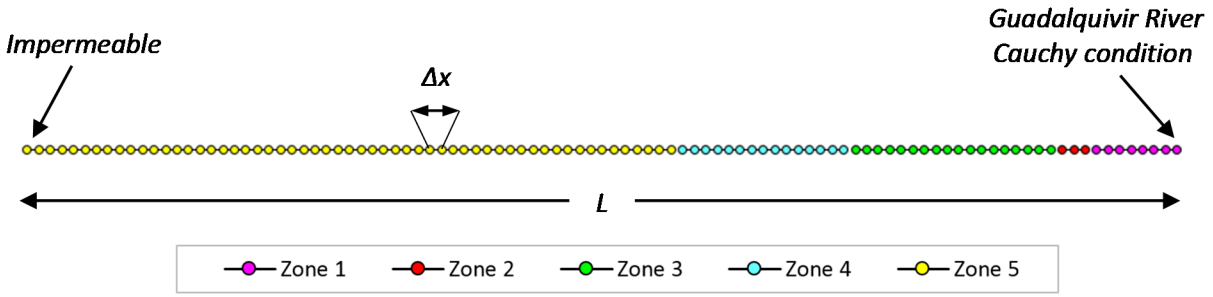

Figure A10.11. 1-D finite element mesh, material zones and boundary conditions for the 1-D numerical model using real hydrological parameters of the Guadalquivir River alluvial in Andújar (Jaén, Spain).

Table A10.1. Hydraulic conductivity, specific yield and location of material zones (distances from the river) in the numerical model of the Guadalquivir River alluvial aquifer

Material zone	Distance from the river (m)	Hydraulic conductivity (m/d)	Specific yield
1	0-74	1	0.11
2	74-104	0.04	0.11
3	104-279	359	0.11
4	279-329	66	0.11
5	329-1000	50	0.11

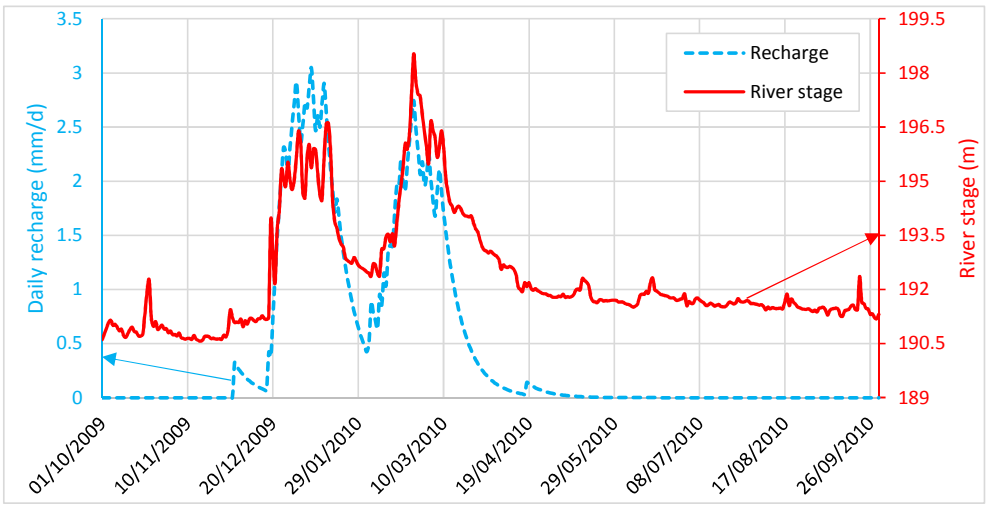

Figure A10.12. Daily values of the groundwater recharge (blue line) and the Guadalquivir River stage (red line) from 01/10/2009 to 30/09/2010.

Figure A10.13 shows the time evolution of the computed hydraulic heads at 10, 50, 100 and 400 m from the river for a run with recharge and another without recharge. Both runs consider the change in the level of the Guadalquivir River. The computed heads near the Guadalquivir River are clearly

influenced by the changes in the river stage. The effect of groundwater recharge on hydraulic heads near the river is not significant. The hydraulic heads away from the river, however, are more influenced by recharge in wells away from the river. The groundwater recharge estimated with the WTF method near the river would contain large errors. The hydraulic conductivity plays also a very important role on the effect of the changes in the river stage in the hydraulic heads. The changes in hydraulic heads for $x > 74$ m are mostly caused by the variability of the recharge because the hydraulic conductivity of the zone 2 of the numerical model is very low.

Figure A10.14 shows the time evolution of the computed hydraulic heads at 10, 50, 100 and 400 m from the river for a run with variable river stage and another with constant river stage. Both runs consider groundwater recharge. The level of the Guadalquivir River controls the time variability of the hydraulic heads near the river. If the recharge is not instantaneous and the response of the hydraulic heads to the recharge is not fast, the time variability of the hydraulic heads can be affected by the changes in the level of the river. Therefore, the uncertainty of the groundwater recharge estimated with the WTF method in wells near the river can be large.

Figure A10.15 shows the sensitivity of the time evolution of the computed hydraulic heads at the node of the grid where the Cauchy condition is defined for different values of the leakage coefficient. The computed hydraulic heads are sensitive to changes in the leakage coefficient used in the Cauchy condition in the river. The computed heads, *h(t)*, coincides with the prescribed head, *H(t)*, when $\alpha > 1.3$ m^2/d. When α decreases, the difference *h(t)- H(t)* increases.

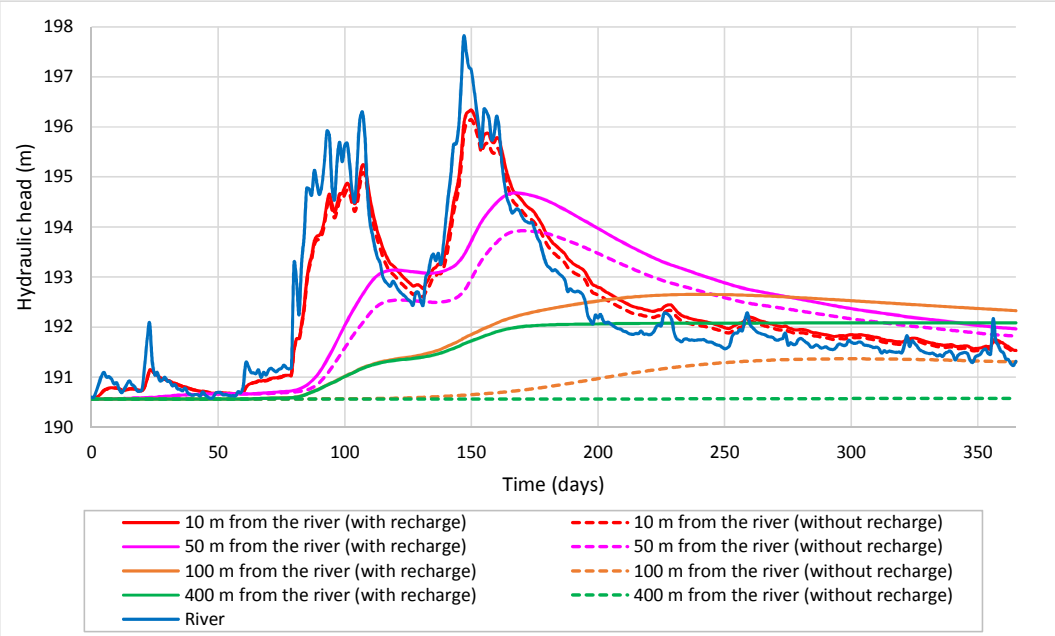

Figure A10.13. Time evolution of the computed hydraulic heads at points located at several distances from the river for a run with recharge (continuous lines) and another without recharge (dashes lines). Both runs account for the changes in the Guadalquivir River level.

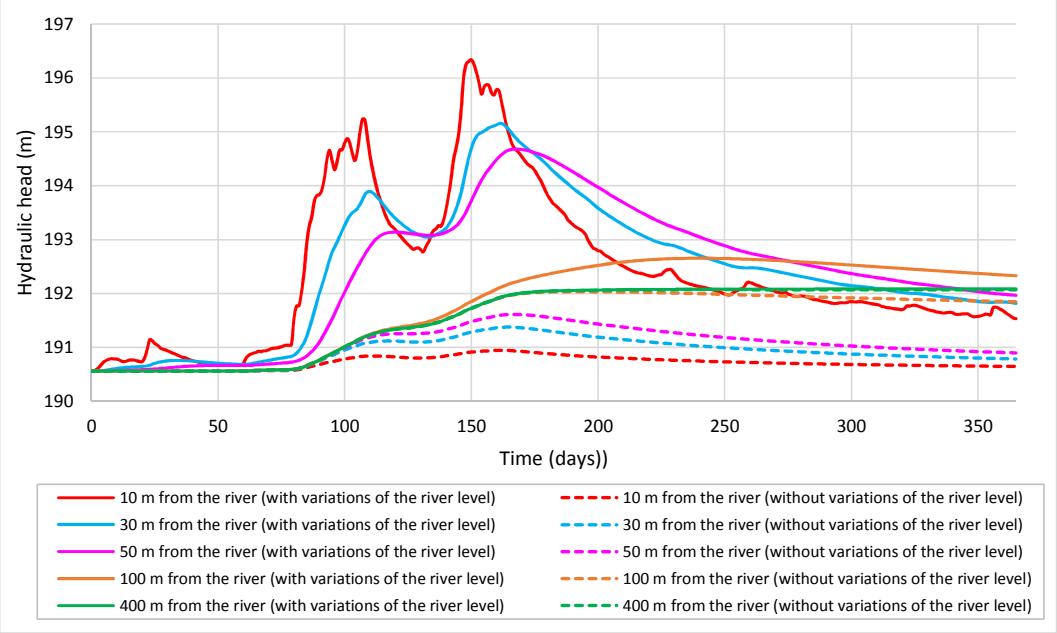

Figure A10.14. Time evolution of the computed hydraulic heads at points located at several distances from the river for a run with variable river level (continuous lines) and another without variations in the river level (dashes lines). In both runs groundwater recharge is considered.

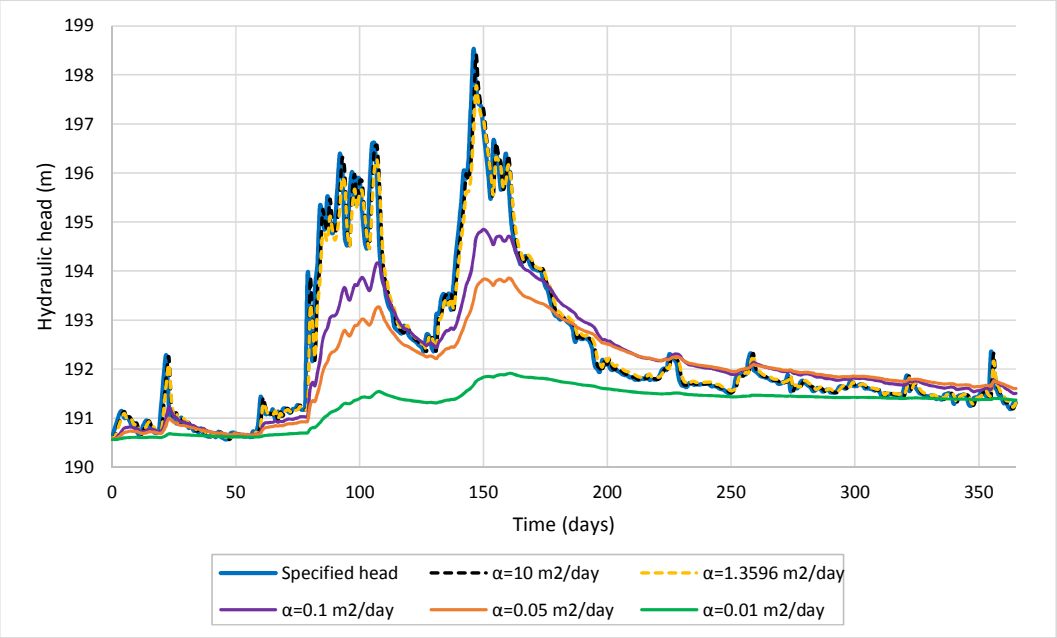

Figure A10.15. Time evolution of the computed hydraulic heads at the node of the grid where the Cauchy condition is imposed for several values of the leakage coefficient.

A10.5. 2-D MODEL RESULTS

A10.5.1. Homogeneous aquifer

2-D flow models have been performed by considering a homogeneous unconfined aquifer to compare and verify the results obtained in the parametric and numeric analysis carried out with 1-D models. The hydraulic parameters of the 2-D model are similar to those used in the 1-D model (K = 50 m/d, S_y = 0.1 and R = 100 mm). Hydraulic heads computed with the 2-D models have been analysed and compared with the results obtained with the 1-D models. The hydrographs calculated with the 2-D models are always identical to those computed with the 1-D models. Therefore, the conclusion of the parametric and numerical analysis performed with 1-D models apply also to 2-D homogeneous aquifer.

Figure A10.16a shows the spatial distribution of the errors made in estimating the recharge with the WTF method when the recharge is not instantaneous. In this case, groundwater recharge is distributed uniformly during the first month of simulation. In an unconfined aquifer with S_y = 0.1 and an instantaneous recharge R = 100 mm, the rise of the water table should be equal to 1 m. In this case, the estimation of recharge with the WTF method is accurate. The errors in estimating the recharge from rises of the hydraulic heads in wells located near the river are especially significant. Groundwater recharge may be underestimated by the WTF method in wells located even 600 m from the river. Similar to the 1-D model, the error made in the estimation of recharge in a well located 100 m from the river is around 50%. At 200 m from the river, the error is equal to 25%. At 400 m from the river, is about 5% and at 800 m from the river the error is negligible.

Figure A10.16b shows the spatial distribution of the errors made in the estimation of recharge with the WTF method when there is a rise of the river stage simultaneously during the recharge period of the aquifer. A rise of the river stage of 2 m during the first week of simulation has been considered. In this case, groundwater recharge in wells located at a distance less than 425 m from the river is overestimated. Similar to the 1-D model, the recharge that would be estimated from a hydrograph of a well located 100 m from the river would be greater than 50% of the actual recharge. At 200 m from the river, the error made is about 20%. At 400 m from the river, the error made is about 5%.

The errors made when the groundwater recharge is estimated with the WTF method in homogeneous aquifers when the recharge is not instantaneous or when there is a rise of the river stage simultaneously during the recharge period are similar near the river. However, the errors when the recharge is not instantaneous are greater than the errors made when there is a rise of the level far from the river (Figure A10.17)

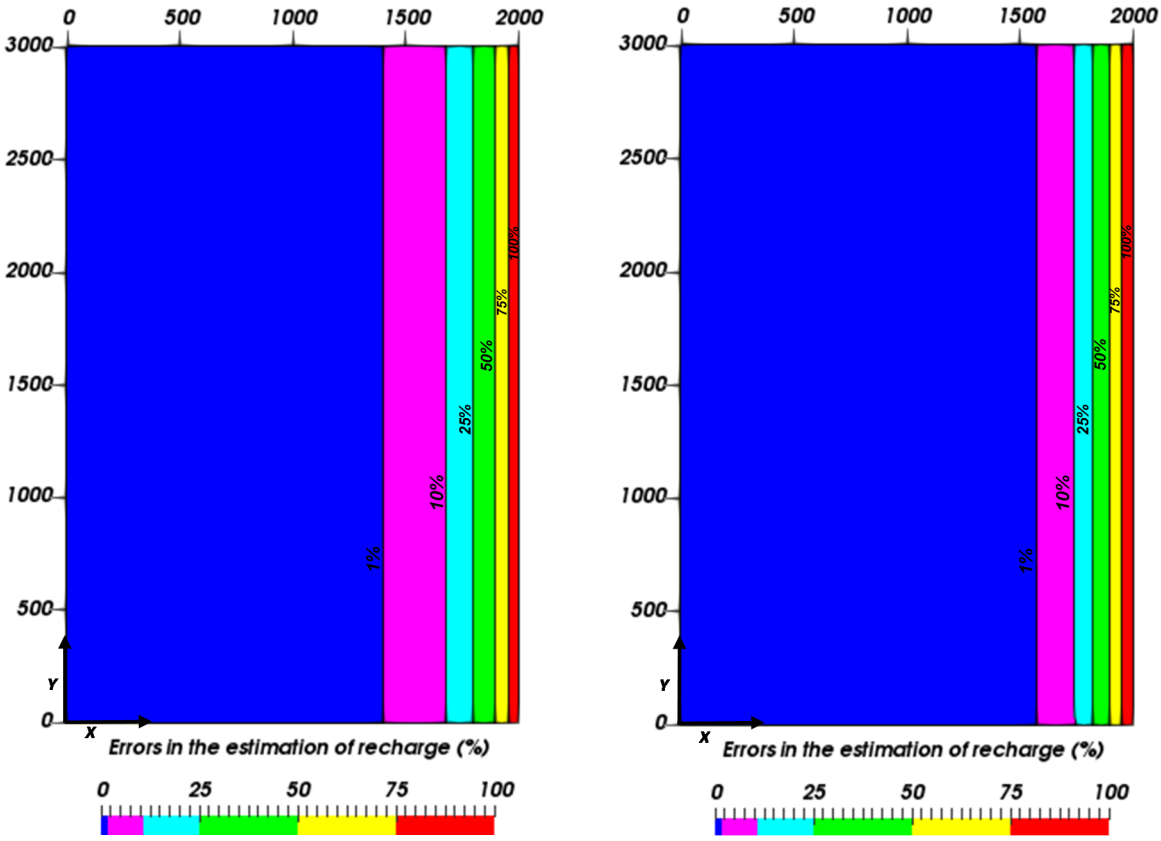

Figure A10.16. Spatial distribution of the errors made in the estimation of recharge with the WTF method when the recharge is not instantaneous (a) and when there is a rise of the river stage simultaneously during the recharge period of the aquifer (b).

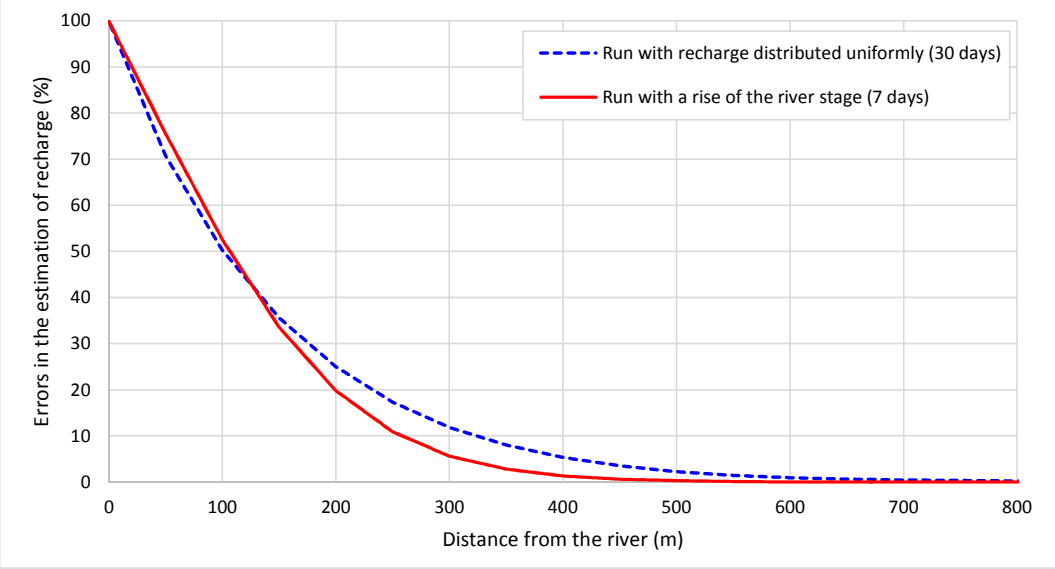

Figure A10.17. Errors made along a section perpendicular to the river (Y = 1500 m) when the groundwater recharge is estimated by WTF method when the recharge is distributed uniformly during the first month of simulation and when there is a rise of the river stage simultaneously during the recharge period of the aquifer (2 m during the first week of the simulation).

A10.5.2. Heterogeneous aquifer

2-D flow models have been performed for stochastically heterogeneous unconfined aquifers with a spatial structure of the hydraulic conductivity generated by geostatistical simulation. The spatial structure of *K* has been generated by assuming that *Ln K* is a Gaussian random field with a spherical semivariogram. The generation of *K* fields has been performed with GCOSIM3D (Gómez-Hernández and Journel, 1993). These stochastic simulations are useful to understand how the degree of spatial heterogeneity and connectivity of the most permeable areas near the river influence the estimation of the groundwater recharge by the WTF method. Figure A10.18 shows the spatial distribution of the values of blocks of *Ln K* of the 2-D model generated by assuming a Gaussian random field with a spherical semivariogram and with a variance, σ^2, equal to 5. Simulations of *Ln K* were generated on 60 by 40 quadrilateral elements. Afterwards, the simulated values of hydraulic conductivities in each block were assigned to the two triangular finite elements and were taken as input parameters for the numerical flow model.

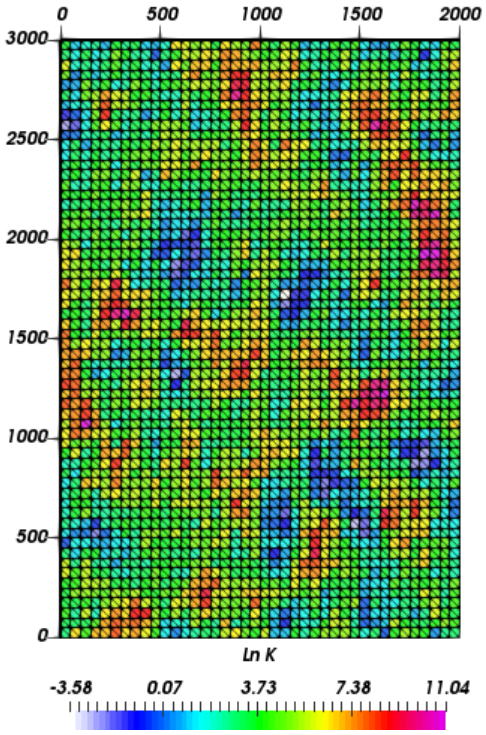

Figure A10.18. Spatial distribution of *Ln K* in the blocks of the 2-D model generated by assuming a Gaussian random field with a spherical semivariogram with a range of 200 m in horizontal direction and 300 m in vertical direction and a variance, σ^2, equal to 5.

Similar to 1-D and 2-D models of homogeneous aquifers, several runs have been performed for 2-D models of heterogeneous aquifers by varying the time distribution of the recharge and by considering the rises of the river stage. Model results and the changes in the hydraulic heads caused by groundwater recharge and the variations of the river stage have been calculated in several sections parallel to the river. The recharge is estimated by the WTF method from the water table rises and the

specific yield (S_y = 0.1). Figure A10.19 shows the errors made along several sections parallel to the river at 100, 400 and 800 m from the river when the groundwater recharge is estimated by WTF method when the recharge is distributed uniformly during the first month of simulation. The errors are especially important near the river and decrease with the distance to the river. If the groundwater recharge is estimated from data of the water table rises recorded in wells located 100 m from the river, the recharge would be underestimated by more than 80% in some areas. At 400 m from the river, the estimated recharge could be less than 60% of the real recharge. However, the errors made in the estimation of recharge are smaller than 5% at 800 m from the river. Figure A10.20 shows the errors made along sections parallel to the river at 100, 400 and 800 m from the river when the groundwater recharge is estimated with the WTF method and when there is a rise of the river stage simultaneously during the recharge period of the aquifer. In this case, the groundwater recharge estimated from the rise of water table would overestimate the actual recharge. The errors far from the river are smaller because the hydraulic heads are less affected by the changes in the river stage. In fact, at 800 m from the river the errors made in the estimation of the recharge are negligible.

The errors made in the estimation of the recharge depend on the extent of spatial heterogeneity of the aquifer and are generally large in the most permeable areas. Figure A10.19 and Figure A10.20 show the *Ln K* along a section 100 m from the river. One can see that the errors made in the estimation of the recharge correlate well with the hydraulic conductivities. The errors are large in the most permeable areas and are smallest in the least permeable zones.

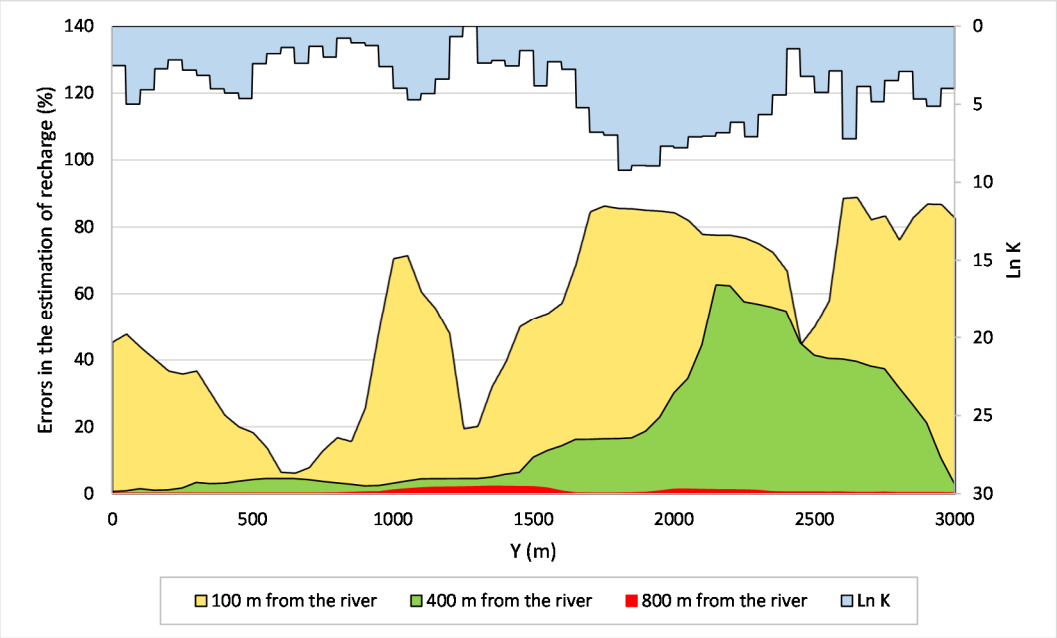

Figure A10.19. Errors made along sections parallel to the river at 100, 400 and 800 m from the river when the groundwater recharge is estimated with WTF method when the recharge is distributed uniformly during the first month of simulation. The values of *Ln K* along a section 100 m from the river is represented in the secondary axis.

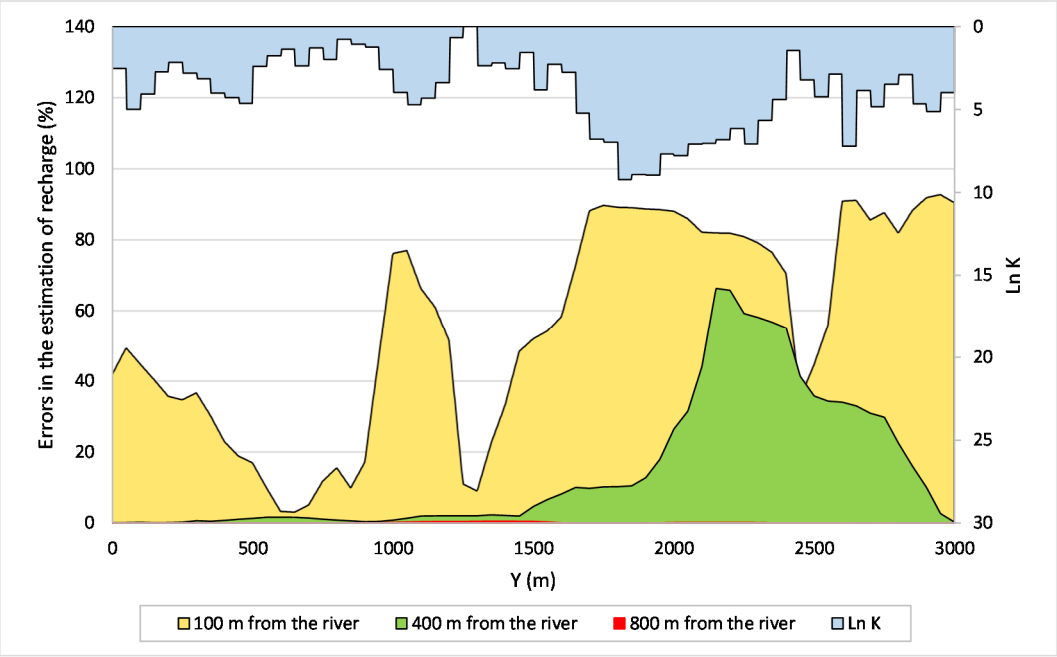

Figure A10.20. Errors made along sections parallel to the river at 100, 400 and 800 m from the river when the groundwater recharge is estimated with WTF method and when there is a rise of the river stage simultaneously during the recharge period of the aquifer (2 m during the first week of the simulation). The values of *Ln K* along a section 100 m from the river is represented in the secondary axis.

Simulations have been performed for Gaussian random fields of *Ln K* with increasing variance, σ^2, equal to 0.1, 1 and 5. The same seed was used to initialize the sequence of random numbers in these three simulations. The mean values of *Ln K* are equal to 3.92, 3.95 and 4.00 for the simulation with σ^2 equal to 0.1, 1 and 5, respectively. The spatial distribution of *Ln K* in the domain of the 2-D model is not modified (similar to Figure A10.18) and only the amount of heterogeneity of the aquifer changes in the three simulations.

Figure A10.21 and Figure A10.22 show the time evolution of the computed level rises at 50, 250 and 500 m from the river at the center of the 2-D model (Y = 1500 m) when a variably distributed recharge occurs during the first month of simulation and when there is a river stage rise of 2 m during the first week of the simulation, respectively. Level rises were computed for variances equal to 0.1, 1 and 5. When the groundwater recharge is not instantaneous, the maximum rises of the hydraulic heads decrease when the variance of *Ln K* increases. When rises of the river stage occur simultaneously during the recharge period, the maximum rises of the hydraulic heads are greater when the variance of *Ln K* is greater. In both cases, if groundwater recharge is estimated from the rise of the water table (WTF method) recorded in wells near the river, the errors increase with increasing variance of *Ln K*. The effect of spatial heterogeneity on the hydraulic heads decreases far from the river. At 500 m from the river, the time evolution of the hydraulic heads do not depend of σ^2 and the error made when the recharge is

estimated by WTF method would not depend on the degree of heterogeneity of the aquifer. In addition to the variance of *Ln K*, the changes in the hydraulic heads depend on the spatial connectivity of the most permeable zones near the river.

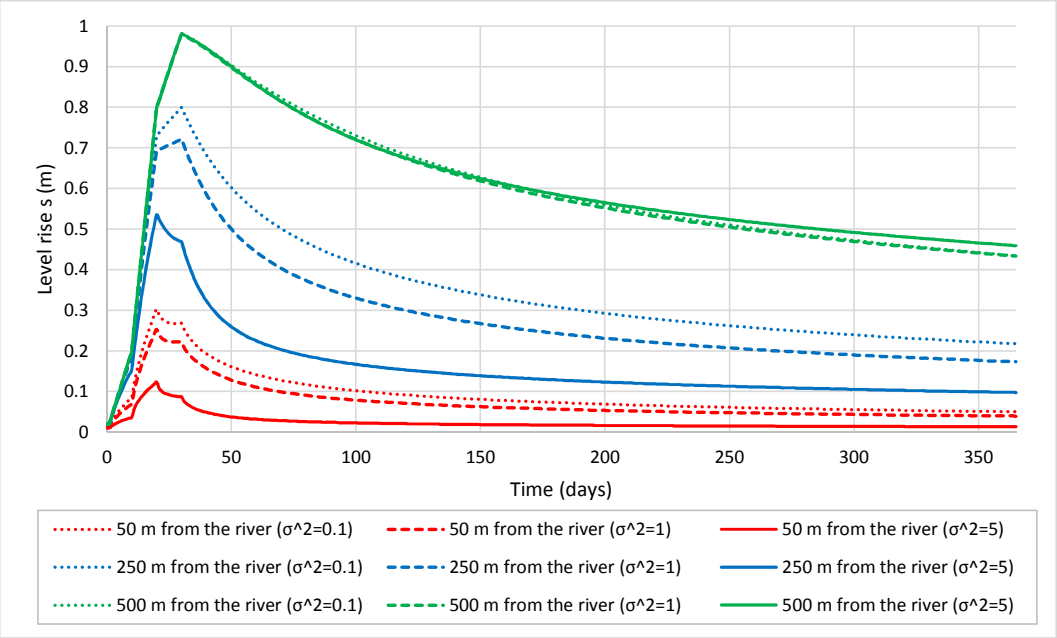

Figure A10.21. Time evolution of the level rises at 50, 250 and 500 m from the river at the center of the 2-D model (Y = 1500 m) with variable recharge during the first month of simulation for variances of *Ln K* equal to 0.1 (dotted lines), 1 (dashed lines) and 5 (continuous lines).

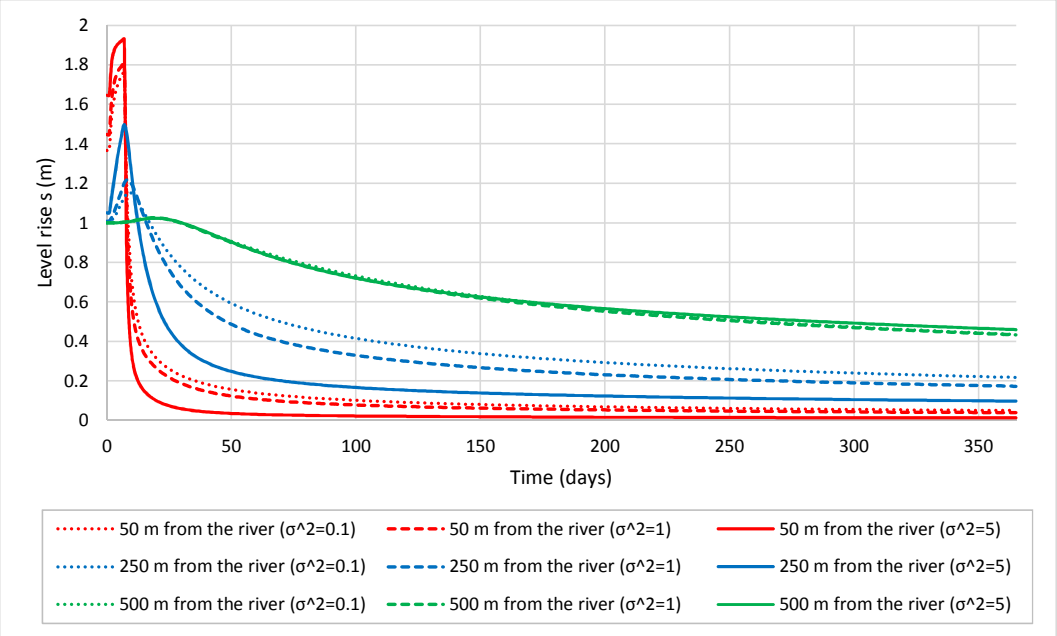

Figure A10.22. Time evolution of the level rises at 50, 250 and 500 m from the river at the center of the 2-D model (Y = 1500 m) when there is a river stage rise of 2 m during the first week of the simulation and considering variances of *Ln K* equal to 0.1 (dotted lines), 1 (dashed lines) and 5 (continuous lines).

Several simulations were performed by assuming anisotropy in the hydraulic conductivity. Four numerical flow models have been performed with different spatial distributions of *K* assuming that the range of the semivariogram along the main direction of anisotropy is equal to 1000 m. The range in the direction perpendicular to the principal direction of anisotropy is equal to 150 m. Figure A10.23 shows the spatial distributions of *Ln K* in the four models generated by geostatistical methods considering anisotropy. The anisotropy axes form angles of -45° (Figure A10.23a), +45º (Figure A10.23b), 0º (Figure A10.23c) and 90º (Figure A10.23d) with respect to the *X* coordinate axes.

Several runs have been performed with each numerical model varying the temporal distribution of the recharge and considering possible rises of the river stage simultaneously during the recharge period of the aquifer. Figure A10.24 shows the spatial distribution of the errors made in the estimation of recharge with the WTF method when the recharge is distributed uniformly during the first month of simulation (Figure A10.24a and Figure A10.24c) and when there is a rise of the river stage of 2 m during the first week of simulation (Figure A10.24b and Figure A10.24d). The anisotropy axes form angles of -45° (Figure A10.24a and Figure A10.24b) and +45º (Figure A10.24c and Figure A10.24d) with respect to the *X* coordinate axes. The errors made when the recharge is estimated by the WTF method depend on the main direction of anisotropy and the spatial connectivity of the most permeable zones near the river. The errors made are propagated preferentially along the anisotropy by following the most permeable zones from the river. In aquifers with anisotropy the errors made in the estimation of the recharge propagate to areas further away from the river than in isotropic aquifers. In the models simulating isotropic aquifers, the errors are very small to 800 m of the river (less than 5%). However, in aquifers with anisotropy, the errors may be greater than 25% to 800 m of the river. In addition, errors may be committed if the recharge is estimated from water table rises recorded in wells located at a distance of 1800 m from the river.

Figure A10.25 shows the spatial distribution of the errors made in the estimation of recharge with the WTF method when the recharge is distributed uniformly during the first month of simulation (Figure A10.25a and Figure A10.25c) and when there is a rise of the river stage of 2 m during the first week of simulation (Figure A10.25b and Figure A10.25d). The anisotropy axes form an angle of 0° (Figure A10.25a and Figure A10.25b) and 90º (Figure A10.25c and Figure A10.25d) with respect to the *X* coordinate axes. In numerical models where the main direction of anisotropy is perpendicular to the river, the errors made in the estimation of the recharge are much greater than the errors made in the models in which the main direction of anisotropy is parallel to the river. In addition, in the runs simulating a rise of the river stage simultaneously to the recharge period, the distance from the river in which errors would be made is less than in the runs simulating non-instantaneous recharge. This is because hydraulic heads in wells away from the river are not affected by variations of the river stage.

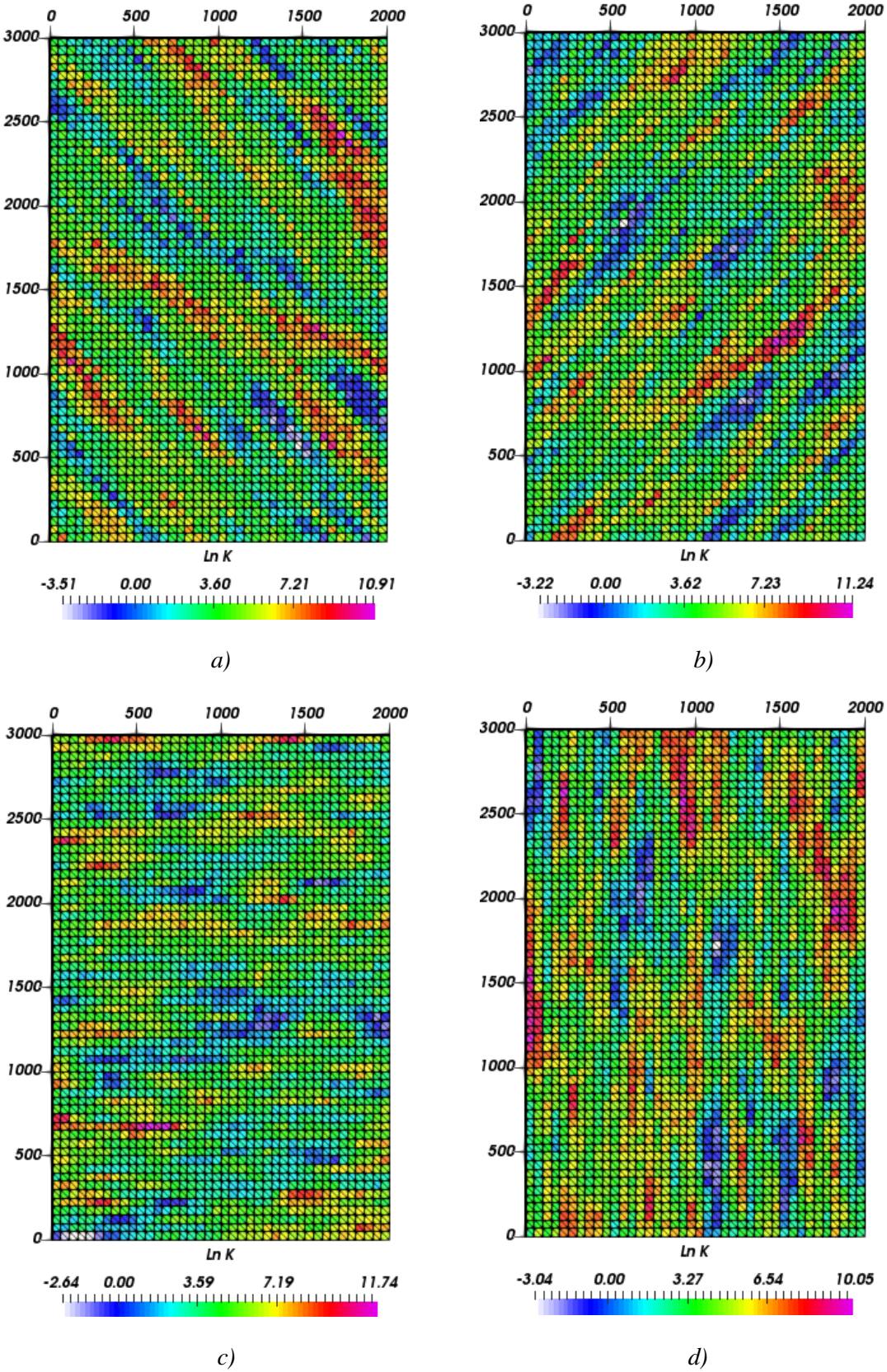

Figure A10.23. Spatial distributions of *Ln K* considering anisotropy. The anisotropy axes form an angle of -45° (a), +45º (b), 0º (c) and 90º (d) with respect to the *X* axis. The units of the model dimensions are in meters.

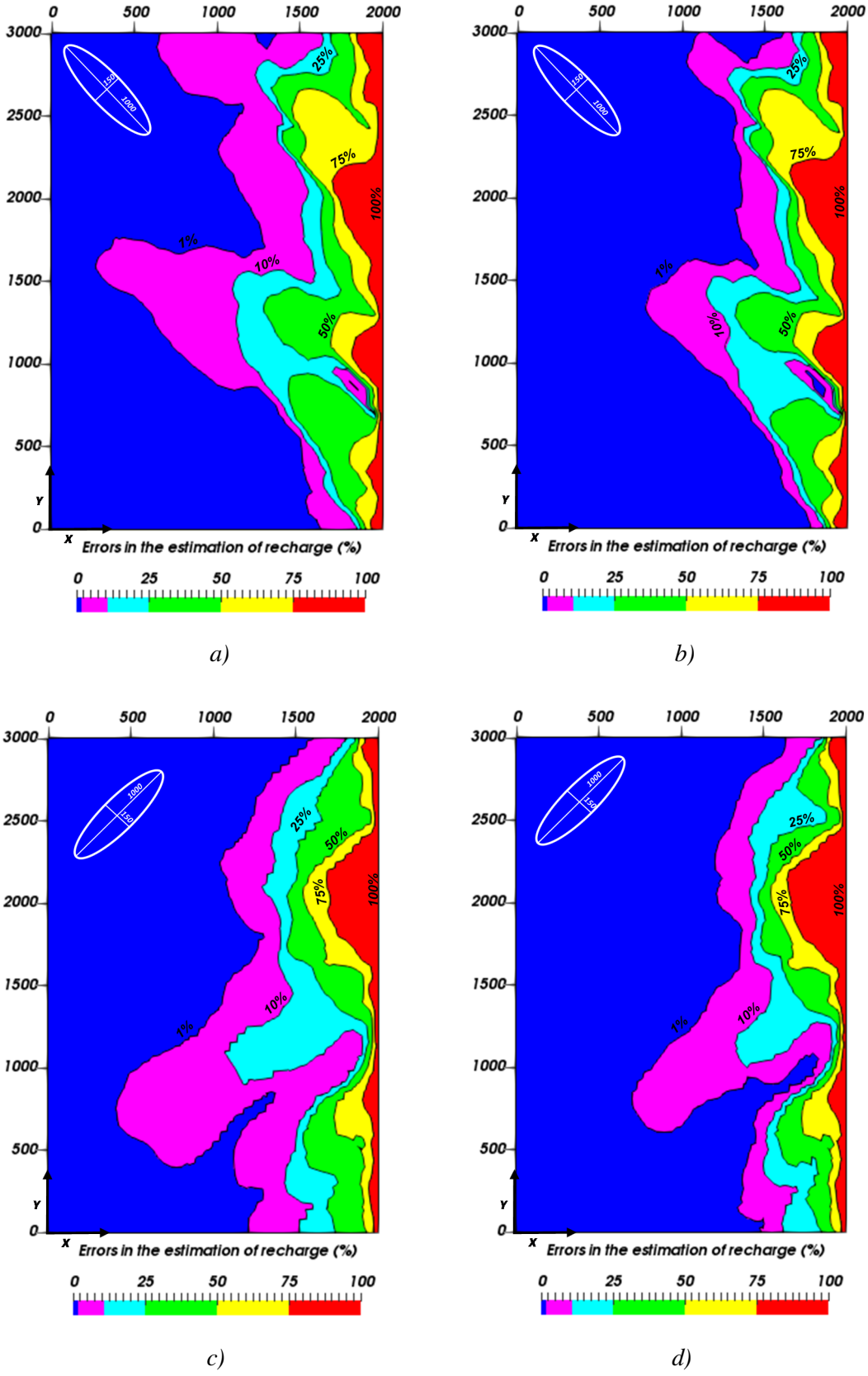

Figure A10.24. Spatial distribution of the errors made in the estimation of recharge with the WTF method when the recharge is not instantaneous (a, c) and when there is a rise of the river stage simultaneously during the recharge period of the aquifer (b, d). The anisotropy axes form an angle of -45° (a, b) and +45º (c, d) with respect to the *Y* coordinate axis.

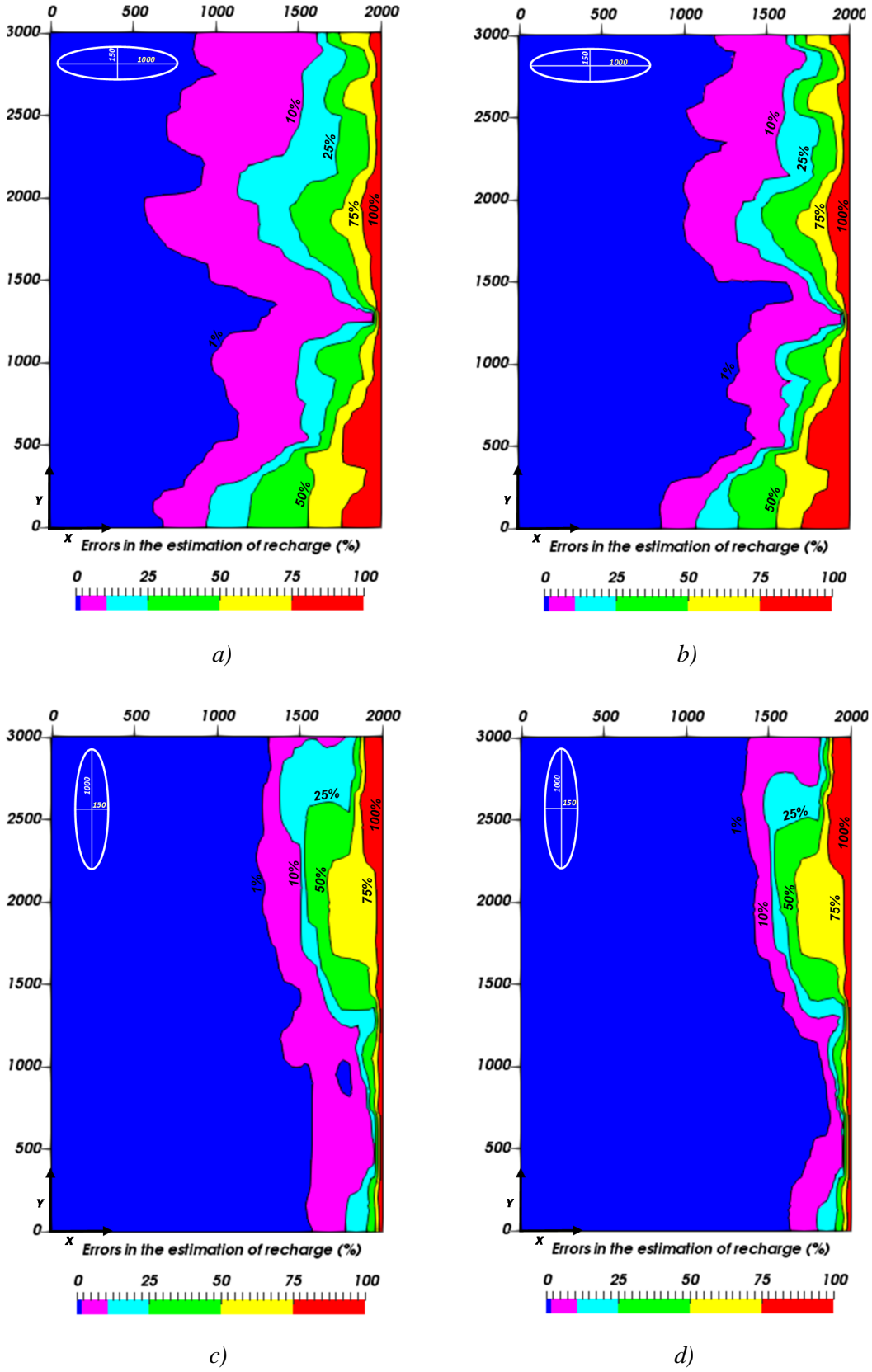

Figure A10.25. Spatial distribution of the errors made in the estimation of recharge by the WTF method when the recharge is not instantaneous (a, c) and when there is a rise of the river stage simultaneously during the recharge period of the aquifer (b, d). The anisotropy axes form an angle of 0° (a, b) and 90º (c, d) with respect to the *X* coordinate axis. The units of the model dimensions are in meters.

A10.6. CONCLUSIONS

The groundwater recharge produced by discrete precipitation events in unconfined aquifers is often estimated from data of the water table rises recorded in shallow wells when aquifer recharge is instantaneous and concentrated and the response of the hydraulic heads to the rainfall event is fast. However, , the Water Table Fluctuation (WTF) method for estimating aquifer recharge may present large uncertainties because recharge is not instantaneous and there may be other processes that can produce fluctuations of groundwater levels. In this appendix, these uncertainties have been numerically quantified by means of a numerical/parametric analysis of the water table fluctuations caused by groundwater recharge and by the variation of the level of a river in an unconfined aquifer. This analysis has been performed with 1-D and 2-D numerical flow models in homogeneous and heterogeneous aquifers.

1-D numerical flow models have been used to study the sensitivity of the hydrographs to changes in several parameter of the aquifer such as the hydraulic conductivity, the specific yield, the length and thickness of the aquifer and the temporal distribution of the recharge and variations of the river stage. The conclusions obtained from the 1-D models are the following:

- The increase in the hydraulic conductivity does not affect the maximum level rise. The recovery of levels after the recharge period is faster when K increases. Increasing the aquifer thickness has a similar effect to the increasing of the hydraulic conductivity.

- The hydraulic heads are very sensitive to variations in the specific yield. For the estimation of the groundwater recharge with the WFT method it is very important to know proper values for specific yield of the aquifer.

- The maximum level rises of the hydraulic heads caused by groundwater recharge do not depend on the aquifer length.

- Groundwater recharge estimates by WTF method with distributed recharge is smaller than the recharge estimated with instantaneous recharge although the total recharge is the same. The errors made in estimating the groundwater recharge from a hydrograph of a well located 100 m from a river may be larger than 50% when the recharge is not instantaneous.

- The estimates of groundwater recharge with the WTF method can be large near river with large rises in water level. The errors made in estimating the groundwater recharge from a hydrograph

of a well located 100 m from a river may be larger than 50% when there is a rise of the river stage simultaneously during the recharge period of the aquifer.

- The computed hydraulic heads are sensitive to changes in the leakage coefficient used in the Cauchy condition in the river.

2-D flow models have been performed to compare and verify the results obtained with the 1-D models and to study the variations of the hydraulic heads caused by groundwater recharge and the rises of the river stage in homogeneous and heterogeneous aquifers. The conclusions obtained from the 2-D models are the following:

- The hydrographs calculated with the 2-D models are always identical to those computed with the 1-D models. Therefore, the conclusion of the parametric and numerical analysis performed with 1-D models apply also to 2-D homogeneous aquifer.

- In heterogeneous and anisotropic aquifers, the hydraulic heads and, consequently, the errors made in estimating groundwater recharge with the WTF method depend on the main direction of anisotropy and the spatial connectivity of the most permeable zones near the river. The errors propagate in the main direction of anisotropy following the most permeable zones connected to the river. In the presence of anisotropy, the estimation errors may be important even at 1800 m from the river.

- The errors made in the estimation of the recharge in the numerical models where the main direction of anisotropy is perpendicular to the river are much greater than the errors made in the models in which the main direction of anisotropy is parallel to the river.

- In the models simulating a rise of the river stage simultaneously to the recharge period, the distance from the river in which errors are large is smaller than in the case where the heads are only affected by a non-instantaneous recharge.

In summary, the parametric and numerical analysis carried out indicates that the estimation of recharge from water table fluctuations (WTF method) may contain large errors, especially near a river with level rises simultaneously during the recharge period of the aquifer or when the recharge is not instantaneous. The errors made in estimating groundwater recharge with the WTF method depend on the parameters of the unconfined aquifer.

A10.7. REFERENCES

Abdulrazzak, M.J., Sorman, A.U., Alhames, A.S., (1989). Water balance approach under extreme arid conditions - a case study of Tabalah Basin, Saudi Arabia. Hydrol. Proc., 3:107-122.

Athavale, R.N., Rangarajan, R., (1988). Natural recharge measurements in the hard-rock regions of semi-arid India using tritium injection - a review. In: Simmers I (ed) Estimation of natural groundwater recharge. Reidel, Dordrecht, pp. 175-195.

Egboka, B.C.E., Cherry, J.A., Farvolden, R.N., Frind, E.O., (1983). Migration of contaminants in groundwater at a landfill: a case study. 3. Tritium as an indicator of dispersion and recharge. J. Hydrol., 63:51-80.

Flury, M., Fluhler, H., Jury, W.A., Leuenberger, J., (1994). Susceptibility of soils to preferential flow of water: a field study. Water Resour. Res., 30:1945-1954.

Freeze, R.A., Cherry, J.A., (1979). Groundwater. Englewood Cliffs, N.J., Prentice-Hall, 604.

Gómez-Hernández, J.J., Journel, A.G., (1993). Joint simulation of multi-Gaussian random variables. In Soares, A., editor, Geostatistics Tróia 92, Vol. 1, pp. 85-94. Kluwer.

Healy, R.W., Cook, P.G., (2002). Using ground-water levels to estimate recharge. Hydrogeol. J., DOI 10.1007/s10040-001-0178-0

Kearns, A.K., Hendrickx, J.M.H., (1998). Temporal variability of diffuse groundwater recharge in New Mexico. N M Water Resour. Res., Inst. Tech. Completion Rep., 309:43.

Lerner, D.N., Issar, A.S., Simmers, I., (1990). Groundwater recharge, a guide to understanding and estimating natural recharge. International Association of Hydrogeologists, Kenilworth, Rep 8, pp. 345.

Kumar, C.P., Seethapathi, P.V., (2002). Assessment of natural ground water recharge in upper Ganga canal command area. Journal of Applied Hydrology, Association of Hydrologists of India, Vol. XV, No. 4, October 2002, pp. 13-20.

Luckey, R.R., Gutentag, E.D., Heimes, F.J., Weeks, J.B., (1986). Digital simulation of ground-water flow in the High Plains aquifer in parts of Colorado, Kansas, Nebraska, New Mexico, Oklahoma, South Dakota, Texas, and Wyoming. US Geol. Surv. Prof. Pap., 1400-D: 57.

Meinzer, O.E., (1923). The occurrence of groundwater in the United States with a discussion of principles. US Geol. Surv. Water-Supply Pap., 489, pp. 321.

Meinzer, O.E., Stearns, N.D., (1929). A study of groundwater in the Pomperaug Basin, Conn. with special reference to intake and discharge. US Geol. Surv. Water-Supply Pap., 597B:73-146.

Rasmussen, W.C., Andreasen, G.E., (1959). Hydrologic budget of the Beaverdam Creek Basin, Maryland. US Geol. Surv. Water-Supply Pap., 1472, pp.106.

Samper, J., Yang, C., Montenegro, L., (2003). CORE^{2D} Version 4: A code for non-isothermal water flow and reactive solute transport. User's Manual. Universidade de A Coruña.

Samper, J., Pisani, B., (2009). Aquifer recharge evaluation by a combination of soil water balance and groundwater flow models. In: Estudios en la Zona no Saturada del Suelo. Vol. IX, O. Silva et al. Barcelona, November 18-20, 2009.

Samper, J., Xu, T., Yang, C., (2009). A sequential partly iterative approach for multicomponent reactive transport with CORE^{2D}. Comput. Geosci., http://dx.doi.org/10.1007/s10596-008-9119-5.

Samper, J., Yang, C., Zheng, L., Montenegro, L., Xu, T., Dai, Z., Zhang, G., Lu, C., Moreira, S., (2011). CORE^{2D}V4: A code for water flow, heat and solute transport, geochemical reactions, and microbial processes, Chapter 7 of the Electronic book Groundwater Reactive Transport Models, F Zhang, G-T Yeh, C Parker & X Shi (Ed), Bentham Science Publishers, pp. 161-186, ISBN: 978-1-60805-029-1.

Samper, J., Naves, A., Pisani, B., Montenegro, L., Mon., A., (2017). Estudio hidrogeológico y análisis de la viabilidad del abastecimiento con aguas subterráneas en Santa María de Oia (2ª fase). Technical report for Augas de Galicia. E.T.S.I. Caminos Canales y Puertos. Universidade da Coruña. pp. 230.

Scanlon, B.R., Goldsmith, R.S., (1997). Field study of spatial variability in unsaturated flow beneath and adjacent to playas. Water Resour. Res., 33:2239-2252.

Scanlon, B.R., Healy, R.W., Cook, P.G., (2002). Choosing appropriate techniques for quantifying ground-water recharge. Hydrogeology Journal, 10, 18-39.

Sharma, M.L., (1989). Groundwater recharge. AA Balkema, Rotterdam.

Todd, D.K., (1989). Groundwater Hydrology, Wiley: New York.

APPENDIX 11. RESUMEN

A11.1. MOTIVACIÓN, OBJETIVOS Y METODOLOGÍA

El estudio de los sistemas de aguas subterráneas, la cuantificación de la contaminación de las aguas o la evaluación de la seguridad de las instalaciones para la eliminación de residuos requieren herramientas de modelización capaces de simular simultáneamente el flujo de agua subterránea, la transferencia de calor, el transporte de solutos y reacciones químicas. Durante las últimas décadas se han realizado avances significativos en los modelos y códigos de flujo y transporte reactivo, de tal manera que ha aumentado su utilización en múltiples disciplinas, especialmente en las relacionadas con el almacenamiento de residuos radiactivos.

El principal objetivo de esta Tesis Doctoral es la actualización y mejora de los modelos de flujo y transporte reactivo en medios porosos y fracturados de baja permeabilidad para su aplicación en almacenamientos de residuos radioactivos. Para alcanzar este objetivo se ha seguido una metodología basada en la ejecución de las siguientes tareas y actividades:

1) Actualización y mejora de los modelos conceptuales y los códigos de flujo y transporte reactivo de la serie CORE desarrollados por el equipo de Javier Samper en la Universidade da Coruña desde 1991. Estas mejoras incluyen:
    - La mejora de CORE^{2D}V5 para considerar los cambios de porosidad producidos por la precipitación /disolución de minerales y sus efectos en los parámetros de flujo, transporte y químicos.
    - La actualización de CORE^{2D}V5 para permitir el uso de herramientas de post-proceso gratuitas.
    - La actualización de CORE^{2D}V5 para poder realizar modelos con transporte conservativo.
    - La actualización de CORE^{2D}V5 para escribir las velocidades de flujo y los caudales de entrada y salida por los contornos.
    - La mejora de la convergencia de CORE^{2D}V5 para la resolución de la ecuación de flujo en medios parcialmente saturados.
    - La actualización de INVERSE-CORE^{2D} para problemas con elevados números de parámetros.

- La recopilación de una base de datos de los parámetros microbiológicos de BIOCORE^{2D}.

2) La aplicación de los modelos de flujo y transporte reactivo en medios porosos y fracturados a ensayos de laboratorio y de campo. Los resultado de los modelos calculados con los códigos de la serie CORE se han comparado con datos medidos y con los resultados obtenidos con otros códigos de transporte reactivo de características similares. Se han elaborado los siguientes modelos:
   - Modelos numéricos de flujo y transporte reactivo de experimentos de laboratorio con fuertes cambios de porosidad debidos a reacciones de disolución/precipitación de minerales.
   - Modelos de transporte de una especie y varias especies para simular la sorción no lineal del cesio en la arcilla Opalinus.
   - Modelo de transporte reactivo a largo plazo de las interacciones del hormigón, la bentonita compactada, los productos de corrosión y la arcilla en un almacenamiento geológico profundo (AGP) en arcilla teniendo en cuenta los cambios de porosidad debidos a la disolución/precipitación de minerales y su efecto sobre los parámetros de flujo, transporte y químicos.
   - Modelos de flujo para simular los bombeos de aguas subterráneas en el emplazamiento del Almacén Temporal Centralizado (ATC) de Villar de Cañas (Cuenca, España).

3) La aplicación de los modelos de flujo y transporte reactivo en medios porosos y fracturados a sistemas hidrogeológicos reales relacionados con el almacenamiento de residuos radioactivos. Se han realizado los siguientes modelos:
   - Modelos 2-D en perfiles verticales a escala local y de detalle y un modelo de flujo totalmente 3-D del emplazamiento del Almacén Temporal Centralizado (ATC) de Villar de Cañas (Cuenca, España). Estos modelos numéricos se han realizado para la caracterización hidrogeológica del emplazamiento del ATC y para la realización de predicciones de los efectos de la construcción de las instalaciones nucleares sobre los niveles piezométricos.
   - Modelos de transporte de calor, de la edad del agua subterránea, de fracciones mezcla de aguas y de transporte reactivo hidrogeoquímico en el emplazamiento del ATC.
   - Modelos 1-D y 2-D determinísticos y estocásticos para el análisis paramétrico y numérico de la estimación de la recarga subterránea a partir de fluctuaciones del nivel freático en acuíferos libres. Estos modelos se aplicaron al estudio de la recarga en el aluvial del río Guadalquivir en Andújar (Jaén, España) en el entorno de la fábrica de uranio de Andújar (FUA).

A11.2. MEJORAS, ACTUALIZACIONES, CORRECCIONES Y EXTENSIONES DE LOS CÓDIGOS DE LA SERIE CORE

Se han realizado mejoras, actualizaciones, correcciones y se han extendido las capacidades de los códigos de la serie CORE de la UDC. La mayoría de las mejoras se han realizado en el código CORE^{2D}V5, aunque también se realizaron actualizaciones en otros códigos tales como INVERSECORE^{2D}, BIOCORE^{2D} y CORE^{3D} (TRANMEF). Las mejoras introducidas en los códigos facilitarán la realización de modelos de flujo y transporte reactivo y el análisis de los resultados. Los detalles de las mejoras introducidas en los códigos de la serie CORE se presentan en el Apéndice 1.

Mención especial merecen las mejoras introducidas en CORE^{2D}V5 relacionadas con los cambios de porosidad y su verificación. CORE^{2D}V5 se ha ampliado para tener en cuenta los cambios de la porosidad debidos a la disolución/precipitación de minerales y actualizar también los parámetros de flujo, transporte y químicos. Las mejoras realizadas en el código se han verificado con soluciones analíticas en 1-D (Hayek et al., 2011) y 2-D (Hayek et al., 2012) y mediante comparación con otros códigos de transporte reactivo (Xie et al., 2015). En el Apéndice 2 se muestran los detalles de las mejoras realizadas en CORE^{2D}V5 para tener en cuenta las variaciones de la porosidad y los casos de verificación utilizados.

Los cambios de porosidad debidos a los procesos de disolución/precipitación de minerales son relevantes en los almacenamientos geológicos profundos (AGP) de residuos radioactivos en los que están en contacto materiales químicamente diferentes como las arcillas y los hormigones. El modelo de transporte reactivo no isotermo de las interacciones de la bentonita compactada, los productos de corrosión del contenedor, el hormigón y la formación arcillosa de un AGP en arcilla de Mon et al. (2017) se ha perfeccionado en esta Tesis Doctoral teniendo en cuenta los cambios de porosidad debidos a la disolución/precipitación de minerales. Se han comparado los resultados de predicciones a 40000 años realizadas con un modelo que tiene en cuenta las variaciones de la porosidad con las obtenidas con el modelo de Mon et al. (2017) que no considera la actualización de la porosidad. Ambos modelos muestran diferencias. Las mayores diferencias en las porosidades calculadas por ambos modelos se producen en el hormigón y en las interfaces hormigón-arcilla y contenedor-bentonita. El espesor afectado por la colmatación de los poros en el hormigón y en la interfaz hormigón-arcilla calculado con el modelo que considera la actualización de la porosidad es menor que el calculado sin actualizar la porosidad. Los detalles de la comparación de ambos modelos se muestran en el Capítulo 3.

A11.3. MODELOS DE FLUJO Y TRANSPORTE REACTIVO DE ENSAYOS DE LABORATORIO CON FUERTES CAMBIOS DE POROSIDAD

La versión actualizada de CORE^{2D}V5 se ha utilizado para simular experimentos de laboratorio con cambios de porosidad producidos por la disolución/precipitación de minerales. Los experimentos fueron realizados en el Paul Scherrer Institut (Suiza) en un tanque que contiene una capa reactiva de celestita ($SrSO_4$(s)) entre dos capas inertes de arena de cuarzo (SiO_2(s)) (Poonoosamy et al., 2015). Se han simulado los dos siguientes experimentos de laboratorio con modelos numéricos bidimensionales: 1) Un modelo de transporte conservativo (Caso 1) y 2) Un modelo de transporte reactivo con cambios de porosidad (Caso 2).

El Caso 1 corresponde a un pulso de un trazador conservativo inyectado por la entrada del tanque. La evolución de la concentración del trazador en el tanque se controló durante 20 horas. El código CORE^{2D}V5 se utilizó para calcular las curvas de llegada del trazador en varios puntos de muestreo, la evolución temporal del trazador en el tanque y las velocidades a lo largo de varias líneas. Los valores calculados se compararon con los datos medidos en el laboratorio y con los valores calculados con otros códigos de transporte reactivo (TOUGHREACT, OpenGeoSys-GEM, Pflotran and MIN3P). Los resultados obtenidos con CORE^{2D}V5 son similares a los proporcionados por otros códigos, aunque existen ligeras diferencias debidas a diferencias en los métodos numéricos utilizados por cada código.

El Caso 2 corresponde a la inyección de una solución de $BaCl_2$ que provoca la disolución de celestita y la precipitación de barita ($BaSO_4$). La porosidad se reduce en la zona reactiva debido a que los volúmenes molares de la barita y la celestita son diferentes. El experimento fue realizado durante 300 horas. Las cantidades totales de los minerales $BaSO_4$(s) y $SrSO_4$(s) en el tanque y las concentraciones disueltas de Cl^-, Sr^{2+} y Ba^{2+} calculadas con CORE^{2D}V5 son similares a las obtenidas con los otros códigos de transporte reactivo. Además, los cambios de porosidad y permeabilidad calculados con CORE^{2D}V5 son similares a los cambios simulados con otros códigos. Hay diferencias en los valores calculados en las interfaces. Un análisis de sensibilidad realizado con CORE^{2D}V5 a la discretización de la malla de elementos finitos confirmó que las diferencias en las porosidades y permeabilidades en las interfaces se deben al diferente grado de discretización espacial de cada código.

Los detalles de los modelos numéricos de flujo y transporte reactivo de los ensayos de laboratorio con fuertes cambios de porosidad debidos a la disolución/precipitación de minerales se muestran en el Apéndice 3.

A11.4. MIGRACIÓN DEL CESIO A TRAVÉS DE LA ARCILLA OPALINUS CALCULADA CON MODELOS DE TRANSPORTE DE UNA ESPECIE Y VARIAS ESPECIES

Se han realizado modelos de transporte de una y varias especies con CORE^{2D}V5 para simular la sorción no lineal del cesio (Cs) en la arcilla Opalinus. Los modelos numéricos se basan en los trabajos realizados por Jakob et al. (2009) y en los ensayos de difusión realizados en el Paul Scherrer Institut (Suiza). Se trata de experimentos de laboratorio de sorción y difusión de Cs a través de una muestra de arcilla Opalinus desde un depósito con una concentración elevada de Cs (10^{-3}, 10^{-5} y 10^{-7} mol/L) hacia otro depósito con una concentración de Cs más baja (10^{-10} mol/L).

En el modelo de una especie se ha utilizado una isoterma de sorción tabulada medida en laboratorio (Van Loon et al., 2009). Se modificó CORE^{2D}V5 para implementar una tabla de valores de K_d en función de la concentración de Cs. Las curvas de llegada de Cs a varios puntos en la arcilla Opalinus calculadas con CORE^{2D}V5, COMSOL Multiphysics y MCOTAC son en general coincidentes. Sin embargo, hay ligeras diferencias debido a: 1) Las diferencias en la discretización espacial utilizada en los diferentes modelos, 2) Las diferentes implementaciones de la isoterma de sorción en los códigos y 3) Las diferencias en los procedimientos de interpolación.

En el segundo modelo, la sorción del Cs en la arcilla Opalinus se simuló con un modelo de transporte reactivo multicomponente con tres lugares de intercambio catiónico (Bradbury y Baeyens, 2000). Las curvas de llegada del Cs calculadas con CORE^{2D}V5 en varios puntos de la arcilla Opalinus son similares a las calculadas con el código MCOTAC. Existen ligeras diferencias debido a las diferencias en la discretización espacial utilizada en los dos modelos.

Las curvas de llegada del Cs en varios puntos de la arcilla Opalinus calculadas con CORE^{2D}V5 con los modelos de una y de varias especies son en general muy similares.

El Apéndice 4 muestra los detalles de los modelos realizados para simular la sorción no lineal del Cs en la arcilla Opalinus.

A11.5. MODELOS DE FLUJO PARA EL ANÁLISIS DE BOMBEOS REALIZADOS EN EL EMPLAZAMIENTO DEL ATC DE VILLAR DE CAÑAS

El 30 de diciembre de 2011, el Gobierno de España designó al municipio de Villar de Cañas (Cuenca) como sede para la construcción del Almacén Temporal Centralizado (ATC) que albergará el combustible gastado de las centrales nucleares españolas y los residuos radioactivos de alta actividad durante al menos 60 años. Desde comienzos de 2012, ENRESA (Empresa Nacional de Residuos Radioactivos S.A.) ha estado trabajando en la caracterización de los terrenos donde se construirá el ATC. Como parte de los trabajos de caracterización, la Universidade da Coruña ha elaborado varios modelos matemáticos. Estos modelos constituyen una parte importante de la Tesis Doctoral.

Se han realizado dos modelos de flujo 2-D en planta para simular el bombeo de aguas subterráneas en el emplazamiento del ATC. El primer modelo se utilizó para simular un ensayo de bombeo de larga duración que se realizó en la vaguada localizada al este de la zona nuclear del ATC. El modelo numérico de este ensayo sirvió para interpretar los datos de los descensos medidos, obtener los parámetros hidrogeológicos de los materiales del subsuelo y definir la extensión espacial de los Yesos de Balanzas (YB) afectados por procesos de disolución. El segundo modelo numérico se realizó para cuantificar los efectos del bombeo en el pozo de abastecimiento del ATC del Chaparral sobre las condiciones hidrogeológicas en la zona nuclear del ATC.

Los modelos de flujo 2-D en planta para simular el bombeo de aguas subterráneas en el emplazamiento del ATC en Villar de Cañas (Cuenca, España) están sujetos a protección de datos debido al compromiso de confidencialidad establecido con ENRESA. Por ello, los modelos realizados en el ATC no se incluyen en la versión reducida de la Tesis Doctoral. Los modelos de flujo de los bombeos de aguas subterráneas en el emplazamiento del ATC de Villar de Cañas se describen en detalle en el Apéndice 5 de la versión completa de la Tesis Doctoral. En el Apéndice 5 de la versión reducida de la Tesis Doctoral se presenta solamente un breve resumen de dichos modelos.

A11.6. MODELOS DE FLUJO 2-D EN PERFILES VERTICALES A ESCALA LOCAL Y DE DETALLE EN EL EMPLAZAMIENTO DEL ATC DE VILLAR DE CAÑAS

Se han realizado tres modelos numéricos de flujo 2-D en perfiles verticales en el emplazamiento del ATC de Villar de Cañas a escala local y de detalle. El primer modelo se realizó en un perfil vertical en dirección E-W a escala local. Los otros dos modelos se realizaron en perfiles verticales en dirección E-W y N-S a escala de detalle. Los modelos numéricos se realizaron dentro de las actividades de caracterización hidrogeológica del emplazamiento del ATC para cuantificar las posibles afecciones de la construcción del ATC sobre las condiciones hidrogeológicas del entorno.

Los modelos numéricos en perfiles verticales en el emplazamiento del Almacén Temporal Centralizado (ATC) de Villar de Cañas (Cuenca, España) están sujetos a protección de datos debido al compromiso de confidencialidad establecido con ENRESA. Por ello, estos modelos no se incluyen en la versión reducida de la Tesis Doctoral. El modelo en el perfil vertical en dirección E-W a escala local en el emplazamiento del ATC se describe en el Apéndice 6 de la versión completa de la Tesis Doctoral. Por otro lado, los modelos en perfiles verticales en dirección E-W y N-S a escala de detalle en el emplazamiento del ATC se describen en el Apéndice 7 de la versión completa de la Tesis Doctoral. Los Apéndices 6 y 7 de la versión reducida de la Tesis Doctoral presentan unos breves resúmenes de dichos modelos.

A11.7. MODELO DE FLUJO 3-D A ESCALA LOCAL EN EL EMPLAZAMINETO DEL ATC DE VILLAR DE CAÑAS

El flujo subterráneo en la zona en la que está previsto construir el ATC de Villar de Cañas tiene un carácter tridimensional. Se ha realizado un modelo de flujo totalmente 3-D a escala local que forma parte de los trabajos de caracterización del emplazamiento del ATC. El modelo 3-D se realizó con el código de elementos finitos CORE^{3D}-TRANMEF.

El modelo de flujo 3-D del emplazamiento del ATC está sujetos a protección de datos debido al compromiso de confidencialidad establecido con ENRESA. Por ello, dicho modelo no se incluye en la versión reducida de la Tesis Doctoral. El modelo de flujo totalmente 3-D a escala local del ATC se describe en detalle en el Apéndice 8 de la versión completa de la Tesis Doctoral. En el Apéndice 8 de la versión reducida de la Tesis Doctoral se presenta solamente un breve resumen de dicho modelo.

A11.8. MODELOS DE CALOR, EDAD DEL AGUA, HIDROGEOQUÍMICOS DE MEZCLA Y TRANSPORTE REACTIVO EN EL EMPLAZAMIENTO DEL ATC

Las tareas de caracterización del emplazamiento del ATC han incluido numerosos estudios sobre la geología, hidrogeología, topografía, meteorología, geotecnia y geoquímica. Toda esta información se ha integrado en varios modelos numéricos realizados con el código CORE^{2D}V5. Estos modelos incluyen: 1) Un modelo de transporte de calor en el perfil vertical en dirección E-W a escala local, 2) Modelos numéricos de transporte para simular la edad del agua subterránea, 3) Un modelo hidrogeoquímico de mezcla de aguas para cuantificar las fracciones de mezcla, 4) Un modelo 1-D de transporte reactivo multicomponente para contrastar el modelo conceptual hidrogeoquímico del ATC formulado por el CIEMAT (Gómez et al., 2013; 2014; 2016) y 5) Un modelo 2-D de transporte reactivo multicomponente para estudiar los procesos de disolución de yesos en el contacto entre las formaciones Yesos de Balanzas y Unidad Inferior lejos de la zona nuclear del ATC.

Los modelos citados anteriormente están sujetos a protección de datos debido al compromiso de confidencialidad establecido con ENRESA. Por ello, dichos modelos no se incluye en la versión reducida de la Tesis Doctoral. Estos modelos se describen en detalle en el Apéndice 9 de la versión completa de la Tesis Doctoral. El Apéndice 9 de la versión reducida de la Tesis Doctoral presenta solamente un breve resumen de dichos modelos.

A11.9. ANÁLISIS PARAMÉTRICO/NUMÉRICO DE LA ESTIMACIÓN DE LA RECARGA SUBTERRÁNEA A PARTIR DE FLUCTUACIONES DEL NIVEL FREÁTICO

La recarga subterránea producida por eventos discretos de precipitación en acuíferos libres se suele estimar a partir de los ascensos de nivel freático registrados en pozos someros. Sin embargo, este método puede presentar importantes incertidumbres. En esta Tesis Doctoral se han cuantificado estas incertidumbres mediante un análisis paramétrico y numérico de las oscilaciones del nivel freático producidas por la recarga subterránea y la variación del nivel de un río en un acuífero libre. El análisis ha sido realizado con modelos de flujo 1-D y 2-D en acuíferos homogéneos y heterogéneos con una distribución espacial de la conductividad hidráulica generada mediante simulaciones geoestadísticas.

Los errores cometidos al estimar la recarga a partir de las variaciones del nivel freático han sido calculados analizando los hidrogramas de niveles a varias distancias de un río simulado en uno de los extremos del modelo. Los modelos 1-D se han utilizado para evaluar cómo varían los hidrogramas al variar: 1) Los parámetros hidráulicos del acuífero (conductividad hidráulica, coeficiente de almacenamiento y espesor del acuífero); 2) La longitud del acuífero perpendicular al río; 3) La distribución temporal de la recarga; y 4) Las variaciones del nivel del río. Los errores cometidos al estimar la recarga dependen de las propiedades del acuífero. Sin embargo, del análisis paramétrico/numérico realizado se puede concluir que los errores cometidos al estimar la recarga a partir de fluctuaciones del nivel freático en pozos cercanos a ríos pueden ser muy importantes cuando la recarga no es instantánea y/o se producen variaciones del nivel del río simultáneamente al periodo de recarga. Además, modelos 1-D han sido realizados utilizando valores reales de los parámetros hidráulicos del aluvial del río Guadalquivir en Andújar (Jaén, España) donde una fábrica de uranio (FUA) estuvo operativa hasta 1981. El modelo reveló la importancia de la heterogeneidad del medio cuando se estima la recarga subterránea a partir de las variaciones del nivel freático en acuíferos libres.

Los modelos 2-D simulando acuíferos heterogéneos y anisótropos indicaron que los errores cometidos cuando la recarga es estimada a partir de variaciones del nivel freático dependen de la dirección principal de anisotropía y de la conectividad de las zonas más permeables cerca del río. Los errores cometidos se propagan en la dirección principal de anisotropía siguiendo las zonas más permeables desde el río. En los modelos numéricos donde la dirección principal de anisotropía es perpendicular al río, los errores cometidos en la estimación de la recarga son mucho mayores que los errores estimados en los modelos en los que la dirección principal de anisotropía es paralela al río.

El Apéndice 10 describe el análisis paramétrico/numérico realizado para cuantificar los errores cometidos al estimar la recarga subterránea a partir de variaciones del nivel freático en acuíferos libres.

A11.10. REFERENCIAS

Bradbury, M.H., Baeyens, B., (2000). A generalised sorption model for the concentration dependent uptake of caesium by argillaceous rocks. J. Contam. Hydrol. 42, 141–163.

Gómez, P., Peña, J., Garralón, A., Torres, E., Buil, B., Turrero, M.J., Robredo, L.M., Domínguez, R., Durán, J.M., Escribano, A., Sánchez, L., (2013). Estudio hidrogeológico del emplazamiento del Almacén Centralizado Temporal (ATC) en Villar de Cañas (Cuenca). Technical Report for ENRESA. CIEMAT, Madrid, 88 pp.

Gómez, P., Peña, J., Torres, E., Buil, B., Garralón, A., Turrero, M.J., Escribano, A., Domínguez, R., Durán, J.M., Sánchez, L., (2014). Estudio hidrogeológico del emplazamiento del Almacén Centralizado Temporal (ATC) en Villar de Cañas (Cuenca). Technical Report for ENRESA. CIEMAT, Madrid, 90 pp.

Gómez, P., Torres, E., Peña, J., Garralón, A., Turrero, M.J., Buil, B., Durán, J.M., Escribano, A., Sánchez, L., Domínguez, R., (2016). Actualización del Modelo Hidrogeoquímico del ATC (Villar de Cañas, Cuenca). Technical Report for ENRESA. CIEMAT, Madrid, 116 pp.

Hayek, M., Kosakowski, G., Churakov, S., (2011). Exact analytical solutions for a diffusion problem coupled with precipitation–dissolution reaction and feedback of porosity change. Water Resour. 47, W07545. http://dx.doi.org/10.1029/2010WR010321.

Hayek, M., Kosakowski, G., Jakob, A., (2012). A class of analytical solutions for multidimensional species diffusive transport coupled with precipitation–dissolution reactions and porosity changes. Water Resour. 48, W03525. http://dx.doi.org/10.1029/2011WR011663.

Mon, A., Samper, J., Montenegro, L., Naves, A., Fernández, J., (2017). Long-term non-isothermal reactive transport model of compacted bentonite, concrete and corrosion products in a HLW repository in clay. J. Contam. Hydrol. https://doi.org/10.1016/j.jconhyd.2016.12.006

Jakob, A., Pfingsten, W., Van Loon, L., (2009). Effects of sorption competition on caesium diffusion through compacted argillaceous rock. Geochimica et Cosmochimica Acta 73, 2441-2456

Poonoosamy, J., Kosakowski, G., Van Loon, L. R. and Mäder, U., (2015). Dissolution-precipitation processes in tank experiments for testing numerical models for reactive transport calculations: Experiment and modelling. J. Contam. Hydrol., 177-178, 1-17.

Van Loon, L.R., Baeyens, B., Bradbury, M.H., (2009). The sorption behaviour of caesium on Opalinus clay: A comparison between intact and crushed material. Appl. Geochem. 24, 999-1004.

Xie, M., Mayer, K.U., Claret, F., Alt-Epping, P., Jacques, D., Steefel, C., Chiaberge, C., Simunek, J., (2015). Implementation and evaluation of permeability-porosity and tortuosity-porosity relationships linked to mineral dissolution-precipitation. Computat. Geosci., 19, 655-671.